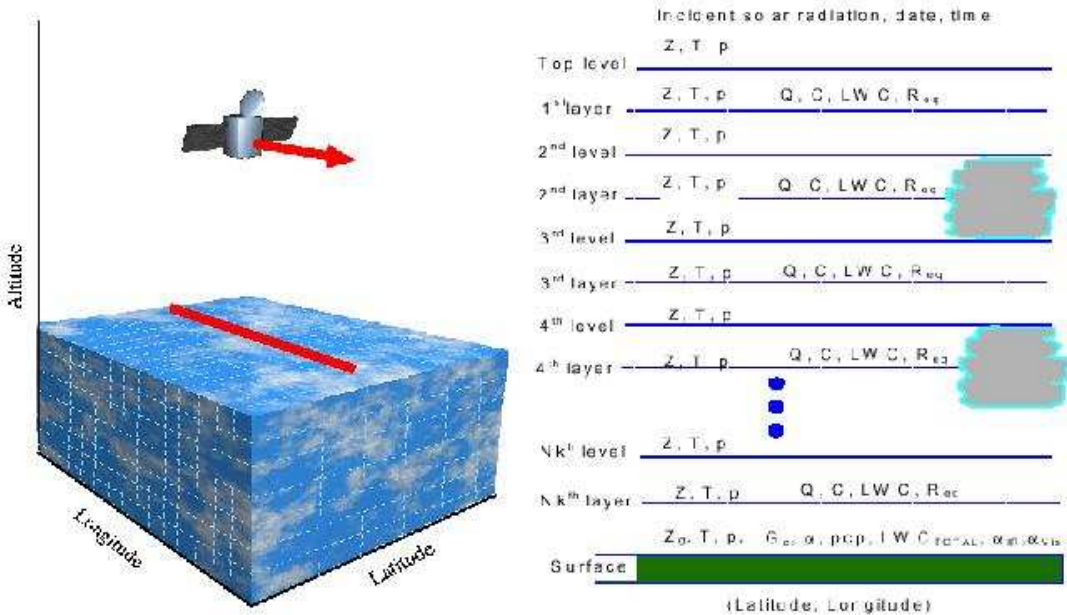


The EarthCARE Simulator

Users Guide and Final Report



ESA: Contract No. 15346/01/NL/MM

Authors

D. P. Donovan, Royal Netherlands Meteorological Institute (KNMI)
PO Box 201, De Bilt, 3730 AE
The Netherlands
donovan@knmi.nl

N. Schutgens ¹, G-J. Zadelhof, Royal Netherlands Meteorological Institute (KNMI)
J-P.V. Poaires Baptista, ESA/ESTEC, Noodwijk, The Netherlands
H. Barker, Meteorological Service of Canada (MSC).
J-P. Blanchet, A. Belaulne ², W. Symeyer. University de Quebec au Montreal (UQAM).
M. Quante, GKSS center for Coastal Research.
I. Schimmer, A. Macke, University of Kiel
J. Testud, C. Tinel ³, Center des Etudes Terrestries et Planetaires, university de Versailles St. Quentin (CETP-UVSQ)
S. Kato, J. Cole ⁴, Penn. State University

¹Now at NICT, Toyko, Japan

²Now at MSC, Montreal, Canada

³Now at ESA/ESTEC, Noordwijk, The Netherlands

⁴Now at MSC, Toronto, Canada

Contents

1	Introduction	1
1.1	Background	1
1.2	General Overview	2
1.2.1	Relationship with the ERM simulator	3
2	Theory	6
2.1	Lidar	7
2.1.1	Basic Considerations	7
2.1.2	Multiple Scattering	8
2.1.3	Polarization Sensitivity	9
2.2	High Spectral Resolution Lidar	11
2.2.1	Effect of Multiple Scattering	14
2.2.2	Lidar Monte-Carlo Calculations	15
2.2.3	Comparison with model of Eloranta	19
2.3	Lidar Instrument Considerations	22
2.3.1	Background Signal	22
2.3.2	Receiver Optical Elements	22
2.3.3	Noise Considerations	24
2.4	Radar	25
2.5	Radar Instrument Considerations	26
2.6	The attenuation due to atmospheric gases.	26
2.7	Simulating the radar instrument	27
2.7.1	Atmospheric Attenuation	28
2.7.2	Footprint Averaging	28
2.7.3	Noise	28
2.7.4	Effect of pulse width (range weighting)	29
2.7.5	The vertical sampling frequency	30
2.8	Short-wave Radiation Calculations	32
2.9	Long-wave Radiation Calculations	35
2.10	Lidar+Radar Level 1 retrievals	37
2.11	MSI only retrievals	38
2.12	Combined Active+Passive 3-D retrievals	39
2.12.1	Cost Function	39
2.12.2	Expansion to 3-D domain	43
3	Using the the package	45
3.1	Package Overview	45
3.2	Executables	47
3.2.1	Screen output	48
3.3	Master Input	50
3.4	Orbit File	51
3.5	Scattering Libraries	53
3.6	Scene Creation	56
3.6.1	<code>scene_creator</code>	56
3.6.2	Input Background atmospheric data	62
3.6.3	Additional trace gas information	62
3.6.4	Using files to specify the size distributions	63
3.6.5	Scene (UFF) file format	63

	2013	
3.7	UFF File Manipulation	64
3.7.1	uff_averager	64
3.7.2	uff_merger	65
3.8	Data extraction programs	67
3.8.1	extract_quantity	67
3.8.2	extract_quantity_hor	68
3.8.3	extract_quantity_3d	69
3.8.4	extract_env_profile	70
3.9	Forward Model Programs	71
3.9.1	rad_filter	71
3.9.2	radar	72
3.9.3	lid_filter	74
3.9.4	lidar	76
3.9.5	MC_sim_main	81
3.9.6	MC_LW_sim_main	85
3.10	Retrieval Programs	90
3.10.1	lidar_ret1	90
3.10.2	msi_ret	97
3.10.3	lw_msi_lidar_radar	99
3.11	Plotting programs	103
3.11.1	plot_slice	103
3.11.2	plot_profile	104
3.11.3	plot_profile_comp	105
3.11.4	plot_3d	107
3.11.5	mcrad_quick_plot	108
4	Example Results	109
4.1	Simple Scene results	109
4.2	Sample UQAM thin-cirrus results	120
4.3	Sample UQAM strato-cumulus results	129
4.4	Sample UQAM Frontal system results	138
4.5	Lidar HSR Aerosol Measurement Example	147
4.6	Multiple scattering Ecare-vs-Calypsio	148
4.7	Stratocummulus: Ecare Radar vs. CLOUDSAT Results	150
5	Conclusions	151
A	Installation	154
A.1	Unix/Linux	154
A.2	MS Windows	155
A.3	Compiler and Platform notes:	157
B	Example scattering master list file	158
C	Example 1-D background atmospheric data input to scene_creator	163
D	Example 3-D background atmospheric data input to scene_creator	164
E	3-D Cloud/Aerosol data input to scene_creator	166
F	Example ASCII UFF file	167

G Example CLOUDSAT and EarthCARE radar Stratocummulus views.	172
H RCM/NARCM/CRM model description	176
H.1 Cloud Resolving Model Version (CRM)	176
H.2 NARCM Version of RCM	178
H.3 References	180
I Generation of the cloud scenes	182
I.1 Cloud types	182
I.1.1 Stratocumulus with Drizzle	186
I.1.2 Cumulus Clouds	186
I.1.3 Cirrus Clouds	186
I.1.4 Bulk microphysics for cirrus	187
I.2 References	198

List of Figures

1	Illustration of the simulation concept.	2
2	Total end-to-end simulation procedure.	3
3	Difference in logical structure between (left) the ERM simulator and (right) the EarthCARE simulator.	4
4	The simulator forward models all draw on information from the UFF file which is combined with information from the common library data.	4
5	Contributions of the first three scattering orders to the lidar return signal	9
6	Idealized view of spectral signature of a lidar return.	11
7	Rayleigh-Brillouin profiles for various y -parameters. x is a normalized frequency parameter.	12
8	Idealized view of space-based HSR lidar returns from a cloud.	13
9	Geometry relevant for determining the observed Doppler shift after multiple scatters.	14
10	(Bottom Panel) Exact Rayleigh-Brillouin line shape (Solid-Line) along with fitted sum of three Gaussian functions (Dashed Dotted line). The three component Gaussian functions are also shown. Here the y parameter is equal to 1.0. The top panel shows the difference between the fitted function and the exact calculation.	16
11	Most photon packet paths fall into CASE 1. However rare events (CASE 2) occur and lead to large fluctuations in the average power. Using effective symmetric phase functions increases the effective number of CASE 2 type events while making the contribution of CASE 1 and CASE 2 type event similar in magnitude thus greatly improving the convergence properties.	17
12	Schematic representation of the various types of paths involving forward and backscatter events for second and third order scattering and their relative contribution to the return signal.	18
13	Exact Monte-Carlo calculation of the first 4 scattering orders from a model cirrus cloud (Top left) along with spectral profile and polarization state (Right Top Panels). The Bottom panels show the results when the approximation discussed in the text is invoked. The ‘spike’ in the top left panel has been produced by a Rayleigh backscatter event followed by a forward scatter back to the lidar receiver (see Fig. 11).	20
14	Comparison between the MC results of total power and the results predicted by the model of Eloranta for (Left) an aircraft mounted lidar operating at a height of 15.0 km with a full-angle field-of-view of 5.0 mrad while the left panel shows the results for the EarthCARE configuration (altitude of 450 km and a fov of 0.0735 mrad). the Cirrus cloud in both cases has an effective particle size of 25 micron and an extinction coefficient of 1/km.	21
15	Etalon reflection and transmission showing non-ideal behavior.	23
16	Absorption coefficient of oxygen and water vapor for a water vapor density of 7.5 gm^{-3} and a pressure of 1 atmosphere (Altschuler and Marr, 1998).	26
17	Attenuation by water vapor in dB/km as a function of temperature for four different values of relative humidity (100, 75, 50 and 25% respectively). The curves labelled ‘U’ denote calculations based on the formulation of Ulaby while the curves labelled ‘L’ are based on the results of Liebe.	27
18	Schematic representation of the averaging carried out over the horizontal reflectivity field for each altitude level according to the radar instrument footprint.	29
19	Losses induced by the Hamming window for different values of α	30

20	Number of independent samples as a function of pulse duration (abscissa) and weighing function (solid lines)	31
21	Point Target Response (PTR) and Impulse Response (IR) for a range resolution Δr normalized to 1.	31
22	Schematic view of the Short-Wave Monte-Carlo approach used.	32
23	Schematic showing how the location in a cloud of different photon trajectories relative to a sensor can result in dramatically different contributions to a radiance estimate. The photon at A is moving away from the sensor and is deep inside the cloud. Thus, its chance of being scattered toward the sensor and making it out of the cloud is low. The photon at B, on the other hand, is moving toward the sensor and experiences a scattering event close to a cloud edge. Thus, its chance of being scattered toward the sensor and making it out of the cloud is extremely high.	33
24	2.2 micron verses 0.6 micron brdfs as a function of cloud optical depth and mode width parameter for (Left) hexagonal columns and (Right) water droplets.	34
25	Schematic view of the Inverse Long-Wave Monte-Carlo approach used.	35
26	Brightness temperature difference arches generated using the long-wave Monte-Carlo code for (Left) hexagonal columns and (Right) water droplets.	36
27	Schematic illustration of how the retrieval resolution volume may be subdivided on a smaller scale.	41
28	Expanding the 2-D profile information to fill a 3-D domain based on finding the “best-match” among the nadir pixels and the off-nadir pixels using the IR brightness temperatures.	44
29	Directory structure of the EarthCARE simulator package.	46
30	Screen shot of <code>scene_creator</code> running.	49
31	A three-dimensional view in terms of optical extinction of the scene created by <code>scene_creator</code> using the input file: <code>./input/scene_creator/scene.inp</code>	61
32	Three dimensional view (left) of a simple scene generated using the <code>scene_creator</code> application with ice cloud, water stratus cloud and aerosol present. The right panels show cross section of water content, effective radius, and true reflectivity respectively.	109
33	Optical depth and average effective radius for the scene depicted in 32.	110
34	Lidar co-polar Mie signal (Top), Co-Polar Rayleigh signal (Middle), Lidar total cross-polar signal (Bottom) for the simple scene depicted in Fig. 32.	112
35	Mie signal, Rayleigh signal and radar reflectivity at 1 km horizontal resolution.	113
36	Lidar only (Top), Radar only (Middle) and combined cloud mask (Bottom)	114
37	Retrieved lidar extinction and backscatters.	115
38	Short Wave MSI BRDFs. Top left Band 1 (660 nm), Top right, Band 2 (865 nm), Bottom left, Band 3 (1.61 microns) , Bottom right (2.2 microns).	115
39	Results of Short Wave MSI retrievals. (Top) Target classification, 11 denotes water, while blue denotes ice. (Middle) Optical depth. (Bottom) Cloud particle effective radius.	116
40	Long Wave MSI brightness temperatures. (Top) Channel 5 (8.85 microns), (Middle) Channel 6 (10.85 microns) and (Bottom) Channel 7 (11.85 microns).	117
41	Three dimensional view of the original and reconstructed scenes. The panels shows cross sections of water content, effective radius, and reflectivity respectively.	118
42	Three dimension view of the extinction field of the thin cirrus example. The right panels show cross section of water content, effective radius, and true reflectivity respectively.	120

43	Optical depth and average effective radius for the scene depicted in Fig. 4.2 .	121
44	Lidar co-polar Mie signal (Top), Co-Polar Rayleigh signal (Middle), Lidar total cross-polar signal (Bottom) for the scene depicted in Fig. 4.2.	122
45	Mie signal, Rayleigh signal and radar reflectivity at 1km horizontal resolution.	123
46	Lidar only (Top), Radar only (Middle) and combined cloud mask (Bottom) .	124
47	Retrieved lidar extinction and backscatters.	125
48	Short Wave MSI BRDFs. Top left Band 1 (660 nm), Top right, Band 2 (865 nm), Bottom left, Band 3 (1.61 microns) , Bottom right (2.2 microns)	125
49	Results of Short Wave MSI retrievals	126
50	Long Wave MSI brightness temperatures. (Top) Channel 5 (8.85 microns), (Middle) Channel 6 (10.85 microns) and (Bottom) Channel 7 (11.85 microns).	127
51	Three dimensional view of the original and reconstructed scenes. The panels show cross section of water content, effective radius, and reflectivity respectively.	128
52	Three dimension view of the extinction field of the Stratocumulus example. The right panels show cross section of water content, effective radius, and true reflectivity respectively.	129
53	Optical depth and average effective radius for the scene depicted in 4.3.	130
54	Lidar co-polar Mie signal (Top), Co-Polar Rayleigh signal (Middle), Lidar total cross-polar signal (Bottom) for the scene depicted in Fig. 4.3.	131
55	Mie signal, Rayleigh signal and radar reflectivity at 1km horizontal resolution.	132
56	Lidar only (Top), Radar only (Middle) and combined cloud mask (Bottom) .	133
57	Retrieved lidar extinction and backscatters.	134
58	Short Wave MSI BRDFs. Top left Band 1 (660 nm), Top right, Band 2 (865 nm), Bottom left, Band 3 (1.61 microns) , Bottom right (2.2 microns).	134
59	Results of Short Wave MSI retrievals	135
60	Long Wave MSI brightness temperatures. (Top) Channel 5 (8.85 microns), (Middle) Channel 6 (10.85 microns) and (Bottom) Channel 7 (11.85 microns).	136
61	Three dimensional view of the orginal and reconstructed scenes. The panels show cross section of water content, effective radius, and reflectivity respectvly.	137
62	Three dimension view of the extinction field of the frontal system example. The right panels show cross section of water content, effective radius, and true reflectivity respectvly.	138
63	Optical depth and average effective radius for the scene depicted in Fig. 4.4 .	139
64	Lidar co-polar Mie signal (Top), Co-Polar Rayleigh signal (Middle), Lidar total cross-polar signal (Botton) for the scene depicted in Fig. 4.4.	140
65	Mie signal, Rayleigh signal and radar reflectivity at 1km horizontal resolution.	141
66	Lidar only (Top), Radar only (Middle) and combined cloud mask (Bottom) .	142
67	Retrieved lidar extinction and backscatters.	143
68	Short Wave MSI BRDFs. Top left Band 1 (660 nm), Top right, Band 2 (865 nm), Bottom left, Band 3 (1.61 microns) , Bottom right (2.2 microns).	143
69	Results of Short Wave MSI retrievals	144
70	Long Wave MSI brightness temperatures. (Top) Channel 5 (8.85 microns), (Middle) Channel 6 (10.85 microns) and (Bottom) Channel 7 (11.85 microns).	145
71	Three dimensional view of the original and reconstructed scenes. The panels show cross section of water content, effective radius, and reflectivity respectively.	146
72	Rayleigh and Mie signals (Left) and retrieved backscatter (Middle) and extinction profile (Right). The dashed dark line in the left panel shows the Rayleigh signal that would be expected if aerosol attenuation was not present. The solid dark lines present in the middle and right panels show the ‘true’ values.	147

73	Comparison between the MC results of total power and the results predicted by the model of Eloranta for (Left) the EarthCARE configuration (altitude of 450 km and a full-angle fov of 0.0735 mrads) and (Right) a configuration similar to CALYPSIO ($\lambda = 532\text{nm}$, altitude=705 km, full-angle fov 0.13 mrads) the Cirrus cloud in both cases has an effective particle size of 25 micron and an extinction coefficient of 1/km.	148
74	Comparison between the MC results of total power and the results predicted by the model of Eloranta for (Left) the EarthCARE configuration (altitude of 450 km and a full-angle fov of 0.0735 mrads) and (Right) a configuration similar to CALYPSIO ($\lambda = 532\text{nm}$, altitude=705 km, full-angle fov 0.13 mrads). Here the Cirrus cloud is based upon in-situ measurements made during EUCROS.	149
75	Extinction, effective radius and reflectivity for the UQAM ASTEX1_1 scene.	150
76	Extinction, effective radius and reflectivity for the UQAM ASTEX1_2 scene.	172
77	Measured reflectivities.	172
78	Extinction, effective radius and reflectivity for the UQAM ASTEX1_4 scene.	173
79	Measured reflectivities.	173
80	Extinction, effective radius and reflectivity for the UQAM ASTEX2_1 scene.	173
81	Measured reflectivities.	173
82	Extinction, effective radius and reflectivity for the UQAM ASTEX2_2 scene.	174
83	Measured reflectivities.	174
84	Extinction, effective radius and reflectivity for the UQAM ASTEX2_3 scene.	174
85	Measured reflectivities.	174
86	Extinction, effective radius and reflectivity for the UQAM ASTEX2_4 scene.	175
87	Measured reflectivities.	175
88	Extinction, effective radius and reflectivity for the UQAM ASTEX5_1 scene.	175
89	Measured reflectivities.	175
90	Diagram showing the structure of aerosol processes and routines within the physics package of the circulation model. (Gong et al, 2000)	178
91	Schematic of the subgrid parameterized physical processes included in within each grid cells of full atmospheric circulation models (RCM). They are mixed layer ocean with thermodynamic ice, deep and shallow convective clouds, atmospheric and solar radiation, land processes like ponding, vegetation, CLASS hydrology, orography and rivers. A particular attention is placed on cloud and aerosol microphysics: sources of wind driven soil, DMS and sea salt aerosols, for anthropogenic emission of sulfur, organics and black carbon. Aerosol microphysics include nucleation of new particles, coagulation, condensation, deposition, basic oxidation chemistry, in cloud oxidation of SO ₂ , wet and dry removal processes. The aerosol is represented by 12 bin size spectra and 5 species requiring 60 dynamic tracers to be exchanged by advection and convection with neighboring grid cells. A grided frame treated by the model is composed of the order of one million cells of this type; each has a similar set of physical processes.	179

92	A schematic of the cloud evolution as observed during the First Lagrangian of ASTEX between 1719 UTC 12 June 1992 and 1302 UTC 14 June 1992. The flights are indicated below the horizontal border. The horizontal distance between Flights 1 and 5 is approximately 1300 km. The grayscale in the lowest horizontal bar represents changing sea surface temperature, with increasing values from left to right. Fluxes of moisture and heat and cloud type are indicated according to the legend. The magnitude of the arrow is proportional to the flux. Day-night changes are schematically represented by the sun or moon symbol. (From Fig. 2 of de Roode and Duynkerke, 1997)	182
93	Single frame (4x4x2.5 km or 160 x 160 x 100 points) showing the integrated liquid water path in stratocumulus field (upper part) and vertical cross section of effective radius for similar region (lower part). (Szyrmer 2002)	184
94	Schematic representation of the droplets model. In the small droplets region, an explicit representation is used (BG) with 20 EDP base functions. In the large droplet region, one mode is used with moments for number and mass concentration. Matching is done at $19\mu\text{m}$	185
95	Single frame (4x4x2.5 km or 160 x 160 x 100 points) showing the cross section of total liquid water path in stratocumulus field (upper part) and drizzle water content only (lower part). (Szyrmer 2002)	185

1 Introduction

THE Earth Clouds and Radiation Explorer (EarthCARE) proposal is a joint initiative between the European Space Agency (ESA) and two Japanese agencies, namely the Japanese Aerospace exploration Agency (JAXA) and the Japanese National Institute of Communications Technology (NICT). EarthCARE is a unique proposal aimed at improving our understanding of the interaction between Clouds and Solar and Thermal radiation within the Earths atmosphere. The EarthCARE platform will carry a combination of active (cloud radar and lidar) and passive instruments for cloud/aerosol and radiation remote sensing. The combination of the active and passive sensor on one platform is a unique feature of EarthCARE and will enable the mission to probe the vertical structure of the atmosphere and relate the observed structure to the top of atmosphere radiances and fluxes. By doing so, EarthCARE will provide observations critical for the accurate modeling of 3-D radiation field. The unique combinations of co-located sensors will also enable new and exciting cloud/aerosol related process studies to be carried out.

The instruments being considered for the EarthCARE platform are:

- An advanced lidar (ATLID).
- A Cloud profiling Radar (CPR).
- A Multi-spectral Imager (MSI).
- A Broad-Band Radiometer (BBR).

In order to develop retrieval algorithms and in order to investigate various instrumental trade-off issues it is necessary to simulate the mission. In order to be useful the simulations of the different instruments must be consistent with each other. As well it is desirable to be able to consider cases ranging from idealized ‘simple’ scenes to complex realistic scenes based on the output of cloud-resolving models. The EarthCARE simulator represents a unified approach to simulating the mission which satisfies these requirements.

This document is meant to serve both as a guide to using the package also to present results of some of the simulation that were preformed in support of the EarthCare mission proposal. Material presented in Section 2 describes the basic philosophy behind the package and a detailed description of each program (with examples) is presented in Section 3. Specific examples of the application of the simulator to explore certain aspects of the EarthCARE mission proposal are overviewed in Section 4. In addition to the main material, installation and additional operational information as well as additional results are presented in various appendices.

1.1 Background

The EarthCARE simulator is similar in concept to the previous ERM simulator (SYPAI). That is, data produced by a state-of-the-art, high-resolution cloud-resolving model (CRM) is intended to serve as the basis for creating ‘scenes’ that will be used as input to various radiative transfer programs and instrument simulation modules. This provides the ability to simulate satellite overpasses and subsequent measurement processes (see Fig. 1).

In this section the requirements for the core capabilities for the simulator will be outlined along with the general structure of the simulator package that evolved to meet these requirements. The background structure of this project is first briefly overviewed in terms of how this package is different from the previous *Earth Radiation Mission* ERM simulator package.

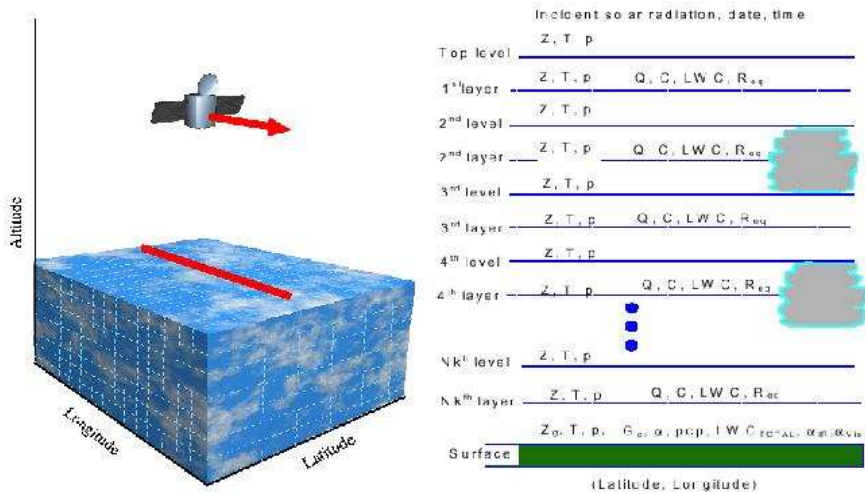


Figure 1: Illustration of the simulation concept.

1.2 General Overview

The main requirements that were formulated for the EarthCARE simulator can be summarized as follows:

1. The simulator must be capable of performing high-fidelity end-to-end simulations of the EarthCARE mission.
2. The simulator must be well-suited for synergetic observation studies.
3. The simulator should be able to handle a range of cases from realistic complex cloudy scenes based on model data or more simple scenes which may be specified by the user.
4. The package should be flexible and extensible with regards to instruments, platforms and range of atmospheric properties.

The Ecare Simulator package satisfies all of these requirements. With regards to point 1, the total simulator package can be used to performing true ‘end-to-end’ simulations of the EarthCARE mission. That is, the output of the forward instrument models can be inverted to yield relevant atmospheric properties. The inversion products may then be compared with the true atmospheric state. Furthermore, in keeping with the mission goal of retrieving the atmospheric column properties so that the flux divergence profiles may be inferred consistent with a TOA flux accuracy of 10 W/m^2 , the accuracy of the inversion products must be expressed in terms of their radiative impact. To do this, it is necessary to feed the inversion products into a compatible radiative transfer code in order to estimate the 3-D radiation field. This retrieved field can then be compared with the true field. The full simulation process is schematically depicted in Figure 1.

With respect to point number 2, in order for the entire simulation process to be meaningful, the calculation of the atmospheric scattering and absorption parameters must be based on a common approach. This is necessary to insure that the results of the various radiative transfer calculations and the various instrument forward model outputs are indeed consistent with each other. Thus the simulator package is structured so that, in essence, all the

necessary parameters for each instrument forward model are calculated separately outside of the instrument models themselves. This is achieved by specifying the cloud and aerosol properties in terms of their explicit size distributions and combining this information with pre-computed size and scattering type dependent scattering and absorption parameters.

With regards to the scope of input scenes (point number 3), on one hand, it is necessary to provide the end user some mechanism for quickly creating their own idealized scenes. On the other hand, it is also necessary for the simulator to be able to utilize complex ‘realistic’ model generated input data sets. To satisfy the requirement for simple scenes, which can be generated on demand by the end user according to their wishes (and which are also

necessary for the testing and development of the software package), a `scene_creator` application has been constructed. This application sets the standards for the data structures and protocols that are used by the simulator as a whole. The requirement to investigate complex realistic scenes is fulfilled by adopting an approach where the data associated with model generated scenes is translated into the appropriate simulator structure.

The strategy outlined above facilitates the fulfillment of point number 4. The modularity of the approach will allow new instrument models to be easily added in the future. The library files could easily be altered or extended to cover different atmospheric components, for example, different specific aerosol type or ice crystal habits. The *translation approach* to handling complex data gives the package the ability to handle data from various sources in various formats (with the creation of an appropriate translator module).

The spatial scales covered by the simulator are in principle, limited only by the memory requirements and the computing time necessary for carrying out the calculations. In practice due to the desire to treat complex scenes at high resolution (on the order of 100-200 meters) practical sizes are limited to the 10-20 km horizontal scale. This scale is sufficient for the simulation of the EarthCARE platform whose lowest resolution instrument (the BBR) has a footprint of 10x 10 km.

1.2.1 Relationship with the ERM simulator

Though the ERM simulator (called SYPAI) and the EarthCARE simulator share some similarities, the Ecare simulator is much more than an extension of SYPAI. There is an important difference in the logical structure of the of the EarthCARE simulator. In SYPAI there was a direct connection between bulk geo-physical model parameters and each of the different instrument modules (see the left panel of Fig. 3). Though expedient, this structure is not fundamentally suited to conducting multi-instrument simulator studies. In SYPAI, the model cloud parameters were limited to IWC/LWC and effective radius. Thus parameterizations were invoked to link these parameters to the quantities necessary for modeling each instrument. These parameterizations were contained within the different instrument models and they were not entirely compatible with each other across the different instrument. This limited the ability of using SYPAI to develop true synergistic retrieval algorithms.

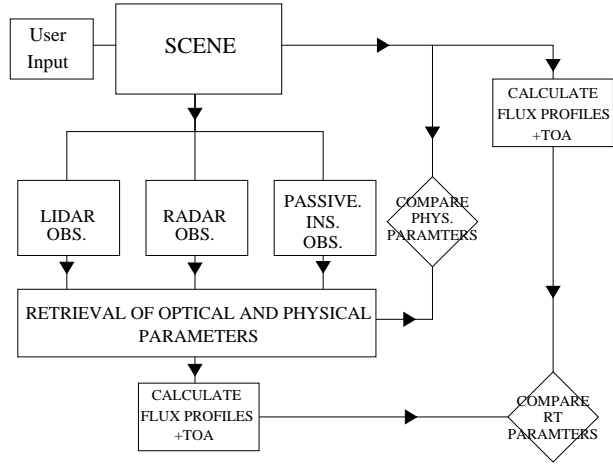


Figure 2: Total end-to-end simulation procedure.

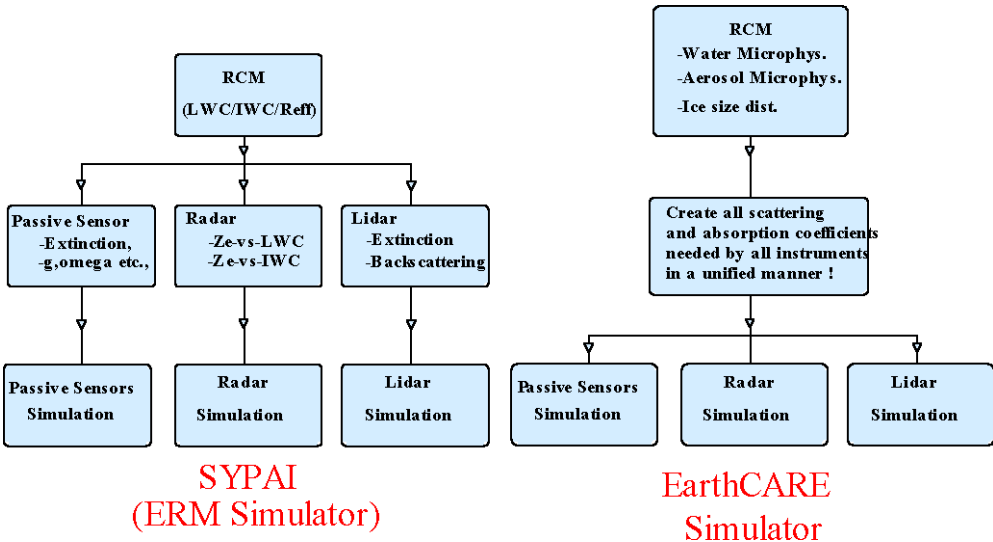


Figure 3: Difference in logical structure between (left) the ERM simulator and (right) the EarthCARE simulator.

In the EarthCARE simulator, cloud and aerosol microphysical properties (such as cloud particle size distribution) will be supplied, so far as possible, by the input geo-physical data sets. Spectral scattering and absorption properties (phase functions and extinction and absorption cross-sections) will be calculated directly from cloud microphysical properties coupled with cloud and aerosol scattering libraries that are common to all the package components.

The package is built in a modular fashion but the final output of each of the different instrument forward models depends on the same set of detailed atmospheric and cloud and aerosol microphysical data. The conceptual structure of the package is outlined in Figure 3.

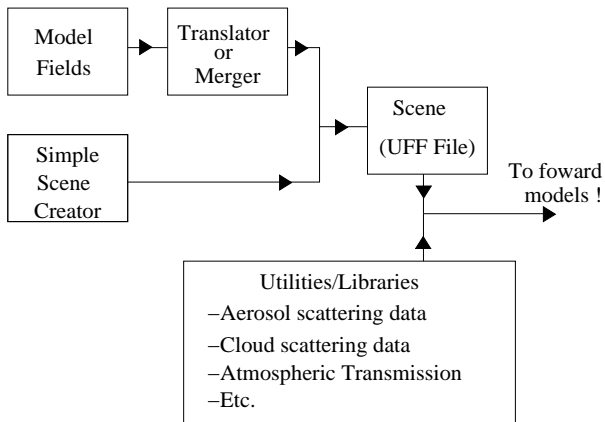


Figure 4: The simulator forward models all draw on information from the UFF file which is combined with information from the common library data.

microphysical data is stored in the UFF in an efficient manner. The scattering phase functions and other characteristics however are not stored in the UFF file but rather are stored

The information defining the scene is encoded in a so-called Universal File Format (UFF)⁵ file. UFF files may be generated by a utility program which may be used to directly create ‘simple’ scenes. More complex UFF scenes may be generated from data from cloud resolving models which has been translated into the UFF format via a purpose-built translator. The UFF file encodes all the atmospheric data necessary to define a scene. In particular, the cloud and aerosol

⁵The UFF designation is certainly not ‘universal’ outside of the simulator package. However, the UFF files contain in a centralized fashion all the atmospheric cloud, gas and aerosol microphysical information necessary to drive each of the simulator programs and are used accessed ‘universally’ by all the forward model elements of the simulator.

in library file which are drawn on by the other programs in the package as necessary. For example, the lidar simulation program needs to ‘know’ the extinction field. This information is not directly stored in the UFF file. Rather, the program reads the cloud size distribution information from the UFF file and then will read the scatterer phase function, extinction, and absorption data it requires from the scattering libraries referenced by the UFF file. The extinction field is then calculated by combining the size distribution data from the UFF file and the information from the scattering libraries. The separation of scattering information and size distribution information enables large detailed scenes to be handled using relatively modest amounts of disk space and RAM.

Another feature of the package as a whole is its use of pointers and dynamic memory allocation. For instance, size distribution information is generally stored in allocatable pointer structures. In this way storage need only be allocated where clouds or aerosols are present. A large reduction in the amount of RAM is thus realized. For example, consider a 10×10 km scene at 0.2 km resolution with 50 vertical levels where a cloud is present at 4 vertical levels and the size distribution is defined for 50 discrete size intervals. If dynamic allocation were not used then it would be necessary to hold $50 \times 50 \times 50 \times 50 = 6.25 \times 10^6$ REAL variables for the size distribution alone. If dynamic memory allocation techniques are used then only $50 \times 50 \times 50 \times 4 = 5 \times 10^5$ REAL variables need to be stored.

2 Theory

Broadly speaking the simulator programs may be divided into four groups

1. Forward Model programs
2. Retrieval programs
3. Utility Programs
4. Plotting programs

Here a brief introduction to the theory behind the core simulator components (the forward model programs and the retrieval programs) is given.

Forward Model Programs

<code>lid_filter</code>	A 3-D Monte-Carlo lidar multiple-scattering engine. The code accounts for polarization and spectral effects
<code>lidar</code>	A lidar instrument module which simulates the lidar optical filtering and other instrument effects. This application relies on the output of <code>lid_filter</code>
<code>rad_filter</code>	Creates idealized radar reflectivity (Z) and radar Doppler velocity (V_d) fields.
<code>radar</code>	Samples the output of <code>rad_filter</code> and accounts for radar sampling and instrument effects.
<code>MC_sim_main</code>	A 3-D Monte-Carlo code for calculating Top-of-Atmosphere (TOA) short-wave radiances as well as Fluxes throughout the domain.
<code>MC_LW_sim_main</code>	A 3-D Monte-Carlo code for calculating Top-of-Atmosphere (TOA) long-wave radiances as well as TOA Fluxes

Retrieval Programs

<code>lidar_ret1</code>	Processes data from <code>lidar</code> and <code>radar</code> and generates level 1 profile output products.
<code>msi_ret</code>	Uses the output of <code>MC_sim_main</code> and <code>MC_LW_sim_main</code> to generate standard MSI level 1 2-D cloud and aerosol products.
<code>lw_msilidar_radar</code>	Combines the output of <code>lidar_ret1</code> together with <code>MC_LW_sim_main</code> in order to retrieve the 3-D cloud property field.

2.1 Lidar

The lidar components of the simulator are divided between the **lid_filter** program and the **lidar** program. In general, **lid_filter** performs quasi-instrument independent MC scattering calculations, while **lidar** implements the instrument specific detection of the calculations preformed by **lid_filter**. The practical operation of these programs is covered in Sections 3.9.3 and 3.9.4 respectively.

The main lidar configuration currently under consideration for EarthCARE is a single-wavelength High Spectral Resolution (HSR) lidar with polarization capability. In addition, to the configurations directly under current industrial development it would be useful to be able to compare the results that would be obtained by less ambitious configurations (i.e. single-wavelength wide FOV lidar) or alternate configurations (i.e. Multiple FOV configuration). Not all of these capabilities can be realized in a practical lidar configuration. However, the lidar programs have been built on a level of detail high enough to encompass all considered capabilities. In the following sections we will present some background material as well as outline the basic theory behind the operation of **lid_filter** and **lidar**.

2.1.1 Basic Considerations

Assuming an atmosphere whose properties may be considered constant within the domain of the instantaneous sampling volume in the directions perpendicular to the lidar line-of-sight, the single-scattered power incident upon the detection element for a completely elastic backscatter lidar (neglecting the background signal) for a an appropriate wavelength interval centered around λ_l can be written as

$$P(z, \lambda_l) = C_{lid} z^{-2} \beta_\pi(z, \lambda_l) \exp \left[-2 \int_0^z \alpha(z', \lambda_l) dz' \right] \quad (1)$$

where λ_l is the laser wavelength, $P(z, \lambda_l)$ is the power the lidar received from a target a distance $z = ct/2$ from the lidar (where t is the elapsed time since the laser pulse was launched from the lidar), $\beta_\pi(z, \lambda_l)$ is the range and wavelength dependent backscatter coefficient in $[m^{-1}sr^{-1}]$, $\alpha(z', \lambda_l)$ is the extinction coefficient. Here both the backscatter and extinction coefficients represent appropriate averages over the wavelength interval of interest. C_{lid} is a constant with takes into account factors related to the lidars physical characterizes. For a simple lidar we may write

where $\overline{T_f P_l(\lambda)}$ is the product of the transmission of the receivers spectral filter and the transmitted laser pulse averaged across the spectral signature of the laser pulse, A_o is the effective receiver telescope area, and $\bar{\xi}$ is the average product of the laser beam profile and the collector efficiency profile, e.g.,

where $\xi_l(z, r, \rho_l)$ is the beam profile function, $\xi_r(z, r, \rho_r)$ is the receiver efficiency, r is the radial distance from the center of the laser beam/field-of-view in the target place, ρ_l is the laser beam half divergence angle, and ρ_r is the half opening angle of the receiver telescope. Here we have assumed that the field of view of the receiver optics in the target plane is a circle of

So we see that for the most basic of lidar systems in order to model the single-scatter power incident upon the detection element we must specify the following parameters.

Table 1:)

Geophysical Variables	
$\beta_\pi(z, \lambda_l)$	The atmospheric backscatter profile.
$\alpha(z, \lambda_l)$	The atmospheric extinction profile.
Instrument Parameters	
$T_f(\lambda)$	Transmission of optical receiver train
A_o	Receiver effective area
$P_l(\lambda)$	Transmitted laser power
$\xi_l(z, r, \rho_l)$	Transmitted laser profile function.
$\xi_r(z, r, \rho_r)$	Receiver efficiency in the target plane.
ρ_l	Laser beam half divergence angle.
ρ_r	Receivers telescope field-of-view half angle.

2.1.2 Multiple Scattering

Eq. (1) is valid only when single-scattering is predominant. In cases where either a high proportion of scattered photons remain within the receiver FOV or the optical depth is such that photon mean-free-path is small compared to the instantaneous sampling volume then multiple scattering effects should be taken into account. It is common in lidar work to separate the multiple scattering contributions into the various orders of scattering (see Fig. 5).

When multiple scattering can not be neglected, in general, the lidar return signal can not be written in a simple closed analytical form. However, approximate methods as well as ‘exact’ Monte-Carlo approaches may be employed. The crucial parameters that determine the contributions of multiple scattering to the total lidar return signal are:

- The ratio of laser divergence angle to the telescope FOV (ρ_r/ρ_l).
- The range from the lidar (z).
- The optical depth from the lidar to the target plane.
- The scattering phase function, in particular, the width of the forward scattering lobe.

If either,

1. The mean free path (MFPs) is small compared to the lidars instantaneous sampling volume (ISV). (this condition is determined by a combination of the previously listed factors.)
2. The angular width of the scatterer’s forward scattering lobe is not much larger than the angular width of the receiver’s field of view (ρ_r).

then multiple scattering must be taken into account. Unlike the case of radiative transfer in the general atmosphere the effect of multiple scattering on the lidar signal very much depends on the characteristics of the lidar as well as the radiative properties of the atmosphere under considerations.

Condition 1 depends on the target extinction coefficient, the range from the lidar and ρ_r . From space, for a lidar with ρ_r on the order of a few mrad, almost all water clouds and many ice clouds would fall into this category. To account for multiple scattering effects in this regime is difficult. Many scattering orders must be considered and in some circumstances the direct time-of-flight and distance from the lidar correspondence will be lost as the photons ‘bounce around in the clouds’ many times and then are scattered back to the lidar (the so-called pulse stretching effects). However, with the narrow ρ_r of the EarthCARE lidar (0.002 mrad or so) virtually no ice or water clouds will fall into this category.

Condition 2 depends primarily on the size of the scatterers and the ρ_r . For cloud particles the forward scattering lobe contains half the scattered energy and the angular width of this lobe decreases with increasing particle size. Even with small field-of-view space based lidars such as the EarthCARE lidar and CALYPSIO will fall into this category. In particular, the small FOV of the proposed EarthCARE lidar will not totally eliminate the effects of MS. However, the MS effects are tractable.

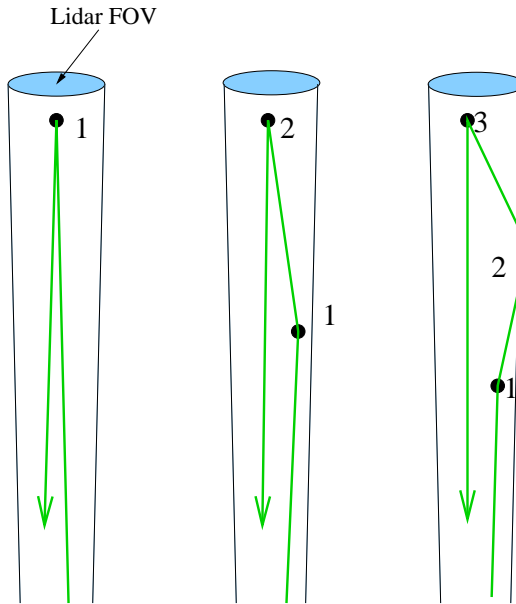


Figure 5: Contributions of the first three scattering orders to the lidar return signal

2.1.3 Polarization Sensitivity

In principle a polarization sensitive lidar is a useful tool for identifying particle phase (spherical water drops or non-spherical ice crystals) and may have some potential of identifying ice particle habit (i.e. orientated plates vs. randomly oriented hexagonal rods). In general, the polarization state of the light scattered in the direct backscatter direction for spherical particles as well as certain ice crystal habits (i.e. perfectly oriented plates whose flat faces are perpendicular to the laser beams direction of propagation) is preserved. For non-spherical particles and most ice crystal size/shape/orientation distribution the Polarization State is altered. The linear depolarization ratio, is defined as,

$$\delta(z, \lambda) = \frac{\beta_{\pi, \perp}}{\beta_{\pi, \parallel}} \quad (2)$$

where β_{\perp} is the backscatter coefficient for scattered light whose plane of polarization is perpendicular to that of the incoming laser beam and β_{\parallel} is the backscatter coefficient for scattered light whose plane of polarization is parallel to that of the incident beam. Other analogous depolarization ratios can be defined when dealing with circularly polarized laser radiation.

Multiple scattering and depolarization Even for spherical targets, δ will be close to zero only if the multiple scattering contribution to the return signal is small compared to the single-scattering only signal. This is due to the fact that for spheres, scattering at angles other than directly forward or backward will give rise to a perpendicularly scattered component. This multiple scattered contribution to the depolarization signal can be large and can complicate the interpretation of the depolarization signal.

In order to properly explore the behavior of the lidar depolarization signal it is not sufficient to specify the phase functions and polarization dependent backscatter coefficient. It is necessary to specify the full scattering matrix. The relationship between the Stokes vectors of the scattered and incident electromagnetic fields (with respect to the scattering plane) can be written as

$$\begin{pmatrix} I \\ Q \\ U \\ V \end{pmatrix} = \begin{pmatrix} P_{11} & P_{12} & P_{13} & P_{14} \\ P_{21} & P_{22} & P_{23} & P_{24} \\ P_{31} & P_{32} & P_{33} & P_{34} \\ P_{41} & P_{42} & P_{43} & P_{44} \end{pmatrix} \begin{pmatrix} I_o \\ Q_o \\ U_o \\ V_o \end{pmatrix} \quad (3)$$

If the target scatterers are rotationally symmetric or randomly oriented then this relationship is reduced to

$$\begin{pmatrix} I \\ Q \\ U \\ V \end{pmatrix} = \begin{pmatrix} P_{11} & P_{12} & 0 & 0 \\ P_{12} & P_{22} & 0 & 0 \\ 0 & 0 & P_{33} & P_{34} \\ 0 & 0 & -P_{34} & P_{44} \end{pmatrix} \begin{pmatrix} I_o \\ Q_o \\ U_o \\ V_o \end{pmatrix} \quad (4)$$

The phase matrix is defined in terms of the scattering plane (i.e. the plane defined by the incoming and outgoing scattered photon paths). Thus, the Stokes vector of the incoming radiation and the resulting vector describing the scattered radiation must be rotated with respect to the scattering plane. The Stokes vector resulting from a photon scattered through an angle (θ, ϕ) is given by

$$\mathbf{S} = \mathbf{L}(\pi - i_2)\mathbf{P}(\theta)\mathbf{L}(-i_1)\mathbf{S}_0 \quad (5)$$

where \mathbf{S}_0 is the incoming Stokes vector and \mathbf{S} is the Stokes vector associated with the scattered radiation. $\mathbf{P}(\theta)$ is the scattering phase matrix and \mathbf{L} is the transformation matrix for the Stokes parameters (Liou (2002))

$$\mathbf{L}(\chi) = \begin{pmatrix} 1 & 0 & 0 & 0 \\ 0 & \cos(2\chi) & \sin(2\chi) & 0 \\ 0 & -\sin(2\chi) & \cos(2\chi) & 0 \\ 0 & 0 & 0 & 1 \end{pmatrix} \quad (6)$$

where χ is the orientation angle. The angles i_1 and i_2 in Equation 5 are given by

$$\cos(i_1) = \frac{-\mu + \mu_o \cos(\theta)}{\pm(1 - \cos(\theta)^2)^{1/2}(1 - \mu_o)^{1/2}} \quad (7)$$

where μ_o is the z component of the direction cosine of the incoming photon and μ is the z component of the direction cosine of the scattered photon. The plus sign is to be used when $\pi < \phi - \phi_o < 2\pi$ and the minus sign is to be used otherwise where the π 's refer to the azimuth angles of the incoming and outgoing photon's respectively.

As was the case with the consideration of unpolarized multiple scattering the general lidar return can not be written in a compact analytical fashion. In order to account for the polarization state of the lidar return in a multiple-scattering environment a Monte-Carlo approach is needed.

2.2 High Spectral Resolution Lidar

So far in this discussion we have only consider the case where the scattering is completely elastic. That is, the scattered photons have the exact same wavelength as the incident photons. In reality this is never quite the case. Even neglecting such process involving the change of energy levels within the target scatterers (i.e. rotational Raman, vibrational Raman scattering, fluorescence etc.) the scattered radiation will be Doppler shifted according to its relative motion with respect to the lidar. In general, a target moving with respect to a fixed lidar will ‘see’ a source whose frequency is given by (neglecting terms of order $(v/c)^2$)

$$f = f_o \left(1 + \frac{v}{c} \cos(\theta) \right) \quad (8)$$

where v is the velocity of the scatterer, c is the speed of light, θ is the angle between the scatterers velocity vector and the line-of-sight directed back toward the receiver, and f_o is the frequency of the source light in the frame of the laser. When the light initially incident upon the moving scatterer is scattered it is equivalent to being instantaneously absorbed and re-emitted so that the scattered light will again be Doppler shifted in frequency depending on the motion of the scatterer with respect to the receiver. Accordingly, the frequency measured by an observed in the same frame as the lidar transmitter will be given by (again neglecting terms of order $(v/c)^2$)

$$f = f_o \left[1 + \frac{v}{c} (\cos(\theta) + \cos(\theta_{sc})) \right] \quad (9)$$

where θ_{sc} is the angle between the velocity vector and the scattered photon’s trajectory. So that light scattered directly forward and measured by a stationary observer would have no Doppler shift while light scattered directly backwards to toward the lidar would be seen to have been shifted in wavelength by an amount twice that predicted by Eq.(8) Thus even if the laser line width was infinitely narrow the return would still be broadened due to the motion of the scatterers relative to the lidar.

A schematic representation of the spectral signature of a general lidar return signal is shown in Fig. 6. The spectral width of the Mie peak will be determined by the spectral width of the laser pulse itself along with any turbulence present in the sampling volume. The spectral width of the laser will be on the order of $10^{-7} f_o$ so that the laser line width would usually be the dominant factor. The molecular backscatter though will be much broader than the Mie scattering return though; this is due to the fact that the atmospheric molecules have a large thermal velocity. For low densities the Half-Maximum Half Width (HMHW) of the broadening produced by the thermal motions alone is given by

$$\Delta f = f_o \left(\frac{8kT \log(2)}{Mc^2} \right) \quad (10)$$

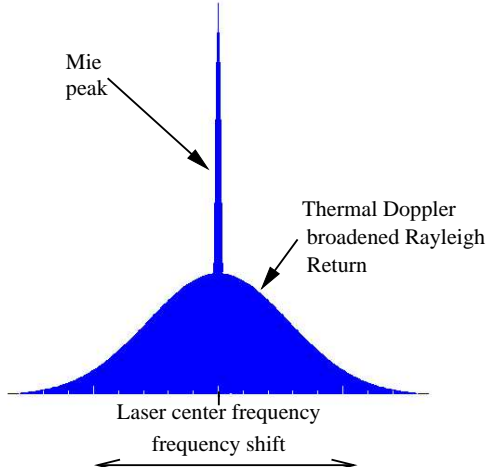


Figure 6: Idealized view of spectral signature of a lidar return.

where, k is Boltzmann’s constant, M is the average molecular mass, and T is temperature. For typical values of atmospheric temperature the HMHM of the Doppler return will be on

the order of $4 \times 10^{-6} f_o$ so that the Doppler broadening will be 10-20 greater than the laser line width. Eq. 10 applies at low gas densities. In general, the central (non-Raman) Rayleigh line profile (Cabannes line) will consist of three components, a central peak together with two flanking “Brillouin-Mandel’shtam” peaks (Miles, Lempert and Forkey (2001)). In the low density or high temperature regime the uncorrelated motion of the scatterers gives rise to a Gaussian velocity distribution centered around the mean velocity of the flow and Eq. 10 applies. As the pressure increases or the temperature decreases density fluctuations on the order of the laser wavelength may appear. These density fluctuations travel at the speed of sound in the gas and will give rise to acoustic side bands.

The Raleigh-Brillouin scattering line shape may be quantified in terms of the so-called y parameter which is defined in terms of the ratio of the laser wavelength to the mean free-path. For the Earth’s atmosphere

$$y = 0.230 \left[\frac{T + 111}{T^2} \right] \left[\frac{P\lambda}{\sin(\frac{\theta}{2})} \right] \quad (11)$$

where T is the temperature in Kelvin, P is the pressure in atmospheres, λ is the laser wavelength and θ is the scattering angle. Sample Rayleigh-Brillouin profiles for various y -parameters are shown in Fig. 7. The profile were calculated using a program due to Pan (2003). Here x is a normalized frequency parameter defined as

$$x = \frac{\sqrt{2}\lambda}{4 \sin(\frac{\theta}{2})} \left(\frac{\nu}{\nu_o} \right) \quad (12)$$

where μ is the frequency shift from the line center and ν_o is the sound speed

$$\nu_o = \sqrt{\frac{kT}{m}} \quad (13)$$

where m is the molecular mass.

In addition to the broadening of the return the entire return spectrum will be Doppler shifted according to the mean velocity of the scatters in the lidar line-of-sight. For nadir viewing, the vertical wind (usually below 1 ms^{-1} but may be on the order of 10 ms^{-1} in convective cloud systems) along with the terminal velocity of large falling cloud droplets and ice-crystal may have to be considered.

In the HSR technique the Mie and Rayleigh returns are detected separately using spectral elements such as filters and Fabry-Perot Etalons. An idealized representation of the signals that may be expected (by a space-based HSR lidar) is shown in Fig. 8. The ratio of signal in the Mie channel to the signal detected in the Rayleigh channel(s) will be directly related to

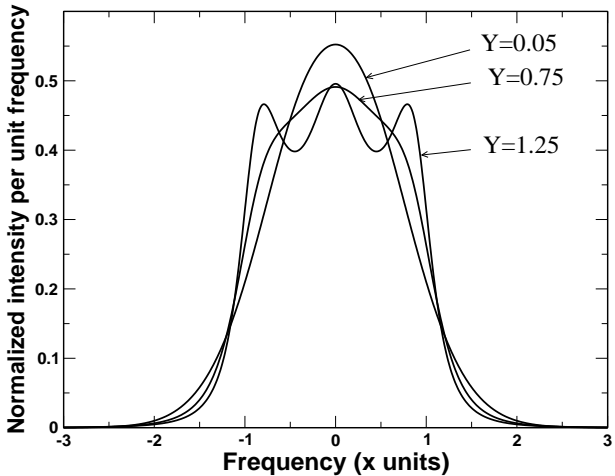


Figure 7: Rayleigh-Brillouin profiles for various y -parameters. x is a normalized frequency parameter.

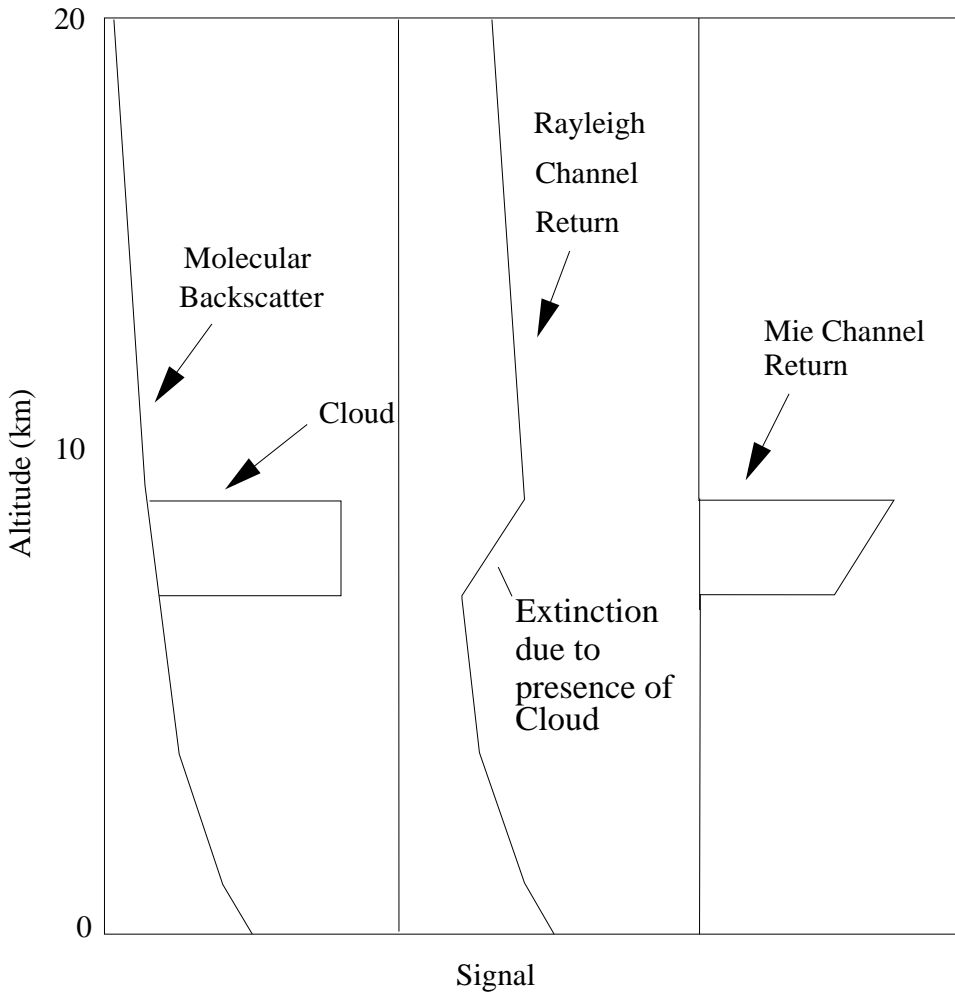


Figure 8: Idealized view of space-based HSR lidar returns from a cloud.

the ratio between the Mie and Rayleigh backscatter coefficients and the Rayleigh channel(s) can be used to retrieved the extinction profile if the molecular density profile is known (or modeled). To see this we will consider the case of an idealized HSR lidar operating in a regime where multiple scattering is unimportant. The equation describing the return in the Mie channel is

$$P_{Mie}(z) = C_{Mie} z^{-2} \beta_{Mie,\pi} \exp \left[-2 \int_0^z \alpha(z') dz' \right] \quad (14)$$

where here we have dropped the wavelength dependence and will assume the various quantities denote appropriate wavelength averaged quantities. The corresponding lidar equation for the Rayleigh signal is

$$P_{Ray}(z) = C_{Ray} z^{-2} \beta_{Ray,\pi} \exp \left[-2 \int_0^z \alpha(z') dz' \right] \quad (15)$$

If we simply divide Eq. 14 by Eq. 15 we then have

$$\frac{P_{Mie}}{P_{Ray}}(z) = \frac{C_{Mie}}{C_{Ray}} \frac{\beta_{Mie,\pi}}{\beta_{Ray,\pi}}(z) \quad (16)$$

Thus, if the calibration coefficients are well known (or an aerosol and cloud free atmospheric return in some height range can be used as a reference) then the backscatter profile can be measured.

Taking logs of Eq. 15 and rearranging yields

$$\int_0^z \alpha(z') dz' = \log \left[\frac{z^2 P_{Ray}(z)}{\beta_{Ray,\pi}(z)} \right] + \log (C_{Ray}) \quad (17)$$

Then differentiate with respect to z gives and using the fact that to a good approximation that $\beta_{Ray,\pi}(z) \propto \rho(z)$; where $\rho(z)$ is the atmospheric density, gives

$$\alpha(z) = \frac{d}{dz} \left(\frac{z^2 P_{Ray}(z)}{\rho(z)} \right) \quad (18)$$

Thus we see that the HSR technique can, in principle, be used to deduce the atmospheric extinction profile. In practice, the presence of noise and cross-talk between the Mie and Rayleigh receiver channels and the occurrence of multiple scattering will complicate the retrieval process.

2.2.1 Effect of Multiple Scattering

So far, the discussion has been limited to the case of single-scattering only. In cases where multiple scattering is significant the extinction profile that may be retrieved by the use of Eq. 18 will tend to underestimate the true extinction profile (due to forward scattering by the cloud particles). The effect of multiple scattering on HSR backscatter measurements (see Eq. 16) will be less than that upon the extinction measurements due to a cancellation effect. That is, to a first approximation the effects of multiple scattering will be the same for the both the molecular

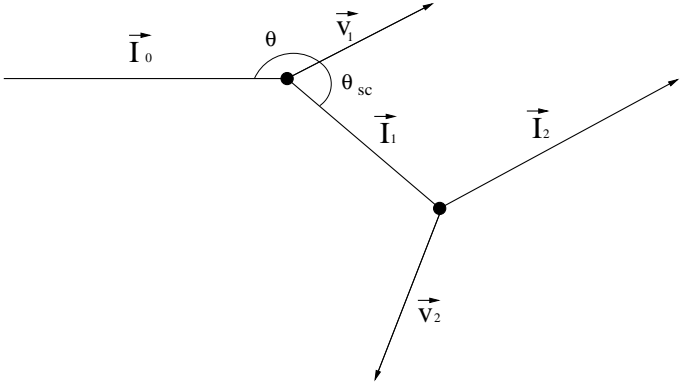


Figure 9: Geometry relevant for determining the observed Doppler shift after multiple scatters.

and the cloud scattering. However, the result of taking the ratio in Eq. 16 will not completely remove the effects of multiple scattering due to differences in the molecular and cloud/aerosol phase functions in the backward direction.

The occurrence of multiple scattering will also have implications with respect to the spectral signature of the lidar return. By repeated application of Eq. 8 (see Fig. 9) it can be shown that the Doppler shifted frequency measured by an observer in the same frame as the lidar after n scatters will be given by

$$f_n = f_o \left(1 + \frac{1}{c} (\mathbf{v}_1 \cdot \mathbf{I}_0 + (\mathbf{v}_1 - \mathbf{v}_2) \cdot \mathbf{I}_1 + (\mathbf{v}_2 - \mathbf{v}_3) \cdot \mathbf{I}_2 + \dots + \mathbf{v}_n \cdot \mathbf{I}_n) \right) \quad (19)$$

where \mathbf{v}_i is the velocity vector of the i th scatterer and \mathbf{I}_i is the unit vector for the photon trajectory for the i th scatter. If the lidar is to observe the photon, to a good approximation, it must be scattered directly backward so that $\mathbf{I}_n = -\mathbf{I}_o$ and we have

$$f_n = f_o \left(1 + \frac{1}{c} (\mathbf{v}_1 \cdot \mathbf{I}_0 + (\mathbf{v}_1 - \mathbf{v}_2) \cdot \mathbf{I}_1 + (\mathbf{v}_2 - \mathbf{v}_3) \cdot \mathbf{I}_2 + \cdots - \mathbf{v}_n \cdot \mathbf{I}_o) \right) \quad (20)$$

It can be seen that multiple scattering will then produce additional spectral broadening depending on the relative velocities of the various scatterers as well as the difference between the scattering direction vectors (the \mathbf{I}_i s). To see this more clearly consider the case where $\mathbf{I}_{i:} = \mathbf{I}_0$ for $i=0$ to $n - 1$, that is, all the scatters are directly forward except for the final backscatter. For this special case we will have

$$\begin{aligned} f_n &= f_o \left(1 + \frac{1}{c} (\mathbf{v}_1 \cdot \mathbf{I}_0 + (\mathbf{v}_1 - \mathbf{v}_2) \cdot \mathbf{I}_0 + (\mathbf{v}_2 - \mathbf{v}_3) \cdot \mathbf{I}_0 + \cdots - \mathbf{v}_n \cdot \mathbf{I}_0) \right) \\ &= f_o \left(1 + \frac{1}{c} (2\mathbf{v}_2 \cdot \mathbf{I}_0) \right) \end{aligned} \quad (21)$$

which is the same as the shift that would be produced by a single-scatter by the n th scatterer. If none of the scatterers are in the direct forward direction then, in principle, each interaction will contribute to the Doppler shift observed at the detector. Thus, multiple scatter photons involving large angle scattering will be shifted the most. Under some circumstances this may cause a significant number photons to ‘flow’ from the Mie scattering peak into the Rayleigh detection channel depending on the velocities of the target scatterers and the width of the Mie channel spectral filter, etc.

2.2.2 Lidar Monte-Carlo Calculations

Keeping in mind the proceeding discussion a semi-analytical Monte-Carlo model was created in order to generate the lidar signals. This model calculates the signal that would be present at the entrance aperture of the lidar as a function of time after the pulse was launched.

A Monte-Carlo approach models the propagation of the laser photons in a stochastic manner. In a pure Monte-Carlo procedure photons are launched from their source (in this case the laser) with an initial direction vector. The photon then travels a distance Δs before interacting with a scatterer or absorber. The probability density function for the step size (Δs) follows Beer’s law, i.e.

$$\mathcal{P}(\Delta s \leq r) = 1.0 - \exp \left[- \int_0^r \alpha(r') dr' \right] \quad (22)$$

where α is the total attenuation coefficient. For each photon Δs is determined stochastically using a suitable pseudo-random number generator according to Eq. (22). Once an interaction has occurred the type and size of particle encountered is determined stochastically according to the contribution each particle present at that grid point makes to the total attenuation. At each event a particle may be scatterer or absorbed. This too is determined stochastically according to the single-scatter albedo of the appropriate interacting particle. If it has been determined that a scattering event (rather than an absorption event) has taken place then the direction of the photon is changed according to its phase function. The polarization state of the return signal is accounted by keeping track of the Stokes vector of the scattered photons (see Section 2.1.3).

Rayleigh-Brillouin Scattering The Doppler shift and thermal broaden of the return signal are also accounted for (see Section 2.2). For low y parameters the lineshape has a simple Gaussian form. For larger values of y (in the range that we must be concerned with)

the line shape becomes complicated and somewhat costly to evaluate. Fortunately, for values of y under about 10 the Rayleigh-Brillouin line shape may be accurately enough (for our purposes) approximated by the sum of three independent Gaussian functions.

For the single scatter return the line shape is determined by the sum of three Gaussian profiles. These calculations are based on the results of pre-computed approximate Gaussian fits made to accurate calculations of the line profile corresponding to various y parameters (See Fig. 10). For the higher order scattering, at each molecular scattering event the probability of the scattered photon packet being shifted to one of the acoustic side bands is calculated. Whether or not the photon packet is shifted is then determined stochastically and the subsequent shift and width of the associated Gaussian profile is used to determine the line shape. This line shape and shift is then used in subsequent calculations.

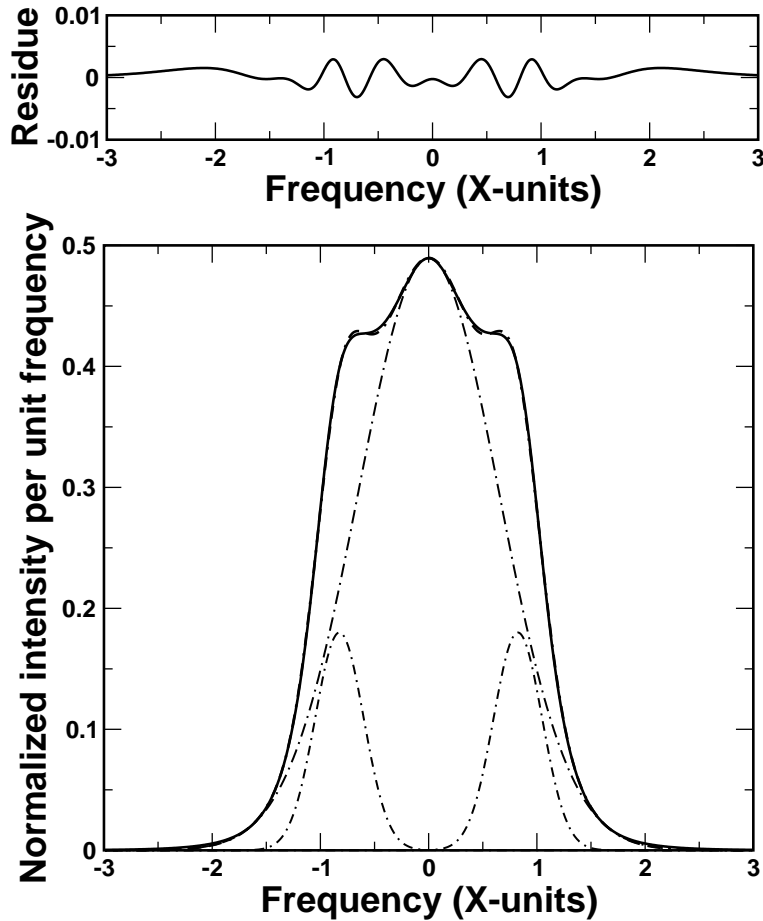


Figure 10: (Bottom Panel) Exact Rayleigh-Brillouin line shape (Solid-Line) along with fitted sum of three Gaussian functions (Dashed Dotted line). The three component Gaussian functions are also shown. Here the y parameter is equal to 1.0. The top panel shows the difference between the fitted function and the exact calculation.

Semi-Analytical Approach In a pure Monte-Carlo approach photons are tracked until they are absorbed, detected, or exit the simulation area. This approach is simple and accurate. However, it is not very efficient as any given photon has a very small chance of being scattered back to the lidar receiver. Thus, it is desirable to modify the basic Monte-Carlo approach to increase its computational efficiency.

In order to increase the efficiency of the calculation, the semi-analytical Monte-Carlo

model analytically calculates the amount of unscattered energy from the lidar present at each altitude and then proceeds to calculate the higher order scattering by launching a number of appropriately weighted photon packets from each altitude bin (here 2000-5000 photons per altitude bin where are typically used). As the photon packets propagate and scatter, for each scattering event, the amount of signal received by the lidar is analytically calculated. In order to increase the efficiency of the calculation, the well-known technique of forcing scattering of the photon packets to occur within a specified distance from the receiver axis (in this case 5 times the receiver field-of-view footprint) was implemented (Platt (1981)). The well-known technique of using symmetric effective phase functions in order to increase the number of backscattering events such that more photon packets travel toward the receiver (but with a suitably reduced weight) was also employed (Platt (1981)). This is done in order to ‘smooth out’ the contribution that various packets have to the return signal (see Fig. 11) in order to improve the statistical convergence properties of the simulation. However, this strategy is of limited utility when Rayleigh scattering is important as the Rayleigh phase function is already symmetric.

The just-described semi-analytical approach is exact and orders of magnitude faster than a pure Monte-Carlo approach. However, by invoking an approximation concerning the contribution of different photon packet paths, the computational efficiency may be improved further still.

Since cloud particles are usually large compared to visible wavelengths their phase function is strongly peaked in the forward direction (Eloranta (1998)). Hence the most probable photon packet paths involve multiple forward scatters (see CASE 1 in Fig. 11). Instead of using symmetric phase functions to smooth out the contribution of rare multiple backscatter events (see CASE 2 in Fig. 11) as explained previously it is possible to eliminate the contribution of these events by only counting the contribution to the return signal in the case where the scattering angle back to the receiver is greater than 90 degrees. By eliminating the contribution of forward scatters directly to the receiver the convergence will be rapid. However, this will lead to a large underestimation of the lidar signal.

This underestimation may be approximately accounted for if consider the contribution from the various types of paths involving 2 or more scatterers. In Fig. 12 the various classes of paths for second and third order scattering are presented. For second order scattering it

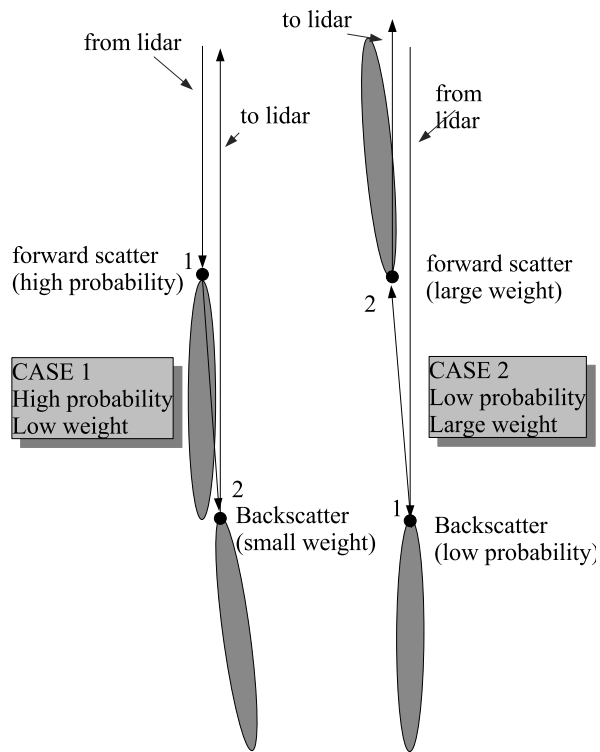


Figure 11: Most photon packet paths fall into CASE 1. However rare events (CASE 2) occur and lead to large fluctuations in the average power. Using effective symmetric phase functions increases the effective number of CASE 2 type events while making the contribution of CASE 1 and CASE 2 type event similar in magnitude thus greatly improving the convergence properties.

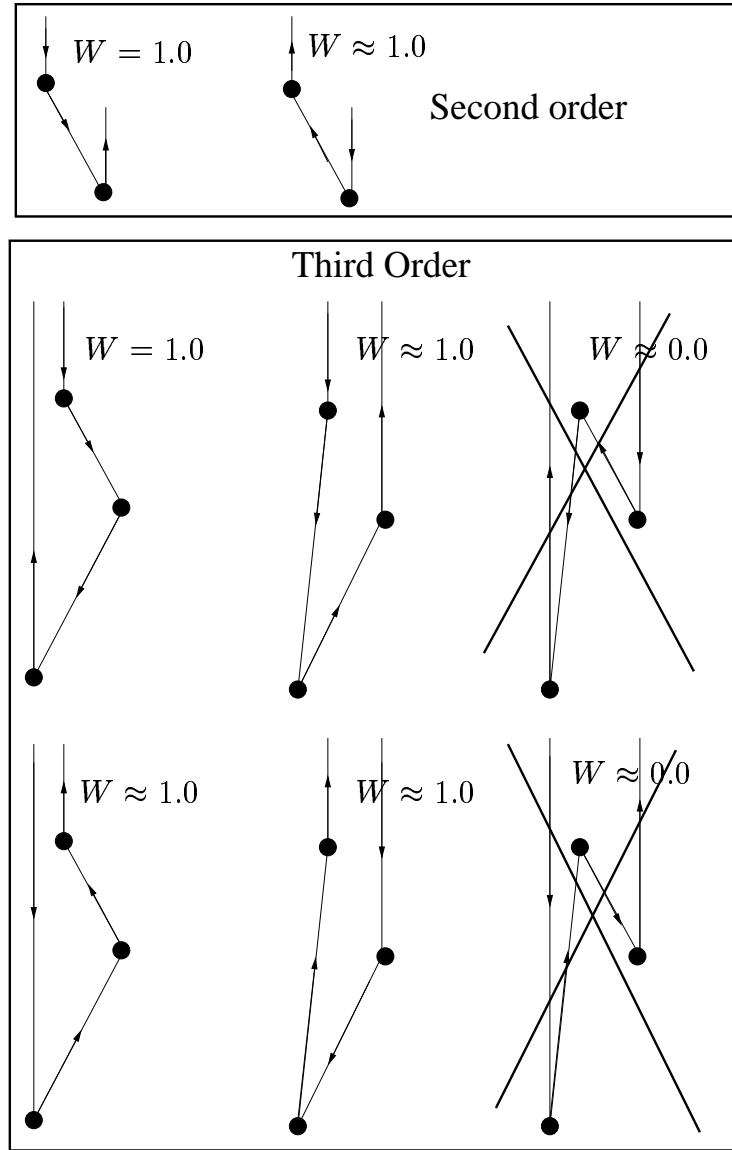


Figure 12: Schematic representation of the various types of paths involving forward and backscatter events for second and third order scattering and their relative contribution to the return signal.

can be seen that only 2 different types of paths exist (namely forward- then back-scatter and back- then forward-scatter) and upon a little consideration, the contribution of both types of paths should be the same. Hence, by not counting the back- then forward-scatter the second order signal will be underestimated by a factor of two. For third order scattering if we eliminate paths involving multiple backscatters we conclude that the underestimation will be a factor of 4. By similar reasoning the factors are found to be

$$F_{path} = 2^{n-1} \quad (23)$$

where F_{path} is the underestimation factor and n is the scattering order.

This procedure is exact in the case when only direct forward (0.0 deg.) and backscatters (180.0 Deg) are involved. For general cases, non exact forward scatters or backscatters will cause give rise to small errors in the polarization and spectral state of the received radiation as well as the total path length. However, for the EarthCARE configuration this approximate

has been tested and shown to produce accurate results (see Fig. 13) and is about 1000 times faster for a given desired statistical error level.

2.2.3 Comparison with model of Eloranta

The analytical model of Eloranta has been shown to be useful when applied to ground and aircraft based lidar observations. The model invokes a number of approximations and does not account for the polarization of spectral state of the return so it can not be used to simulate HSR observations. However, it can be used to confirm the accuracy of the Monte-Carlo model and can usefully be used in retrieval algorithms (see Section 2.10).

Due to the very small field-of-view of the Ecare lidar (0.0735 mrads full-angle) and the relatively low platform orbit (450 km), the instantaneous sampling volume of the EarthCARE lidar is on the order of that of a ground-based lidar with a field-of-view of a few mrads. Under these conditions, it is not unreasonable to expect an approximate analytical model to apply to the Ecare lidar observations. This has been confirmed by calculations that show that the model of Eloranta agrees within a few percent with Monte-Carlo calculations for the total returned energy for both terrestrial and space-based cases (using the EarthCARE lidar parameters). An example of such a calculation is shown in Fig. 14.

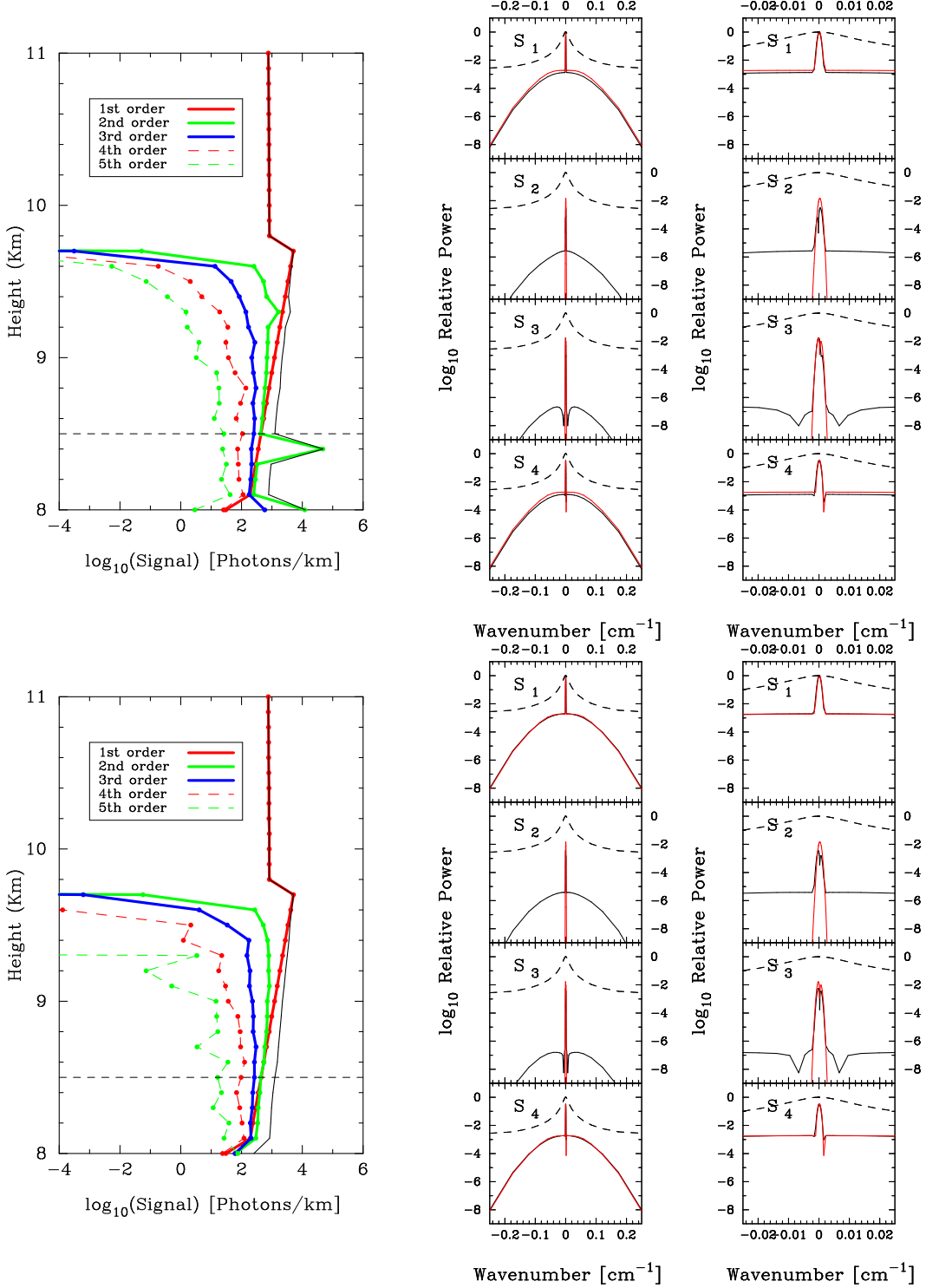


Figure 13: Exact Monte-Carlo calculation of the first 4 scattering orders from a model cirrus cloud (Top left) along with spectral profile and polarization state (Right Top Panels). The Bottom panels show the results when the approximation discussed in the text is invoked. The ‘spike’ in the top left panel has been produced by a Rayleigh backscatter event followed by a forward scatter back to the lidar receiver (see Fig. 11).

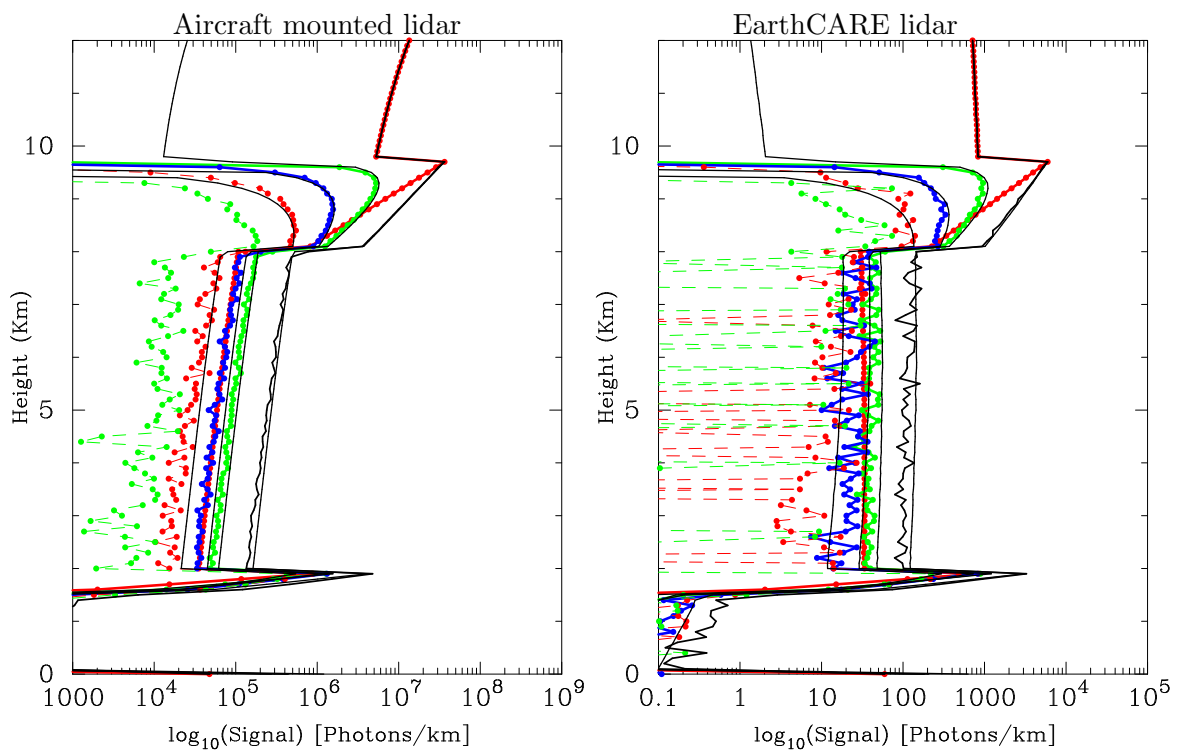


Figure 14: Comparison between the MC results of total power and the results predicted by the model of Eloranta for (Left) an aircraft mounted lidar operating at a height of 15.0 km with a full-angle field-of-view of 5.0 mrad while the left panel shows the results for the EarthCARE configuration (altitude of 450 km and a fov of 0.0735 mrad). the Cirrus cloud in both cases has an effective particle size of 25 micron and an extinction coefficient of 1/km.

2.3 Lidar Instrument Considerations

The lidar instrument component of the simulator package is handled by the **lidar** program. The practical operation of this programs is covered in detail in Section 3.9.4.

2.3.1 Background Signal

The background signal refers to power registered by the lidar receiver that is due to the detection of photons from sources other than backscattered laser light. In the case here, the main source of background light will be scattered sunlight from the Earth's surface and atmosphere. As such, the background will depend on the solar angle, the surface type and the cloud cover. Thus, the lidar background will depend on the same radiance calculations that will be made to drive the passive instrument models.

The background power incident upon the detector level is given by:

$$P_{back} = A_o \pi \rho_t \overline{I_b(\lambda) T_{rec}(\lambda)} \Delta \lambda \quad (24)$$

where A_o is the effective receiver area, ρ_t is the telescope $1/2$ angle field-of-view, and $\overline{I_b(\lambda) T_{rec}(\lambda)}$ is the average product of the receiver wavelength dependent transmission (including filtering) with the upwelling irradiance, and $\Delta \lambda$ is the wavelength interval that must be considered.

2.3.2 Receiver Optical Elements

In general, a the lidar receiver optical train consists of a number of elements that operate on the spectral and polarization state of the lidar return. For simplicity, it is assumed that the polarization elements (i.e. beam splitters, horizontal and vertical linear polarizers, half-wave plates etc..) act perfectly in polarization space (but, however, may have a non-ideal intensity efficiency) while broad-band spectral filters are modeled as having a rectangular passband and are characterized by a single in-band transmission/reflection and a out-of-band reflection/transmission pair.

The Fabry-Perot etalon is the most critical optical element in a HSR lidar's receiver chain. this element is used to separate the Mie signal from the Rayleigh signal. Fabry-Pero Etalons are capable of achieving the necessary narrow pass-bands necessary for this task. Unfortunately, non-ideal effects lead to the Rayleigh-Mie separation being imperfect. This can have a notable effect on the instrument performance. Thus, it is necessary to account for non-ideal Fabry-Perot effects in a realistic manner.

The transmission function of an etalon without taking effects such as finite input beam collimation and surface roughness may be modeled (Saleh and Teich (1991)) as

$$T = \left(1 - \frac{A}{1-R}\right) \times \frac{1}{1 + \frac{4R}{(1-R)^2} \sin^2 \frac{\delta}{2}} \quad (25)$$

where R is the reflection coefficient of the etalon mirrors, A is the relative absorption and scattering loss parameter and $\delta = 2\pi \frac{\lambda - \lambda_o}{\lambda_o}$ where λ_o is the central wavelength. The corresponding etalon reflection function may be written as:

$$R = \frac{(1.0 - R - A)^2}{1.0 - 2.0 * R * \cos(\phi) + R^2}. \quad (26)$$

The effects of non-parallel mirror flatness, diffraction and non-ideal beam collimation are taken into account by convolving the above absorbing etalon transmission and reflection functions by a top-hat function whose width in wavenumbers is given by:

$$\Delta\nu_{total} = \sqrt{\Delta\nu_{np}^2 + \Delta\nu_{ap}^2 + \Delta\nu_{dif}^2} \quad (27)$$

where $\Delta\nu_{np}$ accounts for the broadening due to non-parallel mirror alignment, $\Delta\nu_{ap}$ accounts for collimation or finite aperture effects

$$\Delta\nu_{ap} = 1.0 - \cos \left[\left(\frac{D_t}{D_{fp}} \right)^2 \frac{\rho_t}{2} \right] \quad (28)$$

where D_t is the telescope diameter, D_{fp} is the etalon diameter and ρ_t is the telescope full-angle field-of-view in radians. $\Delta\nu_{dif}$ accounts for diffraction effects and is given by:

$$\Delta\nu_{dif} = 1.0 - \cos \left[\left(\frac{\lambda_o}{D_t} \right) \right] \quad (29)$$

An example etalon transmission and reflection profile as a function of $\nu - \nu_o$ is shown in Fig. 15. Here $T = 0.978$, $A = 0.0$, the Free-spectral-range (the distance between adjacent transmission maximums) is 0.5 cm^{-1} , the flatness parameter is $\lambda_o/300$, the telescope fov is $5 \times 10^{-3} \text{ mrads}$, the telescope diameter is 0.6 m and the etalon diameter is 0.05 m .

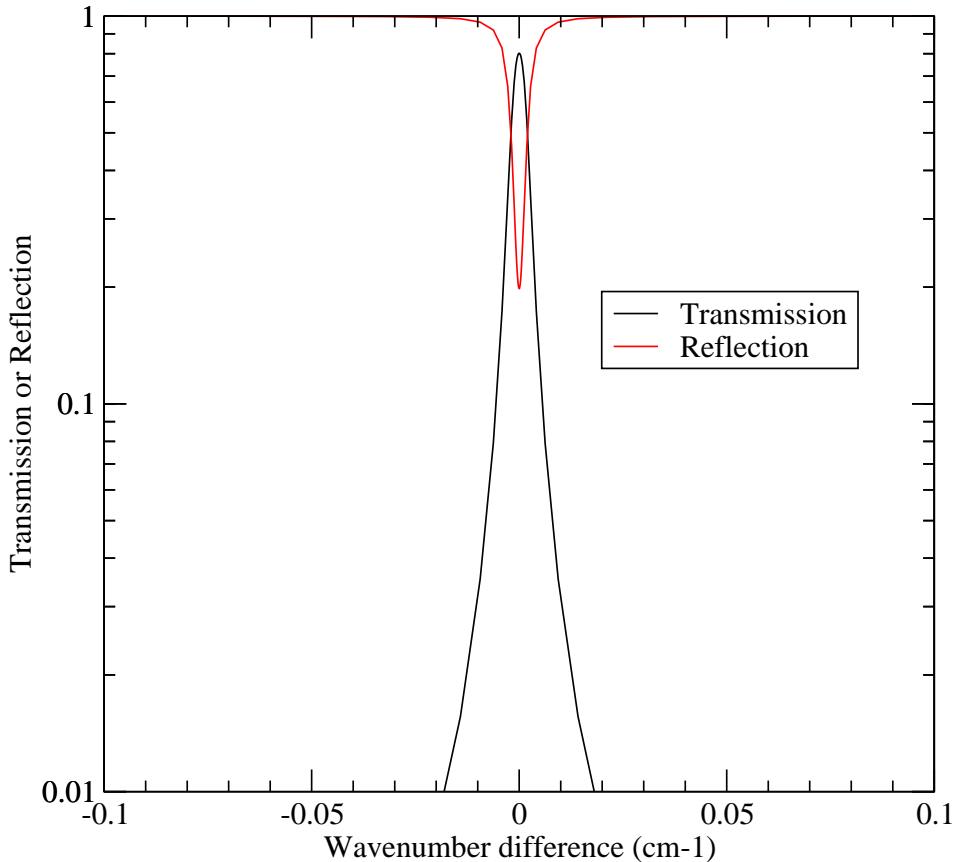


Figure 15: Etalon reflection and transmission showing non-ideal behavior.

2.3.3 Noise Considerations

For a given time interval, the number of photons arriving at a given detector channel is given by

$$N_{det} = \frac{\lambda_o}{hc} (P_{lid} + P_{back}) \Delta t \quad (30)$$

where Δt is the averaging time interval, h is Plank's constant, λ_o is an appropriate mean wavelength for the detector channel in question, P_{lid} is the power received from the lidar and P_{back} is the background power. According to Poisson statistics the standard deviation of N_{det} is simply given by

$$\delta N_{det} = \sqrt{N_{det}} \quad (31)$$

There are several sources of noise that will have to be considered. In general, the noise contributions can be divided into the noise due to the statistical fluctuations in the number of photons arriving at the detector and the noise due to the characteristics of the instrumentation itself. Expressed in terms of the equivalent fluctuations in the number of photon arriving at the detector and assuming standard Gaussian statistics the noise contributions can be written as

$$\delta N_{tot} = \sqrt{\delta N_{det}^2 + \delta N_{dark}^2 + \delta N_{ins(N_{det})}^2} \quad (32)$$

where δN_{dark} is the contribution due to the constant instrument dependent dark current noise while $\delta N_{ins}(N_{det})$ accounts for instrument related noise that may depend on the magnitude of the detected signal itself. Such an example would be read-out noise associated with a CCD type detector.

2.4 Radar

The Radar forward model component of the simulator package are covered by the **rad_filter** and **radar** programs. The practical operation of these programs is covered in detail in Sections 3.9.1 and 3.9.2. Here a brief description of some of the issues relevant to the modeling of the radar signal and the instrument characteristics are covered. First the definition of effective reflectivity used in this work is reviewed.

At 3 GHz where the refractive index of water depends only slowly with temperature, the radar reflectivity Z due a liquid droplet spectrum $N(D)$ (where D is the droplet diameter and N is the number of particles per cubic meter and per interval of diameter) is defined as $Z = \int N(D)D^6 dD$, and may be related without ambiguity to the power of the back-scattered signal.

At 95 GHz, the refractive index of water varies rapidly with temperature T , thus is convenient to refer to the equivalent reflectivity that would be observed at 3 GHz. Moreover, the ice particles have a quite different refractive index from water, and their size may extend into the Mie scattering regime. Thus it is convenient to define an "equivalent radar reflectivity" Z_e , referred to the 3 GHz frequency, and unambiguously related to the *power of the back-scattered signal*, as:

$$Z_e = \frac{1}{K_{w,3GHz}} \frac{\lambda_4}{\pi^5} \int N(D)\sigma_b(D)dD \quad (33)$$

where $\sigma_b(D)$ is the backscattering cross section.

For water cloud particles, it should be noticed that Z_e reduces to:

$$Z_e = \frac{|K_{w,95GHz}(T)|^2}{|K_{w,3GHz}|^2} Z \quad (34)$$

For ice particles, small enough in order that Rayleigh scattering holds we have

$$Z_e = \frac{|K_{w,95GHz}|^2}{|K_{w,3GHz}|^2} \frac{\rho_w}{\rho_i} \int N(D_{eq})D_{eq}^6 dD_{eq} \quad (35)$$

where D_{eq} is the equivalent melted diameter of the particle, and subscripts i and w stand for ice and water, respectively.

The radar reflectivity profile finally measured by the radar is the *apparent* reflectivity profile $Z_a(h)$ [h : altitude]. $Z_a(h)$ is related to the "true" equivalent reflectivity Z_e as:

$$Z_a(h) = Z_e \exp \left[-2 \int_0^h K_t(h') dh' \right] \quad (36)$$

where K_t is the total specific attenuation (in dB/km) in which we distinguish three terms: $K_t = K_g + K_w + K_h$.

- K_g is the attenuation by atmospheric gas other than water vapor;
- K_w is the attenuation by water vapor;
- K_h is the attenuation by hydrometers.

2.5 Radar Instrument Considerations

2.6 The attenuation due to atmospheric gases.

At 35 and 95 GHz, the attenuation by atmospheric gas other than water vapor is mainly due to the oxygen (O_2). A plot of the oxygen and water vapor absorption coefficients as a function of the frequency is shown in Figure 20. The attenuation by oxygen is close to 0.01 dB/km at 35 GHz and close to 0.03 dB/km at 95 GHz. Thus, we consider that it can be neglected at these frequencies.

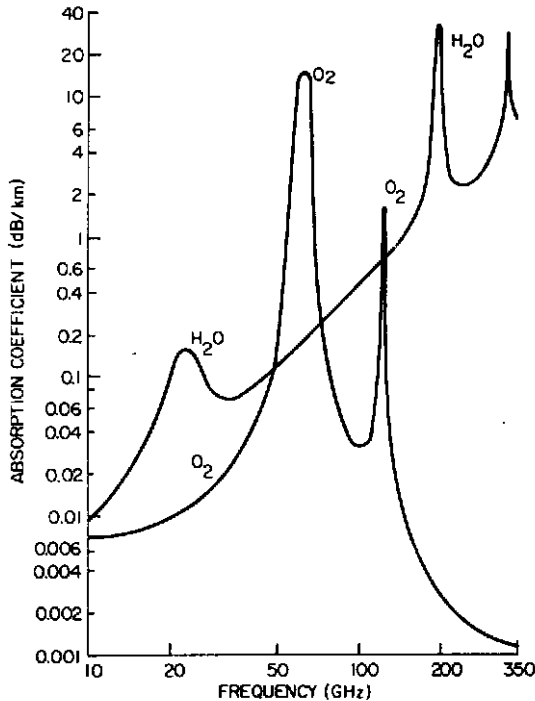


Figure 16: Absorption coefficient of oxygen and water vapor for a water vapor density of 7.5 gm^{-3} and a pressure of 1 atmosphere (Altschuler and Marr, 1998).

To correct Z_a for attenuation by water vapor, a local sounding describing the water vapor profile is necessary. The attenuation by water vapor K_v may be estimated from Liebe (1985) tabulations or through the Ulaby et al. (1981) equation. Fig.17 displays K_v as a function of temperature and relative humidity. For all the temperatures and relative humidity values, the difference between Ulaby and Liebe attenuation is less than 1 dB/km. Our choice is set to the Ulaby formulation given by Eq.(37):

$$K_v = 2f^2\rho_v \left(\frac{300}{T} \right)^{3/2} \left(\frac{\left(\frac{300}{T} \right) \exp(-644/T)}{(494.4 - f^2)^2 - 4f^2\gamma^2} + 1.2 \times 10^{-6} \right) \quad (37)$$

where

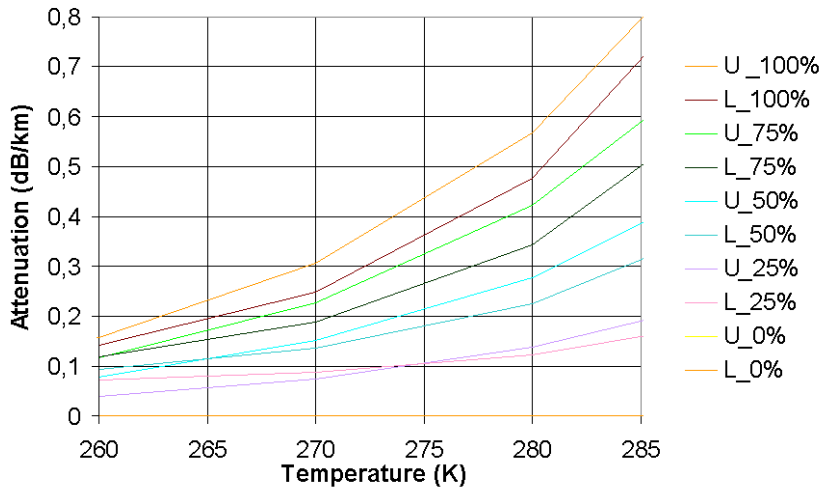


Figure 17: Attenuation by water vapor in dB/km as a function of temperature for four different values of relative humidity (100, 75, 50 and 25% respectively). The curves labelled ‘U’ denote calculations based on the formulation of Ulaby while the curves labelled ‘L’ are based on the results of Liebe.

- K_v is in [dB/Km]
- f is the frequency in [GHz]
- T temperature [K]
- P pressure [hPa]
- ρ_v is the water vapor density [$\text{g} \cdot \text{m}^{-3}$]

The water vapor density ρ_v is expressed as a function of the relative humidity:

$$\rho_v = \frac{U}{100} \frac{e_w}{R_v T} \quad (38)$$

where U is the relative humidity [%], e_w is the saturation water vapor [Pa], and R_v is the water vapor specific constant : $461.51 \text{ J} \cdot \text{kg}^{-1} \cdot \text{K}^{-1}$

2.7 Simulating the radar instrument

Once “true reflectivity profile” Z_e is known, it is possible to retrieve the “measured reflectivity profile” Z_a . To do this, the following factors must be taken into account.

- The atmospheric attenuation.
- The horizontal beam footprint.
- The effects of speckle and thermal noise.
- The effect of range weighting due to the finite width of the transmitted pulse.
- The vertical sampling frequency.

2.7.1 Atmospheric Attenuation

From space: Z_a is defined from Z_e determined as:

$$Z_a(h) = Z_e \exp \left[-2 \int_h^{100km} K_t(h') dh' \right] \quad (39)$$

where K_t is the total attenuation by gasses and hydrometers.

2.7.2 Footprint Averaging

For each altitude level the horizontally averaged reflectivity is determined according to the horizontal sampling averaging and the instrument footprint (see Fig. 18). For simplicity, the instrument footprint is assumed to be Gaussian i.e.

$$FPR(r) = \exp(-2r^2/BeamR^2) \quad (40)$$

where r is the horizontal distance from the beam center and $BeamR$ is the beam radius and is determined according to

$$BeamR = z \tan(0.5\pi\theta_{beam}) \quad (41)$$

where z is the distance to the radar and

$$\theta_{beam} = 66 \frac{\lambda_{rad}}{D_{rad}} \quad (42)$$

where λ_{rad} is the radar wavelength in meters and D_{rad} is the effective diameter of the radar antenna.

2.7.3 Noise

There are two different noise source that must be taken into account, namely speckle noise and the thermal noise. The speckle noise is a multiplicative noise related to the statistics of the signal itself that may be described with respect to the profile $Z_a(h)$ as:

$$Z_{aN}(h_k) = f_1(N_i, h_k) Z_a(h_k) \quad (43)$$

while the thermal noise is an additive noise whose magnitude is defined by the detection threshold at 0dB signal to noise ratio (SNR) noted Z_{a0dB} .

$$Z_{Nt hermal} = [f_2(N_i, h_k) - 1] Z_{a0dB} \quad (44)$$

where $\{h_k\}$ is the discrete altitude set where Z_a is sampled [$h_k = k \cdot \Delta h$ where Δh is the along range sampling interval]; and f_1 and f_2 are random functions whose probability distribution depends on the "number of independent samples N_i and are defined according to:

$$P(f) = \frac{N_i^{N_i} f^{N_i-1} \exp(-N_i f)}{(N_i - 1)!} \quad (45)$$

$P(f)$ is such that $\langle f \rangle = 1$ and $\sigma^2(f) = 1/N_i$. Their dependence of f_1 in Eq.(43) and f_2 in Eq.(44) on h_k means that they are independent from one sampling height to another. It is also assumed in Eq.(43) that the noise is perfectly known (no bias, no noise). To take into account of more realistic condition where the noise is estimated for each profile on N_B independent samples, and where there might be a bias, -1 in Eq. 44 should be replaced by: $f_3(N_B)\varepsilon_B$ where $[\varepsilon_B]$ represents the bias. For a space based lidar we may take $N_i = N_p$ where N_p is the number of pulses considered for along track integration.

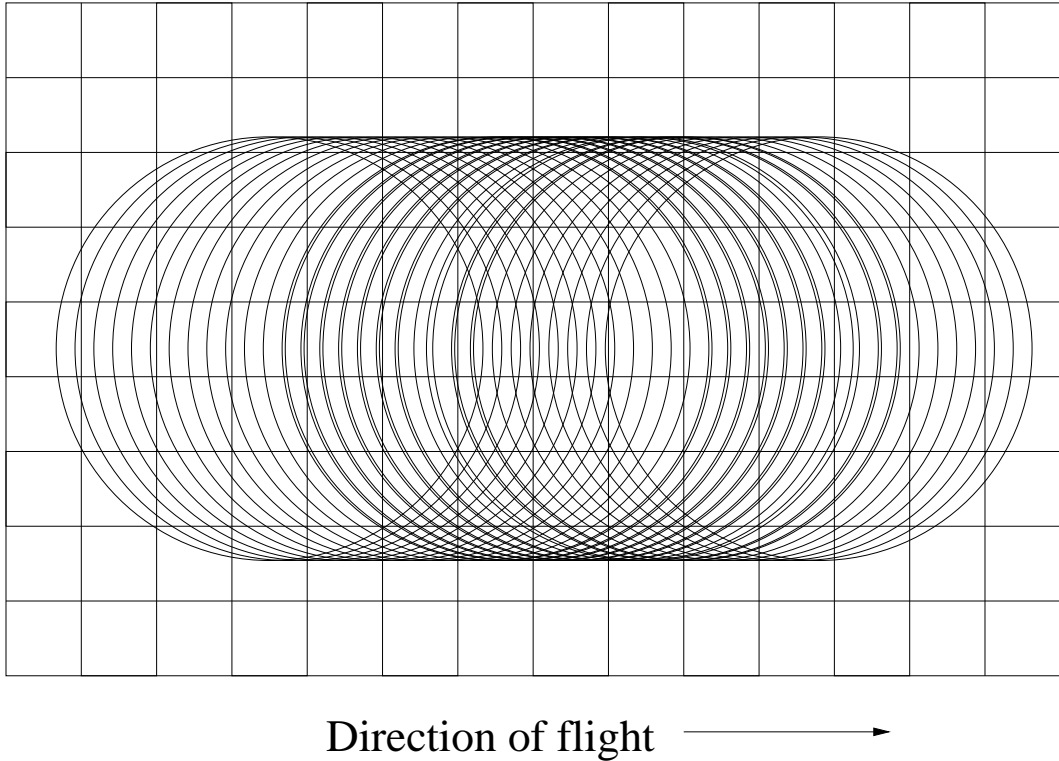


Figure 18: Schematic representation of the averaging carried out over the horizontal reflectivity field for each altitude level according to the radar instrument footprint.

2.7.4 Effect of pulse width (range weighting)

The fact that the radar pulse can not be considered as a delta function but has as finite duration has an impact of the range resolution and noise characteristics of the detected signal. Accordingly the convolution product between the attenuated reflectivity before or after speckle $Z_a(h)$ or $Z_{aN}(h)$ and the Point Target Response (PTR(h)) must be calculated. Also, the convolution product between the thermal noise $Z_{N,thermal}$ and the Impulse Response IR(h) must be calculated.

The Point Target Response and the Impulse Response are modeled as:

$$PTR(k) = \frac{1}{(\alpha\Delta r)^2} \left[\alpha(Deltar - |h|) + (1 - \alpha) \frac{\Delta h}{2\pi} \sin \left(2\pi \frac{|h|}{\Delta r} \right) \right]^2 \quad |h| \leq \Delta r \quad (46)$$

and

$$IR(h) = \frac{w^2(h)}{\int w^2(h)dh} \quad (47)$$

with

$$w(h) = \frac{1}{\alpha} \left[\alpha + (1 - \alpha) \cos \left(2\pi \frac{|h|}{\Delta r} \right) \right] \quad |h| \leq \Delta r \quad (48)$$

The optimal value of α is 0.54. Theoretically, the Point Target Response has a width equal to twice the transmitted pulse duration τ . This means that for altitudes lower than say 500 m ($\tau=3.33\mu s$), cloud response will be contaminated by the ground response. In practice, the radar receiver chain has a limited bandwidth due in particular to digital decimation filters used to select the final data rate. Receive pulses have an infinite spectrum (sinc spectrum).

So, the decimation filters cut some useful signal energy. This gives sidelobes in the PTR outside τ . This phenomenon has been analyzed during MACSIM study (Alcatel (1999)). The Hamming window with a coefficient of 0.54 was the result of the trade-off between several weighting functions.

Losses induced by the Hamming windows for different coefficient α have been plotted in the TN1 “Review of the relevant instrument requirements – Ref. ASPI/99/018355/IRS/0103 – 21/04/1999” page 24 :

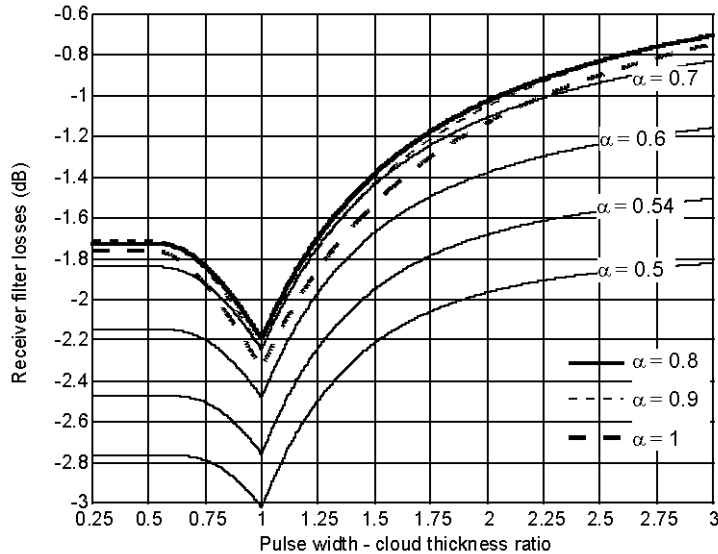


Figure 19: Losses induced by the Hamming window for different values of α .

The hamming window with a coefficient of 0.8 is the matched-filter. It can be seen that, for $\alpha = 0.54$ the loss with respect to the matched-filter is lower than 0.7 dB for thin clouds (cloud thickness $< 2\tau$).

The number of independent noise samples within a PRI increases when using a weighting function as shown in Fig. 20 (extracted from TN1) :

For example, with an Hamming window 0.54 the number of independent noise samples is more than 30% greater than with the matched filter for pulse durations lower than $3.33 \mu s$ (500 m).

Fig. 21 illustrates the PTR and the IR when Δr is normalized to 1 and $\alpha=0.54$.

2.7.5 The vertical sampling frequency.

Due to the long pulse length of space-borne radars (on the order of 100 meters) it is desirable to sample the return signal at a higher resolution than the ‘natural’ range resolution. Such a sampling strategy is known as *over-sampling*.

In the case of oversampling the individual samples will be correlated. Thus the simulated thermal and speckle noise is added to the signal before convolution with the PTR and IR functions. However the number of independent samples must be adjusted to preserve the signal variance. This has been done using the approach of Papoulis (1965) and Doviak and Zrnic (1993).

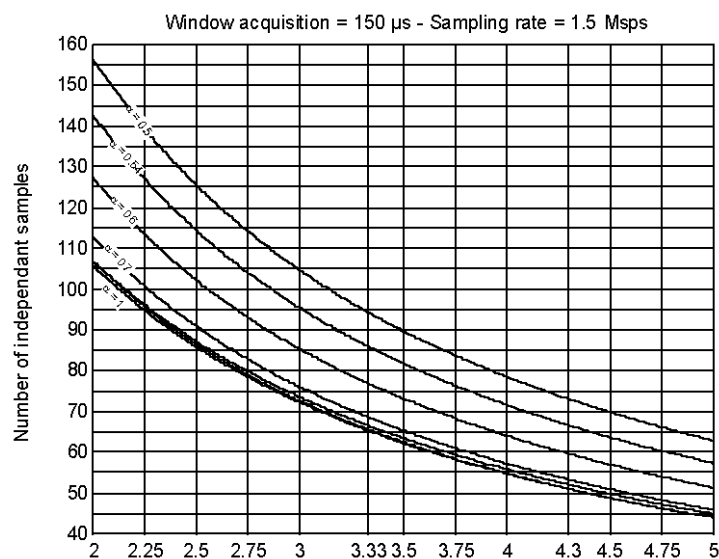


Figure 20: Number of independent samples as a function of pulse duration (abscissa) and weighing function (solid lines)

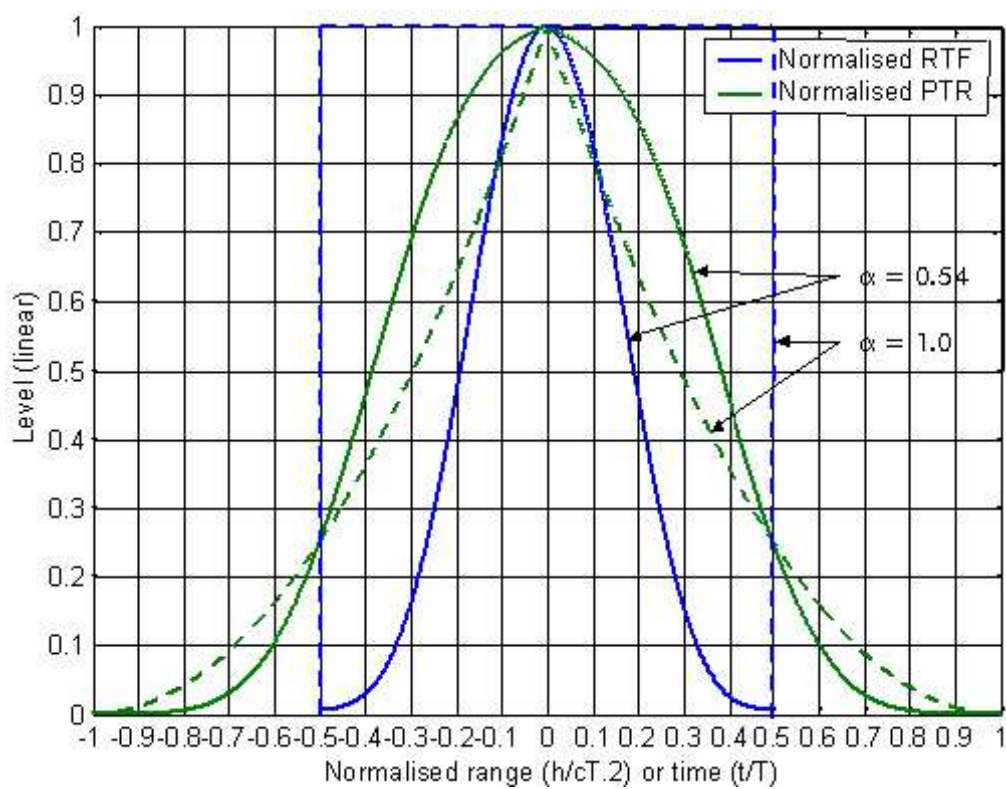


Figure 21: Point Target Response (PTR) and Impulse Response (IR) for a range resolution Δr normalized to 1.

2.8 Short-wave Radiation Calculations

The short-wave calculations are preformed using a semi-analytical Monte-Carlo procedure Barker et al. (2002). In general, photon packets are tracked from the top of the atmosphere until they are (effectively) absorbed or exit the atmosphere (see Fig. 22). The manner this is accomplished in is generally similar to that described for the Lidar Monte Carlo calculations (Sec. 2.2.2). The domain is assumed to be cyclic so that photon packets leaving the right side of the domain will appear back on the left side. At each atmospheric interaction the photon packet is either absorbed or scattered. Interactions with the surface do not result in outright absorption but reduce the statistical weight of the packets.

In order to increase the efficiency of the simulation at each scattering interaction the direct contribution to the received signal is calculated. This results in a great increase in efficiency. However, this procedure can result in the generation of rare events with very high contributions (see Fig. 23). In order to handle these ‘skipped’ events the contribution from each event above a user specified threshold are not counted directly. Instead the ‘excess’ contribution is binned separately and is distributed in a smooth fashion over the whole domain at the end of the simulation thus conserving total energy.

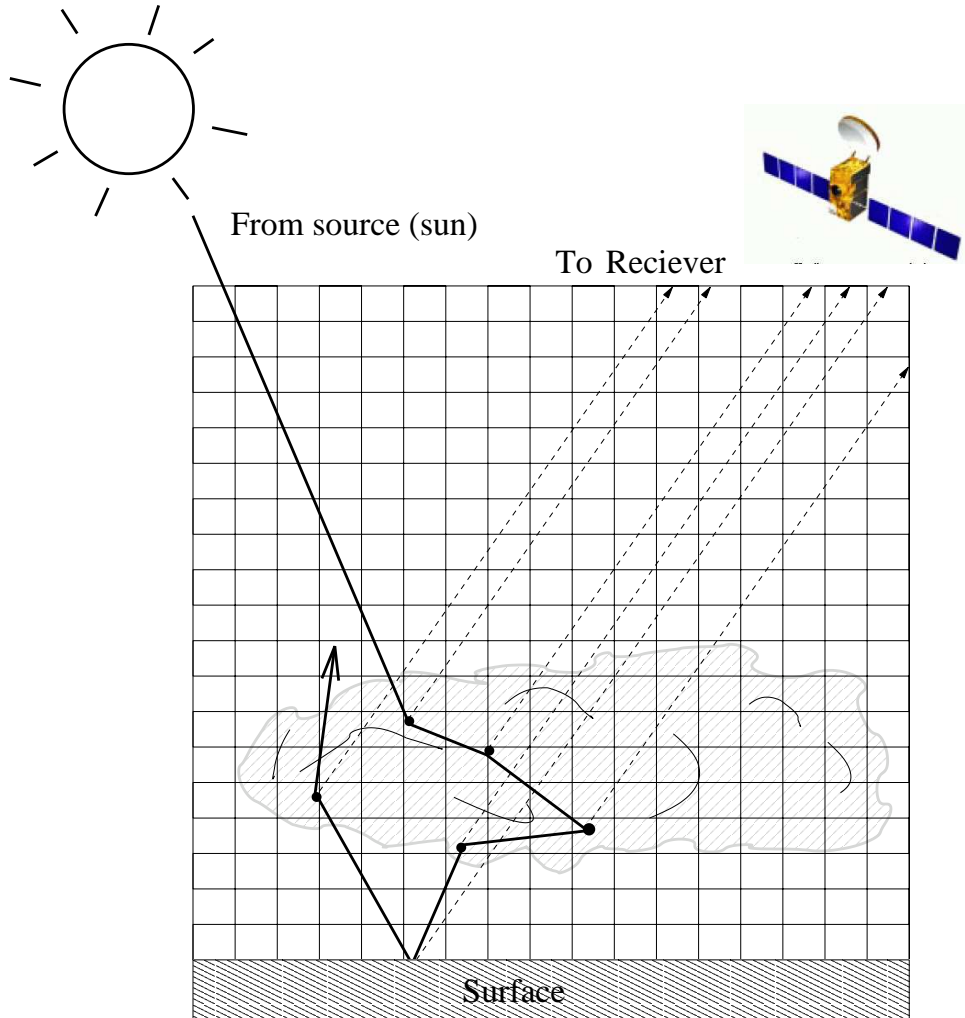


Figure 22: Schematic view of the Short-Wave Monte-Carlo approach used.

Example results for simple plane-parallel cloud scenes above ocean are shown in Fig. 24. The results closely match those generated by other non-Monte-Carlo type programs (For

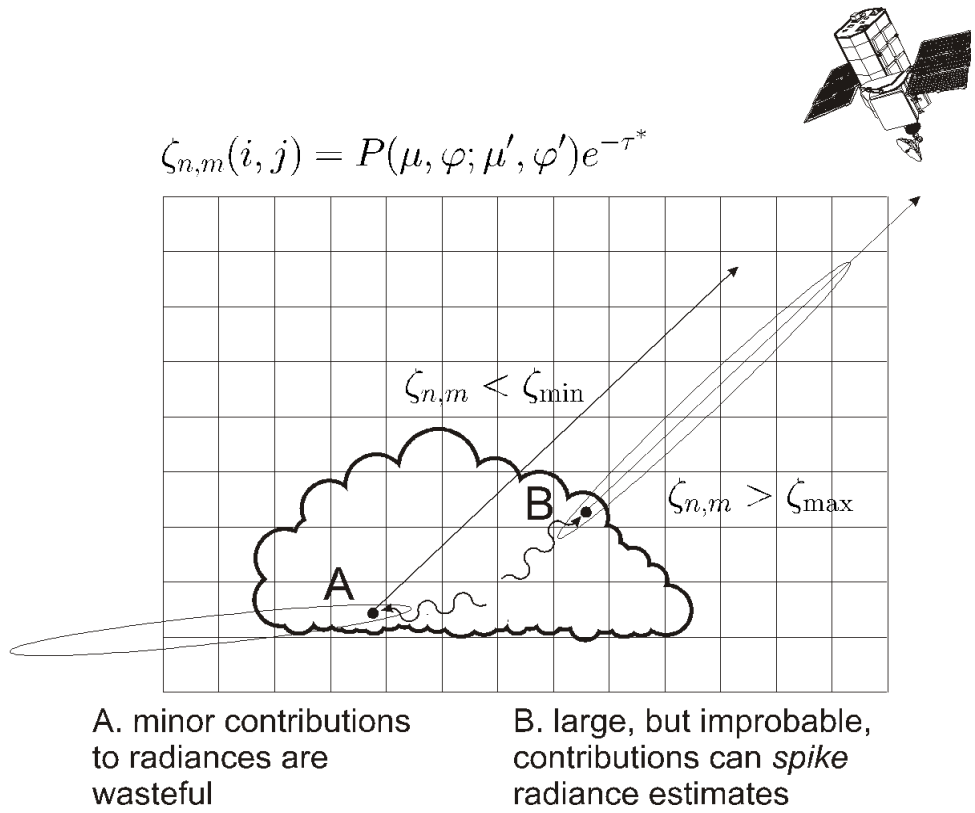


Figure 23: Schematic showing how the location in a cloud of different photon trajectories relative to a sensor can result in dramatically different contributions to a radiance estimate. The photon at A is moving away from the sensor and is deep inside the cloud. Thus, its chance of being scattered toward the sensor and making it out of the cloud is low. The photon at B, on the other hand, is moving toward the sensor and experiences a scattering event close to a cloud edge. Thus, its chance of being scattered toward the sensor and making it out of the cloud is extremely high.

example see Liou (2002), Section 7.3.5.1). These ‘look-up table’ type calculations are used in the MSI retrieval program (See Section 2.11).

For details on the treatment of the scatterers, surfaces, and atmospheric absorption see Sec. 3.9.5.

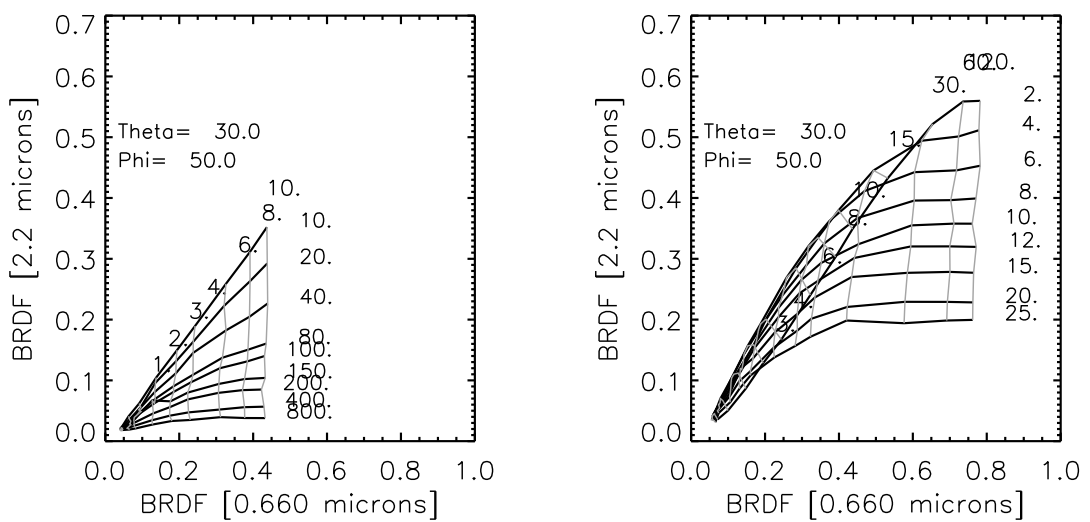


Figure 24: 2.2 micron verses 0.6 micron brdfs as a function of cloud optical depth and mode width parameter for (Left) hexagonal columns and (Right) water droplets.

2.9 Long-wave Radiation Calculations

At wavelengths past 4.0 microns thermal emission within the Earth's atmosphere dominates over the amount of solar radiation in this wavelength regime. Unlike the case for solar short-wave radiation the source of the radiations is dispersed throughout the atmosphere itself. This makes a standard Monte-Carlo approach impractical. However, an inverse Monte-Carlo approach is very efficient in these circumstances.

An inverse Monte-Carlo technique tracks photon packets back from the receiver. The photon packet paths are tracked back to where they are absorbed (emitted) (See Fig.2.9). Once the path of a particular packet is determined its contribution to the receiver signal is determined. This contribution depends of the wavelength in question and the temperature of the atmosphere where the packet was first emitted.

Top-of-atmosphere fluxes are also computed by this method. The flux calculation precedes by calculating radiances at 5 emergent angles (random azimuths) and using a weighted sum of the radiances as an approximation to the flux (i.e. 5-stream approximation).

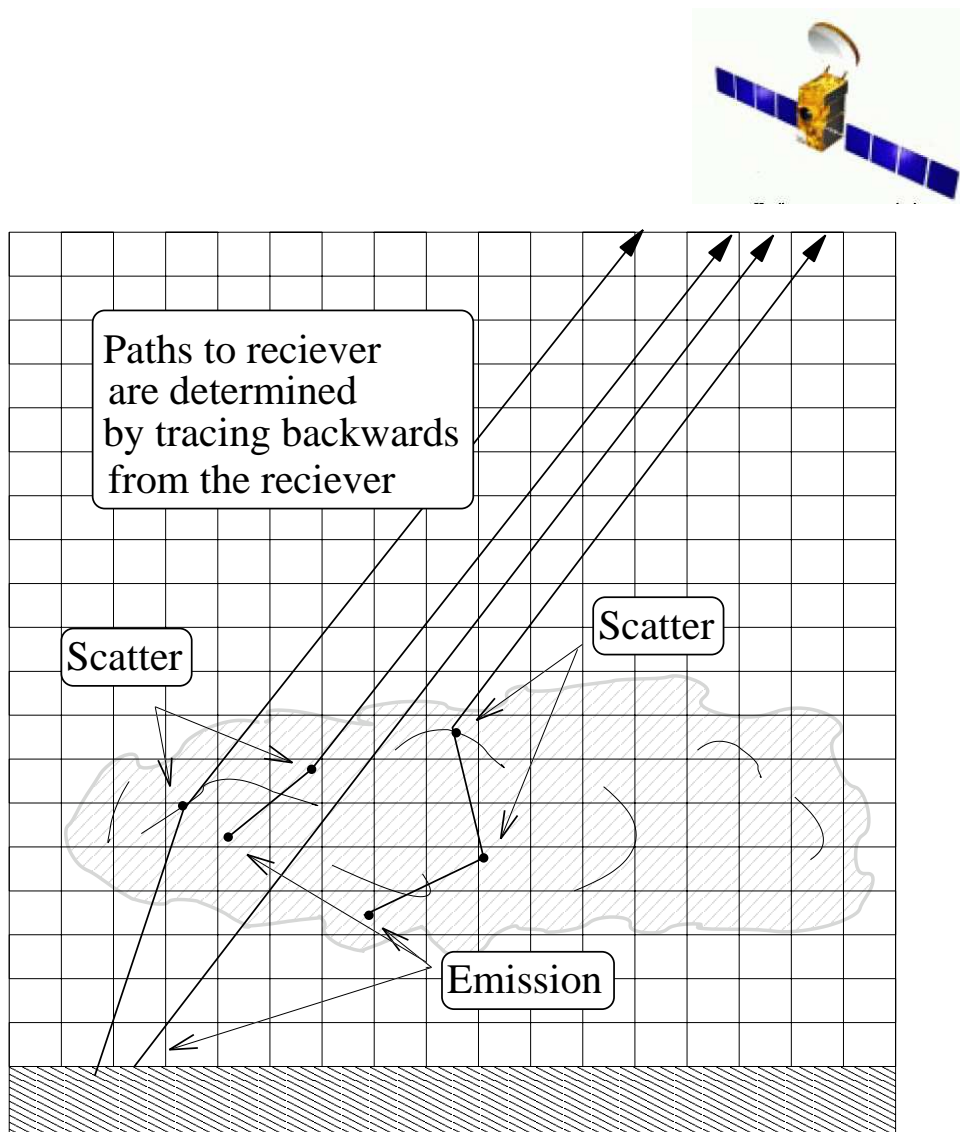


Figure 25: Schematic view of the Inverse Long-Wave Monte-Carlo approach used.

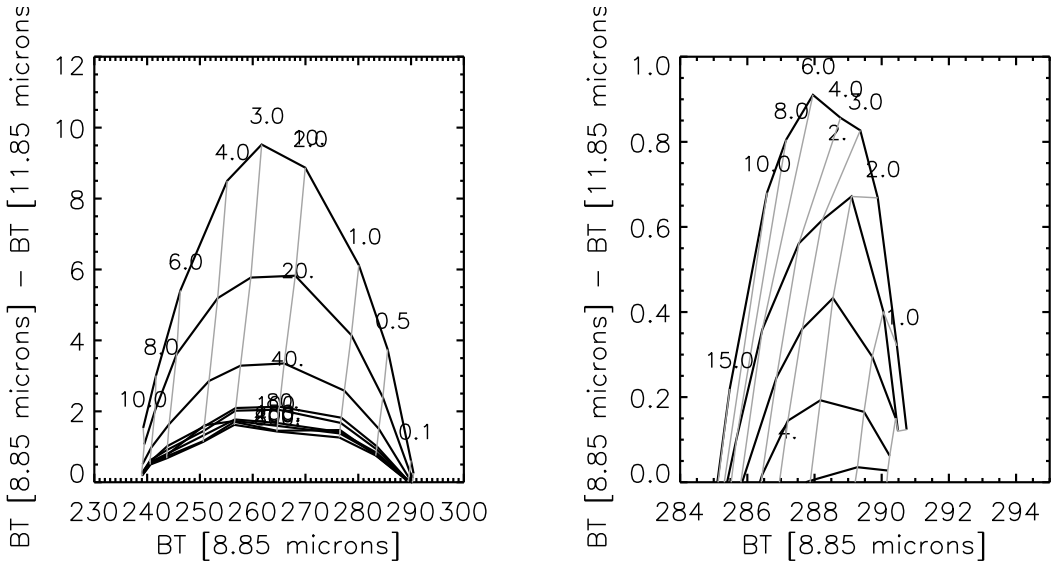


Figure 26: Brightness temperature difference arches generated using the long-wave Monte-Carlo code for (Left) hexagonal columns and (Right) water droplets.

Example results for simple plane-parallel cloud scenes above ocean are shown in Fig. 2.9. The results closely match those generated by other non-Monte-Carlo type programs (For example see Minnis et al. (1998)). These ‘look-up table’ type calculations are used in the MSI retrieval program (See Section 2.11).

For details on the treatment of the scatterers, surfaces, and atmospheric absorption see Sec. 3.9.5.

2.10 Lidar+Radar Level 1 retrievals

The level 1 processing of the combined outputs of the radar and lidar instrument simulation programs is preformed by the **lidar_ret1** program. It reads the output from **lidar**, **radar** and creates a number of *level 1* products at a common height and horizontal distance grid. Aspects of the processing are specific to the HSR capability of the EarthCARE lidar so that adapting this program to other platforms will require re-coding.

In general the main products of this program fall into the following categories.

1. Cloud/aerosol masks.
2. Cloud Extinction and backscatter profiles.
3. Lidar/Radar effective particle size profiles.
4. Aerosol extinction and backscatter profiles.

For more details see Section 3.10.1.

2.11 MSI only retrievals

This program reads in output from **MC_sim_main** and attempts to deduce the cloud/aerosol scattering type, optical depth, and effective radius using look-up tables previously generated using **MC_sim_main**.

Standard short-wave MSI products such as target classification, effective particle size, and optical depth are generated. The technique used is very simple. For each pixel, the specified lookup tables for the appropriate surface, solar, and viewing geometry are scanned and following cost function is evaluated

$$Diff(is, itau, isize) = \sum_{i=1}^4 \left[\frac{R_{obs}(i) - Rad_{tab}(i, is, itau, isize)}{R_{obs}(i)} \right]^2 \quad (49)$$

where i is the MSI band, is is the scattering type (i.e. water, columns, sulphate etc..), $itau$ is the optical thickness index and $isize$ is the effective cloud/aerosol particle size index.

After scanning through all the table entries, the closest match between the lookup table entries and the observed radiances is used to determine the pixel's apparent cloud and aerosol properties.

General Notes The present version uses only the short-wave MSI radiances. Use of the long-wave radiances would entail the use of many more lookup-tables covering a range cloud heights and atmospheric temperature profiles.

2.12 Combined Active+Passive 3-D retrievals

This program combines the EarthCARE long-wave MSI images as well as the profile outputs from `lidar_ret1` in an effort to reconstruct the cloud fields. In brief, for each of the nadir columns, profiles of lidar extinction, lidar backscatter and radar reflectivity are calculated based on height dependent cloud particle size distributions of various scattering types (small mode water, large mode water, small mode ice, and large mode ice). Using the same information, a simple forward model is used to calculate the long-wave MSI TOA radiances.

In order to determine a plausible set of height-dependent cloud particle size distribution parameters a suitable *cost-function* is based on the cloud parameters is minimized. . The cost function includes contributions from a priori information as well as terms representing the uncertainty weighted differences between the model quantities and the lidar measured extinction and backscatter, the radar reflectivity profile and the MSI BTs. The cost function is minimized using a simulated annealing approach (*see Numerical Recipes*).

Once the nadir cloud property profiles are determined the MSI images are used in order to map the profiles to the off-nadir pixels. This is done on the scanning through the 2-d off nadir image pixels and finding the closest match in terms of radiances among the nadir pixels.

The approach to retrievals embodied by this program should be considered very promising but still experimental, all the pitfalls are definitely not yet known. In particular, care and thought must be exercised in determining useful weights for the components of the cost function in order to obtain useful results. Also, the annealing schedule as specified in the sample input file is likely far from optimal. Further, the program as it stands can only ingest simple a-priori estimates of the cloud properties that must be specified by the user. A mechanism could be introduced where a priori estimates (and initial values) are derived from the measurements themselves, for example, by using conventional LWC/IWC -vs- Z_e relationships.

2.12.1 Cost Function

The cost function that, on a column by column, basis that the inversion procedure attempts to minimize can be expressed as

$$C_f(N_{isc,iz}, Rm_{isc,iz}) = \sum_{i=1}^{12} \sum_{iz=1}^{Nz} E_{i,iz} \quad (50)$$

where isc denotes the scatterer type and iz is the altitude index. Four scatterer types are considered by default

1. Small mode ice
2. Large mode ice
3. Small mode water
4. Large mode water

The underlying parameter set that is adjusted to minimize 50 are the parameters of height dependent cloud particle size distributions. Modified gamma type size distributions are used for each scattering type i.e. for each scattering type used in the inversion and at each cloudy altitude we have

$$\frac{dN_{isc}(r)}{dr} = N_{o,isc} \left(\frac{1}{\Gamma(\gamma)} \right) \left(\frac{1}{Rm_{isc}} \right) \left(\frac{r}{Rm_{isc}} \right)^{\gamma_{isc}-1} \exp \left[-\frac{r}{Rm_{isc}} \right] \quad (51)$$

here isc is the scatter-type index (see above), Rm_{isc} is the corresponding mode radius, $N_{o,isc}$ is the total number density, and γ , isc is the width parameter. By default, the width parameters are fixed and the other two parameters are adjusted to minimize the cost function. Water and ice are assumed not to exist within the same range gate. Thus, for each altitude where a cloud is present we will have 2 free parameters.

The cloud mask supplied by `lidar_ret1` is used to decide between the cloudy and non-cloudy altitudes. Presently, temperature is used to distinguish between water and ice. A more sophisticated criteria involving an improve classification scheme that would be provided by `lidar_ret1` is an option for future implementation.

In the remainder of this section the various components cost function will be described in detail.

Observation terms The first three components of the cost function are defined as follows:

$$E_1 = \sum_{iz=1}^{N_z} \left[W_{1,isc,iz} \left(\frac{\alpha_{obs,zi} - \sum_1^4 \alpha_{calc,isc}(N_{isc,iz}, Rm_{isc,iz})}{\Delta \alpha_{obs,iz}} \right)^2 \right] \quad (52)$$

$$E_2 = \sum_{iz=1}^{N_z} \left[W_{2,isc,iz} \left(\frac{\beta_{obs,zi} - \sum_1^4 \beta_{calc,isc}(N_{isc,iz}, Rm_{isc,iz})}{\Delta \alpha_{obs,iz}} \right)^2 \right] \quad (53)$$

$$E_3 = \sum_{iz=1}^{N_z} \left[W_{3,isc,iz} \left(\frac{Ze_{obs,iz} - \sum_1^4 Ze_{calc,isc}(N_{isc,iz}, Rm_{isc,iz})}{\Delta Ze_{obs,iz}} \right)^2 \right] \quad (54)$$

where iz is the height index, $\alpha_{obs,zi}$ is the observed lidar extinction, $\beta_{obs,zi}$ is the observed lidar backscatter, and $Ze_{obs,iz}$ is the observed radar reflectivity (as output from `lidar_ret1`).

The lidar and radar data are usually not useful at scales less than 1 km. However, the MSI data has a resolution of 0.5×0.5 km. In order to use the higher resolution MSI data together with lidar and radar data a cloud fraction parameter ($f_{i,j}$) is introduced such that,

$$\sum_{i,j=1}^{n_s} f_{i,j} = 1 \quad (55)$$

where n_s is the number of discrete intervals that the square retrieval resolution volume is divided into (see Fig. 2.12.1).

Within each resolution volume, the microphysical cloud/aerosol properties are assumed to be the same except that the number density of each scatterer type is scales according to the fraction parameter ($f_{i,j}$). Taking the sub-scale inhomogeneity into account (and dropping the height subscript for clarity) then leads to the following forward retrieval model model expressions for $\alpha_{calc,isc}$

$$\alpha_{calc,isc} = \frac{\sum_{i,j}^{n_s} \alpha_{i,j,isc} \exp(-2\alpha_{i,j,isc})}{\sum_{i,j}^{n_s} \exp(-2\alpha_{i,j,isc})} \quad (56)$$

where

$$\alpha_{i,isc} = \sum_{is=1}^{Ns} N(D_{is}, Rm_{isc}) \sigma_{isc}(D_{is}) \delta D_{is}(isc) \quad (57)$$

here D_{is} is the maximum size of the particles in size bin is and σ_{isc} is the corresponding extinction cross-section. Similar expressions hold for $\beta_{calc,isc}$. $Ze_{calc,isc}$ is also calculated in an analogous manner except the vertical profile is convolved with a Gaussian function in order to simulate the effect of the Radar pulse width (see Section. 2.4).

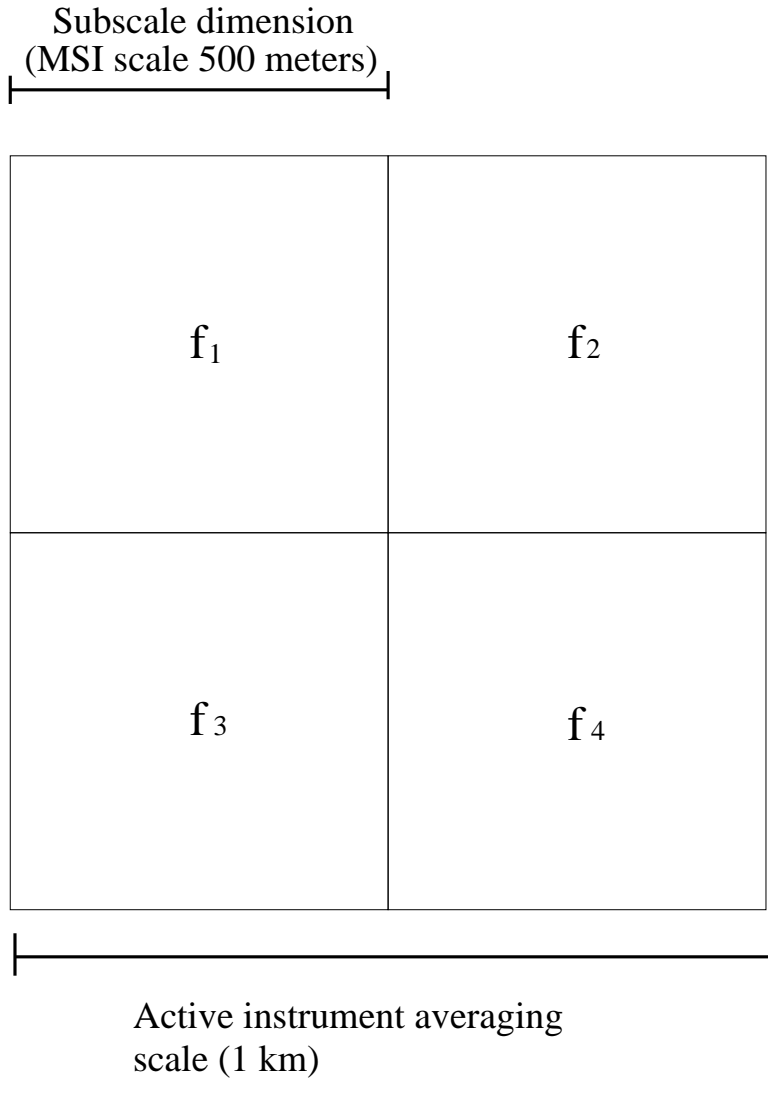


Figure 27: Schematic illustration of how the retrieval resolution volume may be sub-divided on a smaller scale.

The next term in the cost function is

$$E_4 = N_{cld} \sum_{ic=1}^3 \left[W_{4,ic}^2 \frac{(It_{obs}(ic) - It_{calc}(ic))^2}{It_{obs}(ic)} \right] \quad (58)$$

where $It_{obs}(ic)$ is the observed thermal IR radiance in channel ic . N_{cld} is the number of cloudy altitudes in the considered column and is used to scale the contribution so it of the same order as the other vertically resolved energy function terms. $W_{4,ic}$ is the assigned weighting coefficient (by default equal to $1 / [0.2 \times It_{obs}(ic)]$). $It_{calc}(ic)$ is the retrieval forward model value of the brightness temperature and is calculated for the given Nadir pixel columns using approximately accounting for scattering effects using a delta-Eddington approach. The IR radiance $It_{ic,calc}$ is

$$It_{ic,calc}(ic) = B_{ic}(T_o) e^{-\tau_{ic}(z_{top})} + \int_0^{z_{top}} z_{top} B_{ic}(z') e^{-(\tau_{ic}(z_{top}) - \tau_{ic}(z'))} \frac{d\tau_{ic}}{dz'} dz' \quad (59)$$

where B_{ic} is the average Planck function corresponding to the wavelength band corresponding to channel number ic and T_o is the surface temperature. $\tau_{ic}(z)$ is the effective optical thickness

between the surface and z . $\tau_{ic}(z)$ is comprised of both an atmospheric and a cloud component so that

$$\tau_{ic}(z) = \int_0^z (\sigma_{ic,atmos}(z') + \sigma_{is,cld}) dz' \quad (60)$$

where $\sigma_{ic,atmos}(z')$ is the atmospheric gaseous absorption coefficient appropriate for the narrow wavelength range of back ic . $\sigma_{is,cld}$ is the cloud absorption coefficient. In order to approximately account for scattering effects the values of $\sigma_{is,cld}$ are adjusted using the δ -Eddington approximation.

A-priori weighting terms In certain circumstances, it is necessary to stabilize the solution of the cost function minimization by introducing a-priori information. These constraints can also be used to help “fill-out” areas where direct information is lacking (i.e. areas where the lidar or radar may not provide a useful return in terms of signal-to-noise ratio.)

$$E_5 = \sum_{iz=1}^{N_z} \sum_{is=1}^4 \left[W_{5,isc,iz} \frac{(Rm(is, iz) - Rm_a(is, iz))^2}{\Delta Rm_a(is, iz)} \right] \quad (61)$$

This term accounts for the a-priori size of the cloud particles (Rm_a). While

$$E_6 = \sum_{iz=1}^{N_z} \sum_{is=1}^4 \left[W_{6,isc,iz} \frac{(\alpha_{calc,isc}(iz) - \alpha_{a,isc}(iz))^2}{\Delta \alpha_{a,isc}(iz)} \right] \quad (62)$$

accounts for the a-priori extinction coefficient (which, for a given value of R_m is directly linked to the number density N_o).

Smoothness terms The E_7 and E_8 terms of the cost function control the vertical smoothness of the retrieval results

$$E_7 = \sum_{iz=1}^{N_z} \sum_{is=1}^4 W_7 \left[\frac{(Rm(is, iz) - Rm(is, iz + 1))}{\min(Rm(is, iz), Rm(is, iz + 1))} \right]^2 \quad (63)$$

where both $Rm(is, iz)$ and $Rm_{fit}(is, iz + 1)$ are greater than zero. Similarly for the optical extinction

$$E_8 = \sum_{iz=1}^{N_z} \sum_{is=1}^4 W_8 \left[\frac{(\alpha(is, iz) - \alpha(is, iz + 1))}{\min(\alpha(is, iz), \alpha(is, iz + 1))} \right]^2 \quad (64)$$

The E_{10} term in the cost function determines the horizontal smoothness of the retrieved extinction field (cloud fraction). This term plays a role only when sub-scale horizontal variations are allowed (see Fig. 2.12.1).

$$E_{10} = W_{10} \sum_{iz=1}^{N_z} \sum_{i,j=1}^{n_s} (f_{i,j}(iz) - 1.0)^2 \quad (65)$$

Stratocumulus terms The remaining terms in the cost function are particular to the case of semi-adiabatic water clouds

The term E_{11} is used to impose a constant number density in the vertical with respect to the small water mode number (isc=3) density

$$E_{11} = W_{11} \sum_{iz=1}^{N_z} \left[\frac{(No(3, iz) - No(3, iz + 1))}{\min(No(3, iz), No(3, iz + 1))} \right]^2. \quad (66)$$

The E_{12} term measures the departure of the liquid-water content (LWC) slope of both the small and large water modes

$$\begin{aligned}
E_{12} &= W_{12} \left(\frac{2}{\frac{dLWC_{adb}}{dz}} \right)^2 \\
&\times \sum_{iz=1}^{N_z} \left[\frac{(LWC(3, iz+1) + LWC(4, j+1) - (LWC(3, iz) + LWC(4, iz)))}{(z(iz+1) - z(iz))} \right. \\
&\left. - \frac{dLWC_{adb}}{dz} \right]^2
\end{aligned} \tag{67}$$

where $\frac{dLWC_{adb}}{dz}$ is the a-priori *semi-* adiabatic water content slope (hard coded at 0.0125 g/m³/km).

The E_{13} term is applied to the mode radius and extinction of the small-mode water particles.

$$\begin{aligned}
E_{13} &= W_{13} \\
&\times \sum_{iz=1}^{N_z} \left[\left(\left(\frac{2}{\frac{dRm_{adb}}{dz}} \right)^2 \frac{(Rm(3, iz+1) - Rm(3, iz))}{((z(iz+1) - H_o)^{1/3} - (z(iz) - H_o)^{1/3})} - \frac{dRm_{adb}}{dz} \right)^2 \right.
\end{aligned} \tag{68}$$

$$\begin{aligned}
&+ \left. \left(\left(\frac{2}{\frac{d\alpha_{adb}}{dz}} \right)^2 \frac{(\alpha(3, iz+1) - \alpha(3, iz))}{((z(iz+1) - H_o)^{2/3} - (z(iz) - H_o)^{2/3})} - \frac{d\alpha_{adb}}{dz} \right)^2 \right]
\end{aligned} \tag{69}$$

(70)

where H_o is the observed cloud base from the combined lidar and radar measurements, $\frac{dRm}{dz}_{adb}$ is the a-priori *semi-* adiabatic mode radius slope (hard coded at 12.2 microns/km^{1/3}) and $\frac{d\alpha}{dz}_{adb}$ is the a-priori *semi-* adiabatic extinction slope (hard coded at 0.0184 m⁻¹/km^{2/3}).

2.12.2 Expansion to 3-D domain

Once the sub-satellite track profile properties have been determined the profile properties are mapped to the non-nadir MSI pixels using a simple strategy. For each non-nadir pixel the profile information for the best matching nadir pixel with known profile matching is used (see Fig. 28).

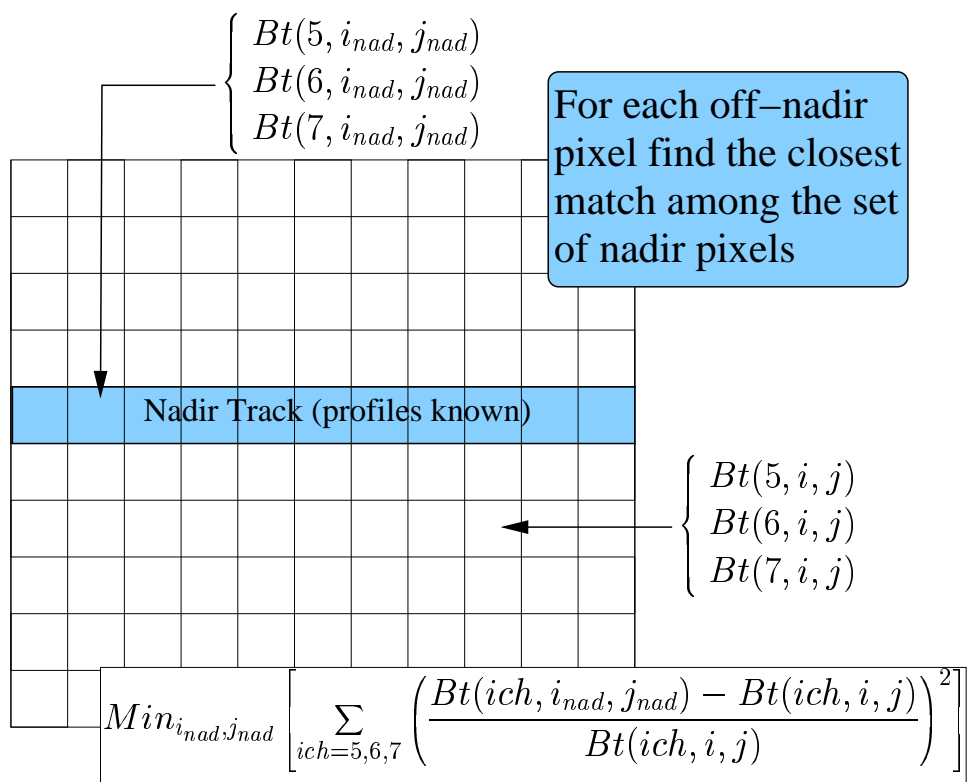


Figure 28: Expanding the 2-D profile information to fill a 3-D domain based on finding the “best-match” among the nadir pixels and the off-nadir pixels using the IR brightness temperatures.

3 Using the package

In order to install the package please follow the directions given in Appendix A. The package simulator is written in Fortran90 and has been designed to run primarily under a Unix/Linux environment but it will build and run under the Cygwin (see: www.cygwin.com) environment under Windows98 or WindowsXP.

With the exception of a few **Numerical Recipes** F90 routines the Ec care simulator code is entirely in the public domain. The source code for these routines can not be freely distributed. The absence of these routines will not effect the forward model components of the simulator package but will prevent one of the retrieval programs from being compiled. Accordingly, in addition to the source code, pre-built binaries for this simulator component for Linux and Windows are included in the distribution.

3.1 Package Overview

After installation the following directory structure shown in Fig. 29 will be in place.

simulator This is the root directory of the distribution. Most of the simulator programs expected to be executed from this directory.

ck_files Contains the correlated-k lookup-tables. These tables are discussed in Section 3.9.6.

std_atmos Contains various standard atmospheric profile data (McClatchey et al. (1972)) that is used by the scene creation program.

scripts Contains some example shell scripts that illustrate how the operation on the simulator can be automated.

bin Contains the various executable programs. This directory can either be added to the users **path** or these programs may be executed from the simulator root directory by adding the path information before the executables name (i.e. `./bin/lidar` will execute the `lidar` program from the **simulator** directory.)

doc Contains the simulator documentation.

data Contains various data files.

scatt_master_lists Contains files which define the scattering types. A file will be present for each cloud or aerosol type.

src Contains the simulator source code. The **pgxtal** subdirectory contains the source code of the PGXTAL distribution. This code extends the 3-D plotting capabilities of PGPlot. The **nrf** is empty. However, if you have access to Numerical Recipes in Fortran90 several routines should be placed here. A README file present in this subdirectory gives more information.

input Contain default MASTER input files as well as ORBIT files. MASTER input files are described in Section 3.3 while ORBIT files are described in Section 3.4. The various subdirectories contain default input files specific to various simulator programs.

output The various subdirectories of output are the default locations for the output files of various simulator programs.

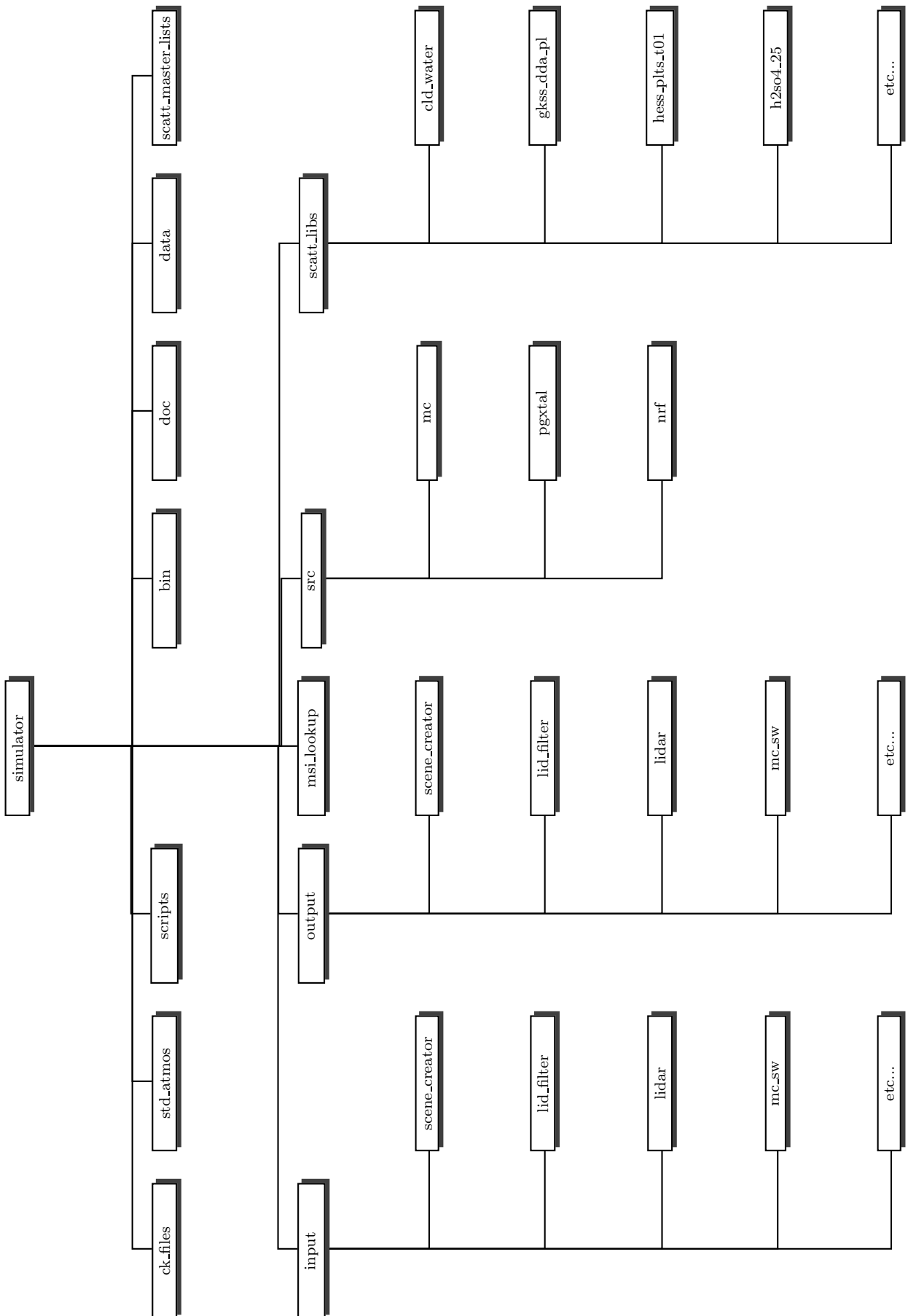


Figure 29: Directory structure of the EarthCARE simulator package.

3.2 Executables

The individual programs which comprise the simulator package are briefly listed here. A more complete description of each program is given later in this document.

Forward Model Programs

<code>lid_filter</code>	A 3-D Monte-Carlo lidar multiple-scattering engine. The code accounts for polarization and spectral effects
<code>lidar</code>	A lidar instrument module which simulates the lidar optical filtering and other instrument effects. This application relies on the output of <code>lid_filter</code>
<code>rad_filter</code>	Creates idealized radar reflectivity (Z) and radar Doppler velocity (V_d) fields.
<code>radar</code>	Samples the output of <code>rad.filter</code> and accounts for radar sampling and instrument effects.
<code>MC_sim_main</code>	A 3-D Monte-Carlo code for calculating Top-of-Atmosphere (TOA) short-wave radiances as well as Fluxes throughout the domain.
<code>MC_LW_sim_main</code>	A 3-D Monte-Carlo code for calculating Top-of-Atmosphere (TOA) long-wave radiances as well as TOA Fluxes

Retrieval Programs

<code>lidar_ret1</code>	Processes data from <code>lidar</code> and <code>radar</code> and generates level 1 profile output products.
<code>msi_ret</code>	Uses the output of <code>MC_sim_main</code> and <code>MC_LW_sim_main</code> to generate standard MSI level 1 2-D cloud and aerosol products.
<code>lw_msi_lidar_radar</code>	Combines the output of <code>lidar_ret1</code> together with <code>MC_LW_sim_main</code> in order to retrieve the 3-D cloud property field.

Utility Programs

<code>scene_creator</code>	Generates a <i>scene file</i> in the so-called simulator <i>Universal File Format</i> (UFF). The UFF file generated can be a ‘simple-scene’ based on direct user input. <code>scene_creator</code> can also be used to facilitate the translation of more complex cloudy scenes (i.e. those derived from cloud resolving atmospheric models) into a UFF file.
<code>extract_quantity</code>	A utility for extracting 2-D ‘slices’ of various quantities from a UFF file
<code>extract_quantity_hor</code>	A utility for extracting 2-D integrated column values of various quantities from a UFF file
<code>extract_quantity_3d</code>	A utility for extracting 3-D fields of various quantities from a UFF file
<code>extract_env_profile</code>	A utility for extracting profiles of average temperature, pressure, water vapor and ozone mixing ratios from a UFF file
<code>uff_merger</code>	A utility for merging two UFF files together in the vertical
<code>uff_averager</code>	A utility for creating a lower resolution version of a UFF file.

In addition to the forward model, inverse model and utility programs a number of plotting utilities exist. **Note:** the plotting programs require that the **PGPLOT** graphics subroutine library be installed on the system the simulator package is running on. For more information see the installation information in Appendix A.

Graphics Programs

<code>plot_slice</code>	A utility for plotting the results of <code>extract_quantity</code> , <code>lidar</code> , <code>radar</code> and , <code>lidar_ret1</code> .
<code>plot_hor</code>	A utility for plotting the results of <code>extract_quantity_hor</code> and , <code>msi_ret</code> .
<code>plot_3d</code>	A utility for producing 3-D plots from the results of <code>extract_quantity_3d</code> .
<code>plot_profile</code>	As <code>plot_slice</code> but plots vertical profiles.
<code>plot_profile_comp</code>	As <code>plot_slice</code> but plots vertical profiles from two different data files together
<code>mcrad_quick_plot</code>	A utility for plotting the results of <code>MC_sim_main</code> and <code>MC_LW_sim_main</code> .

Approximate running times for the forward and retrieval programs for a 10km square UFF file are given below. These numbers correspond to a single processor 2.0 GHZ Intel Pentium 4 machine with 500 MB of memory.

Approximate running times for core Programs

<code>lid_filter</code>	\approx 15-20 mins for one shot every 100 meters.
<code>lidar</code>	\approx 1-2 mins for one shot every 100 meters.
<code>rad_filter</code>	\approx 2-3 mins.
<code>radar</code>	\approx 1-2 mins 1 lm horizontal resolution
<code>MC_sim_main</code>	\approx 1-2 hrs. per channel for a radiance error under 1%.
<code>MC_LW_sim_main</code>	\approx 0.5-1 hrs. per channel for a radiance error under 1%.
<code>lidar_ret1</code>	\approx 1-2 minutes, 1 km horizontal resolution.
<code>msi_ret</code>	\approx 0.25 minutes, 0.5 km horizontal resolution.
<code>lw_msi_lidar_radar</code>	\approx 5-10 minutes, 0.5 km horizontal resolution.

As can be seen, the Monte-Carlo short-wave calculations consume by far the most time.

3.2.1 Screen output

When many of the programs are run, by default, they will draw on a very basic ASCII windowing package in order to generate screen output. An example screen shot of `scene_creator` is shown in Figure. 30. This package is largely based on the use of control character sequences common to `vt200`, `xterm`, and `rxvt` terminals execution in other terminal environment may produced garbled screen output. In order to disable the use of ASCII windowed output set the environment variable `NOXTERMFWIN`. For example, under a csh environment

```
setenv NOXTERMFWIN
```

. With this environment variable set no control characters will be written to the standard output and only plain ASCII output will be generated.

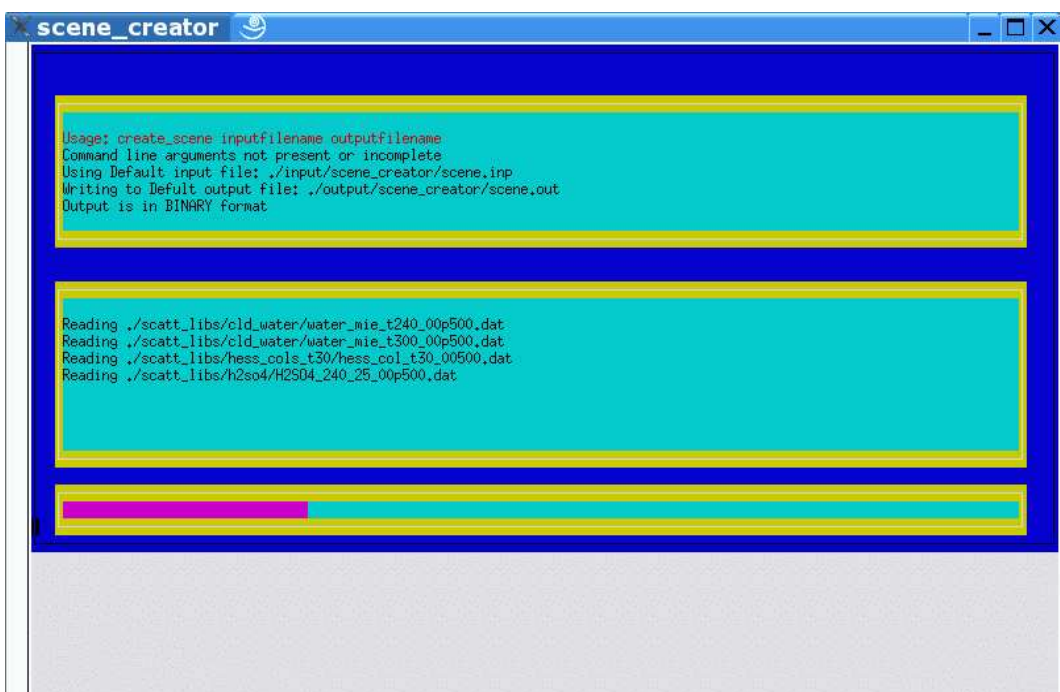


Figure 30: Screen shot of scene_creator running.

3.3 Master Input

The simulator package is more than a collection of separate programs and utilities, like the proposed mission itself, the programs and utilities are designed to work together. This philosophy is reflected in the main input strategy for the package. Apart from `scene_creator`, all the core programs read from a *master input file*. The default master input file is `input/master.inp`. The master input file, in effect, tells each of the core programs what file they will read and where they should write their output to. The example master input file contained with the distribution is listed below:

Example MASTERFILE Listing

```

1  #
2  =====
3  # Size dist scaling factor
4  # 1.0 ==> N is in 1/cm^3
5  =====
6  #
7  1.0
8  #
9  =====
10 # Override the Surface type
11 # and sub-type
12 # in the UFF file ?
13 # -1,-1 ==> use the surface
14 # info in rthe scene file
15 # For list of Valid surface
16 # types see the
17 # scene_creator input file
18 =====
19 #
20 -1,-1
21 #
22 =====
23 # Input directory to be substituted
24 # for '$inpath' in inputfiles.
25 # Enter 'null' if not used
26 =====
27 #
28 null
29 #
30 =====
31 # Output directory to be substituted
32 # for '$outpath' in outputfiles.
33 # Enter 'null' if not used
34 =====
35 #
36 null
37 #
38 =====
39 # UFF FILE DEFINING THE SCENE
40 =====
41 #
42 ./output/scene_creator/scene.out
43 #
44 =====
45 # Orbit file defining altitude and where
46 # we will fly over the scene
47 =====
48 #
49 ./input/orbit.inp
50 #
51 =====
52 # File containing Surface model info
53 =====
54 #

55 ./data/RPV_parameters.txt
56 #
57 =====
58 # LIDAR FILES
59 =====
60 #
61 # lid_filter input
62 ./input/lid_filter/lid_filter.inp
63 #
64 # lid_filter output
65 ./output/lid_filter/lid_filter.out
66 #
67 # lidar instrument module input
68 ./input/lidar/lidar.inp
69 #
70 # lidar instrument module output
71 ./output/lidar/lidar.out
72 #
73 =====
74 # RADAR FILES
75 =====
76 #
77 # rad_filter input
78 ./input/rad_filter/rad_filter.inp
79 #
80 # rad_filter output
81 ./output/rad_filter/rad_filter.out
82 #
83 # radar instrument module input
84 ./input/radar/radar.inp
85 #
86 # radar instrument module output
87 ./output/radar/radar.out
88 #
89 =====
90 # SW MC FILES
91 =====
92 #
93 # MC_Sim_main input file
94 ./input/sw_mc/sw_mc.inp
95 # MC_Sim_main output file
96 ./output/SW_MC/sw_mc.out
97 #
98 =====
99 # LW MC FILES
100 =====
101 #
102 # MC_LW_sim_main input file
103 ./input/lw_mc/lw_mc.inp
104 # MC_LW_sim_main output file
105 ./output/LW_MC/lw_mc.out
106 #
107 =====
108 # Lidar+Radar level 1

```

```

109 # product retrievals
110 =====
111 #
112 # lidar_ret1 input
113 ./input/lidar_ret1/lidar_ret1.inp
114 # lidar_ret1 output
115 ./output/lidar_ret1/lidar_ret1.out
116 #
117 =====
118 # lidar+radar+LW msi ret
119 =====
120 #
121 # lw_msi_lidar_radar input
122 ./input/lw_msi_lidar_radar/lw_msi_lidar_radar.inp
123 # lw_msi_lidar_radar output
124 ./output/lw_msi_lidar_radar/lw_msi_lidar_radar.out
125 #
126 =====
127 # MSI only ret
128 =====
129 #
130 # msi_ret input
131 ./input/msi_ret/msi_ret.inp
132 # msi_ret_output
133 ./output/msi_ret/msi_ret.out
134 #
135 #####
136 # END #
137 #####
138
139
140
141
142
143

```

The lines beginning with the ‘#’ symbols are comment lines. They are ignored by the programs which read this file. There are no limits to the number of comment lines that may occur in the inputfile. It is only the order of the arguments that is important.

The first two input files (here lines 7 and 20) provide a quick mechanism for overriding settings contained in the UFF file. For instance, entering 2.0 on line 7 will effectively double the particle number density of all the clouds and aerosol present in the UFF file without having to change the UFF file itself. In a similar fashion the entries on line 20 can be used to change the surface properties.

Referring to lines 22-37, a limited substitution facility has been included in the code that reads the masterfile (see the description of `read_file_list_file.mod`). If the string ‘\$inpath’ were to appear in any of the specified filenames then the string entered in the 3rd input filed (here on line 28) will be substituted at each occurrence. A similar procedure is applied to ‘\$outpath’. For example, in the previous listing, if line 28 was changed to:

`run01`

and line 62 would read

```
./$inpath/input/lid_filter/lidar.inp
then the lid_filter input file specified would effectively be

.\run01/input/lid_filter/lidar.inp
```

Obviously the input files and their paths specified in the MASTERFILE must exist before the simulator programs that use these input files can be ran. However, the output directory structures will be created if they do not already exist.

3.4 Orbit File

In addition to the MASTERFILE, another key file is the *orbit file*. The orbit file associated with a specific run is specified on the second non-comment line of the master file. In this example the orbit file is called `orbit.inp` and contains the following information

Example ORBITFILE Listing

```

1 | #-----#
2 | #-----#
3 | # 0==> fly along y axis
4 | # 1==> fly along x axis
5 | #-----#
6 | #
7 | 1
8 | #
9 | #-----#
10| # Constant x or y corresponding
11| # to orbit track (km)
12| #-----#
13| #
14| 5.0
15| #
16| #-----#
17| # Start of flight (km)
18| #-----#
19| #

20| 0.0
21| #
22| #-----#
23| # Finish (km)
24| #-----#
25| #
26| 10.00
27| #
28| #-----#
29| # Satellite altitude (km)
30| #-----#
31| #
32| 400.0
33| #
34| #-----#
35| # Orbit speed (km/sec)
36| #-----#
37| #
38| 7.0

```

As before the hash symbols denote comment lines.

Once the **MASTERFILE** (along with each of the input files referred to) and the **ORBIT** files have been created the simulator forward model and retrieval programs can be ran. All of the forward and retrieval programs expect as a single command line argument to be given the name of the **MASTERFILE** to use. If the command line argument is missing then the default file `./input/master.inp` is used.

3.5 Scattering Libraries

A number of scattering library files are included with the Simulator distribution. These files contain scattering phase function data, extinction, and absorption data covering wavelengths from 200 nm to 4000 microns as well as radar reflectivity at 95 GHz. The default scattering types included with the simulator are presented in Table 2. The VIS/UV/IR scattering information is stored at approximately 166 discrete wavelengths with a spacing of 0.05 microns between 0.2 and 7.0 microns, 0.5 microns between 7.0 microns and 25.0 microns, a spacing of 10.0 microns between 30.0 and 100.0, and a spacing of 100.0 microns out to 400 microns. The Radar information has been calculated only for a frequency of 94 GHz.

Name	r_{min} [microns]	r_{max}	No. of sizes
Cloud Water	1.0	50.0	50
Drizzle	10.0	500.0	10
H ₂ SO ₄ 25%	0.01	10.0	30
H ₂ SO ₄ 50%	0.01	10.0	30
H ₂ SO ₄ 75%	0.01	10.0	30
Soot	0.01	10.0	30
Sea Salt	0.01	10.0	30
Dust	0.01	10.0	30
Columns (perfect)	1.75	650.0	8
Columns (rough)	1.75	650.0	8
Plates (perfect)	15.0	650.0	6
Plates (rough)	15.0	650.0	6
Ice	0.5	50.0	50
Snow (large ice)	25.0	2500.0	50

Table 2: Default scattering types.

Size[microns]	Extinction-to-backscatter ratio
15	30.71344
30	40.51598
65.0	56.23513
150.0	68.74404
300.0	104.2081
600.0	138.7090
1300.0	167.1114

Table 3: Extinction-to-backscatter ratios at 353 nm for perfect Plates.

Mie calculations has been used to generate the UV-IR-Radar information for all the spherical scatterers. For ice crystals, 3D random orientation has be assumed and DDA calculations have been used to calculate radar reflectivity (Lemke and Quante (1999)) while Ray-tracing code (Hess et al. (1998)) have been used to calculate the UV-IR scattering properties. The Ray-tracing results will only be approximate (especially at the longer wavelengths) and should be replaced with more accurate calculations (i.e. FTDT calculations (Liou (2002))) at IR wavelengths.

The base sizes of the ice crystal models was taken from Hess and Wiegne (1994). The sizes as well as the lidar extinction-to-backscatter ratio at 353 nm for each crystal size and

Size[microns]	Extinction-to-backscatter ratio
15	75.47950
30	88.70643
65.0	210.8057
150.0	190.3914
300.0	184.0189
600.0	277.1708
1300.0	451.2094

Table 4: Extinction-to-backscatter ratios at 353 nm for rough Plates.

Size[microns]	Extinction-to-backscatter ratio
1.75	10.52451
5.0	10.62634
15	11.85058
30	10.44579
65.0	11.70344
150.0	16.17703
300.0	22.39486
650.0	30.94386

Table 5: Extinction-to-backscatter ratios at 353 nm for perfect columns.

Size[microns]	Extinction-to-backscatter ratio
1.75	49.61674
5.0	50.09644
15	47.51034
30	47.51780
65.0	66.88847
150.0	97.98457
300.0	81.62260
650.0	160.1475

Table 6: Extinction-to-backscatter ratios at 353 nm for rough columns.

type are listed in Tables 3-6. The extinction-to-backscatter ratio of real ice crystals size distributions appearer to be in the range of 25-25. Thus, it is recommend that clouds should be modeled using predominately columns since the extinction-to-backscatter ratio of the plate models appears to be higher than what is usually encountered in nature.

For each scattering-type a *scatterer master list file* is used to define the scattering scattering types properties and to point to the files where the actual scattering calculations (**the scattering library files**) are stored. An example scatterer master list file is presented in Appendix B.

The scattering files listed in the scatterer master list file contain information on the volume, area, extinction, absorption as well as the P11, P22, P33, P44, P12 and P34 scattering matrix elements at a high angular resolution. The exact format of the data is somewhat different for the different scattering types. For detailed information on the file format refer to the source code file `./src/read_scatt_info.f90`.

3.6 Scene Creation

3.6.1 scene_creator

USAGE: scene_creator INPUTFILE OUTPUTFILE

Description

Program for creating user definable scenes in the simulator format. Simple scenes can be directly defined. The program can also act as a processor for reading in more complex 3-D cloud and aerosol information in order to build a complex scene in the simulator format. See `/input/scene_creator/scene.inp` for an example input file.

If the command line arguments are missing then

INPUTFILE defaults to `./input/scene_creator/scene.inp` and
OUTPUTFILE defaults to `./output/scene_creator/scene.out`

Output

A single output file (OUTPUTFILE) is generated in either binary or ASCII format. It is recommended that Binary output be used. ASCII output is usually only desirable for debugging purposes.

The example `scene.inp` file included with the distribution is listed below.

./input/scene-creator/scene.inp Listing

```
1 #####  
2 # EXAMPLE SCENE_CREATOR INPUT FILE #  
3 #-----#  
4 # #  
5 # The '#' symbols denote comment lines. #  
6 # The '&' symbols are used to represent #  
7 # comment line continuation similar #  
8 # to f90 free format style #  
9 #####  
10 #  
11 #####  
12 # Names of scatter/absorber types #  
13 # and name of files which contain #  
14 # the list of files where the #  
15 # scattering parameters and #  
16 # (for ice) habit info are stored #  
17 #####  
18 #  
19 # Number of scatterer species  
20 # used in this scene.  
21 #-----  
22 3  
23 #  
24 # Scatterer name and corresponding name  
25 # of list file for each scatterer type  
26 #-----  
27 'water','./scatt_master_lists/water.list'  
28 'columns_2','./scatt_master_lists/Col_hess_scatt_tilt_30.list'  
29 'H2SO4_25','./scatt_master_lists/H2SO4_25.list'  
30 #  
31 # Number of extra trace gasses  
32 # (apart from O2,N2,CO2,H2O, and O3)  
33 #-----  
34 0  
35 #1  
36 #  
37 # Gass name, vol mixing ratio, mixing ratio profile file  
38 # if (vol mixing ratio) < 0  
39 #  
40 # For example, To specify a constant 1ppm CH4 profile  
41 #'CH4',1.0e-6,'NULL'  
42 #  
43 # OR  
44 #  
45 # Or to specify a altitude (z)  
46 # or (x,y,z) dependent CH4 profile  
47 #  
48 #'CH4',-9.0,'my_ch4_profile.dat'  
49 #  
50 #  
51 #####  
52 # Domain and resolution of Scene #  
53 #####  
54 #  
55 # x_extent,y_extent,z_extent in km  
56 #-----  
57 10.0,10.0,100.0  
58 #  
59 # horizontal resolution in km  
60 #-----  
61 0.5  
62 #  
63 #####  
64 # Number of vert. resolution #  
65 # domains #  
66 #####  
67 #  
68 4  
69 #  
70 # 0.1 km resolution from the ground to 5.0 km  
71 0.1,5.0  
72 # 0.25 km resolution from 5.0 to 15.0 km  
73 0.25,15.0  
74 # 5.0 km resolution from 15.0 to 30.0 km  
75 5.0,30.0  
76 # 10 km resolution from 30.0 km to 100.0 km  
77 10.0,100.0  
78 #  
79 #####  
80 # T,p,h2o,o3 profile data file #  
81 #####  
82 #  
83 #-----  
84 # 1-D files
```

```
58
85 #-----
86 #'./std_atmos/Arctic_summer.dat'
87 #'./std_atmos/Arctic_winter.dat'
88 './std_atmos/Mid-latitude_summer.dat'
89 #'./std_atmos/Mid-latitude_winter.dat'
90 #'./std_atmos/Subarctic_summer.dat'
91 #'./std_atmos/Subarctic_winter.dat'
92 #'./std_atmos/Tropical.dat'
93 #
94 # -----
95 # A 3-D example file
96 # Make sure domain spans
97 # the domain of the scene
98 # you want to create.
99 # (could run into interpolation
100 # problems otherwise)
101 #-----
102 #'./three_3d_mod_atmos_tst.dat'
103 #
104 #
105 # CO2 Volume mixing ratio
106 #-----
107 350.0e-6
108 #
109 # H2O scale factor
110 #-----
111 1.0
112 #
113 # O3 scale factor
114 #-----
115 1.0
116 #
117 # Wind velocity m/s (Vx,Vy,Vz)
118 #-----
119 1.0,0.0,0.0
120 #
121 ######
122 # Number of surface regions #
123 # (including default) #
124 ######
125 #
126 1
127 #
128 ######
129 # Default surface type and sub-type for #
130 # scene                         #
```

```
131 ######
132 #
133 00,00
134 #
135 ######
136 # If the number of surface regions #
137 # is greater than 1 then for each #
138 # surface region #
139 # the following must be specified: #
140 #
141 # surface_type, surface_subtype, xl,y2,y1,y2 #
142 #-----
143 #
144 # Current choices for surface types are: #
145 # (subtypes are not yet used) #
146 # see ./data/RPV_parameters.txt #
147 #
148 # 0-open water (ocean) #
149 # 1-bog summer #
150 # 2-coniferous forest #
151 # 3-corn (maize) #
152 # 4-grass lawn #
153 # 5-hardwood forest summer #
154 # 6-hardwood forest winter #
155 # 7-cultivated land #
156 # 8-avondale loam soil #
157 # 9-orchard grass #
158 # 10-pasture land #
159 # 11-pine forest #
160 # 12-plowed field #
161 # 13-savannah #
162 # 14-soya beans #
163 # 15-irrigated wheat #
164 # 16-aspen #
165 # 17-spruce #
166 # 18-jack pine #
167 ######
168 #
169 ######
170 # Number of scatterer #
171 # 'regions'          #
172 # (regions can be overlapped) #
173 ######
174 #
175 004
176 #005
```

```

177 #
178 ######
179 #
180 # FOR EACH REGION WE MUST SPECIFY : #
181 #
182 # scatter_type_number,scatterer_type_label,& #
183 # & global(0 or 1), & #
184 # & (x1,x2,y1,y2,z1,z2 all in km for region 1 # #
185 #
186 #-----#
187 # followed by ONE OF: #
188 #-----#
189 # 0 ==> We will specify a multi-modal generalized & #
190 # & Gamma type distributions & #
191 # & (Scale by mass [g/m^3]),Number_of_modes #
192 #
193 # OR #
194 #
195 # 1 ==> We will specify a multi-modal generalized & #
196 # & Gamma type distributions & #
197 # & (Scale by extinction [1/m]),Number_of_modes #
198 #
199 # OR #
200 #
201 # 10 ==> As option 0 but read size parameters from file #
202 #
203 # OR #
204 #
205 # 11 ==> As option 1 but read from file #
206 #
207 #-----#
208 # If option 0 or 1 then the format of folowing entry is: #
209 #-----#
210 # Number_of_relative_altitudes (0.0=z1,1.0=z2) #
211 # Alt1 (0.0=> bottom of region) #
212 # Mass_density(g/m3) OR Ext(1/m), & #
213 # & g1,reff(um),rmin1(um),rmax1(um) (Alt1,mode 1) #
214 # Mass_density or Ext ,g2,reff2,rmin2,rmax2 (Alt1,mode 2) #
215 # Etc... #
216 # Alt2 (1.0=> top of region) #
217 # Mass_Density or Ext ,g1,reff,rmin1,rmax1 (Alt2,mode 1) #
218 # Mass_Density or Ext ,g2,reff2,rmin2,rmax2 (Alt2,mode 2) #
219 # Etc.. #
220 # Etc.. #
221 #
222 # Note: AT LEAST 2 Relative ALtitudes (0.0 and 1.0) #

223 # must be specified ! #
224 #
225 #-----#
226 # If option 10 or 11 then format of next entry is: #
227 #-----#
228 #
229 #'size_distribution_file_name' #
230 # (see ./input/scene_creator/file_region_tst.dat #
231 # for an example.) #
232 #
233 ######
234 #
235 #
236 ######
237 # Information for Region 1 #
238 #####
239 #
240 # Region 1 contains a background sulfate aerosol layer (global=1)
241 # present from the ground up to 3 km
242 #
243 # scatter_type_number,scatterer_type_label,global(0 or 1),&
244 # & x1,x2,y1,y2,z1,z2 all in km for region 1
245 3,H2SO4_25,1,0.0,10.0,0.0,10.0,0.0,2.0
246 #
247 # Distribution described by gamma type distributions &
248 # & scale by extinction 1/m, one mode
249 1,1
250 #
251 # Parameters will be entered at 2 altitudes
252 2
253 # Bottom of layer
254 0.0
255 #
256 # extinction(1/m),g1,reff(um),rmin1,rmax1 : For Alt1,mode 1
257 5.0e-5,2,0.1,0.0,1.0
258 #
259 1.0
260 #
261 # extinction(1/m),g1,reff(um),rmin1,rmax1 : For Alt2,mode 1
262 5.0e-5,2,0.1,0.0,1.0
263 #
264 ######
265 # Parameters for Region 2 #
266 #####
267 #
268 # Region 2 contains a gamma-type single mode water present

```

```

269 # from x=4.0-10.0 km and y=0.0-10.0 km
270 # between 1.5 and 2.0 km with Reff=10.0 microns
271 #
272 1,water,0,4.0,10.0,0.0,10.0,1.5,2.0
273 # scale by Ext 1/m, 1 mode
274 1,1
275 2 , 2 altitudes
276 0.0 , Bottom of Region
277 0.01,3,10.0,0.0,20.0
278 1.0 , Top of Region
279 0.01,3,10.0,0.0,20.0
280 #
281 ######
282 # Parameters for Region 3 #
283 ######
284 #
285 # A bi-modal ice cloud between 8.0 and 10.0 km present
286 # from x=2.0-7.5 and y=2.0-7.0.
287 #
288 2,columns_2,0,2.0,7.5,2.0,7.0,8.0,10.0
289 # Scale by ext 1/m, 2 modes
290 1,2
291 2 , 2 altitudes
292 0.0 ,Bottom of Region
293 1.e-4,1,10.0,0.0,150.0
294 9.e-4,3,150.0,0.0,1000.0
295 1.0 , Top of Region
296 1.0e-4,1,10.0,0.0,150.0
297 9.0e-4,3,150.0,0.0,1000.0
298 #
299 ######
300 # Parameters for Region 4 #
301 ######
302 #

303 # B-modal ice cloud between 6 and 8 km present
304 # from x=6.0-7.5 and y=2.0-7.0 km.
305 #
306 2,columns_2,0,6.0,7.5,2.0,7.0,6.0,8.0
307 # Scale by ext 1/m, 2 modes
308 1,2
309 2 , 2 altitudes
310 0.0 , Bottom of Region
311 1.e-4,1,10.0,0.0,150.0
312 1.1e-3,3,200.0,0.0,2000.0
313 1.0 , Top of Region
314 1.0e-4,1,10.0,0.0,150.0
315 1.1e-3,3,200.0,0.0,2000.0
316 #
317 ######
318 # Parameters for region 5 (parameters read from file) #
319 ######
320 #
321 #2,columns_2,0,0.0,6.0,0.0,6.0,4.0,8.0
322 #Scale by extinction [1/m]+read from file, 1 mode,
323 #11,1
324 #'./input/scene_creator/file_region_tst.dat'
325 #
326 ######
327 # ASCII (1) or BINARY (0) OUTPUT #
328 # Binary is recommended for general #
329 # usage #
330 #####
331 0
332 #####
333 # END OF INPUT #
334 #####
335 END

```

A three-dimensional view of the scene created by the previous inputfile is shown in Figure 3.6.1 along with the sections of the input file which define the various scattering regions. The figure was produced using `extract_quantity_3d` and `plot_3d` which are described in 3.8 and 3.11.4.

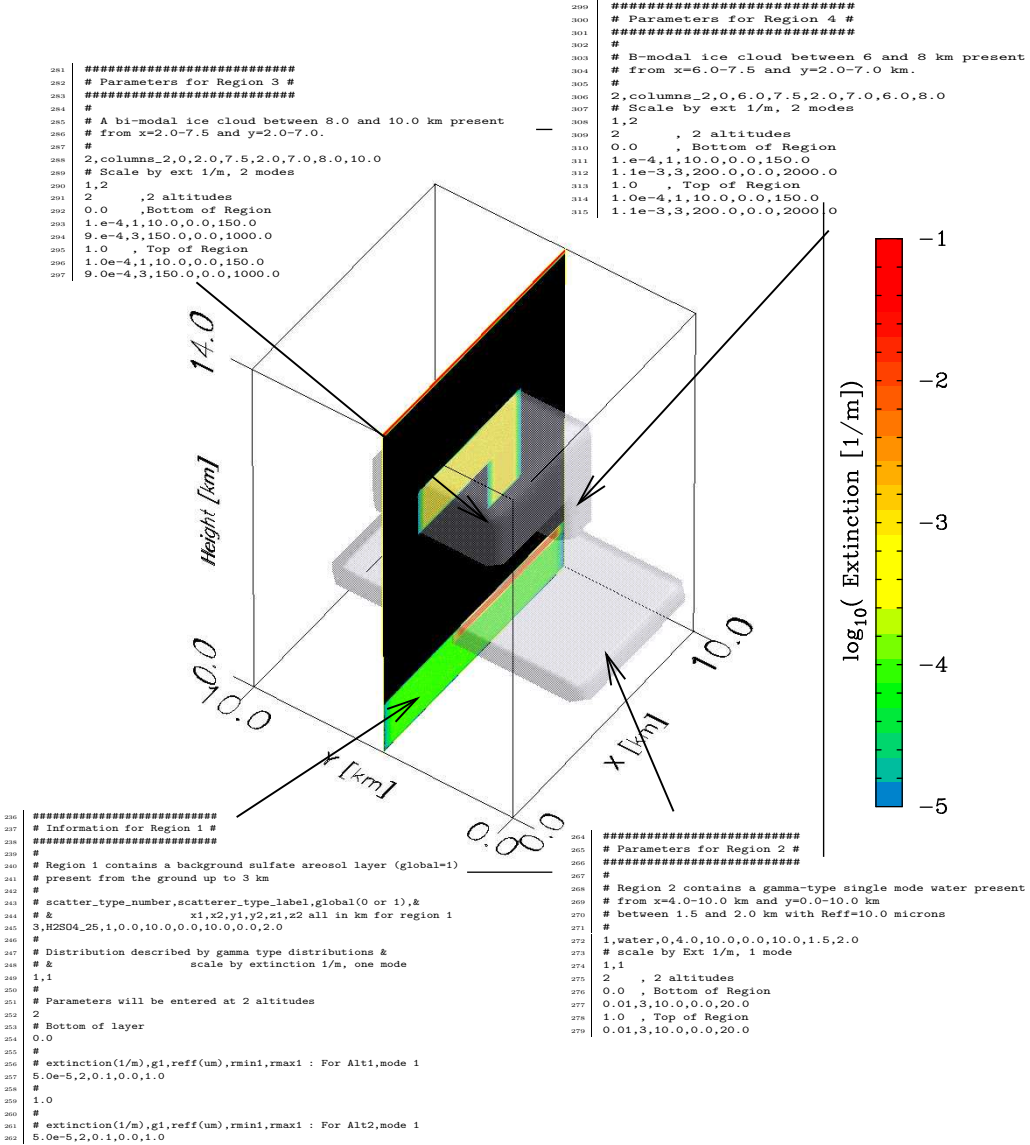


Figure 31: A three-dimensional view in terms of optical extinction of the scene created by `scene_creator` using the input file: `./input/scene_creator/scene.inp`

The comments embedded in the file provide a useful degree of explanation. However, some additional comments are in order:

- The number of scattering species is limited only by the available memory and the available scattering library information
- The names of the scattering species is arbitrary and is only used internally by the `scene_creator`. The *scattering master list file* must correspond to an existing file (see `./scatt_master_lists.`)

- The scale factors for H_2O and CO_2 simply scale the input profile contained in the specified atmosphere file.
- Both binary and ASCII output is possible. The ASCII files are useful for debugging however binary files are preferred for general use as they can be read and written much faster.
- Global scattering regions are intended to provide a mechanism for specifying background fields (i.e. aerosols) which may be considered horizontally homogeneous across the domain of the scene. To save disk space and memory they are stored and treated differently than the non-global regions.
- Cloud and Aerosol information can be directly specified within the input file or it can be read from other files. Specifying the scattering information within the input file is only useful for simple (block) clouds.
- The only currently active option for specifying the size distribution parameters for the clouds and aerosols is based on the generalized gamma distribution formalism (Hu and Stamnes (1993)).

A generalized gamma distribution has the form:

$$n(r) = \frac{N_o}{R_m} \frac{1}{\Gamma(\gamma)} \left(\frac{r}{R_m} \right)^{\gamma-1} \exp(-r/R_m), \quad (71)$$

where R_m is the mode radius, N_o is the total number of particles in the distribution, and γ is the width parameter. For the generalized gamma distribution the relationship between the effective radius R_{eff} and R_m is given by

$$R_{eff} = R_m(\gamma + 2). \quad (72)$$

3.6.2 Input Background atmospheric data

A number of 1-D model atmospheric data file have been included to form the basis of simple scenes. These files are located in `./std_atmos`. An example model atmospheric 1-D data file is presented in Appendix C.

An option exists to specify the input atmospheric conditions in terms of x,y, and z coordinates. If the specified input file (see lines 56–79) is of the correct 3-D format, `scene_creator` will use 3-D interpolation to find the temperature, Pressure, water Vapor mixing ratio etc.. To avoid interpolation artifacts, the domain of the input 3-D field should exceed that of the scene being created. An example 3-D file is listed in Appendix D.

3.6.3 Additional trace gas information

Information about gasses other than (O_2 , N_2 , CO_2 , H_2O and O_3) can also be specified (see lines 34–48). If an input file is specified it may be of either 1-D or 3-D format. The file formats are similar to the formats, respectively, described in Appendix C and Appendix D except that the data columns will correspond to

z (km)	p (mb)	t (K)	x_vol
--------	--------	-------	-------

where `x_vol` is the volume mixing ratio of the gas in question. Each separate file corresponds to a single particular extra gas.

3.6.4 Using files to specify the size distributions

In order to more easily accommodate cloud/aerosol information from other sources, a simple mechanism for specifying cloud information using ASCII files exists (see lines 229-236). An example input file is listed in Appendix D. `scene_creator` will use 3-D interpolation in order to find the size distributions at the scene coordinates.

3.6.5 Scene (UFF) file format

The `scene_creator` program writes its output in the UFF format. Both binary and ASCII format files can be written. The use of Binary files is recommended. An example UFF file is shown in E.

3.7 UFF File Manipulation

3.7.1 uff_averager

```
USAGE: uff_averager INPUT_DATA_FILE OUTPUT_DATA_FILE hor_res[km]
v_res[km]ascii_or_bi(0,1) max_number_of_hor_points
```

Description

This program reads an UFF file and using simple averaging it outputs a UFF file of lesser resolution. Size distributions are averaged on a bin-by-bin basis over the desired domain. The following arguments are expected

input_data_file	Orginal UFF file.
output_data_file	Output file.
hor_res	Desired output horizontal resolution in km.
v_res	Desired output vertical resolution in km.
ascii_or_bi	ASCII or Binary output 0→ Binary output (Recommended) 1→ ASCII output
max_number_of_hor_points	Maximum number of horizontal data points to read from the input UFF file. This can be useful when the desired horizontal output resolution does not mesh with the orginal input resolution.

Output

A single file OUTPUT_DATA_FILE is generated.

3.7.2 uff_merger

```
USAGE: uff_merger MASTER SLAVE z1 z2 buff1 buff2 OUTFILE ascii_or_bi
```

Description

This program merges two UFF files in the vertical coordinate. This program reads a master UFF file and a slave UFF file. The information in the slave UFF file is then put on the same vertical grid as the master. The master and slave files must have the same X and Y dimensions.

Between **z1** and **z2** the cloud/aerosol, temperature and gas volume mixing ratios of the slave file are used. Between **z1** and **z1+buff1** and **z2** and **z2+buff2** the temperature profile is obtained by linearly interpolating between **T_master(z1+buf)** and **T_slave(z1)** and **T_slave(z2)** and **T_slave(z2+buf2)** respectively. A similar procedure is used for the gas volume mixing ratios. The pressure profile is then constructed from the surface pressure and the resulting temperature and water vapor profile assuming hydrostatic equilibrium conditions.

The following arguments are expected:

MASTER	Master UFF file.
SLAVE	Slave UFF file.
z1	Starting altitude to use slave info.
z2	Ending altitude to use slave info.
buff1	Buffer distance over which t,p,rho etc fields are merged (z1+buff1 to z1).
buff2	Buffer distance over which t,p,rho etc fields are merged (z2 to z2+buff2).
OUTFILE	name of output UFF file.
ascii_or.bi	ASCII or Binary output 0 → Binary output (Recommended) 1 → ASCII output

Output

A single file OUTFILE is generated.

3.8 Data extraction programs

3.8.1 extract_quantity

```
USAGE: extract_quantity INPUTFILENAME OUTPUTFILENAME  
slice_x_or_y(0 or 1)constant_coord(km) start(km) finish(km) z1(km) z2(km)  
vert_res(km) qindex qindex2
```

Description

Extract quantity is used to extract information from a UFF file along a constant-x or constant-y track. The program will read the UFF file as well as any relevant information from the scattering libraries in order to build-up the requested data.

The following command line arguments are expected:

INPUTFILENAME	UFF file to read from.
OUTPUTFILENAME	ASCII file to write data to.
slice_x_or_y	0→ Fly along X=constant, 1→ Fly along Y=constant.
constant_coord	Value of constant in km (see above).
start	Starting X or Y position in km.
finish	Final X or Y position in km.
z1	Lower altitude bound in km.
z2	Upper altitude bound in km.
vert_res	Vertical output resolution in km.
qindex	Index of quantity to extract (see table below).
qindex2	Index of scattering type (0→ use all scattering types).

Current Choices For qindex are:

1	Temperature [K].
2	Pressure [mb].
3	Density [molecules/cm ³].
4	Xvol H ₂ O.
5	Xvol O ₃ .
10	mass [g/m ³].
11	R _{eff} [um].
12	Mean maximum dimension [um].
13	Extinction at 353 nm [1/m].
14	Extinction/Backscatter Ratio at 353 nm [1/sr].
15	Backscatter at 353 nm [1/m/sr].
16	R'eff [microns].
17	No [#/cm ³].
100	Idealized Radar reflectivity [mm ⁶ /m ³].
101	Attenuation at 94 GHz [1/m].

If the incorrect number of commandline arguments are given then an error message is printed along with a help message.

Output

OUTFILENAME will contain the output information which may then be plotted using plot_slice.

3.8.2 extract_quantity_hor

```
USAGE: extract_quantity_hor INPUTFILENAME OUTPUTFILENAME  
qindex qindex2.
```

Description

This program reads an entire UFF file and extracts various column integrated quantities and outputs them to the specified output file

The following command line arguments are expected:

INPUTFILENAME	UFF file file to read from.
OUTPUTFILENAME	ASCI file to write data to.
qindex	Index of quantity to extract (see table below).
qindex2	Index of scattering type (0→ use all scattering types).

Current Choices For qindex are:

10	Mass path [g/m ²].
11	Average Reff [microns].
13	Optical Depth at 353 nm.
100	Integrated Idealized Radar reflectivity [mm ⁶ /m ³]*m.

If the incorrect number of commandline arguments are given then an error message is printed along with a help message.

Output

OUTFILENAME will contain the output information which may then be plotted using plot_hor.

3.8.3 extract_quantity_3d

```
USAGE: extract_quantity INPUTFILENAME OUTPUTFILENAME
x_start(km) x_finish(km) y_start(km) y_finish(km) z1(km) z2(km) vert_res(km)
qindex qindex2.
```

Description

This program reads a 3-D domain from a UFF file and extracts various averaged quantities and outputs them to the specified output file.

The following command line arguments are expected:

INPUTFILENAME	UFF file file to read from.
OUTPUTFILENAME	ASCII file to write data to.
x_start	Starting X position in km.
x_finish	Final X position in km.
y_start	Starting Y position in km.
y_finish	Final Y position in km.
z1	Lower altitude bound in km.
z2	Upper altitude bound in km.
vert_res	Vertical output resolution in km.
qindex	Index of quantity to extract (see table below).
qindex2	Index of scattering type (0→ use all scattering types).

Current Choices For qindex are:

1	Temperature [K].
2	Pressure [mb].
3	Density [molecules/cm ³].
4	Xvol H ₂ O.
5	Xvol O ₃ .
10	mass [g/m ³].
11	R _{eff} [um].
12	Mean maximum dimension [um].
13	Extinction at 353 nm [1/m].
14	Extinction/Backscatter Ratio at 353 nm [1/sr].
15	Backscatter at 353 nm [1/m/sr].
16	R'eff [microns].
17	No [#/cm ³].
100	Idealized Radar reflectivity [mm ⁶ /m ³].

If the incorrect number of commandline arguments are given then an error message is printed along with a help message.

Output

OUTFILENAME will contain the output information which may then be plotted using plot_3d.

3.8.4 extract_env_profile

USAGE: extract_env_profile INPUTFILENAME OUTPUTFILENAME x_start(km) x_finish(km) y_start(km) y_finish(km) z1(km) z2(km) vert_res(km)
--

Description

This program reads a UFF file and outputs the average P,T,wv and X_mass_O3 profile. The resulting file can be used in place of a standard atmosphere profile in `scene_creator`. This is particularly useful for helping to build ‘reconstructed’ scenes based on the output of `lw_msilidar_radar`.

The following command line arguments are expected:

INPUTFILENAME	UFF file file to read from.
OUTPUTFILENAME	ASCI file to write data to.
x_start	Starting X position in km.
x_finish	Final X position in km.
y_start	Starting Y position in km.
y_finish	Final Y position in km.
z1	Lower altitude bound in km.
z2	Upper altitude bound in km.
vert_res	Vertical output resolution in km.

If the incorrect number of commandline arguments are given then an error message is printed along with a help message.

Output

OUTFILENAME

The format of the output file follows that of the standard atmosphere files. See Appendix C and the files in `./std_atmos/`.

3.9 Forward Model Programs

3.9.1 rad_filter

USAGE: `rad_filter MASTERFILE`

Description

The program reads a UFF file and calculates the idealized radar reflectivity Doppler velocity as well as gaseous and hydrometer attenuation. The output of `rad_filter` is then meant to be read by the `radar` program.

The input and output files are taken from the appropriate entry in the `MASTERFILE`. If `MASTERFILE` is not present the default masterfile `./input/master.inp` is used. See `./input/rad_filter/rad_filter.inp` for an example input file.

Output

A single output file as specified in the `MASTERFILE` is generated.

General `rad.filter` input file

```
1 #####  
2 # Default radar filter input file  
3 # General configuration  
4 #####  
5 #  
6 # Extract info for all scene (limits are very very big) + a buffer  
7 #  
8 # Constant x(y) [0 or 1] slice  
9 1  
10 #  
11 # y= ?  
12 5.0  
13 #  
14 # start=?  
15 0.0  
16 # finish=?  
17 1.0e+6  
18 #  
19 # Width of slice  
20 1.0e+6  
21 #  
22 # Starting altitude (km)  
23 #  
24 0.0  
25 #  
26 # Ending altitude (km)  
27 #  
28 14.0  
29 #  
30 # Desired resolution of output (km)  
31 # (if < zero the use z1,z2,dz values  
32 # in UFF file)  
33 #-99  
34 0.1
```

3.9.2 radar

USAGE: radar MASTERFILE

Description

This program reads a file generated by **rad_filter** and processes the reflectivities according to various instrument parameters in order to calculate the measured reflectivities.

Note: The output reflectivities are corrected for atmospheric attenuation but not hydrometer attenuation ! The correction for hydrometer attenuation is (in effect) carried out in the inversion program **lw_msi_lidar_radar**.

The input and output files are taken from the appropriate entry in the MASTERFILE. If MASTERFILE is not present the default masterfile `./input/master.inp` is used. See `./input/radar/radar.inp` for an example input file.

NOTE: Doppler velocities are not processed by this current version even though they are available from the output of **rad_filter**.

Output

A single output file as specified in the MASTERFILE is generated.

Example radar input file

```
#####
# Default RADAR filter input file
#####
#
#
# location of radar albedo for different surfaces file
./input/radar/radar.surf
#
# Pulselength of CPR [m]
1000.0
# Oversampling number
5
# Horizontal sampling length of CPR [m]
1000.0
# Pulse Repetition Frequency [Hz]
6800.0
# Emitted power [kW]
1.5
# Operating frequency [GHz]
94.0
# Antenna diameter [m]
2.25
# Transmitter attenuation [dB]
2.0
# Receiver attenuation [dB]
2.0
# Attenuation filter [dB]
2.3
# Noise function [dB]
3.0
# Hamming window coefficient
0.54
# At present, the refractive index of water is hard-coded, KW2=0.92
#
# Detection threshold at 0 dB signal-to-noise
# Normally, this is calculated from the above parameters.
# Should you want to specify it yourself, please use a value =< 0.0
# Za0dB_dB [dB]
-21.3
#1.0
# Specify whether noise should be taken into account
# 0: no noise; 1: speckle and thermal noise
1
```

```
44  #
45  # Seed for random number generator (-1 to use system date and time)
46  #
47  -1
```

3.9.3 lid_filter

USAGE: lid_filter MASTERFILE

Description

This program reads a UFF file and calculates the lidar return binned as a function of time after the pulse has been launched. The calculation is done using a semi-analytical Monte-Carlo technique which tracks the polarization state and the spectral width of the photon packets.

The Monte-Carlo calculation launches a fixed number of packets for each range gate. Multiple rounds are used so that the MC error may be estimated. The calculation proceeds until a fixed number of rounds is reached or, for each altitude and scattering order, the MC error is below the expected random Poisson error for a perfect lidar receiver.

The output of lid_filter is meant to be read by the program lidar. The output of lid_filter is specific to the laser and telescope FOV. If results at a different laser and/or telescope FOV are desired then this program must be run again.

The input and output files for lid_filter are taken from the appropriate entry in the MASTERFILE. If MASTERFILE is not present the default masterfile **./input/master.inp** is used. See **./input/lid_filter/lid_filter.inp** for an example input file.

Output

A single output file as specified in the MASTERFILE is generated.

Example lid.filter input file

```
1 #####  
2 # Default Lidar filter input file  
3 # Ecare configuration  
4 #####  
5 #  
6 #  
7 # max radius from beam center to consider (km)  
8 0.25  
9 #  
10 # Laser PRF in Hz  
11 70.0  
12 #  
13 0.353  
14 #  
15 # Lidar wavelength (microns)  
16 #  
17 0.0  
18 #  
19 # Starting altitude (km)  
20 0.0  
21 #  
22 14.0  
23 #  
24 # Ending altitude (km)  
25 #  
26 14.0  
27 #  
28 # Desired resolution of output (km)  
29 # (if < zero the use z1,z2,dz values  
30 # in UFF file) Only works for uniform vert. resolution  
31 # UFF files though  
32 #-99  
33 0.1  
34 #  
35 # telescope fov full-angle mrads  
36 #  
37 0.0735
```

```
38 #  
39 # Laser fov full-angle mrads  
40 #  
41 0.05  
42 #  
43 # Laser Effective receiver ares (m^2)  
44 #  
45 1.0  
46 #  
47 # Laser pulse energy (Joules)  
48 #  
49 0.035  
50 #  
51 # Laser Line-width in MHz  
52 #  
53 30.0  
54 #  
55 #  
56 # Laser polarization state (Stokes vector...must be real)  
57 #  
58 1.0  
59 0.0  
60 0.0  
61 1.0  
62 #  
63 # Seed for random number generator  
64 #  
65 -1
```

3.9.4 lidar

USAGE: lidar MASTERFILE

Description

This program reads the output of lid_filter and processes the data according to the characteristics of the physical lidar system. Spectral and polarization filtering is preformed according to the defined receiver chain elements and instrument and shot noise is added according to the signal levels and detector characteristics.

The input and output files for lidar are taken from the appropriate entry in the MASTERFILE. If MASTERFILE is not present the default masterfile ./input/master.inp is used. See ./input/lidar/lidar.inp for an example input file.

Output

Depending on the defined receiver configuration a number of output files can be generated. A brief description of the files than may be generated follows:

Note: OUTFILE represents the name of the output file specified in the appropriate MASTERFILE, LAM represents the lidar wavelength, and CHAN represents the channel number.

OUTFILE_LAM_CHAN.dat	Background+darkcount subtracted output from physical channel CHAN.
OUTFILE_LAM_noise_CHAN.dat	Variance used to calculate the noise in channel CHAN.
OUTFILE_LAM_mie_interchannel.dat	Cross-talk(leakage) factors for the Mie signal for all channels.
OUTFILE_LAM_para_mie_CHAN.dat	Output of the virtual co-polar Mie channel.
OUTFILE_LAM_perp_mie_CHAN.dat	Output of the virtual cross-polar Mie channel.
OUTFILE_LAM_para_Ray_CHAN.dat	Output of the virtual co-polar Rayleigh channel.
OUTFILE_LAM_perp_Ray_CHAN.dat	Output of the virtual cross-polar Rayleigh channel.
OUTFILE_LAM_tot_para_CHAN.dat	Output of the virtual total co-polar channel.
OUTFILE_LAM_tot_perp_CHAN.dat	Output of the virtual total cross-polar channel.
OUTFILE_LAM_para_mie_error_CHAN.dat	Variance used to calculate the noise in the virtual co-polar Mie channel.
OUTFILE_LAM_perp_mie_error_CHAN.dat virtual cross-polar Mie channel.
OUTFILE_LAM_para_Ray_error_CHAN.dat virtual co-polar Rayleigh channel.
OUTFILE_LAM_perp_Ray_error_CHAN.dat virtual cross-polar Rayleigh channel.
OUTFILE_LAM_tot_para_error_CHAN.dat virtual total co-polar channel.
OUTFILE_LAM_tot_perp_error_CHAN.dat virtual total cross-polar channel.
OUTFILE_LAM_Ray_X_talk_CHAN.dat	Cross-talk(leakage) factors for the Rayleigh signal.
OUTFILE_LAM_Temperature_CHAN.dat	Atmospheric Temperature profile at the lidar output resolution (same for all channels).
OUTFILE_LAM_Ray_ext_CHAN.dat	Rayleigh extinction profiles at the lidar output resolution (same for all channels of the same wavelength).

Example lidar input file

```
1 #=====
2 # single scattering results (1)
3 # MS results (0)
4 #=====
5 #
6 0
7 #
8 #=====
9 # Add instrument noise and stat noise
10 # l==> yes
11 #=====
12 #
13 1
14 #
15 #=====
16 # horizontal and vertical resolution
17 # of output (km) < 0 ==> use that
18 # specified in lid_filter output
19 #=====
20 #
21 #1.5,0.1
22 -1.5,-0.1
23 #
24 #=====
25 # Background light W/M2/um (assume unpolarized)
26 # negative ==> read from file generated by
27 # SW_MC
28 #=====
29 #
30 0.0
31 #
32 #200.0
33 #
34 #=====
35 # File from SW_MC containing radiances to
36 # use as lidar background
37 #=====
38 #
39 null
40 #
41 #=====
42 # Name of Configuration
43 #=====
44 #
45 ASTRIM
46 #
47 #=====
48 # Number of Detection
49 # Channels
50 #=====
51 #
52 3
53 #
54 #=====
55 # Channel type identification arrays
56 # (2==> main, 1==> contributes via X-talk), 0==> not involved
57 # (No polarization X-talk as yet !!!!)
58 #=====
59 #
60 # TOTAL
61 #
62 0,0,0
63 #
64 # TOTAL_PARA
65 #
66 0,0,0
67 #
68 # TOTAL_PERP
69 #
```

```

70  0,0,2
71  #
72  # TOTAL_RAY
73  #
74  0,0,0
75  #
76  # TOTAL_MIE
77  #
78  0,0,0
79  #
80  # MIE_PARA
81  #
82  2,1,0
83  #
84  # MIE_PERP
85  #
86  0,0,0
87  #
88  # RAY_PARA
89  #
90  1,2,0
91  #
92  # RAY_PERP
93  #
94  0,0,0
95  #
96  #
97  =====
98  # Info for channel #1
99  =====
100 #
101 # Name of this channel
102 Mie Co-Polar
103 #
104 # Type of detector (PMT or ACD), if ACD add number of shots between readouts
105 #
106 PMT
107 1
108 #
109 #ACD
110 #4
111 #
112 # Quantum Efficiency of Detector
113 0.2
114 #0.75
115 #
116 # Photon Equivalent dark noise current for this channel (Hz) if PMT: Readout noise of ACD
117 #0.0
118 0.0
119 #
120 # Number of optical Elements in this channel
121 #
122 4
123 #
124 P45QW
125 1.0
126 #
127 HLP
128 1.0
129 #
130 SF
131 T,1.0,0.8,1.0e-6
132 #
133 FP
134 #
135 # FP reflectivity, FP absorption,FSR (cm-1), Flatness parameter, FP aperture diameter (m)
136 T,0.978,0.0,0.5,300.0,0.05
137 # Differences between true and assumed values
138 # % shift,dR,dA,dFSR,dflat_fp
139 0.0,0.0,0.0,0.0,0.0
140 #

```

```

141 #=====
142 # Info for channel #2
143 #=====
144 #
145 # Name of this channel
146 Rayleigh Co-Polar
147 #
148 # # Type of detector (PMT or ACD), if ACD add number of shots between readouts
149 #
150 PMT
151 1
152 #ACD
153 #4
154 #
155 # Quantum Efficiency of Detector
156 0.2
157 #0.75
158 #
159 # Photon Equivalent dark noise current for this channel (Hz)
160 #0.0
161 0.0
162 #
163 # Number of optical Elements in this channel
164 #
165 4
166 #
167 P45QW
168 1.0
169 #
170 HLP
171 1.0
172 #
173 SF
174 T,1.0,0.8,1.0e-6
175 #
176 FP
177 # FP reflectivity, FP absorption,FSR (cm-1), Flatness parameter, FP aperture diameter (m)
178 R,0.978,0.0,0.5,300.0,0.05
179 # Differences between true and assumed values
180 # % shift,dR,dA,dFSR,dflat_fp
181 0.0,0.0,0.0,0.0
182 #
183 #
184 #=====
185 # Info for channel #3
186 #=====
187 #
188 # Name of this channel
189 Mie cross-polar
190 #
191 # Type of detector (PMT or ACD), if ACD add number of shots between readouts
192 #
193 PMT
194 1
195 #
196 #ACD
197 #4
198 #
199 # Quantum Efficiency of Detector
200 0.2
201 #
202 # Photon Equivalent dark noise current for this channel (Hz)
203 #0.0
204 0.0
205 #
206 # Number of optical Elements in this channel
207 #
208 3
209 #
210 P45QW
211 0.2

```

```
212 #  
213 VLP  
214 1.0  
215 #  
216 SF  
217 T,1.0,0.8,1.0e-6  
218 #  
219 #####  
220 # Seed for random number generator  
221 #####  
222 #  
223 -1  
224 #  
225 #####  
226 # End of input  
227 #####  
228 #
```

3.9.5 MC_sim_main

USAGE: MC_sim_main MASTERFILE

Description

This program calculates TOA radiances and net fluxes for both wide and narrow bands for the scene file specified in the MASTERFILE. The solar angle, wavelength bands, and viewing angles are specified in the MC_SW inputfile.

The input and output files for MC_sim_main are taken from the appropriate entry in the MASTERFILE. If MASTERFILE is not present the default masterfile `./input/master.inp` is used. See `./input/sw_mc/sw_mc.inp` for an example input file.

Output

For each channel, band, and viewing angle several output files are written: Note: that in the following, OUTFILE represents the name of the output file specified in the appropriate MASTERFILE, BND is the band number, THETA and PHI are the viewing angles, and THETA0 and PHI0 are the solar angles

OUTFILE_THETA0_PHI0_brdf_bnd_BND_Ang_THETA_PHI.dat	BRDF.
OUTFILE_THETA0_PHI0_brdf_error_bnd_BND_Ang_THETA_PHI.dat	Error estimate in the BRDF.
OUTFILE_THETA0_PHI0_dimensions.dat	Dimensions of the output.
OUTFILE_THETA0_PHI0_srf_absorptance_bnd_BND.dat	Surface absorptance.
OUTFILE_THETA0_PHI0_srf_absorptance_error_bnd_BND.dat	Error estimate in the surface absorptance.
OUTFILE_THETA0_PHI0_summary_bnd_BND.dat	Domain average TOA albedo and srf absorptance.
OUTFILE_THETA0_PHI0_toa_albedo_bnd_BND.dat	TOA albedo.
OUTFILE_THETA0_PHI0_albedo_error_bnd_BND.dat	Error estimate in TOA albedo.
OUTFILE_THETA0_PHI0_flux_div_bnd_BND.dat	Atmospheric flux divergence.
OUTFILE_THETA0_PHI0_error_flux_div_bnd_BND.dat	Error estimate in atmospheric flux divergence.

Note on the viewing angle conventions:

`ANGLES(1,:)` = ZENITH (THETA).

`ANGLES(2,:)` = AZIMUTH (PHI).

ZENITH = 180 → nadir viewing.

ZENITH = 90 → limb viewing.

AZIMUTH = 0 → viewing in opposition to Sun.

AZIMUTH = 180 → viewing in (inferior) conjunction to Sun.

Note on the Solar angle convention:

THETA0 = solar zenith angle (degrees off nadir)

PHI0 = solar azimuth angle

Notes

A forward Monte-Carlo method is used to perform the calculations. At each scattering event, the expected contribution to the TOA radiance is calculated. For each grid cell a number of photon packets are launched from the TOA according to the solar elevation and azimuth.

This process is repeated a minimum of two rounds. Up to a specified maximum number of rounds, the calculation proceeds until the standard deviation of the calculated radiances or the TOA fluxes for each output pixel is below a specified threshold.

Statistically infrequent, but large contributions to the TOA signal can be generated by photon packets that have ‘turned-around’ and are then scattered while traveling upward to the top of the atmosphere. In order to improve the convergence statistics, contributions that exceed a certain threshold are sent to an excess bin. The contents of this excess bin may be discarded (not recommended) or distributed across the scene in proportion to the calculated radiances excluding the excess.

Atmospheric absorption: C-K tables

Atmospheric transmission is calculated using a correlated-k method and for each narrow-band the scattering properties are assumed to be constant across the range of the narrow band limits. The approach and the bands follow those used by (Kato et al. (1999)). The various narrow bands can be grouped together to define bands for i.e. broad-band calculations. See `./data/band_info_BB.dat` for an example of how the bands can be defined.

Channel	v_1 cm $^{-1}$	v_2 cm $^{-1}$	Gasses
MSI_1 660 nm	14948.	15408.	H ₂ O, O ₃
MSI_2 865 nm	11429.	11696.	H ₂ O
MSI_3 1.61 um	6098.	6329.	CO ₂
MSI_4 2.2 um	4444.	4651.	H ₂ O, CH4

Table 7: Short-wave multispectral imager (MSI) bands.

Broad-Band Short Wave 0.2-4.0 μ m							
Center λ	Gasses	Center λ	Gasses	Center λ	Gasses	Center λ	Gasses
0.254998	O ₃	0.277389	O ₃	0.294507	O ₃	0.317148	O ₃
0.344614	O ₃	0.384187	O ₃	0.428872	O ₃	0.482614	O ₃
0.528597	O ₃	0.544707	H ₂ O	0.557927	O ₃	0.585172	H ₂ O O ₃
0.614836	O ₃	0.645182	H ₂ O O ₃	0.675333	O ₃	0.694179	H ₂ O O ₃ O ₂
0.723040,	H ₂ O	0.766254	O ₂	0.817094	H ₂ O	0.866138	H ₂ O
0.929973	H ₂ O	1.00908	H ₂ O	1.11501	H ₂ O	1.33592	H ₂ O
1.56311	H ₂ O CO ₂	1.77179	H ₂ O	2.05465	H ₂ O CO ₂	2.21263	H ₂ O
2.58866	H ₂ O CO ₂	3.28839	H ₂ O O ₃	3.80445	H ₂ O CO ₂	4.27991	H ₂ O CO ₂

Table 8: Center wavelengths used for broad-band short-wave calculations and relevant gasses.

Surface properties

Surface BRDFs are handled by the Pinty RPV formalism (Pinty et al., (2002)) from land surfaces while a full Cox and Munk treatment (Cox and Munck (1954)) is used for ocean surfaces. The Pinty RPV parameters are only available for two SW wavelength bands (below and above 0.700 microns respectively) but do capture detailed angular dependencies. See `./data/RPV_parameters.txt`.

Example MC_sim_main input file

```

1 ######
2 # Prototype MC input file

```

```

3 ######
4 #
5 #
6 # RPV parameters for surface BRDF's
7 #
8 ./data/RPV_parameters.txt
9 #
10 # Domain to use (x1,x2,y1,y2) km
11 #
12 0.0,10.0,0.0,10.0
13 #
14 # Resolution of output (km) (negative entry ==> use UFF resolution)
15 #
16 0.5
17 #
18 # Number of photons per columns (relative to output resolution)
19 #
20 500           Thus for each round  $(\frac{10}{0.5})^2 \times 500$  photon packets will be used
21 #100000
22 #
23 # Maximum Number of Rounds
24 4
25 #
26 # Stop when all radiances (normalized by incident solar radiance) above a certain
27 # threshold have a relative error less than some amount
28 #
29 #0.00,0.005
30 0.00,0.001      Simulation will stop when BRDF values above 0.0
31 #               have converged to within 0.1 %
32 # Convergence criteria for fluxes
33 #
34 0.00,1.00       Operates as above. For this particular run we do not
35 #               care about the fluxes so here a convergence value of 1.0
36 #               has been specified.
37 #
38 # number of Mie scatterers before switching to HG phase functions
39 3
40 #
41 # Radiance min and max,discard
42 #
43 1.e-5,1.0,0     Photon packets are tracked until their weight is
44 #               below  $1.0 \times 10^{-5}$ . Contributions to the BRDF in excess of 1.0
45 #               are placed in the excess bin. Discard = 0 means that the excess
46 #               will be tracked and accounted for (See Sections 2.8
47 #               and 3.9.5) Discard = 1 means that excess values will be discarded entirely.
48 #
49 # Solar position (theta,phi)
50 #
51 #10.0,180.0
52 30.0,50.0
53 #
54 # Number of viewing angles
55 #
56 #3
57 #
58 # Zenith angles
59 #
60 #180.0,135.0,100.0
61 #
62 # Azimuth angles
63 #
64 #90.0,90.0,90.0
65 #
66 # Number of viewing angles
67 #
68 1
69 #
70 # Zenith angles
71 #
72 180.0
73 #

```

```

74 # Azimuth angles
75 #
76 0.0
77 #
78 # C-k band information file
79 #
80 ./data/band_info_BB.dat
81 #
82 # Number of bands to preform runs at
83 #
84 1
85 #
86 # band number and name of band The band names must match those listed in the C-k band
87 # information file as specified above.
88 1,MSI_1 660 nm
89 #2,MSI_2 865 nm
90 #3,MSI_3 1.61 um
91 #4,MSI_4 2.2 um
92 #5,MSI_5 8.85 um (ONLY FOR LW)
93 #6,MSI_6 10.85 um (ONLY FOR LW)
94 #7,MSI_7 11.85 um (ONLY FOR LW)
95 #8,SW 0.2-4.0 um (SW BB FLUX)
96 #
97 #
98 # Seed for random number generator (negative number to use time and date as seed)
99 #
100 -1

```

3.9.6 MC_LW_sim_main

USAGE: MC_LW_sim_main MASTERFILE

Description

This program calculates TOA, radiances and TOA fluxes for both wide and narrow bands for the scene file specified in the MASTERFILE. The wavelength bands, and viewing angles are specified in the MC_LW input file.

The input and output files for MC_sim_main are taken from the appropriate entry in the MASTERFILE. If MASTERFILE is not present the default masterfile ./input/master.inp is used. See ./input/sw_mc/sw_mc.inp for an example input file.

Output

For each channel, band, and viewing angle several output files are written: Note: that in the following, OUTFILE represents the name of the output file specified in the appropriate MASTERFILE, BND is the band number, and THETA and PHI are the viewing angles. If a radiance calculation was preformed the following output files are generated:

OUTFILE_BT_bnd_BND_Ang_THETA_PHI.dat	TOA Brightness Temperature.
OUTFILE_BT_error_bnd_BND_Ang_THETA_PHI.dat	Error estimate in the BT.
OUTFILE_dimensions.dat	Dimensions of the output .
OUTFILE_Radiance_bnd_BND_Ang_THETA_PHI.dat	TOA radiances in W/M ² /sr.
OUTFILE_Radiance_error_bnd_BND_Ang_THETA_PHI.dat	Error estimate in the TOA radiances.
OUTFILE_summary_bnd_BND_Ang_THETA_PHI.dat	Domain average TOA Radiances.
OUTFILE_gass_abs_BND.dat	Approximate effective gass absorption in 1/m. (not useful for broad-band calculations !)

If a flux calculation was preformed the following output files are generated:

OUTFILE_flux_bnd_BND.dat	TOA flux in W/M ² .
OUTFILE_error_flux_bnd_BND.dat	Error estimate in TOA flux in W/M ² .
OUTFILE_flux_summary_bnd_BND.dat	Domain average TOA flux in W/M ² .
OUTFILE_gass_abs_BND.dat	Approximate effective gass absorption in 1/m. (not useful for broad-band calculations !).

Note on the viewing angle conventions:

ANGLES(1,:) = ZENITH (THETA).

ANGLES(2,:) = AZIMUTH (PHI).

ZENITH = 180 → nadir viewing.

ZENITH = 90 → limb viewing.

AZIMUTH = 0 → viewing in opposition to Sun.

AZIMUTH = 180 → viewing in (inferior) conjunction to Sun.

Notes

An inverse MC technique is used in order to calculate radiances. TOA fluxes are computed by calculated TOA radiances at various elevations angles and summing them appropriately. For each grid cell a number of photon packets are launched from the TOA according to the observation angles. This process is repeated a minimum of two rounds. Up to a specified

maximum number of rounds, the calculation proceeds until the standard deviation of the calculated radiances or the TOA fluxes for each output pixel is below a specified threshold.

Atmospheric absorption: C-K tables

Atmospheric transmission is calculated using a correlated-k method and for each narrow-band the scattering properties are assumed to be constant across the range of the narrow band limits. The band structure used here follows that used by the Streamer package (Key and Schweiger (1998)). The various narrow bands can be grouped together to define bands for i.e. broad-band calculations. See `./data/band_info_BB.dat` for an example of how the bands can be defined.

Channel	$v_1 \text{ cm}^{-1}$	$v_2 \text{ cm}^{-1}$	Gasses
MSI_5 8.85 μm	1064.	1205.	H ₂ O, O ₃
MSI_6 10.85 μm	885.	962.	H ₂ O, O ₃
MSI_7 11.85 μm	813.	877.	H ₂ O, CO ₂

Table 9: Long-wave multispectral imager (MSI) Bands.

Long-Wave 4.0-400.0 μ m

Center λ	Gasses								
4.07997	H ₂ O	4.23729	H ₂ O	4.38596	H ₂ O	4.54545	H ₂ O	4.71698	H ₂ O
4.90196	H ₂ O	5.02513	H ₂ O	5.07614	H ₂ O	5.12820	H ₂ O	5.18135	H ₂ O
5.23560	H ₂ O	5.29101	H ₂ O	5.34759	H ₂ O	5.40541	H ₂ O	5.46448	H ₂ O
5.52486	H ₂ O	5.58659	H ₂ O	5.64972	H ₂ O	5.71429	H ₂ O	5.78035	H ₂ O
5.84795	H ₂ O	5.91716	H ₂ O	5.98802	H ₂ O	6.06061	H ₂ O	6.13497	H ₂ O
6.21118	H ₂ O	6.28931	H ₂ O	6.36943	H ₂ O	6.45161	H ₂ O	6.53595	H ₂ O
6.62252	H ₂ O	6.71141	H ₂ O	6.80272	H ₂ O	6.89655	H ₂ O	6.99301	H ₂ O
7.09220	H ₂ O	7.19424	H ₂ O	7.29927	H ₂ O	7.40741	H ₂ O	7.51880	H ₂ O
7.63359	H ₂ O	7.75194	H ₂ O	7.87402	H ₂ O O ₃	8.00000	H ₂ O O ₃	8.13008	H ₂ O O ₃
8.26446	H ₂ O O ₃	8.40336	H ₂ O O ₃	8.54701	H ₂ O O ₃	8.69565	H ₂ O O ₃	8.84956	H ₂ O O ₃
9.00901	H ₂ O O ₃	9.17431	H ₂ O O ₃	9.34579	H ₂ O O ₃	9.52381	H ₂ O O ₃	9.70874	H ₂ O O ₃
9.90099	H ₂ O O ₃	10.1010	H ₂ O O ₃	10.3093	H ₂ O O ₃	10.5263	H ₂ O O ₃	10.7527	H ₂ O O ₃
10.9890	H ₂ O O ₃	11.2360	H ₂ O	11.4943	H ₂ O	11.7647	H ₂ O	12.0482	H ₂ O CO ₂
12.3457	H ₂ O CO ₂	12.6582	H ₂ O CO ₂	12.9870	H ₂ O CO ₂	13.3333	H ₂ O CO ₂	13.6986	H ₂ O CO ₂
14.0845	H ₂ O CO ₂	14.4928	H ₂ O CO ₂	14.9254	H ₂ O CO ₂	15.3846	H ₂ O CO ₂	15.8730	H ₂ O CO ₂
16.3934	H ₂ O CO ₂	16.9492	H ₂ O CO ₂	17.5439	H ₂ O CO ₂	18.1818	H ₂ O CO ₂	18.8679	H ₂ O CO ₂
19.6078	H ₂ O CO ₂	20.4082	H ₂ O	21.2766	H ₂ O	22.2222	H ₂ O	23.2558	H ₂ O
24.3902	H ₂ O	25.6410	H ₂ O	27.0270	H ₂ O	28.5714	H ₂ O	30.3030	H ₂ O
32.2581	H ₂ O	34.4828	H ₂ O	37.0370	H ₂ O	40.0000	H ₂ O	43.4783	H ₂ O
47.6190	H ₂ O	52.6316	H ₂ O	58.8235	H ₂ O	66.6667	H ₂ O	76.9231	H ₂ O
90.9091	H ₂ O	111.111	H ₂ O	142.857	H ₂ O	200.000	H ₂ O	333.333	H ₂ O

Table 10: Center wavelengths used for broad-band long-wave calculations and relevant gasses.

Surface properties

Surfaces are assumed to be black at all wavelengths. This should be improved in forthcoming versions.

Example MC_LW_sim_main input file

```
#####
# Prototype LW_MC input file
#####
#
# Calculate Radiances (0) or Fluxes (1)
0
#
# Domain to use (x1,x2,y1,y2) km
#
0.0,10.0,0.0,10.0
#
# Resolution of output (km) (negative entry ==> use UFF resolution)
#
#10.00
0.5
#
# Number of photons per columns (relative to output resolution)
#
1000           Thus for each round ( $\frac{10}{0.5}$ )2 × 1000 photon packets will be used
#100000
#
# Maximum Number of Rounds
#
#100
100
#
# Stop when all radiances above a certain
# threshold have a relative error less than some amount
#
0.00,0.001 Simulation will stop when BRDF values above 0.0 have converged to within 0.1 %
#
# number of Mie scatterers before switching to HG phase functions
3
#
#
# Number of viewing angles
#
#3
#
# Zenith angles
#
#180.0,135.0,100.0
#
# Azimuth angles
#
#90.0,90.0,90.0
#
# Number of viewing angles
#
1
#
# Zenith angles
#
#180.0
#
# Azimuth angles
#
0.0
#
# C-k band information file
#
./MC/band_info_BB.dat
#
```

```

66 # Number of bands to preform runs at
67 #
68 3
69 #
70 # band number and name of band The band names must match those listed in the C-k band
71 # information file as specified above.
72 #
73 #1,MSI_1 660 nm (SW ONLY)
74 #2,MSI_2 865 nm (SW ONLY)
75 #3,MSI_3 1.61 um (SW ONLY)
76 #4,MSI_4 2.2 um (SW ONLY)
77 5,MSI_5 8.85 um
78 6,MSI_6 10.85 um
79 7,MSI_7 11.85 um
80 #8,SW 0.2-4.0 um (SW BB FLUX)
81 #9,LW 4.0-400.0 um (LW BB FLUX)
82 #
83 #
84 # Seed for random number generator (negative number to use time and date as seed)
85 #
86 -1

```

General Notes The current version (v1.0) is limited with respect to flux calculations. In particular currently only TOA values can be calculated. There is a version to allow fluxes to be calculated at levels other than the TOA in development.

3.10 Retrieval Programs

3.10.1 lidar_ret1

Usage: lidar_ret1 MASTERFILE

Description

This program reads the output of lidar and radar and finds

- | |
|--|
| 1. Cloud/aerosol masks. |
| 2. Cloud Extinction and backscatter profiles. |
| 3. Lidar/Radar effective particle size profiles. |
| 4. Aerosol extinction and backscatter profiles. |

This version is particular to the EARTHCARE 3-channel lidar configuration

The input and output files for MC_sim_main are taken from the appropriate entry in the MASTERFILE. If MASTERFILE is not present the default masterfile ./input/master.inp is used. See ./input/lidar_ret1/lidar_ret1.inp for an example input file.

Output

A large number of files are output, a brief description of the contents of each file follows
Note: that OUTFILE represents the name of the output file specified in the appropriate MASTERFILE.

Signal products

These output files contain the various radar and lidar signals at the desired output horizontal and vertical resolution

OUTFILE_ray_para_lr.dat

The lidar co-polar Rayleigh signal at the output resolution.

OUTFILE_error_ray_para_lr.dat

The standard error of the lidar co-polar Rayleigh signal at the output resolution.

OUTFILE_mie_para_lr.dat

The lidar co-polar Mie channel signal at the specified output resolution.

OUTFILE_error_mie_para_lr.dat

The standard error of the lidar co-polar Mie channel signal at the specified output resolution.

OUTFILE_perp_lr.dat

The lidar cross-polar signal at the specified output resolution.

OUTFILE_error_perp_lr.dat

The standard error of the lidar cross-polar signal at the specified output resolution.

OUTFILE_Ze.dat

The Radar reflectivity at the specified output resolution

OUTFILE_error_Ze.dat

The standard error of the Radar reflectivity at the specified output resolution

Target masks

OUTFILE_cld_mask.dat

Cloud mask based solely on the lidar signals. It is a multi-value integer field.

0	Likely a cloud is not present. SNR in the co-polar channel is greater than a user-specific threshold but the scattering ratio is below a user-specified threshold.
1	Likely a cloud is present. SNR in the co-polar channel is greater than a user-specific threshold and the scattering ratio is greater than a user-specified threshold. In addition the detected pixel has two or more cloudy neighbors.
2	Highly likely a cloud is present. As 1, but the scattering ratio is twice the user-specified threshold no cloudy neighbors are necessary.
-1	Uncertain. SNR is too low or as condition 1 except not enough cloudy neighbors are present.

OUTFILE_aerosol_mask.dat

0	Likely a cloud is present. SNR in the co-polar channel is greater than a user-specified threshold and scattering ratio is above a user-specified threshold.
1	Likely clear or aerosol.. SNR in the co-polar channel is greater than a user-specified threshold and scattering ratio is below a user-specified threshold.
-1	Uncertain. SNR is too low.

`OUTFILE_rad_cld_mask.dat`

0	Likely no cloud. Ze is below the noise threshold or the observed SNR is below a defined threshold.
1	Likely a cloud. Ze is above the thresholds used for condition 0 and the pixel has three or more cloudy neighbors.
-1	Uncertain. In area where ground effects may be present and/or as 1 except not enough neighbors are present.

`OUTFILE_lid_rad_cld_mask.dat`

1	Likely cloud. ((Radar mask =1 and Lidar mask =1 OR Radar mask =1 and Lidar mask =-1 OR Radar mask =-1 and Lidar mask =1) AND Pixel has 3 or more neighbors) OR Lidar mask = 2.
-1	Uncertain. (Radar mask =-1 and Lidar mask =-1) OR as 1 except not enough neighbors exist.
0	Likely no cloud. All pixels not designated either 1 or -1

Cloud products

These files will contain cloud-related quantities derived from the lidar and radar signals. The quantities are reported at the at the specified output resolution.

`OUTFILE_mie_0.dat`

The total Mie (cross+co-polar) Mie signals

`OUTFILE_error_mie_0.dat`

The standard error of the total Mie (cross+co-polar) Mie signals

`OUTFILE_mie_R_0.dat`

The lidar scattering ratio $1 + \frac{\beta_{Mie}}{\beta_{Ray}}$ calculated by dividing the Mie signal by the Rayleigh signal. No correction for multiple-scattering effects.

`OUTFILE_error_mie_R_0.dat`

The estimated standard error in the above.

`OUTFILE_mie_R_1.dat`

The lidar scattering ratio $1 + \frac{\beta_{Mie}}{\beta_{Ray}}$ calculated using the Mie signal and the extinction data contained in `OUTFILE_ext_1.dat`.

`OUTFILE_error_mie_R_1.dat`

The estimated standard error in the above.

`OUTFILE_mie_R_2.dat`

As `OUTFILE_mie_R_1.dat` except masked according to `OUTFILE_cld_mask.dat`.

`OUTFILE_error_mie_R_2.dat`

The estimated standard error in the above.

`OUTFILE_mie_R_4.dat`

As `OUTFILE_mie_R_1.dat` except masked according to the combined lidar+radar cloud mask (`OUTFILE_lid_rad_cld_mask.dat`).

`OUTFILE_error_mie_R_4.dat`

The estimated standard error in the above.

`OUTFILE_mie_beta_0.dat`

The profile of β_{Mie} derived from the data contained in `OUTFILE_mie_R_0.dat`.

`OUTFILE_error_mie_beta_0.dat`

The estimated standard error in the above.

`OUTFILE_mie_beta_1.dat`

The profile of β_{Mie} derived from the data contained in `OUTFILE_mie_R_1.dat`.

`OUTFILE_error_mie_beta_1.dat`

The estimated standard error in the above.

`OUTFILE_mie_beta_2.dat`

As `OUTFILE_mie_beta_1.dat` except masked according to the lidar only cloud mask (`OUTFILE_cld_mask.dat`).

`OUTFILE_error_mie_beta_2.dat`

The estimated standard error in the above.

`OUTFILE_mie_beta_4.dat`

As `OUTFILE_mie_beta_1.dat` except masked according to the lidar+radar cloud mask (`OUTFILE_lid_rad_cld_mask.dat`).

`OUTFILE_error_mie_beta_4.dat`

The estimated standard error in the above.

`OUTFILE_ext_1.dat`

Aerosol extinction derived by taking the logarithmic derivative of the Rayleigh signal profile.
No correction for Multiple-scattering.

`OUTFILE_error_ext_1.dat`

The estimated standard error in the above.

`OUTFILE_ext_2.dat`

As `OUTFILE_ext_1.dat` but masked according to `OUTFILE_cld_mask.dat`.

`OUTFILE_error_ext_2.dat`

The estimated standard error in the above.

`OUTFILE_ext_3.dat`

As `OUTFILE_ext_2.dat` except a iterative correction for multiple-scattering has been applied. For simplicity a value of R_a of 10 microns has is used for warm clouds while a value of R_a of 100 microns is used for ice clouds.

`OUTFILE_error_ext_3.dat`

The estimated standard error in the above.

`OUTFILE_ext_4.dat`

As `OUTFILE_ext_3.dat` except that the data has been masked accoring to the combined lidar+radar cloud mask.

`OUTFILE_error_ext_4.dat`

The estimated standard error in the above.

`OUTFILE_adb_1.dat`

The extinction-to-backscatter ratio derived from the data in `OUTFILE_ext_1.dat` and `OUTFILE_R_0.dat`.

`OUTFILE_error_adb_1.dat`

The estimated standard error in the above.

`OUTFILE_adb_2.dat`

As `OUTFILE_adb_1.dat` but masked according to `OUTFILE_cld_mask.dat`.

`OUTFILE_error_adb_2.dat`

The estimated standard error in the above.

`OUTFILE_adb_3.dat`

The extinction-to-backscatter ratio derived from the data in `OUTFILE_ext_3.dat` and `OUTFILE_R_1.dat`.

`OUTFILE_error_adb_3.dat`

The estimated standard error in the above.

`OUTFILE_adb_4.dat`

As `OUTFILE_error_adb_3.dat` except that the data has been masked according o the combined lidar+radar cloud mask.

`OUTFILE_error_adb_4.dat`

The estimated standard error in the above.

`OUTFILE_rpeff.dat`

The lidar/radar effective radius (R'_{eff}) profile deduced from the data in `OUTFILE_Ze.dat` and `OUTFILE_ext_3.dat`.

`OUTFILE_error_rpeff.dat`

The estimated standard error in the above.

Aerosol products

These quantities are deduced from the average signals over the entire cloud-free part of the scene.

`OUTFILE_aero_ray_signal.dat`

Rayleigh signal averaged over the cloud-free areas.

`OUTFILE_aero_error_ray_signal.dat`

The estimated standard error in the above.

`OUTFILE_aero_mie_signal.dat`

Mie signal averaged over the cloud-free areas.

`OUTFILE_aero_error_mie_signal.dat`

The estimated standard error in the above.

`OUTFILE_aero_ext_0.dat`

The extinction derived from the average cloud-free Rayleigh channel signal.

`OUTFILE_aero_error_ext_0.dat`

The estimated standard error in the above.

`OUTFILE_aero_beta_0.dat`

The backscatter derived from the average cloud-free Mie and Rayleigh channel signal.

`OUTFILE_aero_error_beta_0.dat`

The estimated standard error in the above.

Misc Information

`OUTFILE_temperature.dat`

The temperature field in Kelvin at the specified output resolution .

Example lidar_retr1 input file

```
1  #
2  #=====
3  # Input file for lidar and radar
4  # Level 1 retrievals
5  #=====
6  #
7  #-----
8  # Desired vertical resolution (km)
9  #-----
10 0.2
11 #
12 #-----
13 # Desired horizontal resolution (km)
14 #-----
15 1.0
16 #
17 #-----
18 # Rayleigh atmosphere Normalization altitude range (km)
19 #-----
20 10.5,13.5
21 #
22 #-----
23 # Derivative window for determining direct extinction
24 # From the ground up to h2.
25 # Width of window is (2*iwin+1)*Hor. res
26 #-----
27 1
28 #
29 #-----
30 # h2 and Derivative window for determining direct extinction
31 # above h2
32 #-----
33 3.0,3
34 #
35 #-----
36 # Min SNR and min R for cld detection
37 #-----
38 2.0,1.4
39 #
40 #-----
41 # Are we including the radar data (1==> yes)
42 #-----
43 1
44 #
45 #-----
46 # Radar noise floor (dBz), Min SNR for target detection (dBz)
47 #-----
48 -35.0,3.0
49 #
50 #-----
51 # Minimum altitude (km) to consider radar data (to avoid surface return effects)
52 #-----
53 #
54 0.5
```

3.10.2 msi_ret

USAGE: msi_ret MASTERFILE

Description

This program reads in output from **MC_sim_main** and **MC_LW_sim_main** and attempts to deduce the cloud/aerosol scattering type, optical depth, and effective radius using look-up tables previously generated using **MC_sim_main** and **MC_LW_sim_main**. The looktables were generated automatically using the shell script `./scripts/make_lookup.sh`. Only nadir viewing is currently considered.

The input and the root name for the output file are taken from the appropriate entry in the **MASTERFILE**. If **MASTERFILE** is not present the default masterfile `./input/master.inp` is used. See `./input/msi_ret/msi_ret.inp` for an example input file.

Output

Three files are generated, a brief description follows. Note: that OUTFILE represents the name of the output file specified in the appropriate MASTERFILE, THETA0 represents the solar zenith angle and PHI0 represents the solar azimuth angle

OUTFILE_scatt_type_Ang_THETA0_PHI0.dat	Retrieved scattering type (see below)
OUTFILE_tau_Ang_THETA0_PHI0.dat	Retrieved optical depth.
OUTFILE_reff_Ang_THETA0_PHI0.dat	Retrieved mode radius parameter. This parameter is equal to $Rm(\gamma + 2)$ where the size distribution is described by $\frac{dN(r)}{dr} = \left(\frac{1}{\Gamma(\gamma)} \right) \left(\frac{1}{Rm} \right) \left(\frac{r}{Rm} \right)^{\gamma-1} \exp \left[-\frac{r}{Rm} \right]$

The output files may be plotted using **plot_hor**.

Current Scattering types (refer to the *scattering lists* in `./input/scatt_master_lists`).

1	Col_hess_scatt_tilt_30.list
2	Col_hess_scatt_tilt_01.list
3	Plt_hess_scatt_tilt_30.list
4	Plt_hess_scatt_tilt_01.list
5	Dry_Dust.list
6	Dry_Salt.list
7	Dry_Soot.list
8	H2SO4_25.list
9	H2SO4_50.list
10	H2SO4_75.list'
11	water.list
12	drizzle.list

Example msi_ret input file

```

1 ######
2 # Example MSI retrieval
3 # input file

```

```
4 #####  
5 #  
6 # Solar position  
7 #  
8 40.0,35.0  
9 #  
10 # Number of pairs of MSI lookup table files  
11 #  
12 9  
13 #  
14 ./msi_lookup/msi_lookup-3-3-00-5-40.0-35.0.dat  
15 ./msi_lookup/msi_lookup-3-3.dat  
16 ./msi_lookup/msi_lookup-3-1-00-5-40.0-35.0.dat  
17 ./msi_lookup/msi_lookup-3-1.dat  
18 ./msi_lookup/msi_lookup-3-5-00-5-40.0-35.0.dat  
19 ./msi_lookup/msi_lookup-3-5.dat  
20 ./msi_lookup/msi_lookup-3-6-00-5-40.0-35.0.dat  
21 ./msi_lookup/msi_lookup-3-6.dat  
22 ./msi_lookup/msi_lookup-3-7-00-5-40.0-35.0.dat  
23 ./msi_lookup/msi_lookup-3-7.dat  
24 ./msi_lookup/msi_lookup-3-8-00-5-40.0-35.0.dat  
25 ./msi_lookup/msi_lookup-3-8.dat  
26 ./msi_lookup/msi_lookup-3-9-00-5-40.0-35.0.dat  
27 ./msi_lookup/msi_lookup-3-9.dat  
28 ./msi_lookup/msi_lookup-3-10-00-5-40.0-35.0.dat  
29 ./msi_lookup/msi_lookup-3-10.dat  
30 ./msi_lookup/msi_lookup-3-11-00-5-40.0-35.0.dat  
31 ./msi_lookup/msi_lookup-3-11.dat
```

3.10.3 lw_msi_lidar_radar

USAGE: `lw_msi_lidar_radar MASTERFILE`

Description

This program combines the EarthCARE long-wave MSI images as well as the profile outputs from `lidar_ret1` in an effort to reconstruct the cloud fields. In brief, for each of the nadir columns, profiles of lidar extinction, lidar backscatter and radar reflectivity are calculated based on height dependent cloud particle size distributions of various scattering types (small mode water, large mode water, small mode ice , and large mode ice). Using the same information, a simple forward model is used to calculate the long-wave MSI TOA radiances. In order to determine a plausible set of height-dependent cloud particle size distribution parameters a suitable *cost-function* is based on the cloud parameters is minimized. . The cost function includes contributions from a priori information as well as terms representing the uncertainty weighted differences between the model quantities and the lidar measured extinction and backscatter, the radar reflectivity profile and the MSI BTs. The cost function is minimized using a simulated annealing approach (*see Numerical Recipes*).

Once the nadir cloud property profiles are determined the MSI images are used in order to map the profiles to the off-nadir pixels. This is done on the scanning through the 2-d off nadir image pixels and finding the closest match in terms of radiances amongst the nadir pixels.

The approach to retrievals embodied by this program should be considered very promising but still experimental, all the pitfalls are definitely yet not known. In particular care and thought must be exercised in determining useful weights for the components of the cost function in order to obtain useful results. Also, the annealing schedule as specified in the sample input file is likely far from optimal.

The input and the root name for the output file are taken from the appropriate entry in the **MASTERFILE**. If **MASTERFILE** is not present the default masterfile `./input/master.inp` is used. See `./input/lw_msi_lidar_radar/lw_msi_lidar_radar.inp` for an example **scene_creator** input file.

Output

For each mode (2-water, 2 ice) a file containing the retrieved size distribution parameters is output. These files can then be read by **scene_creator** in order to create a UFF file which then can be treated as any other scene file. One can use the extract quantity utilities in order to assess the accuracy of the retrieved scene or one can run the Monte-Carlo programs in order to assess the accuracy of the retrieval in radiative terms.

Aerosols are not automatically considered by **lw_msi_lidar_radar**. Aerosol properties are assumed to be horizontally constant in the retrieved scenes. The aerosol properties in the reconstructed UFF must be manually inserted into the global input field of the **scene_creator** input file used to reconstruct the scene. (see `./input/scene_ret1.inp`). Ideally the aerosol information should be based on the appropriate output of `lidar_ret1` together with the average cloud free output of `msi_ret`.

NOTE:

This program requires the use of several routines from **Numerical Recipies** in Fortran 90. These routines can not be freely distributed with this package. The user must supply this code. See `./src/makefile` in order to see what routines are required.

———— Example lw_msi_lidar_radar input file ————

```
1 #####  
2 # INPUTFILE FOR THE LONG_WAVE MSI + LIDAR + RADAR  
3 # INVERSION PROGRAM  
4 #####  
5 #  
6 #-----  
7 # Allow variations of the cloud cover  
8 # on this scale (km). Must be less than or equal to the  
9 # hor. scale of the lidar and radar measurements.  
10 # A good choice is the MSI pixel scale.  
11 #-----  
12 #  
13 0.50  
14 #  
15 #####  
16 # SCATTERING TYPES TO USE IN THE INVERSION  
17 #####  
18 #-----  
19 # scattering model for small ice  
20 #-----  
21 #  
22 ./scatt_master_lists/Col_hess_scatt_tilt_30.list  
23 #  
24 #-----  
25 # scattering model for large ice  
26 #-----  
27 #  
28 ./scatt_master_lists/Col_hess_scatt_tilt_30.list  
29 #  
30 #-----  
31 # scattering model for water  
32 #-----  
33 #  
34 ./scatt_master_lists/water.list  
35 #  
36 #####  
37 # A-PRIORI BIASES AND STARTING SIMPLEX  
38 # BOUNDS FOR CLOUD-PARAMETERS  
39 #####  
40 #-----  
41 # small-ice Reff_guess[um],ext_guess[1/m]  
42 #-----  
43 10.0,1.0e-4  
44 # Corresponding bounding factors  
45 4.0,2.0  
46 #-----  
47 # large-ice Reff_guess[um],ext_guess[1/m]  
48 #-----  
49 200.0,1.1e-3  
50 # Corresponding bounding factors  
51 4.0,2.0  
52 #-----  
53 # small water Reff_guess[um],ext_guess[1/m]  
54 #-----  
55 #10.0,0.5e-2  
56 10.0,1.0e-2  
57 # Corresponding bounding factors  
58 4.0,2.0  
59 #-----  
60 # large water Reff_guess[um],ext_guess[1/m]  
61 #-----  
62 30.0,5.0e-4  
63 # Corresponding bounding factors  
64 4.0,2.0  
65 #  
66 #####  
67 # FACTORS/OPTIONS FOR EVALUATING THE COST FUNCTION  
68 #####  
69 #
```

```

70 #-----
71 # Extinction residue multiplier (TERM E1 in the cost function).
72 #-----
73 1.0
74 #-----
75 # Backscatter residue multiplier (TERM E2 in the cost function).
76 #-----
77 1.0
78 #-----
79 # Radar reflectivity residue multiplier (TERM E3 in the cost function).
80 #-----
81 1.0
82 #-----
83 # LW MSI B(t) residue multiplier (TERM E4 in the cost function).
84 #-----
85 1.0
86 #-----
87 # apriori Reff residue multiplier (TERM E5 in the cost function).
88 #-----
89 1.0
90 #-----
91 # apriori extinction residue multiplier (TERM E6 in the cost function).
92 #-----
93 1.0
94 #-----
95 # Reff derivative weight for each scattering type (TERM E7 in the cost function)
96 # useful for smoothing the result.
97 #-----
98 1.0,1.0,1.0,1.0
99 #-----
100 # Extinction derivative weight for each scattering type (TERM E8 in the cost function)
101 # useful for smoothing the result.
102 #-----
103 1.0,1.0,1.0,1.0
104 #-----
105 # 2-D ext_dist weight (TERM E10 in the cost function)
106 # The higher the weight, the smoother the cloud cover
107 # within the resolution volumes
108 #-----
109 100.0
110 #-----
111 # No (number concentration) derivative weight
112 # (TERM E11 in the cost function) (FOR SMALL WATER MODE ONLY !!!)
113 # Useful only where No is expected to be somewhat
114 # constant (i.e. (semi-)adiabatic clouds)).
115 #-----
116 0.0
117 #-----
118 # Pseudo-adiabatic LWC slope weight
119 # (TERM E12 in the cost function) (WATER ONLY)
120 # Useful only LWC profile is expected to be (semi-)adiabatic.
121 #-----
122 0.0
123 #-----
124 # Pseudo-adiabatic Reff slope
125 # (TERM E13 in the cost function) (FOR SMALL WATER ONLY !!!)
126 # Useful only LWC profile is expected to be (semi-)Adiabatic.
127 #-----
128 0.0
129 #-----
130 # Suppress large water mode [1=yes, 0=no]
131 #-----
132 0
133 #-----
134 # Exclude extinction in water clouds in cost function evaluation [1=yes, 0=no]
135 # (Set Term E1 to zero only for water but not for ice)
136 #-----
137 0
138 #
139 ######
140 # ANNEALING SCHEDULE AND NUMBER OF

```

```

141 # ITERATIONS
142 ######
143 #
144 #-----
145 # Relative error tolerance in
146 # minimization process
147 #-----
148 #
149 2.5e-3
150 #
151 #
152 #-----
153 # Maximum number of iterations
154 #-----
155 #
156 5000
157 #
158 #-----
159 # Number of iterations
160 # at each temperature (Iter)
161 #-----
162 #
163 100
164 #
165 #-----
166 # After Iter iterations
167 # at a fixed temperature
168 # then temperature is set
169 # to T_new= beta_a*(Min_E-Min_E_best)
170 # beta_a=??
171 #-----
172 #
173 10.0
174 #
175 #-----
176 # However,
177 # The new temperature can
178 # not be less than
179 # Max_T_fac*T_old
180 #-----
181 #
182 0.9
183 #
184 #-----
185 # If the temperature has
186 # decreased by a factor
187 # T_reset_fac since the
188 # last restart then we will
189 # restart the optimization
190 # at the present temperature
191 # level
192 #-----
193 #
194 0.5
195 #
196 ######
197 # SEED FOR RANDOM NUMBER GENERATOR (INTEGER: LESS THAN 0 ==> USE SYSTEM TIME)
198 ######
199 #
200 -1

```

3.11 Plotting programs

3.11.1 plot_slice

```
Usage: plot_slice INPUTFILE x_start x_stop alt_start alt_stop p1 p2 log pgplot_device.
```

Description

This program reads a 2-D data file generated by **extract_quantity**, **lidar**, **radar** or **lidar_ret1** and produces a 2-D image plot. The following arguments are expected:

INPUTFILE	The file containing the data to plot.
x_start	Horizontal starting point (km).
x_finish	Horizontal ending point (km).
alt_start	Vertical starting point (km).
alt_stop	Vertical ending point (km).
p1	Lower plot scale limit.
p2	Upper plot scale limit.
log	0→ linear plot. 1→ Logarithmic (base10), plot. 2→ DBz $10.0 * \log(\text{base10})$ plot.
pgplot_device	PGPLOT output device to use.

Example pgplot_device options:

/xserve	Use the PGPLOT X-window server.
myplot.ps/cps	Output a color postscript file called myplot.
/win	MS window output.
myplot.gif/gif	Output a GIF file called myplot.
/?	Gives a complete list of available plot options.

The labels for the plot axis are read from the input data file itself.

If an incorrect number of commandline arguments are given then an error message is printed along with a help message.

This program requires that PGPLOT be installed on the system. The main PGPLOT web site can be found at <http://www.astro.caltech.edu/~tjp/pgplot/>.

3.11.2 plot_profile

Usage: plot_profile INPUTFILE x_start alt_start alt_stop p1 p2 log pgplot_device.
--

Description

This program reads a 2-d data file generated by EXTRACT_QUANTITY, LIDAR, RADAR or LIDAR_RET1 and produces a profile plot corresponding to a specific along track point. The following arguments are expected:

INPUTFILE	The file containing the data to plot.
x_start	Along track point to plot.
alt_start	Vertical starting point (km).
alt_stop	Vertical ending point (km).
p1	Lower plot scale limit.
p2	Upper plot scale limit.
log	0 → linear plot. 1 → Logarithmic (base10). 2 → DBz $10.0 \cdot \log_{10}$ plot.
pgplot_device	PGPLOT output device to use.

Example pgplot_device options:

/xserve	Use the PGPLOT X-window server.
myplot.ps/cps	Output a color postscript file called myplot.ps
/win	MS window output.
myplot.gif/gif	Output a GIF file called myplot.gif
/?	Gives a complete list of available plot options.

The labels for the plot axis are read from the input data file itself.

If an incorrect number of commandline arguments are given then an error message is printed along with a help message.

This program requires that PGPLOT be installed on the system. The main PGPLOT web site can be found at <http://www.astro.caltech.edu/~tjp/pgplot/>.

3.11.3 plot_profile_comp

```
Usage: plot_profile_comp INPUTFILE INPUTFILE2 x_start alt_start alt_stop  
p1 p2 log pgplot_device.
```

Description

This program reads two 2-d files generated by EXTRACT_QUANTITY, LIDAR, RADAR or LIDAR_RET1 and produces a profile plot corresponding to a specific along track point. The following arguments are expected:

INPUTFILE	The file containing data set 1.
INPUTFILE2	The file containing data set 2.
x_start	Along track point to plot.
alt_start	Vertical starting point (km).
alt_stop	Vertical ending point (km).
p1	Lower plot scale limit.
p2	Upper plot scale limit.
log	0→ linear plot. 1→ Logarithmic (base10) plot. 2→ DBz $10.0 * \log(\text{base10})$ plot. 3,4,5 as 0,1,2 except data in inputfile 1 is along with the +/- the data in inputfile 2 (useful for plotting error bounds). In the case of log=5. The $10 * \log_{10}(\text{data1}) +/- 10(\log_{10}(\text{data2}))$ is plotted.
pgplot_device	PGPLOT output device to use.

Example pgplot_device options:

/xserve	Use the PGPLOT X-window server.
myplot.ps/cps	Output a color postscript file called myplot.ps
/win	MS window output.
myplot.gif/gif	Output a GIF file called myplot.gif
/?	Gives a complete list of available plot options.

The labels for the plot axis are read from the input data file itself.

If an incorrect number of commandline arguments are given then an error message is printed along with a help message.

This program requires that PGPLOT be installed on the system. The main PGPLOT web site can be found at <http://www.astro.caltech.edu/~tjp/pgplot/>.

DRAFT December 13, 2004 DRAFT December 13, 2004

3.11.4 plot_3d

```
Usage: plot_3d INPUTFILE x_start x_stop y_start y_stop z_start z_stop zscale
p1 p2 lplotFsurf slice buf pgplot_device (phi1 theta1 phi2)
```

Description

This program reads a 3-D file from **extract_3d** and produces 3-D isosurface plot along with a 2-D color scale plot slice.

The following arguments are expected:

INPUTFILE	The file containing the data set to plot.
x_start	Starting X coordinate.
x_stop	Ending X coordinate.
y_start	Starting Y coordinate.
y_stop	Ending Y coordinate.
z_start	Starting Z coordinate.
z_stop	Ending Z coordinate.
zscale	Scaling factor between horizontal and vertical dimensions. The greater the value of zscale the ‘taller’ the plot will appear.
p1	Lower plot scale limit.
p2	Upper plot scale limit.
lplot	0 → linear plot, 1 → Logarithmic (base10) plot
Fsurf	Value that will be used to plot the iso surface
slice	Option for the 2-d slice plot 0 → Slice along middle of X axis +. 1 → Slice along middle of Y axis. 2 → Slices along middles of both the X axis and the Y axis.
buf	Option for adding empty data along edges to prevent wrap around effects 1 → enable buffer
pgplot_device	PGPLOT output device to use.
phi1	First Euler angle for view (optional)
theta1	2nd Euler angle for view (optional)
phi2	3rd Euler angle for view (optional)

Example pgplot_device options:

/xserve	Use the PGPLOT X-window server.
myplot.ps/cps	Output a color postscript file called myplot.ps
/win	MS window output.
myplot.gif/gif	Output a GIF file called myplot.gif
/?	Gives a complete list of available plot options.

The labels for the plot axis are read from the input data file itself.

If an incorrect number of commandline arguments are given then an error message is printed along with a help message.

This program requires that PGPLOT be installed on the system. The main PGPLOT web site can be found at <http://www.astro.caltech.edu/~tjp/pgplot/>.

As well as PGPLOT the program makes use of the PGXTAL package. The PGXTAL package is included in the simulator distribution. For infomation on PGXTAL see: <http://www.isis.rl.ac.uk/dataanalysis/dsplot/>.

3.11.5 mcrad_quick_plot

Usage: mcrad_quick_plot INPUTFILE x1 x2 y1 y2 p1 p2 lplot pgplot_device

Description

This program reads the output of MC_sim_main or MC_LW_sim_main and produces a 2-d image plot of the TOA BRDF or LW Brightness temperature or Radiance field. The following arguments are expected

INPUTFILE	The file containing the data to plot.
x1	Starting value of X to plot in km.
x2	Ending value of X to plot in km.
y1	Starting value of Y to plot in km.
y2	Ending value of Y to plot in km.
lplot	Plotting options
p1	Lower range to plot.
p2	Upper range to plot. 0 → Plot using linear color (blue-white) scale. 1 → Plot using logarithm color (blue-white) scale. 2 → Plot using linear grey scale. 3 → Plot using logarithm grey scale.
pgplot_device	PGPLOT output device to use.

Example pgplot_device options:

/xserve	Use the PGPLOT X-window server.
myplot.ps/cps	Output a color postscript file called myplot.
/win	MS window output.
myplot.gif/gif	Output a GIF file called myplot.
/?	Gives a complete list of available plot options.

If an incorrect number of commandline arguments are given then an error message is printed along with a help message.

4 Example Results

4.1 Simple Scene results

In this section we will present results for a simple scene generated by using the `scene_creator` application. The scene considered here is the same one used earlier as a example (see 3.6). The structure of the scene is shown in Fig. 32. Here ice cloud, a stratus deck and a boundary layer aerosol layer are present together. Though this is a ‘simple’ scene it is, in fact, much more complicated than a standard plane parallel situation and does compactly illustrate a range of situations in a single scene. The three dimensiona view was plotted using `extract_quantity_3d` along with `plot_3d`. The two dimension slices were generated using `extract_quantity` in combination with `plot_slice`.

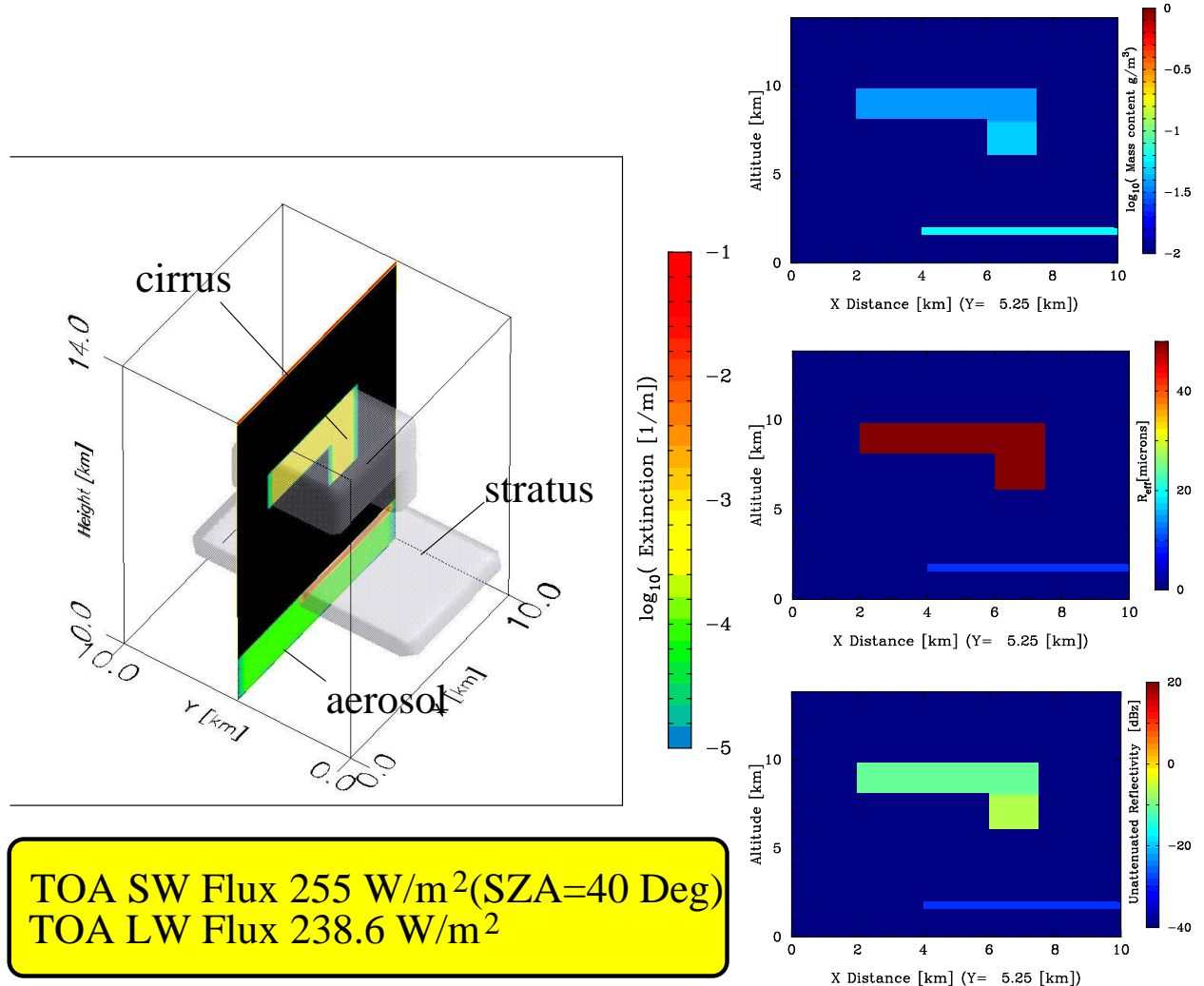


Figure 32: Three dimensional view (left) of a simple scene generated using the `scene_creator` application with ice cloud, water stratus cloud and aerosol present. The right panels show cross section of water content, effective radius, and true reflectivity respectively.

The view from above for this scene is shown in Fig. 33. This images were generated using `extract_quantity_hor` and the `plot_slice` programs. The lidar signals in each channel of the EarthCARE lidar for this scene are shown in Fig. 34. Here the resolution is about 100 meters in both the horizontal dimension and in altitude. The cross-polarized return from the water clouds is a cosequence of multiple-scattering. The results shown in Fig. 34 come from

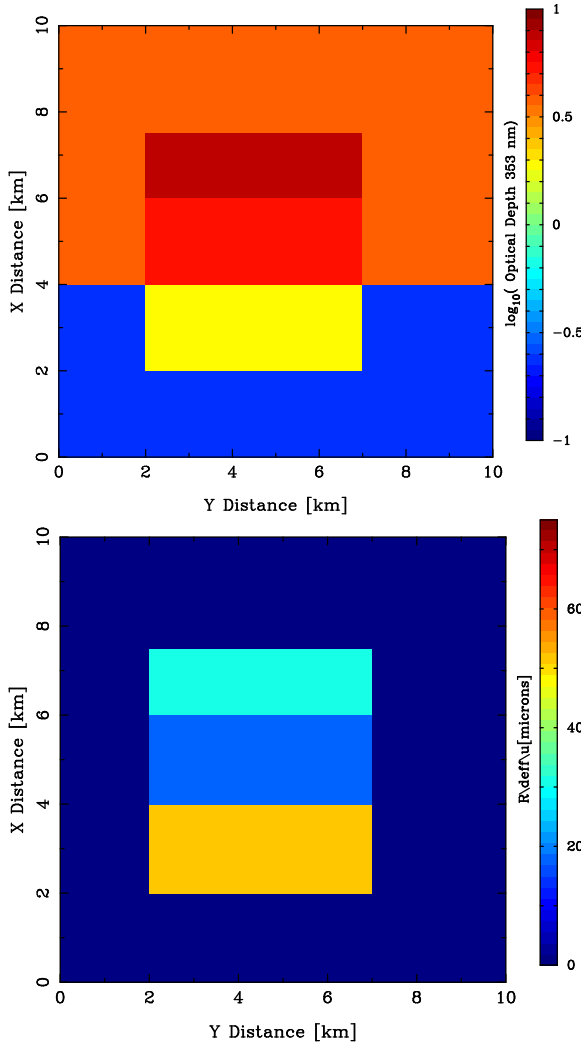


Figure 33: Optical depth and average effective radius for the scene depicted in 32.

`lid.filter` and `lidar` and are plotted using `plot_slice`. Here is can be seen that the lidar is able to detect the water cloud and aerosol layer under the thin portion of the cirrus cloud but is unable to detect the water cloud under the thicker portion of the cirrus deck.

The lidar returns in the co-polar Mie and Rayleigh channels averaged to a horizontal resolution of 1 km along with the corresponding radar reflectivity is depicted in Fig. 4.1. The data plotted in these figure is a product of the `lidar_ret1` program. Here it can be seen that the stratus layer is just on the edge of detectability by the radar.

The target mask corresponding to Fig. 4.1 is shown in Fig. 4.1. In the top two target masks, 0 implies no cloud, 2 implies certain presence of cloud, 1 implies likely cloud and -1 denotes no imformation (SNR too low). In the combined lidar/radar cloud mask (bottom pannel) 0 implies no cloud detected for certain by boh the lidar and the radar, 1 implies cloud while detected by the lidar and the radar while -1 is used to flag areas where cloud is detected by either the lidar or the radar or areas where no information is avaiable for either the lidar or radar. The masks are products of the `lidar_ret1` program. The corresponding retrieved lidar extinction and backscatter fields are shown in Fig. 4.1.

The BRDF's for the EarthCARE imager short-wave bands are shown in Fig. 4.1. Here shadow effects are clearly seen. Also, the effect of increased absorption by the ice cloud at longer wavelengths (Bands 3 and 4) is also visable. The corresponding shortwave imager

parducts produced by `msi_retr` are shown in Fig. 4.1. Here the retrieval program is cabable of distinguishing between water and ice cloud (but mistakenly classifies the aerosol only sections as water also). The quantative properties are generally somewhat correct. However, the effect of shadowing is clearly visable in the top right corner. The brightness temperatues for channels 5, 6 and 7 are shown in Fig. 4.1. Here three dimensional scattering effects are not pronounced as in the short-wave case.

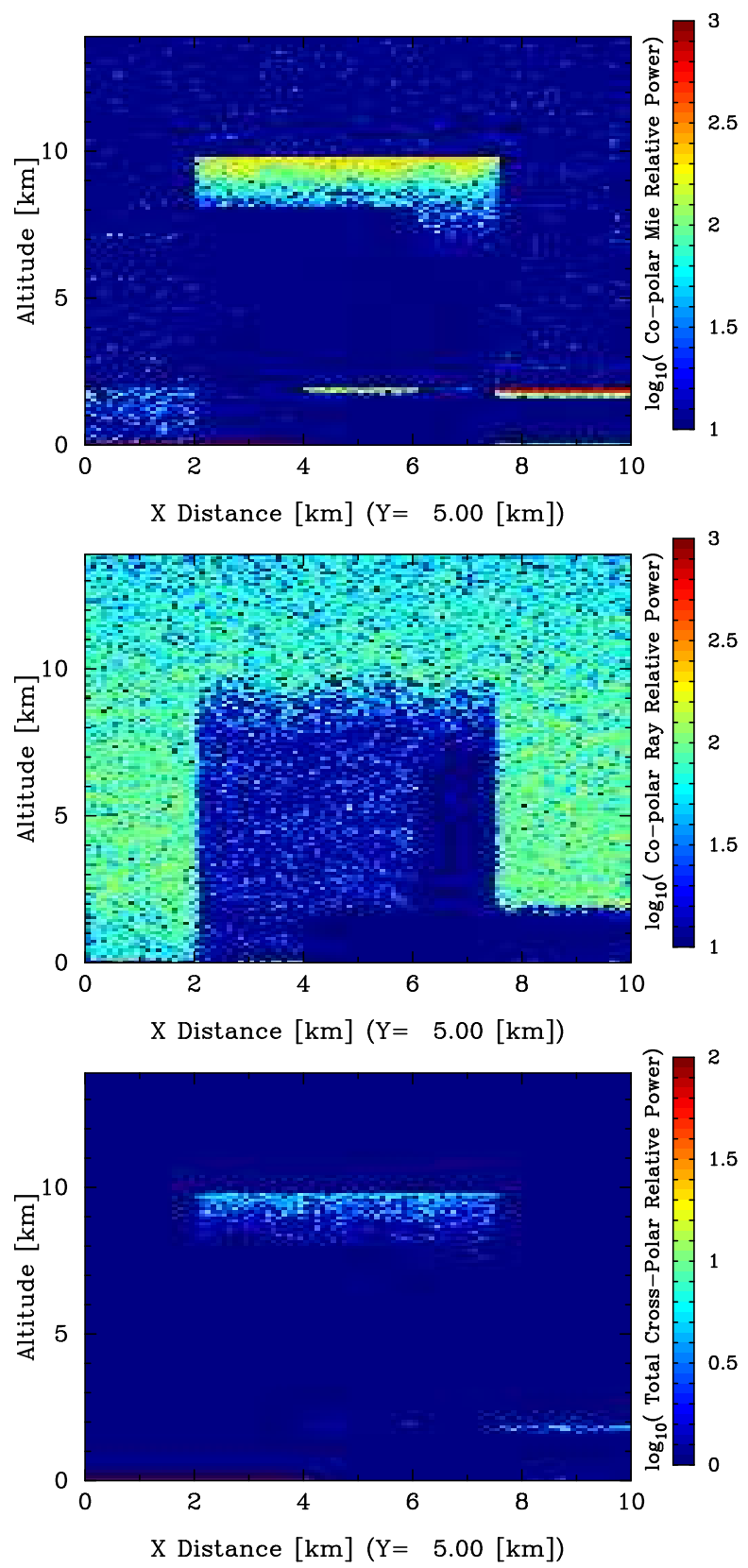


Figure 34: Lidar co-polar Mie signal (Top), Co-Polar Rayleigh signal (Middle), Lidar total cross-polar signal (Bottom) for the simple scene depicted in Fig. 32.

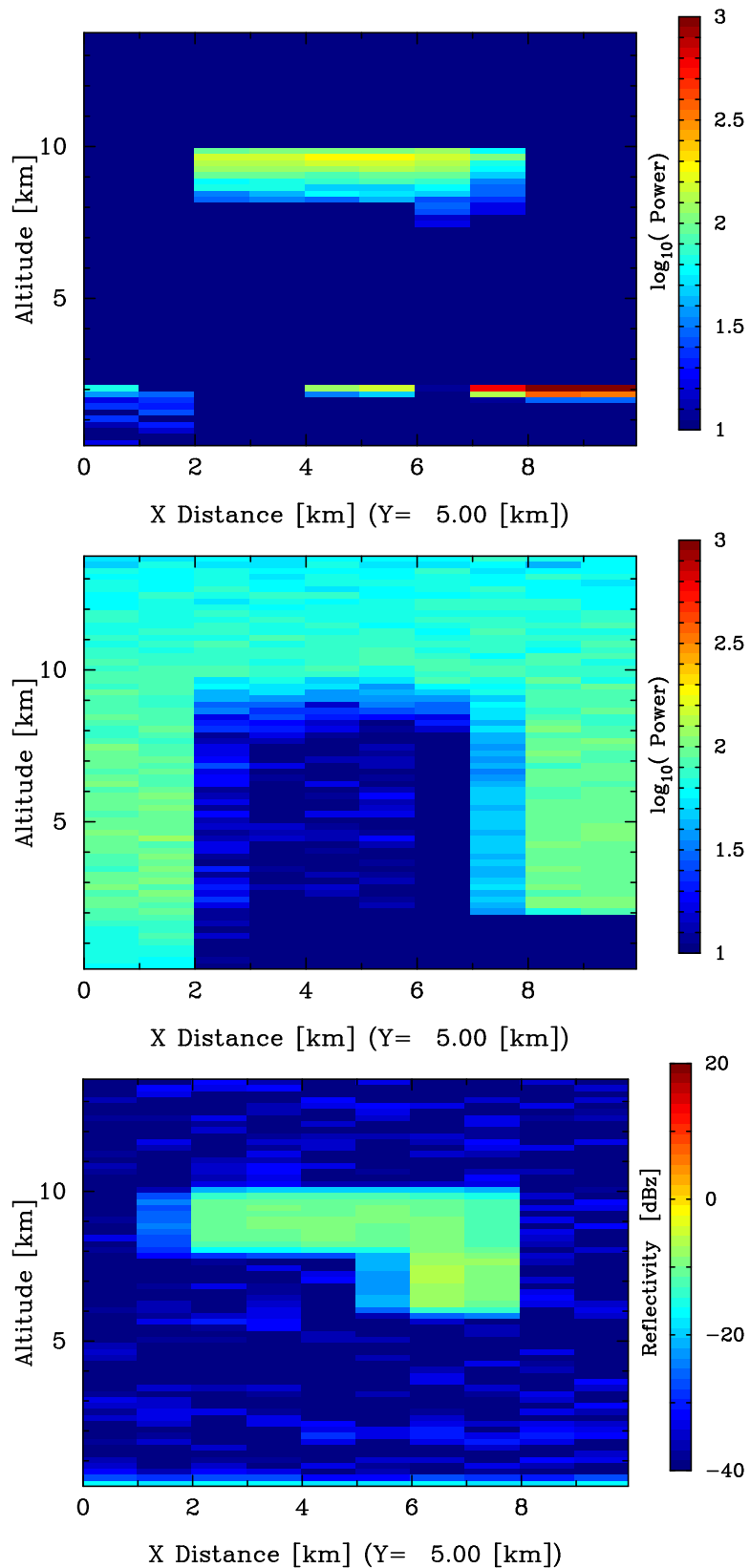


Figure 35: Mie signal, Rayleigh signal and radar reflectivity at 1 km horizontal resolution.

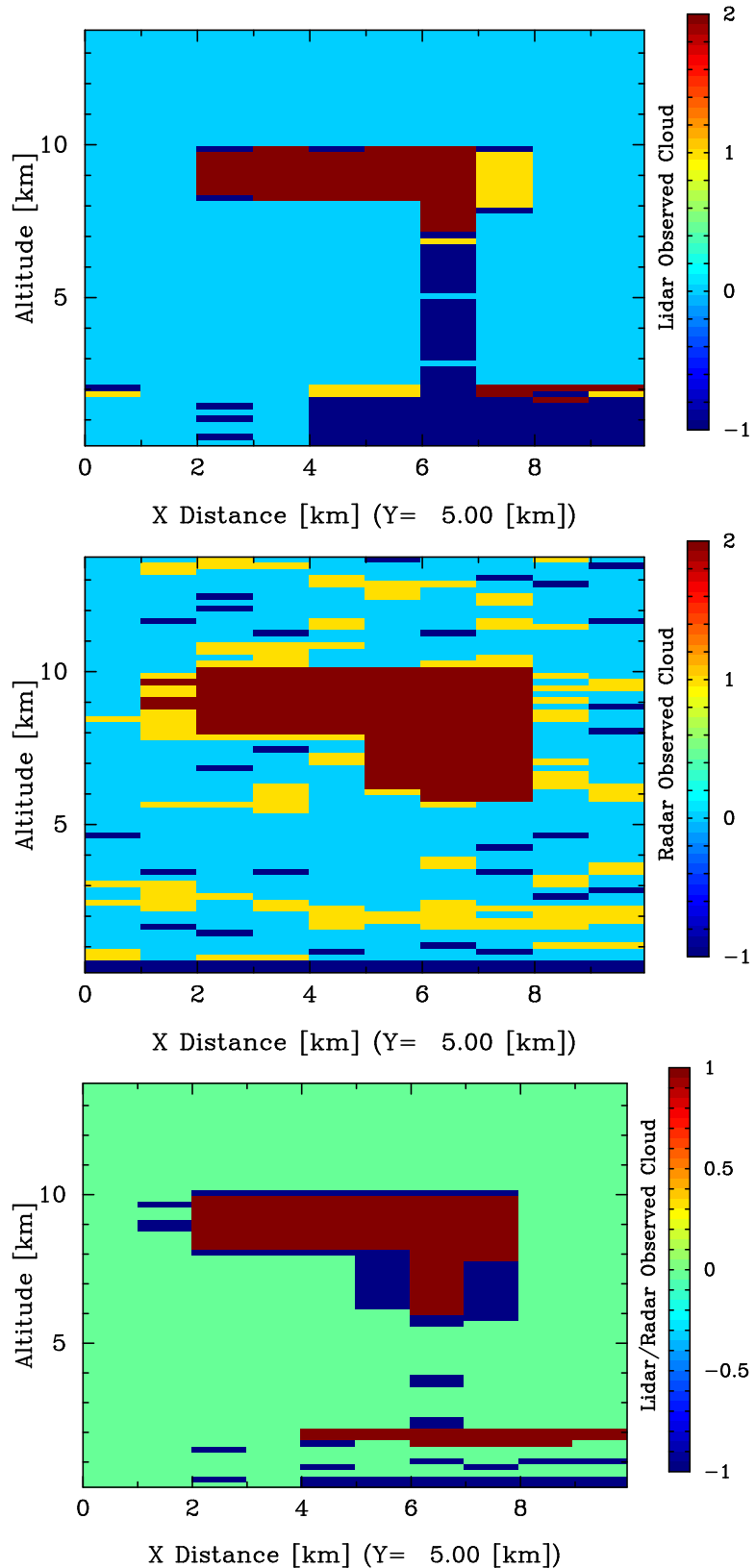


Figure 36: Lidar only (Top), Radar only (Middle) and combined cloud mask (Bottom)

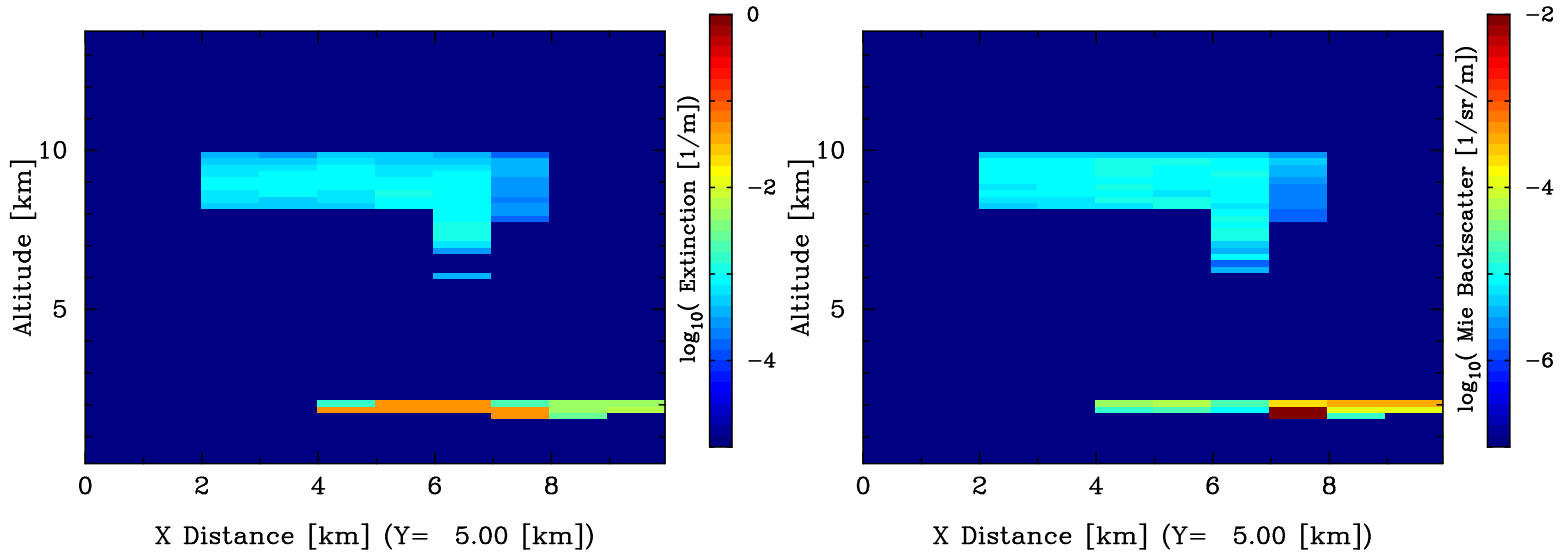


Figure 37: Retrieved lidar extinction and backscatters.

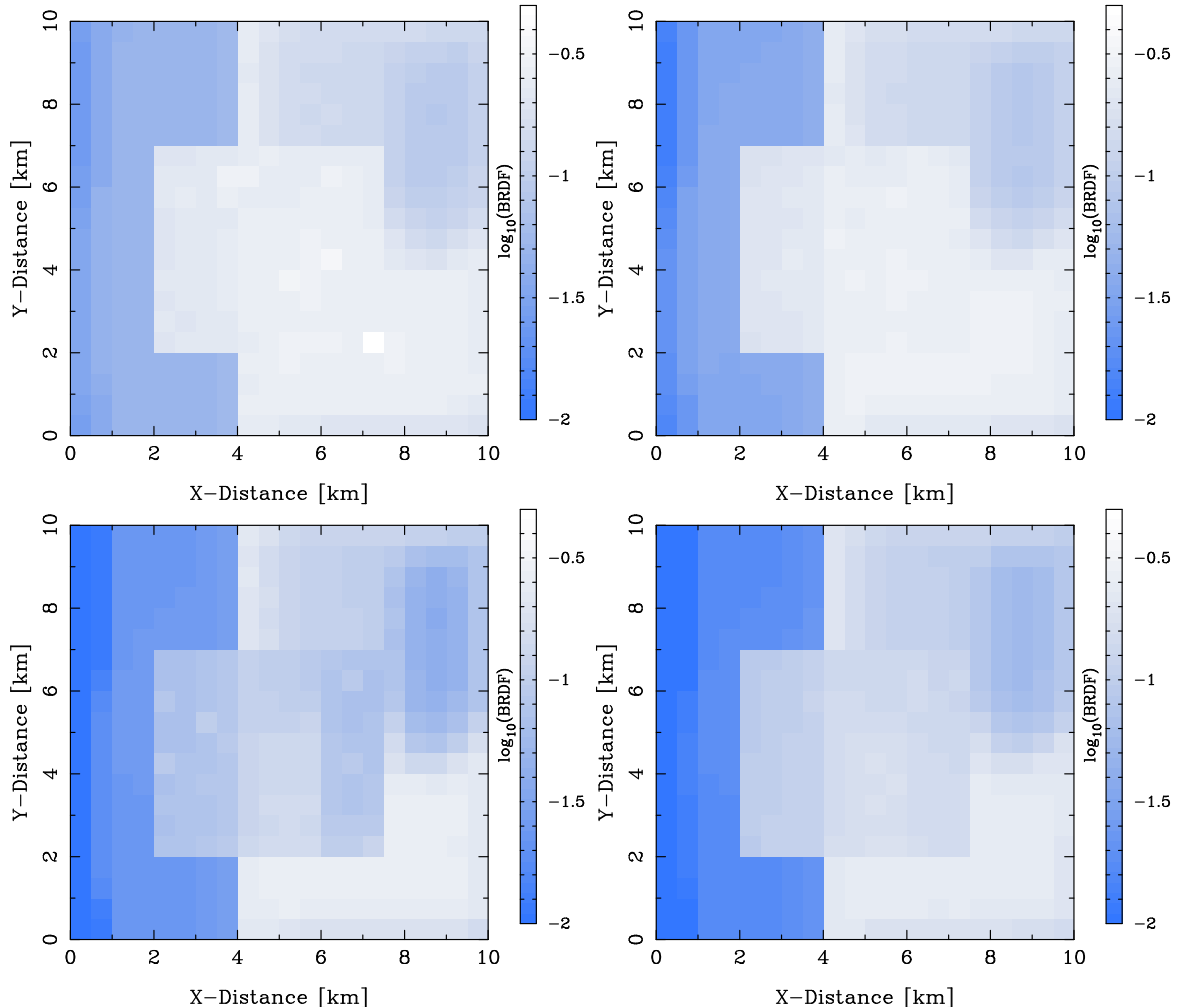


Figure 38: Short Wave MSI BRDFs. Top left Band 1 (660 nm), Top right, Band 2 (865 nm), Bottom left, Band 3 (1.61 microns) , Bottom right (2.2 microns).

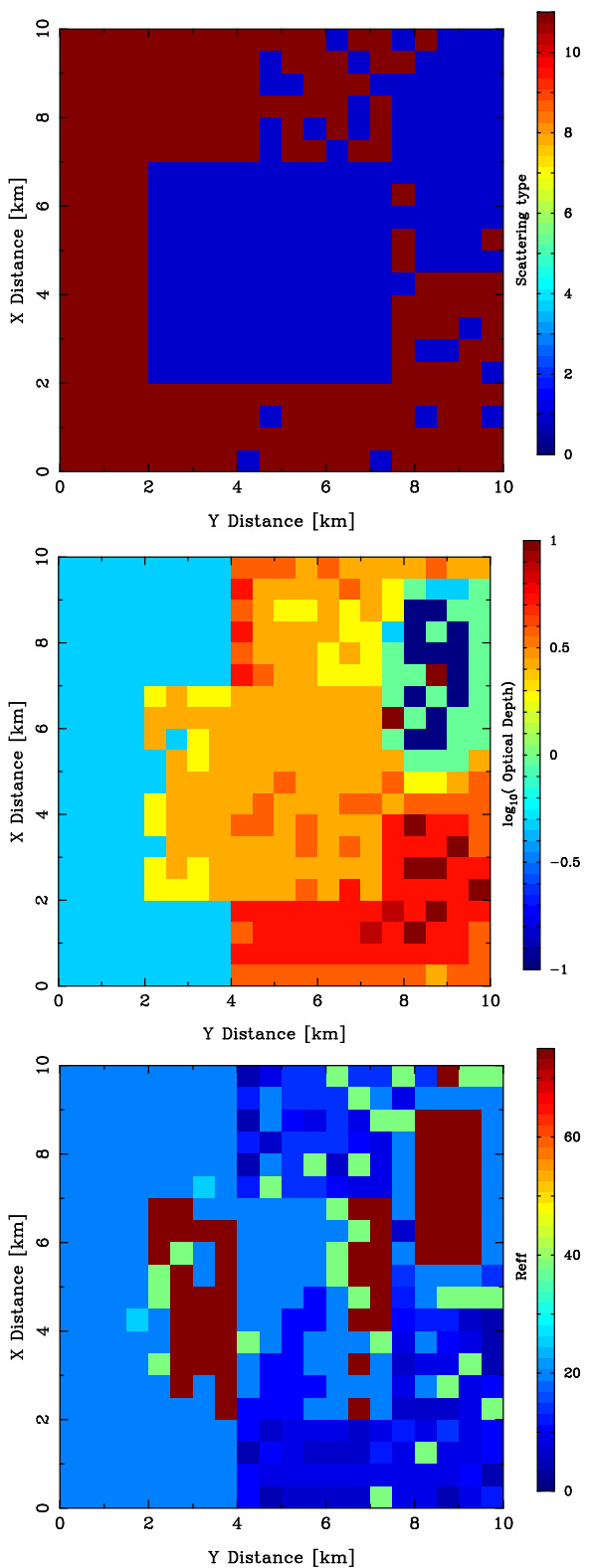


Figure 39: Results of Short Wave MSI retrievals. (Top) Target classification, 11 denotes water, while blue denotes ice. (Middle) Optical depth. (Bottom) Cloud particle effective radius.

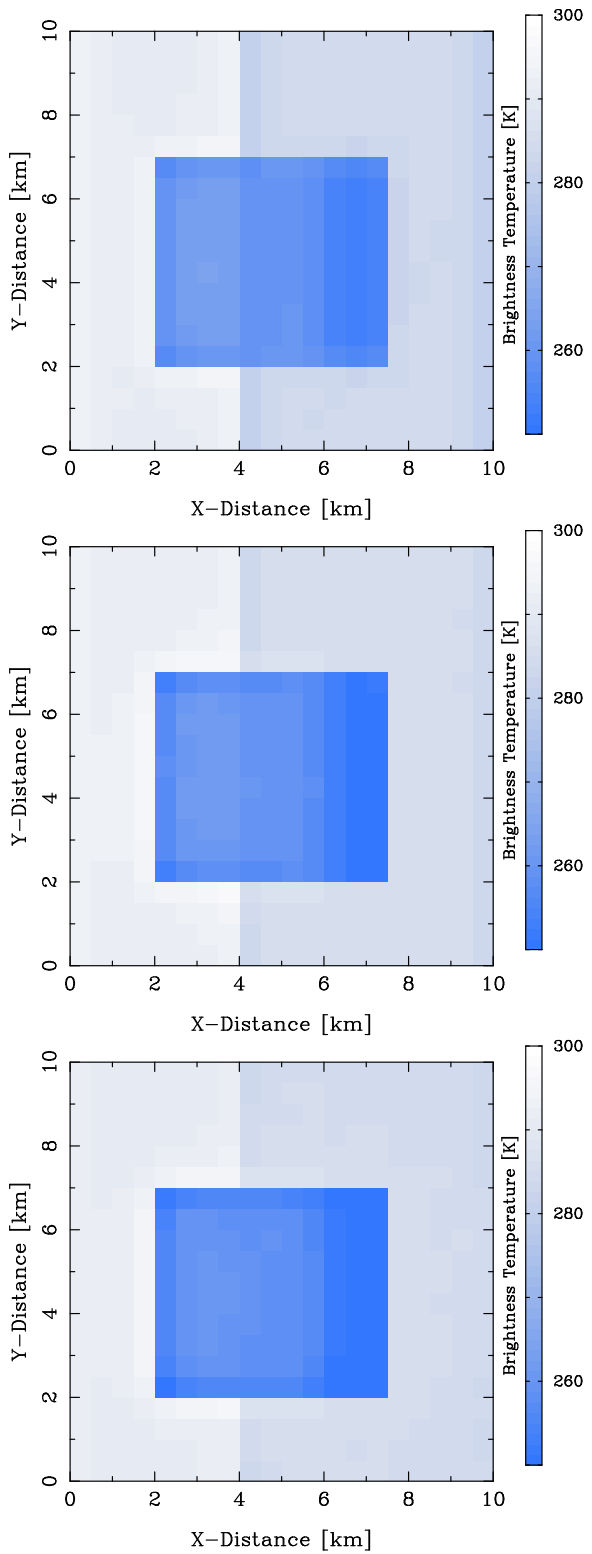


Figure 40: Long Wave MSI brightness temperatures. (Top) Channel 5 (8.85 microns), (Middle) Channel 6 (10.85 microns) and (Bottom) Channel 7 (11.85 microns).

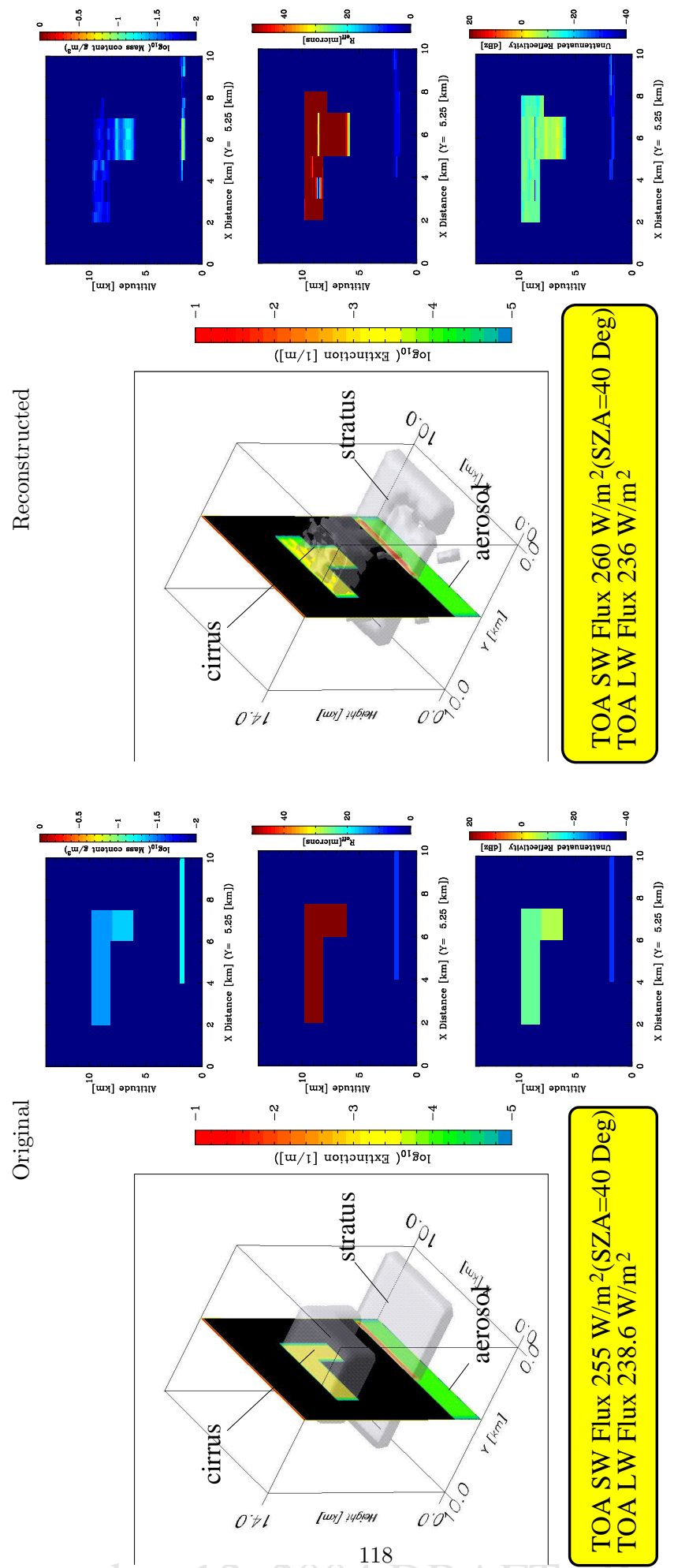


Figure 4: Three dimensional view of the original and reconstructed scenes. The panels shows cross sections of water content, effective radius, and reflectivity respectively.

A comparison between the true and the reconstructed scenes is shown in Fig. 4.1. The reconstructed scene was generated using `lw_msi_lidar_radar` and `scene_creator`. Long and short wave top-of-atmospher (TOA) fluxes were computed using both the orginal scene and the reconstructed scenes using `MC_sim_main` and `MC_LW_sim_main`. In this instance the difference between the ‘true’ and reconstructed TOA fluxes are within a few W/m².

4.2 Sample UQAM thin-cirrus results

In this section results from a scene comprised of a thin cirrus cloud are presented. The presentation follows the same general format as that of Section 4.1. See Appendix H for a description of the data the scene is based upon.

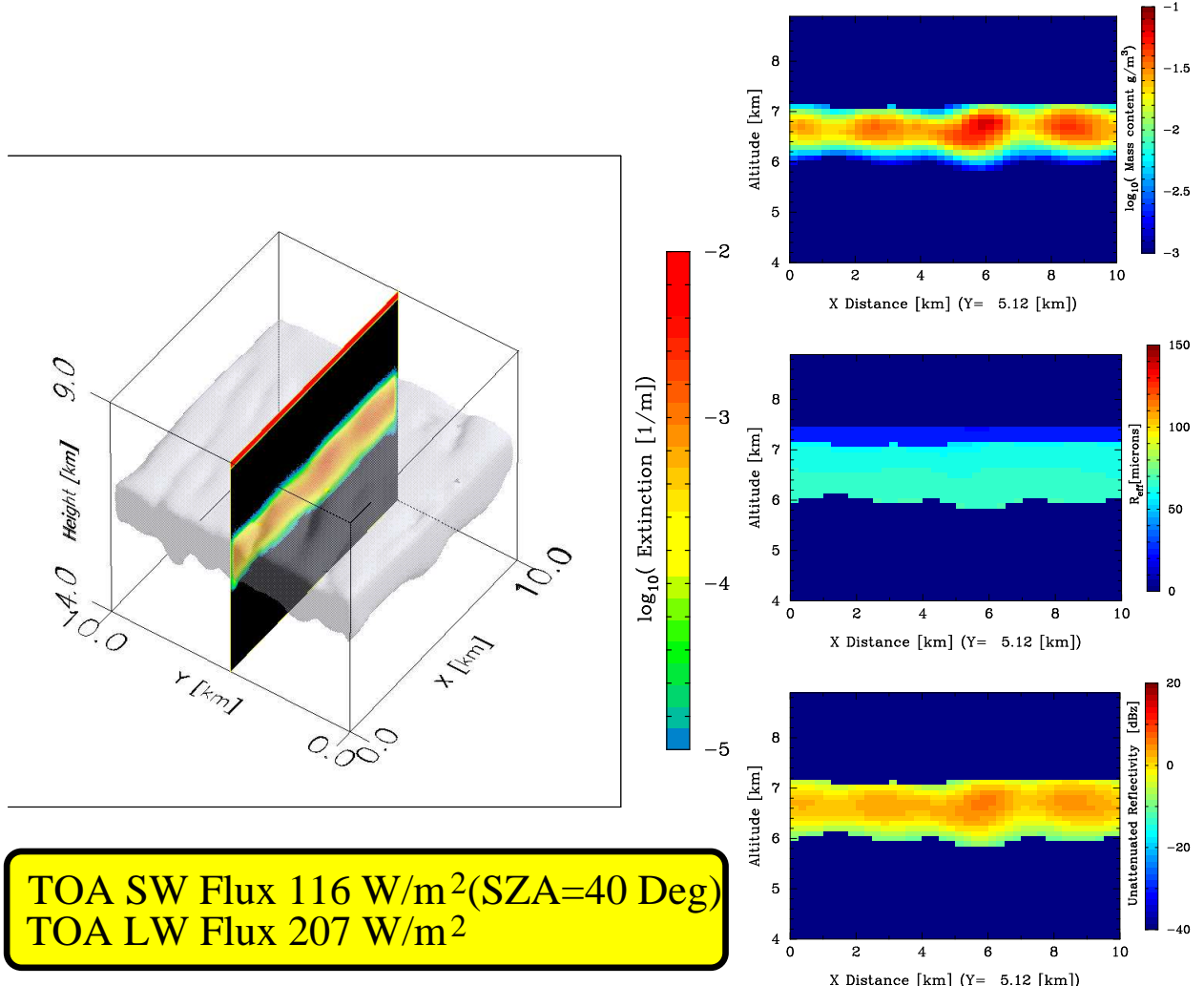


Figure 42: Three dimension view of the extinction field of the thin cirrus example. The right panels show cross section of water content, effective radius, and true reflectivity respectively.

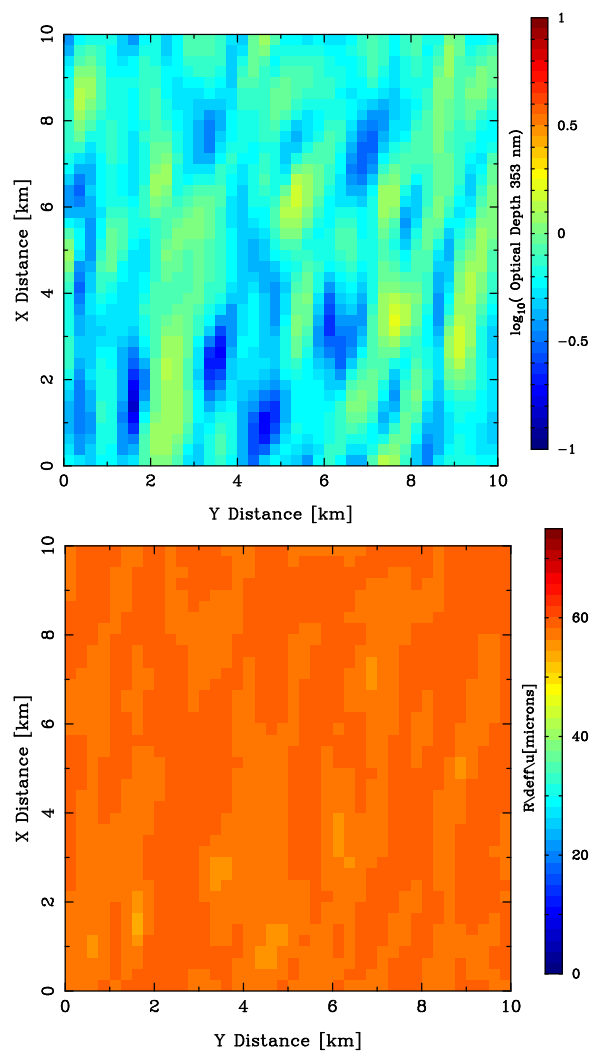


Figure 43: Optical depth and average effective radius for the scene depicted in Fig. 4.2

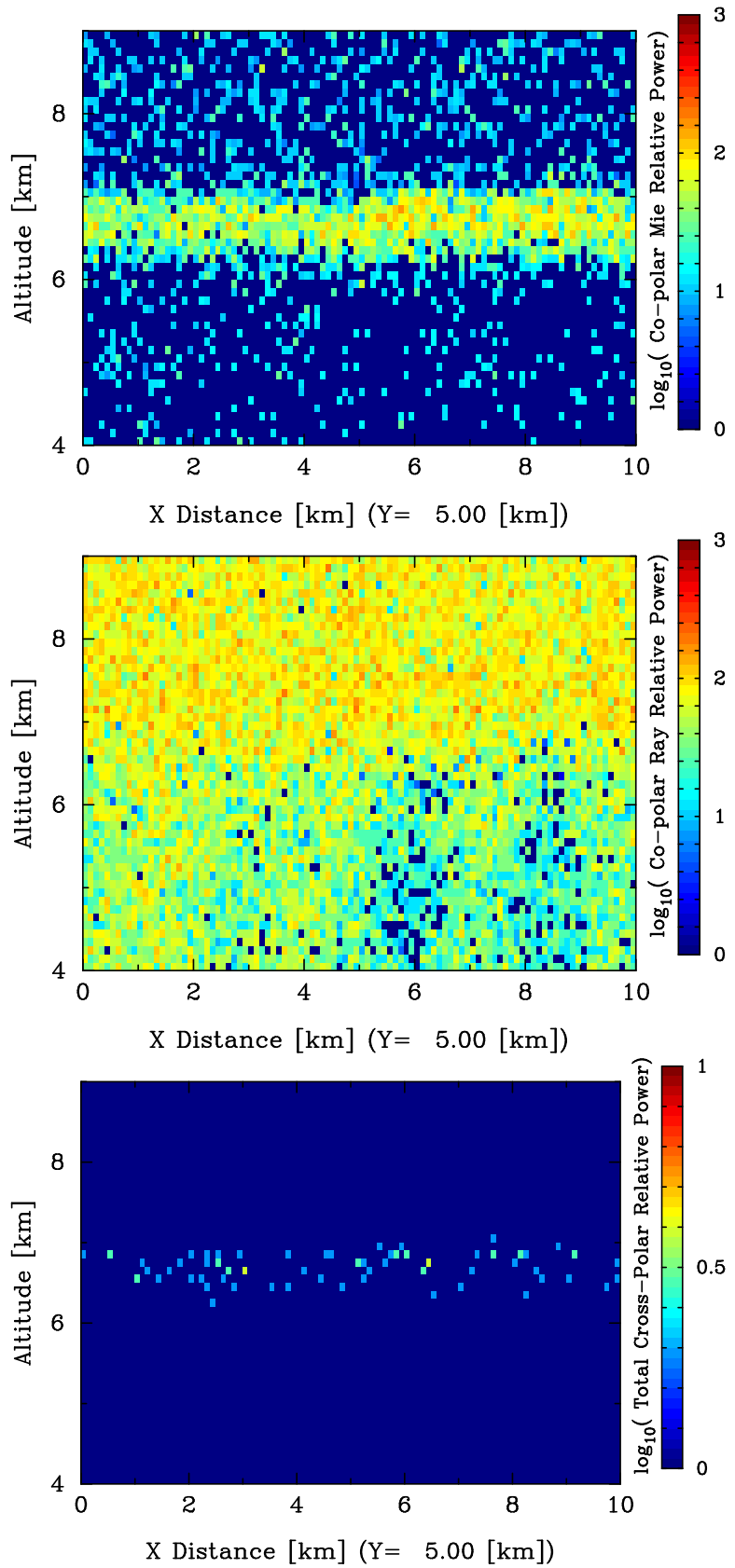


Figure 44: Lidar co-polar Mie signal (Top), Co-Polar Rayleigh signal (Middle), Lidar total cross-polar signal (Bottom) for the scene depicted in Fig. 4.2.

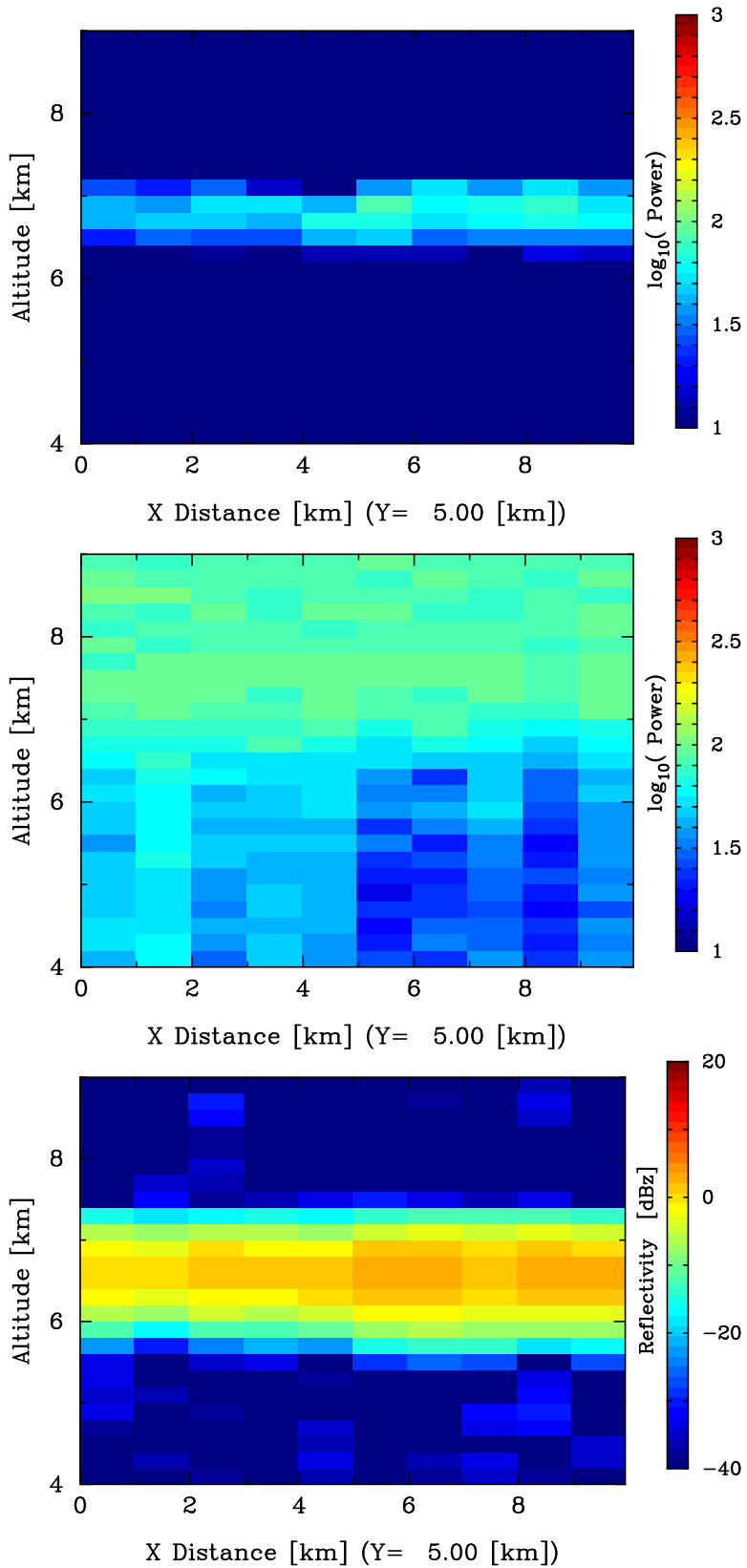


Figure 45: Mie signal, Rayleigh signal and radar reflectivity at 1km horizontal resolution.

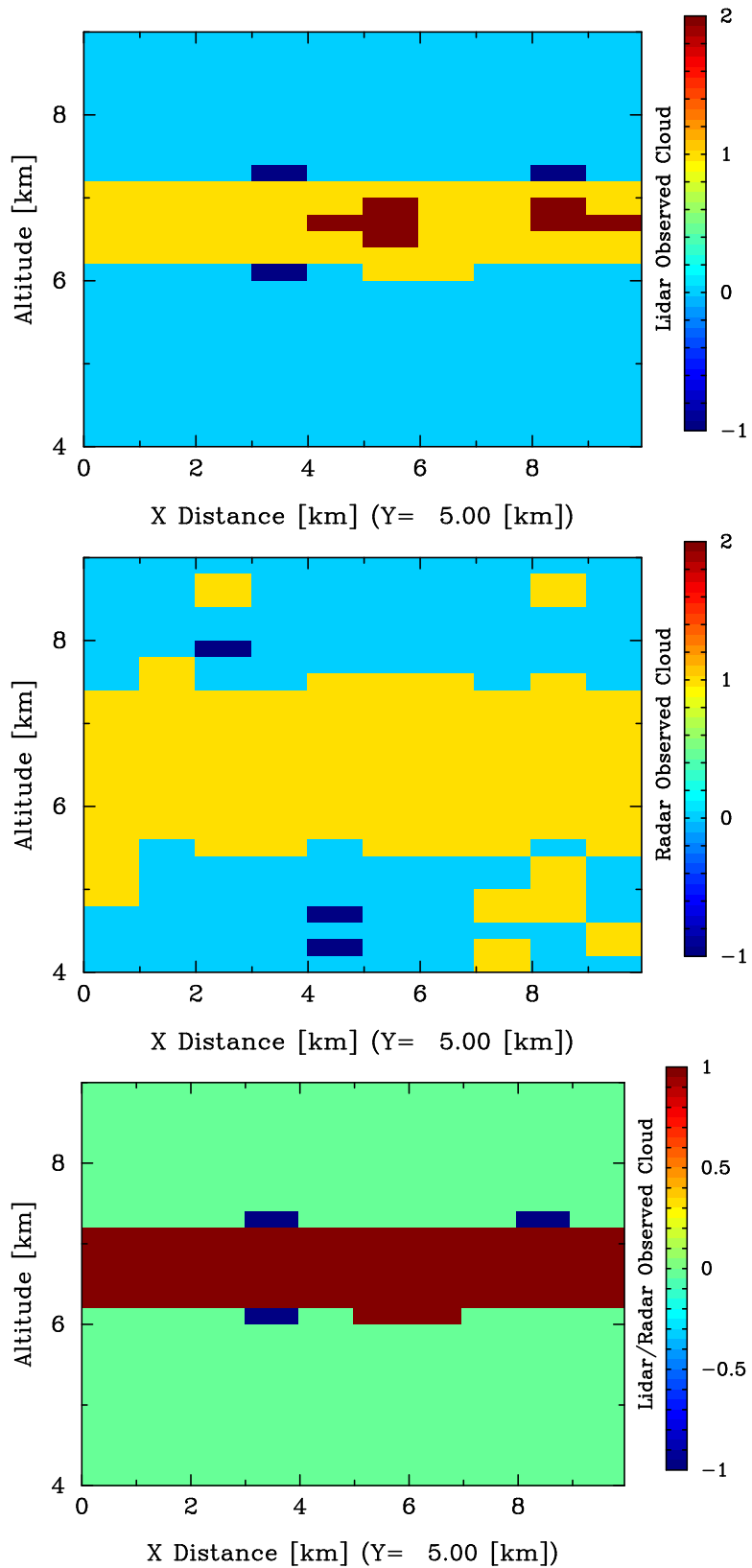


Figure 46: Lidar only (Top), Radar only (Middle) and combined cloud mask (Bottom)

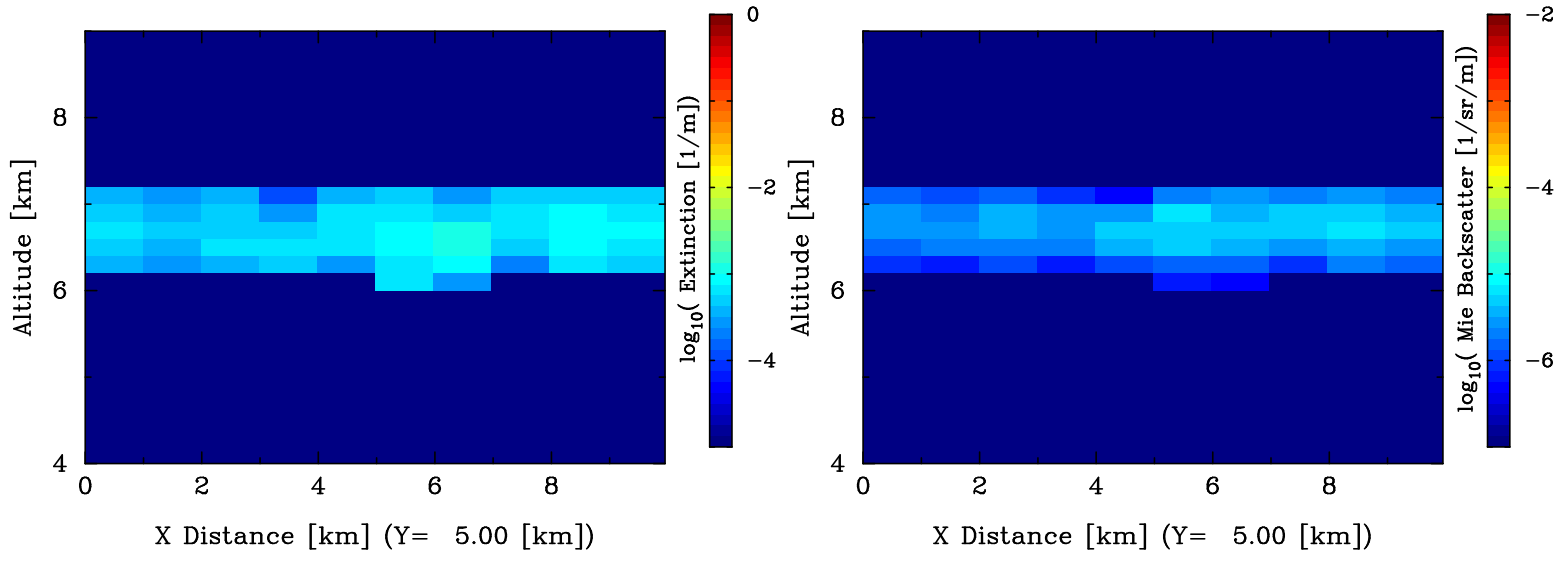


Figure 47: Retrieved lidar extinction and backscatters.

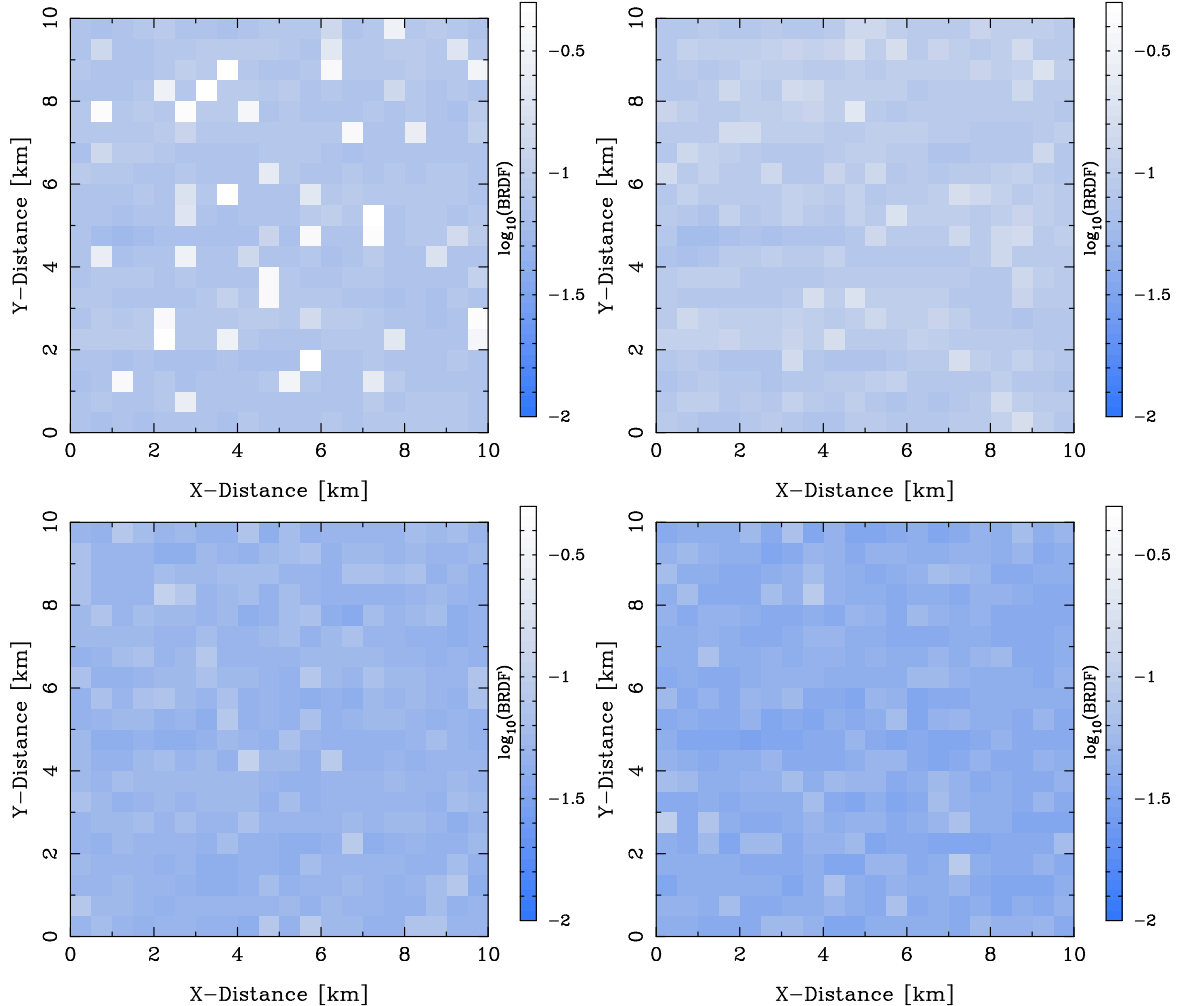


Figure 48: Short Wave MSI BRDFs. Top left Band 1 (660 nm), Top right, Band 2 (865 nm), Bottom left, Band 3 (1.61 microns) , Bottom right (2.2 microns)

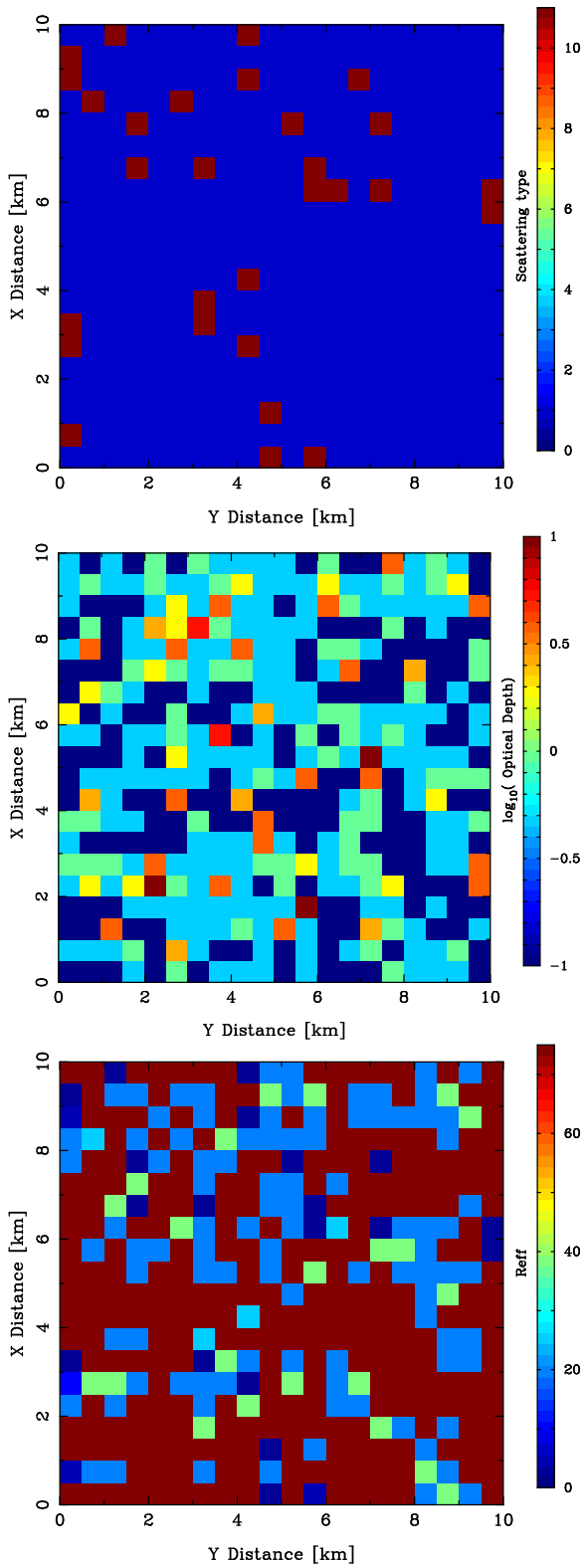


Figure 49: Results of Short Wave MSI retrievals

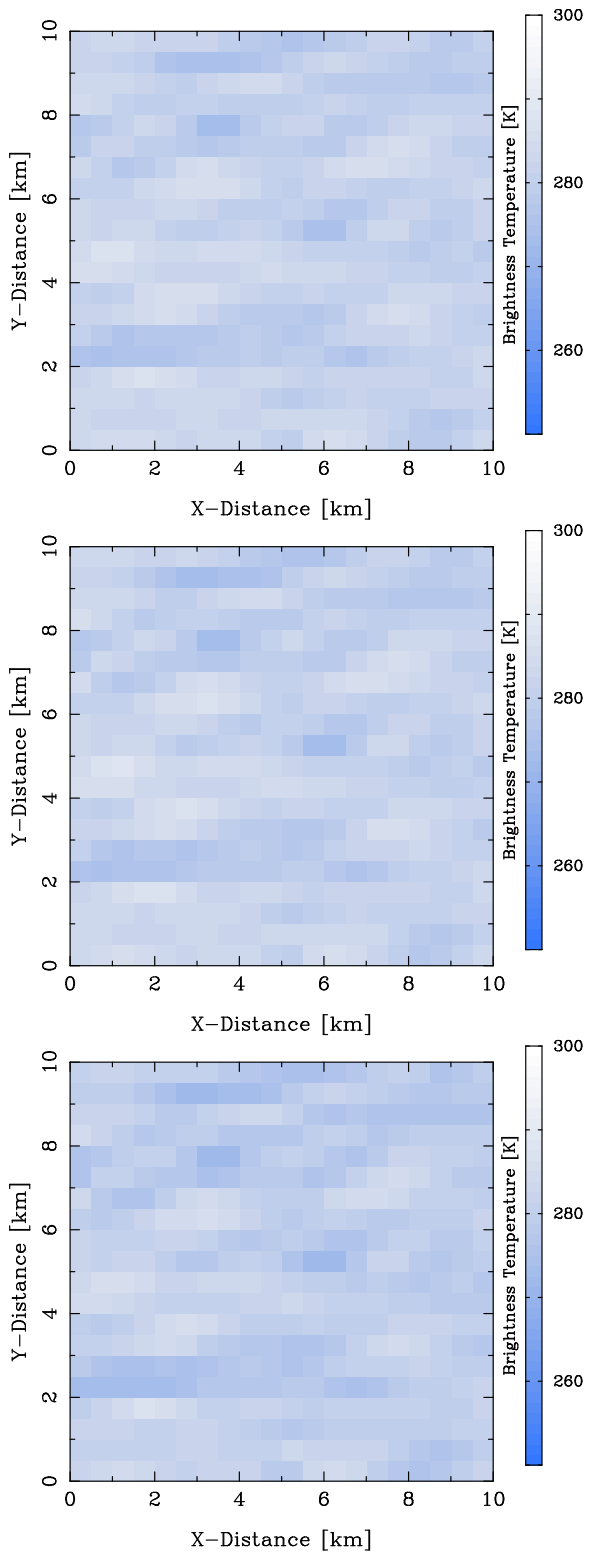
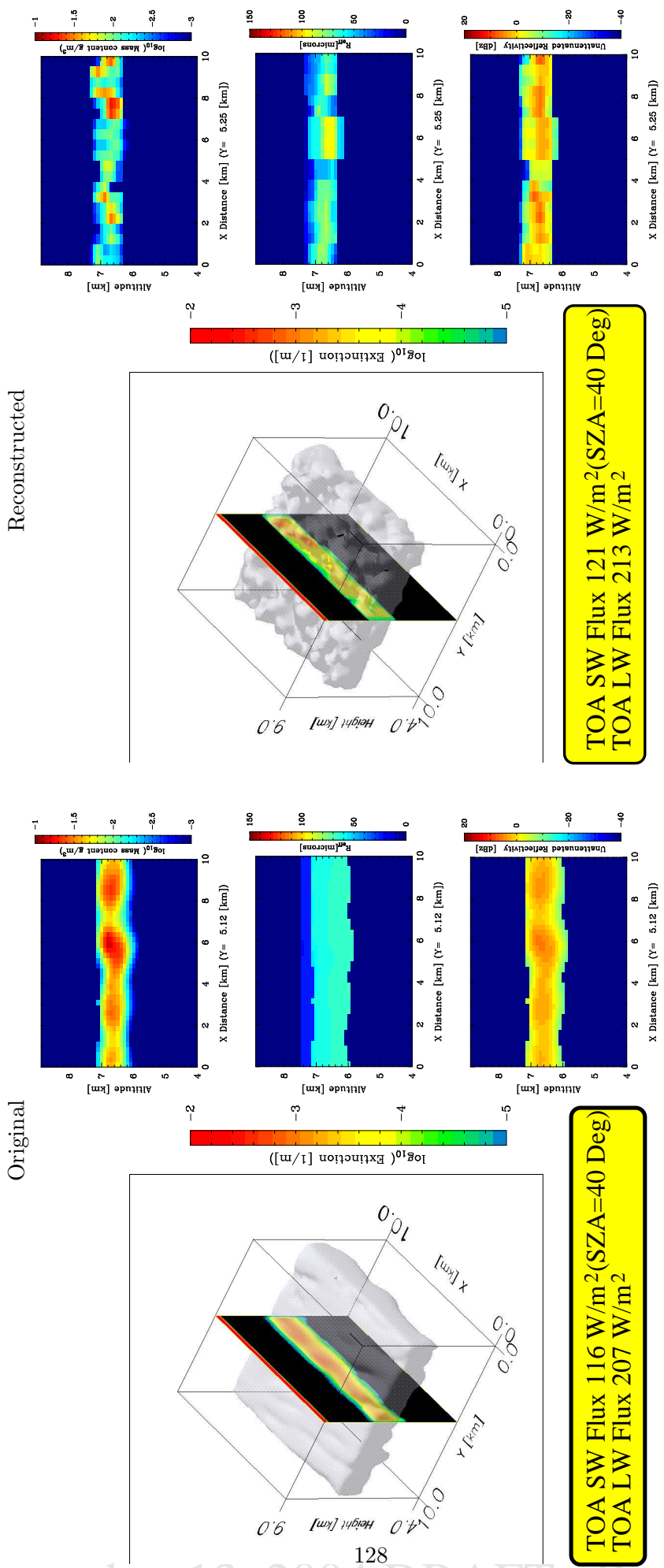


Figure 50: Long Wave MSI brightness temperatures. (Top) Channel 5 (8.85 microns), (Middle) Channel 6 (10.85 microns) and (Bottom) Channel 7 (11.85 microns).

TOA SW Flux 121 W/m²(SZA=40 Deg)

TOA LW Flux 213 W/m²

Figure 51: Three dimensional view of the original and reconstructed scenes. The panels show cross section of water content, effective radius, and reflectivity respectively.



4.3 Sample UQAM strato-cumulus results

In this section results from a scene comprised of a strato-cumulus field are presented. The presentation follows the same general format as that of Section 4.1. See Appendix H for a description of the data the scene is based upon.

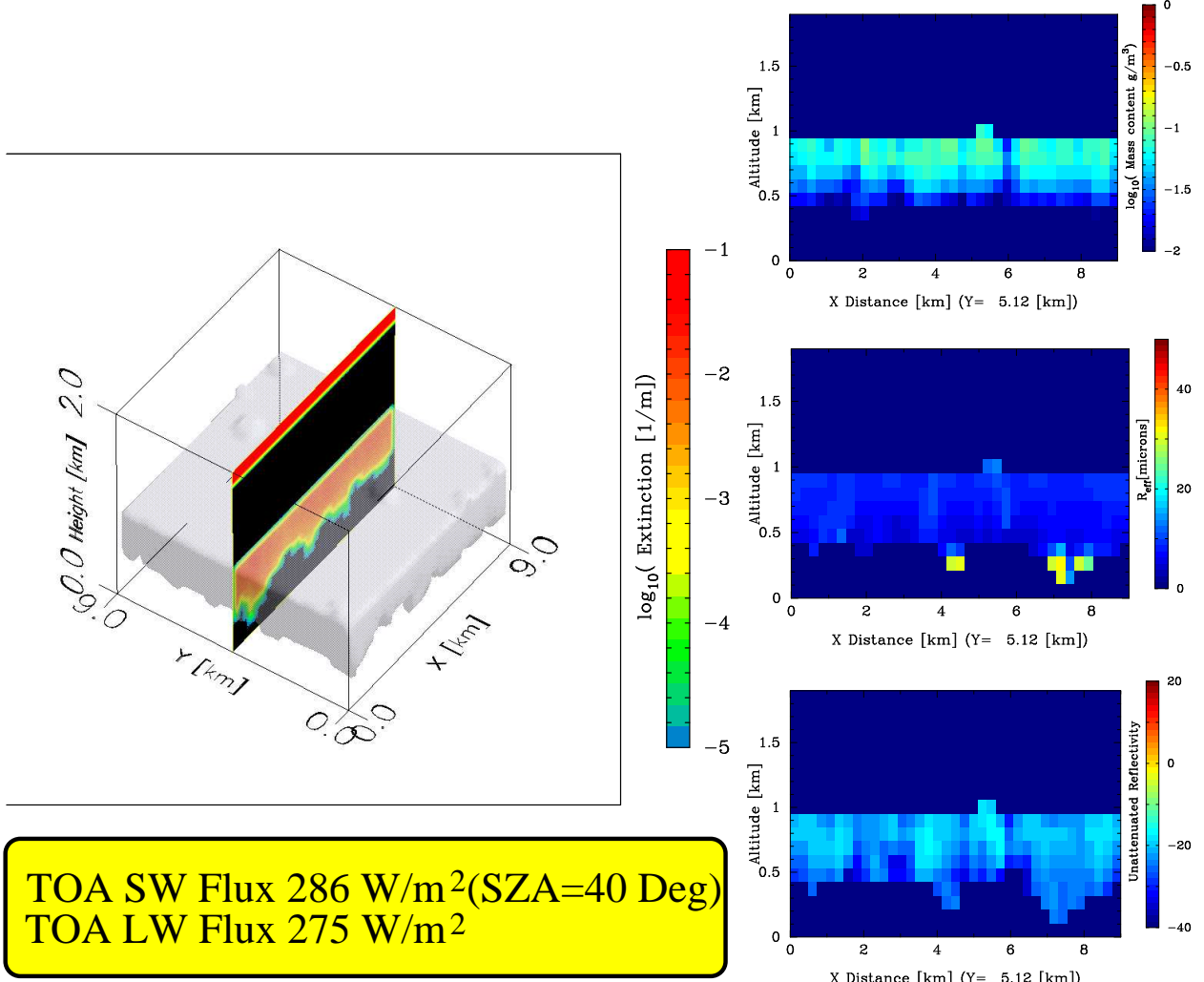


Figure 52: Three dimension view of the extinction field of the Stratocumulus example. The right panels show cross section of water content, effective radius, and true reflectivity respectively.

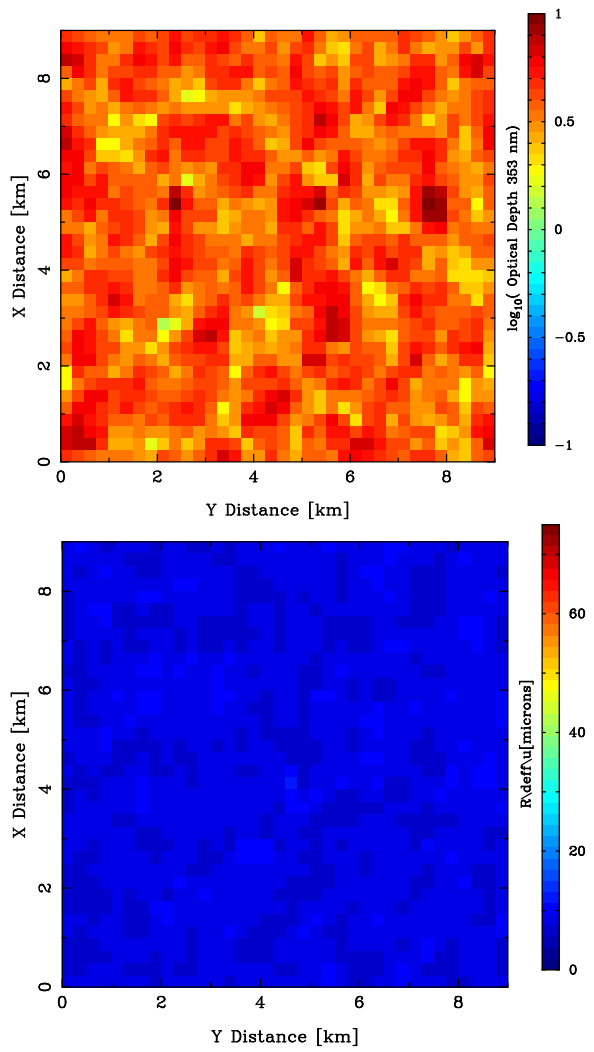


Figure 53: Optical depth and average effective radius for the scene depicted in 4.3.

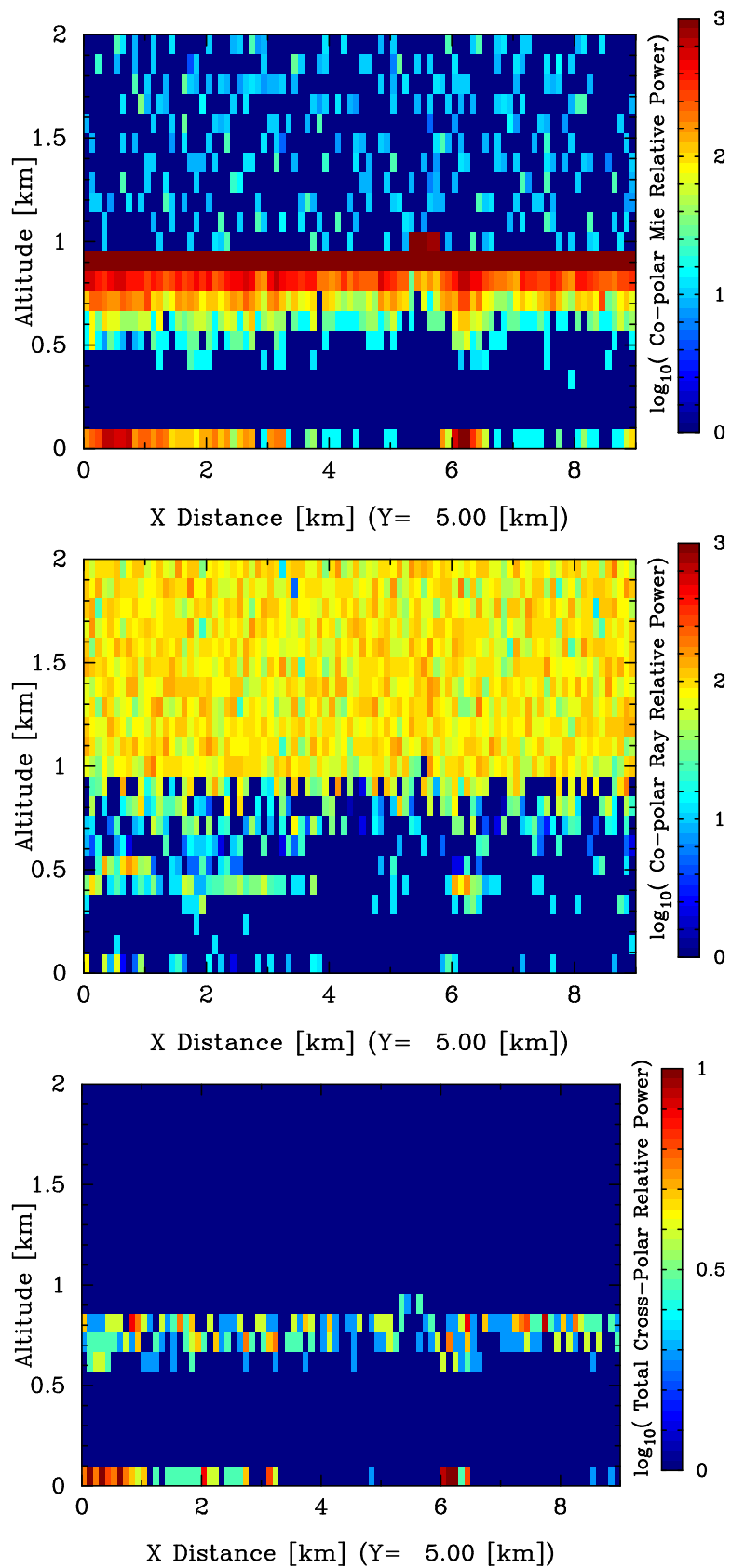


Figure 54: Lidar co-polar Mie signal (Top), Co-Polar Rayleigh signal (Middle), Lidar total cross-polar signal (Bottom) for the scene depicted in Fig. 4.3.

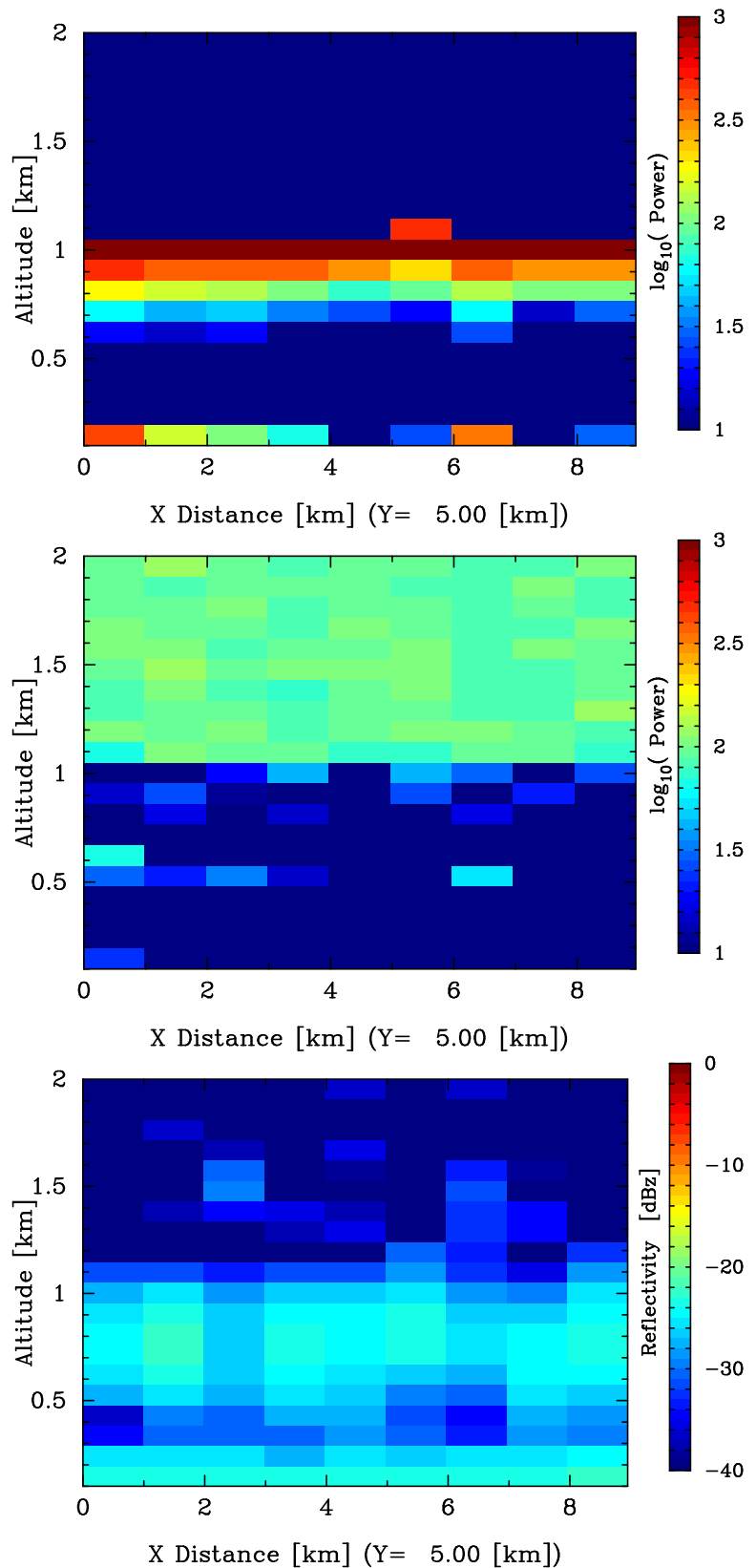


Figure 55: Mie signal, Rayleigh signal and radar reflectivity at 1km horizontal resolution.

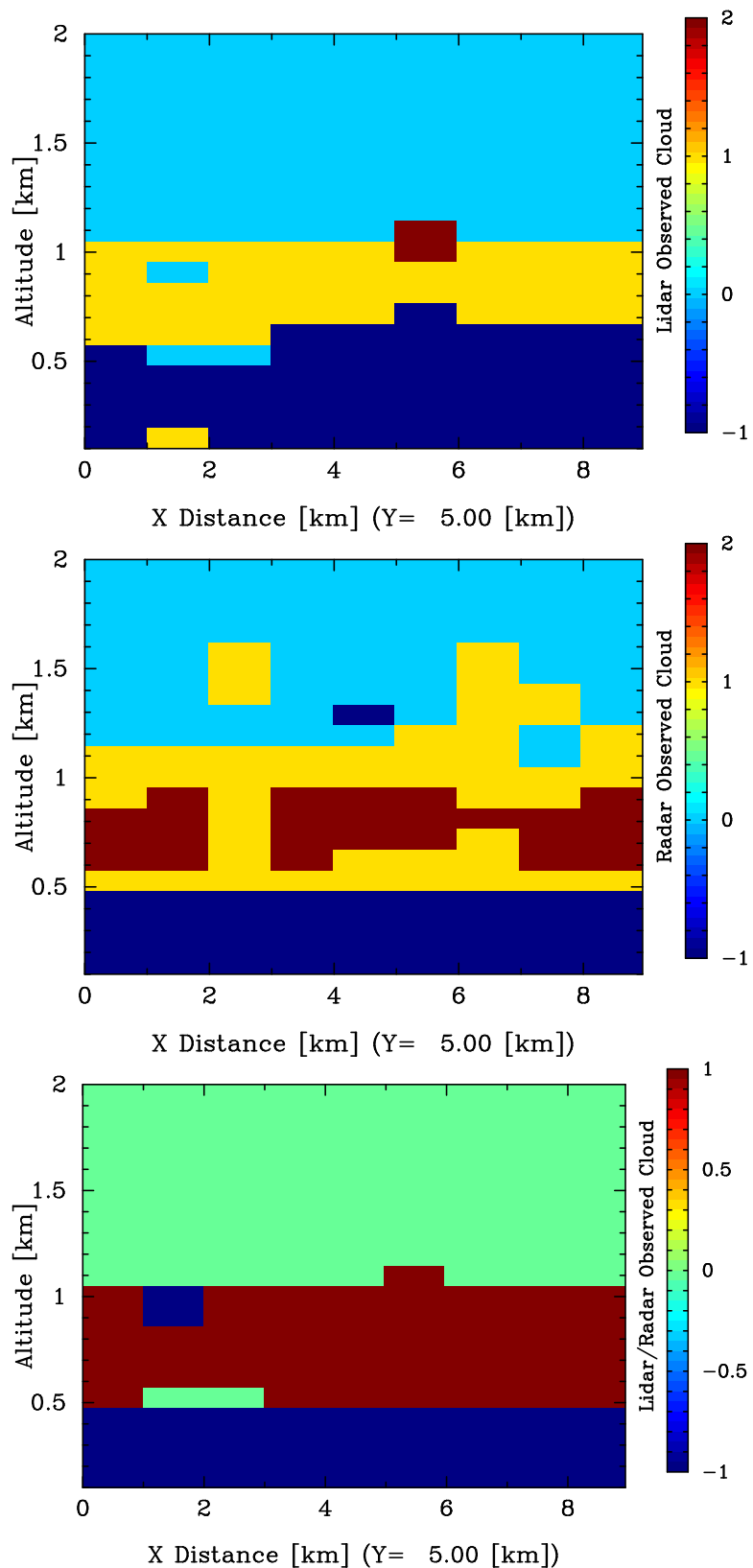


Figure 56: Lidar only (Top), Radar only (Middle) and combined cloud mask (Bottom)

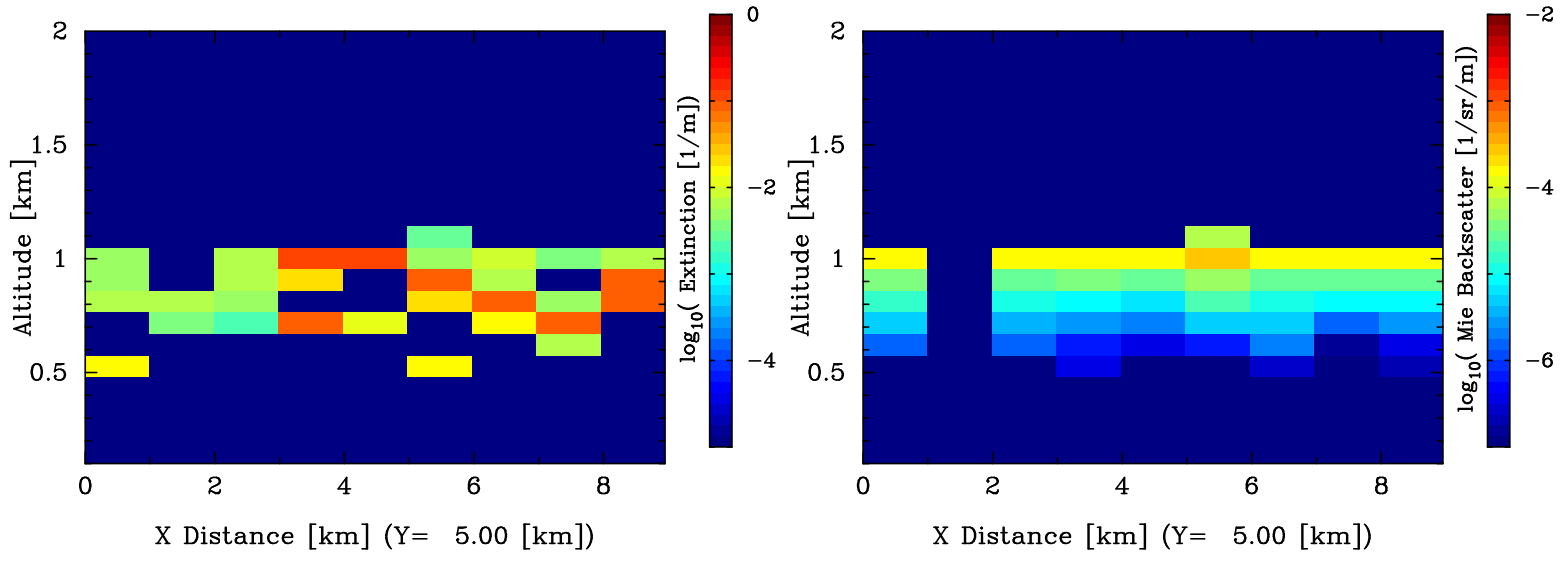


Figure 57: Retrieved lidar extinction and backscatters.

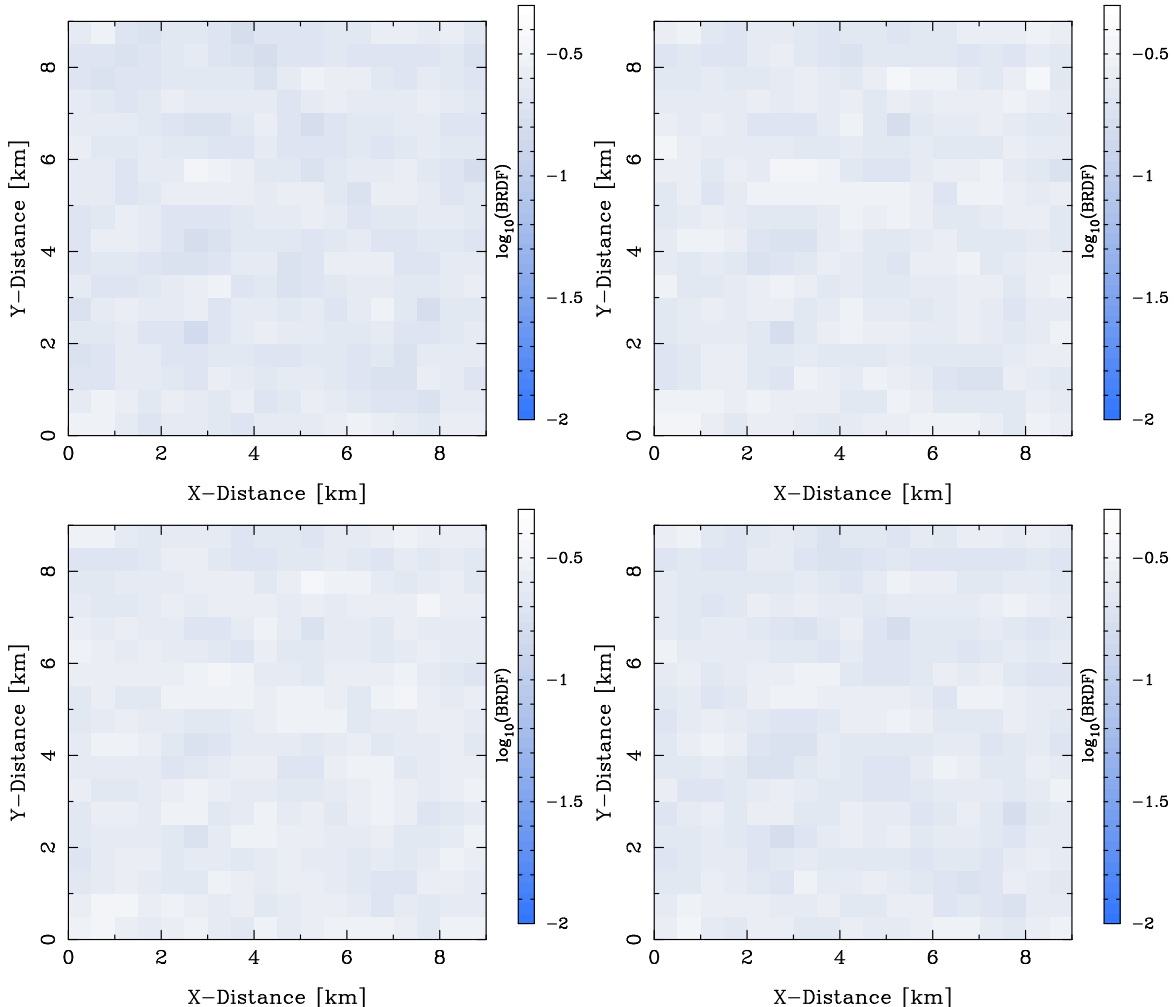


Figure 58: Short Wave MSI BRDFs. Top left Band 1 (660 nm), Top right, Band 2 (865 nm), Bottom left, Band 3 (1.61 microns) , Bottom right (2.2 microns).

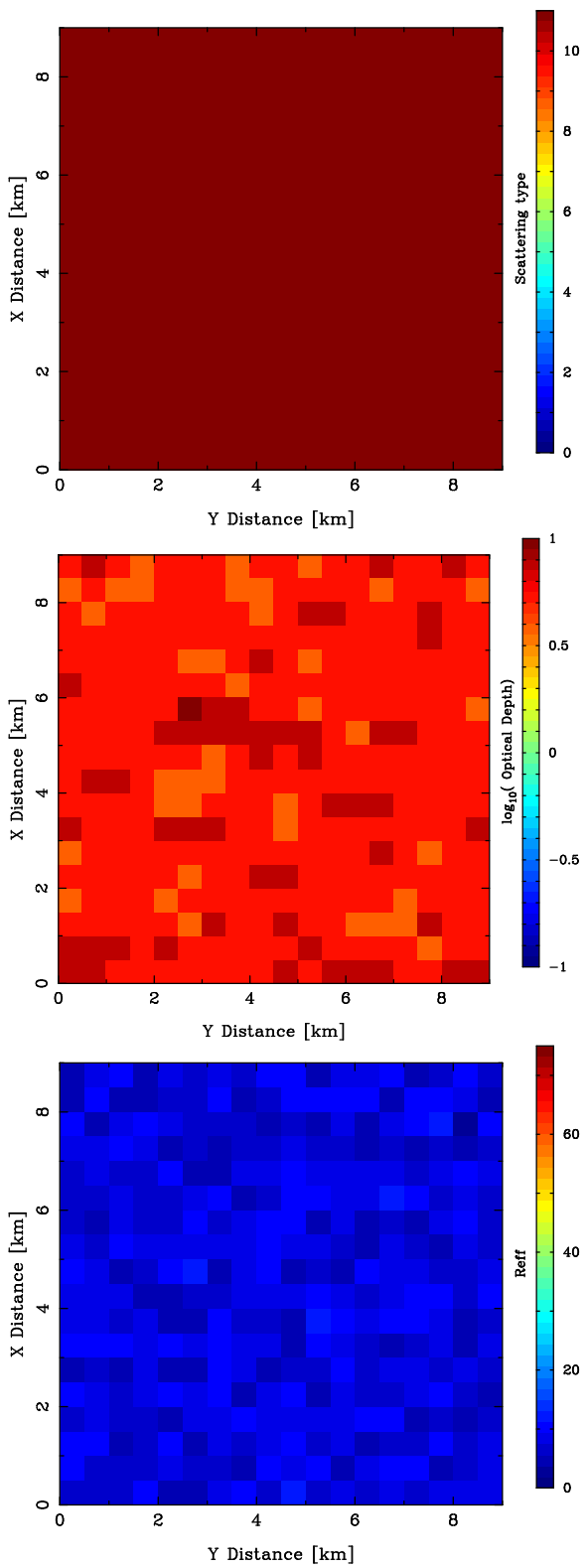


Figure 59: Results of Short Wave MSI retrievals

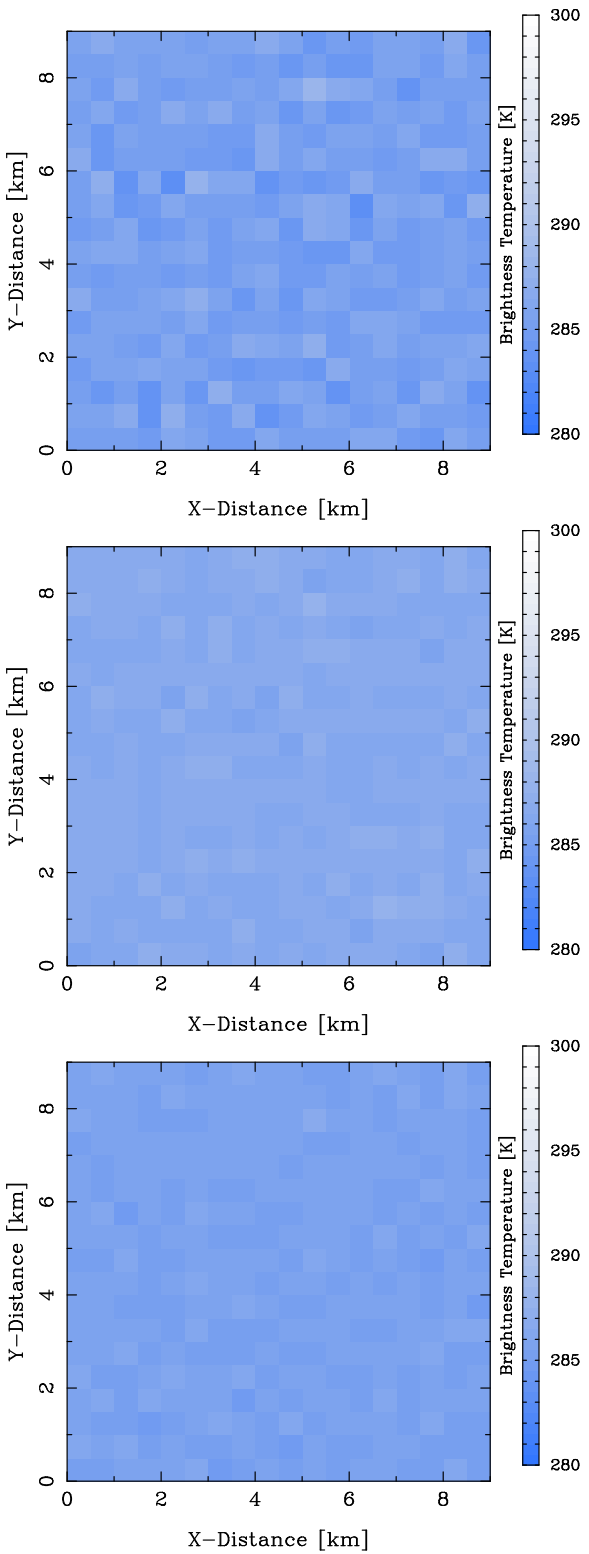


Figure 60: Long Wave MSI brightness temperatures. (Top) Channel 5 (8.85 microns), (Middle) Channel 6 (10.85 microns) and (Bottom) Channel 7 (11.85 microns).

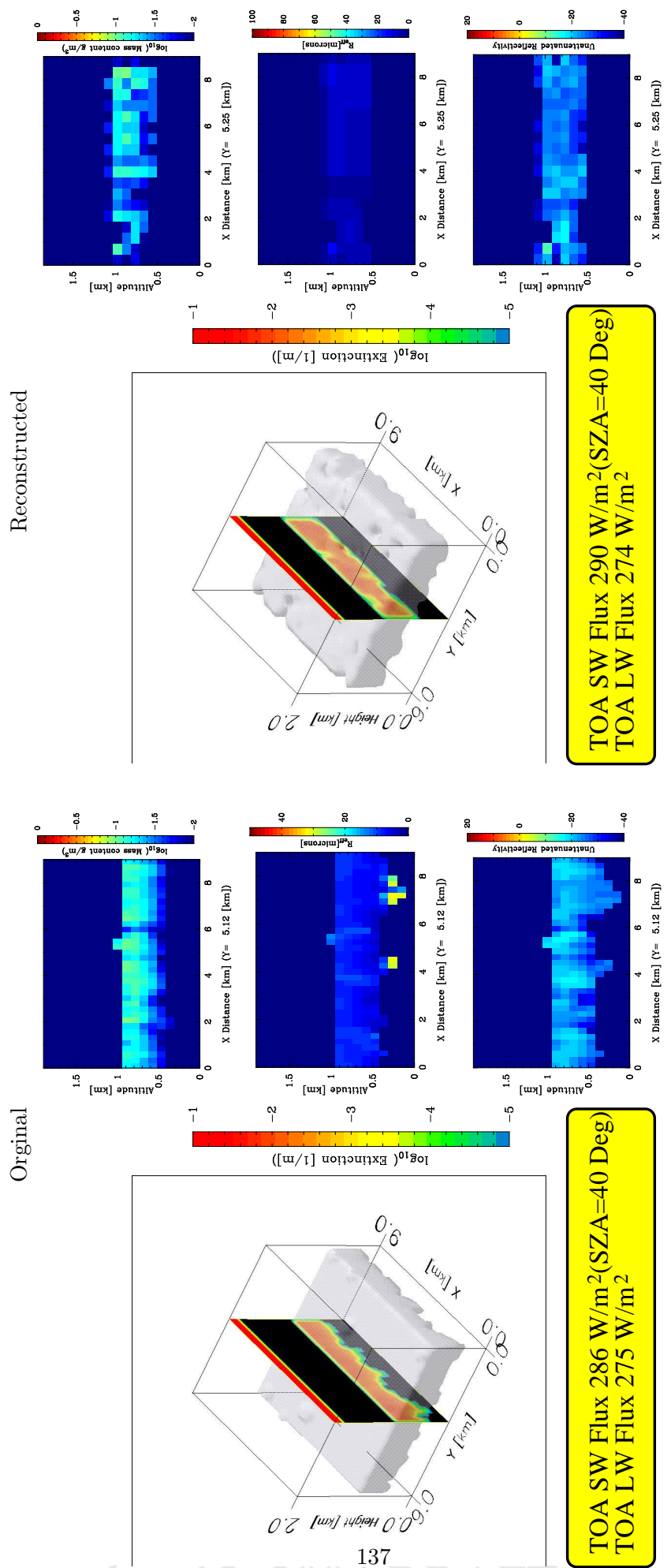


Figure 61: Three dimensional view of the original and reconstructed scenes. The panels show cross section of water content, effective radius, and reflectivity respectively.

4.4 Sample UQAM Frontal system results

In this section results from a scene comprised of complex thick frontal cloud system are presented. The presentation follows the same general format as that of Section 4.1. See Appendix H for a description of the data the scene is based upon. This is a particularly challenging scene to retrieve properly. In particular, a more advanced use of a-priori information that is presently coded in `lw_msilidar_radar` is likely needed to reliably deal with such situations.

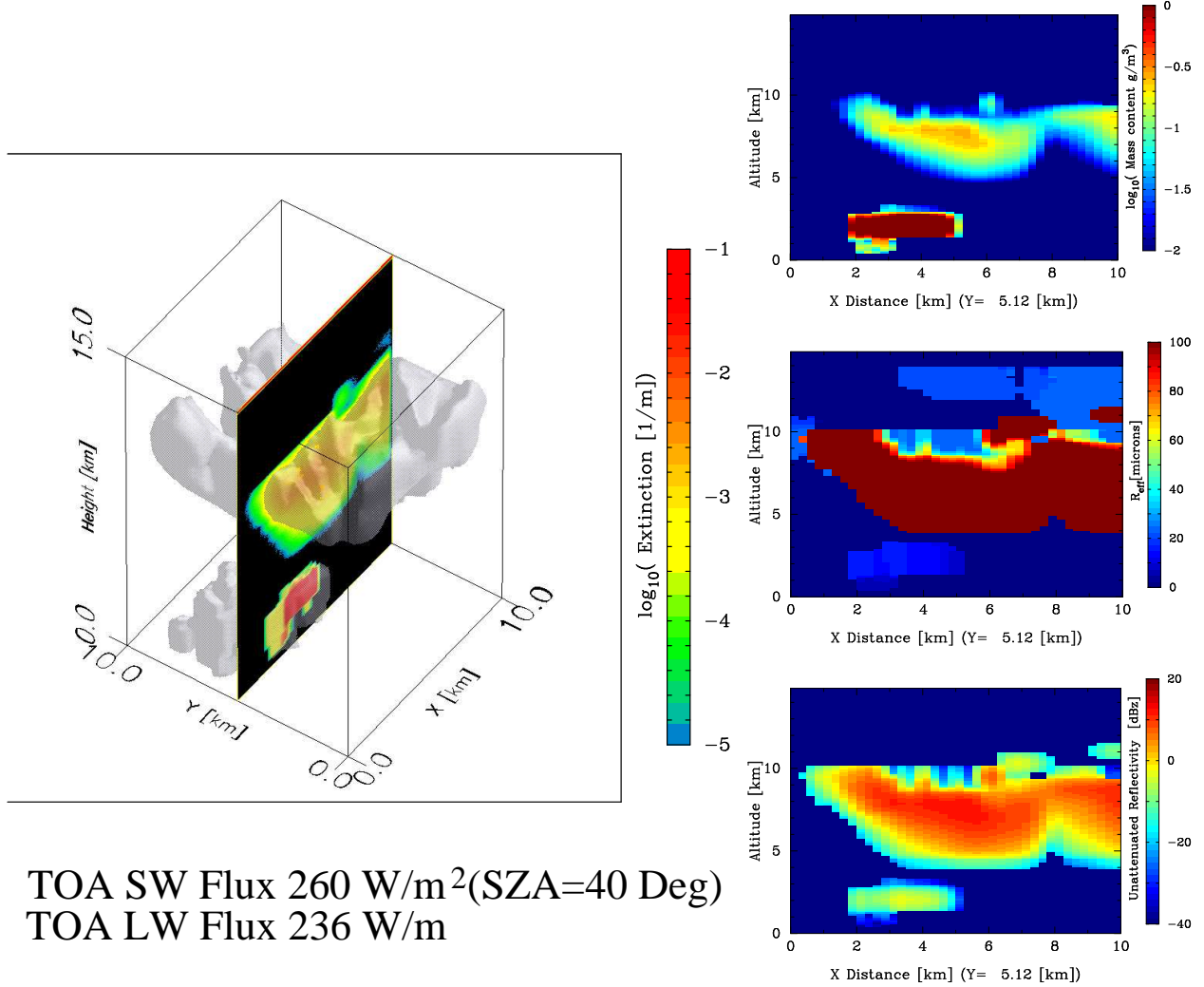


Figure 62: Three dimension view of the extinction field of the frontal system example. The right panels show cross section of water content, effective radius, and true reflectivity respectively.

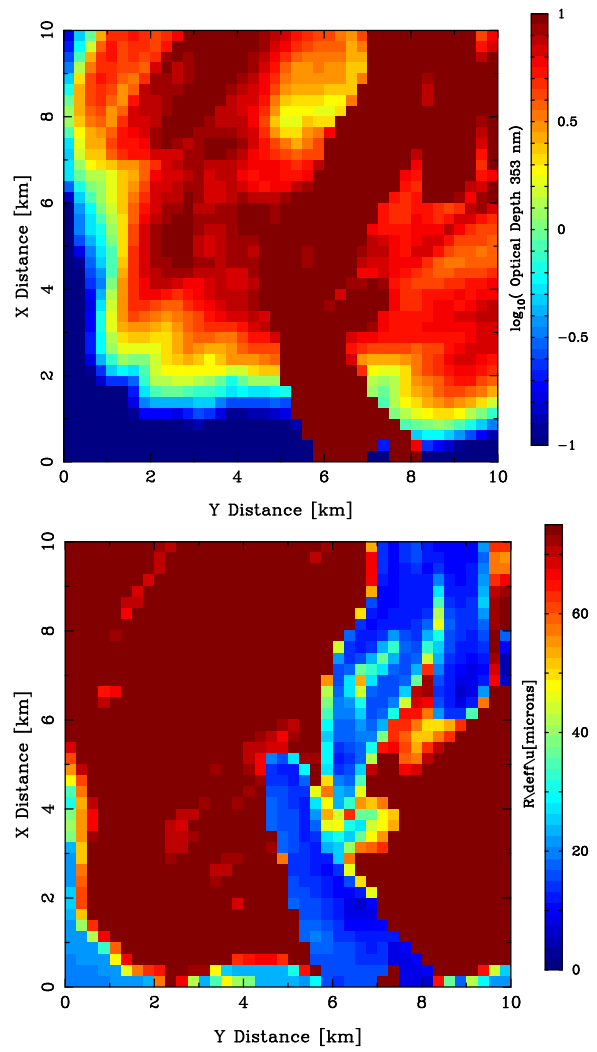


Figure 63: Optical depth and average effective radius for the scene depicted in Fig. 4.4

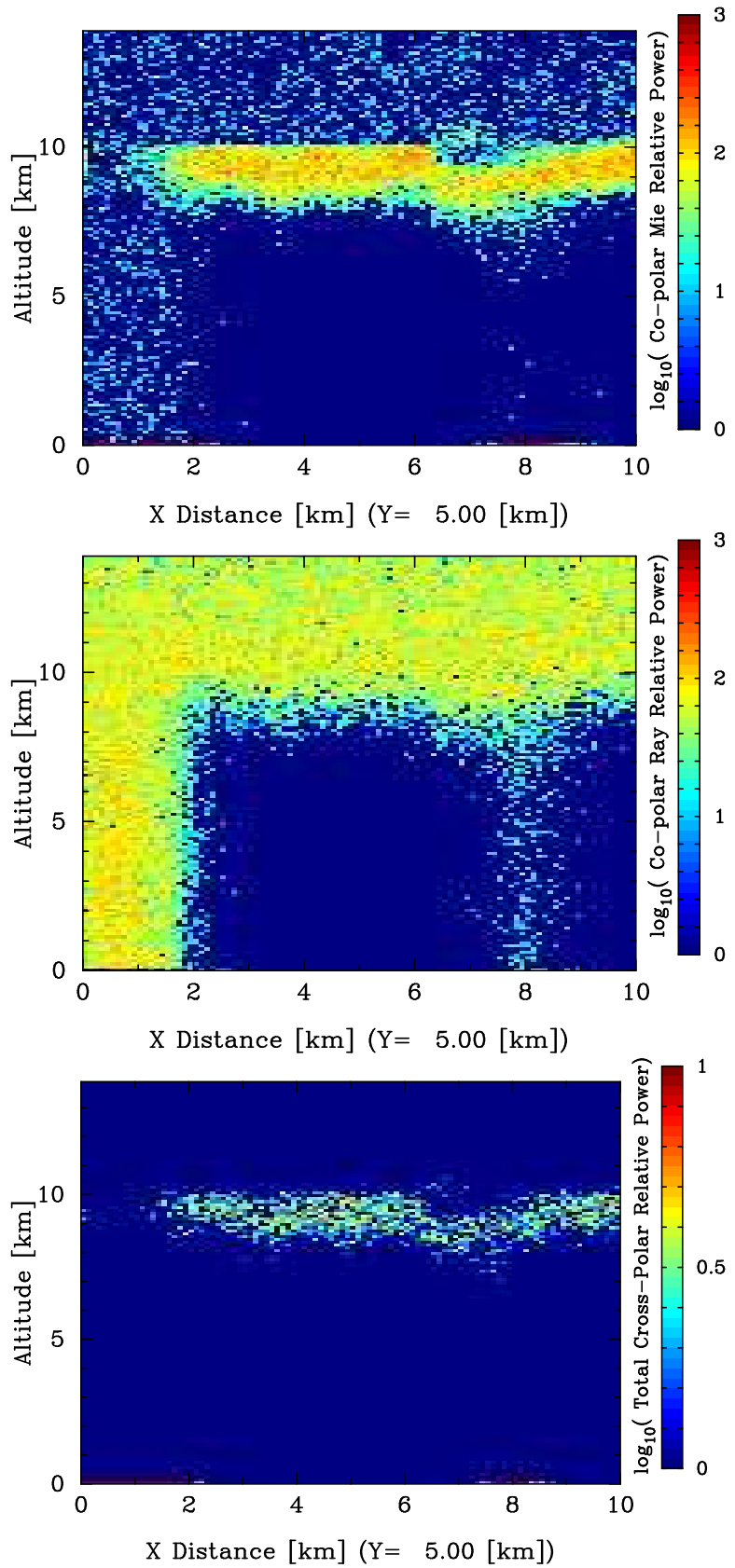


Figure 64: Lidar co-polar Mie signal (Top), Co-Polar Rayleigh signal (Middle), Lidar total cross-polar signal (Bottom) for the scene depicted in Fig. 4.4.

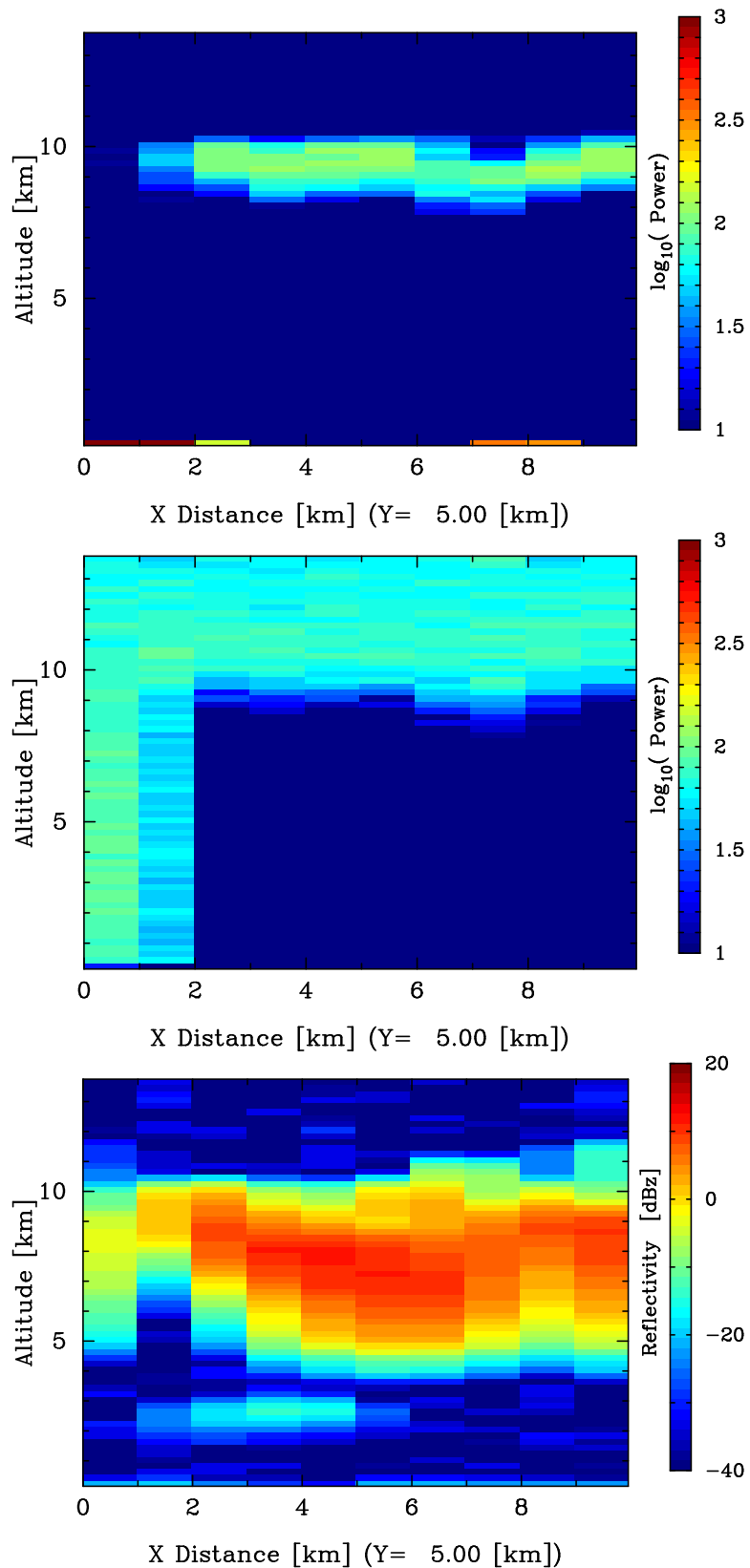


Figure 65: Mie signal, Rayleigh signal and radar reflectivity at 1km horizontal resolution.

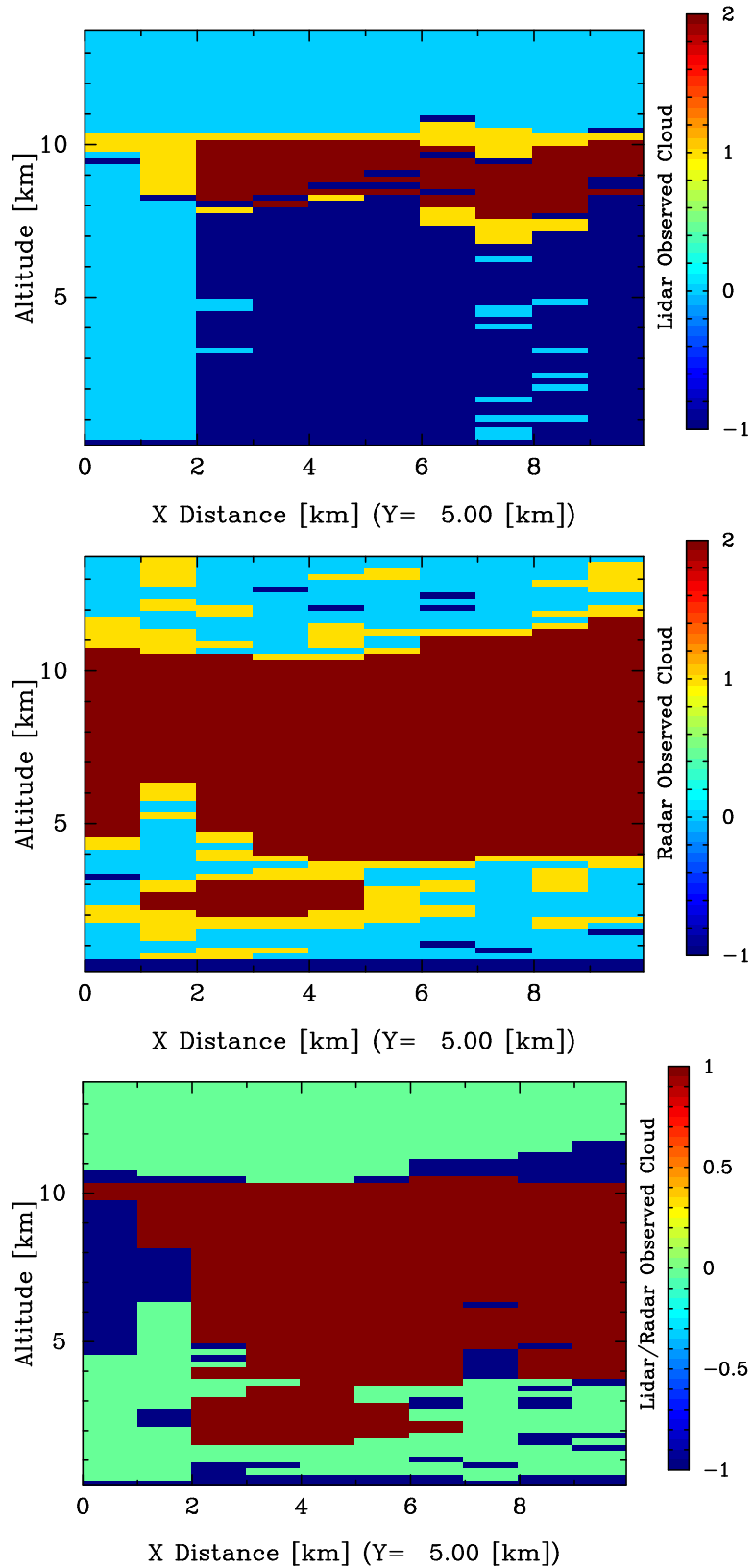


Figure 66: Lidar only (Top), Radar only (Middle) and combined cloud mask (Bottom)

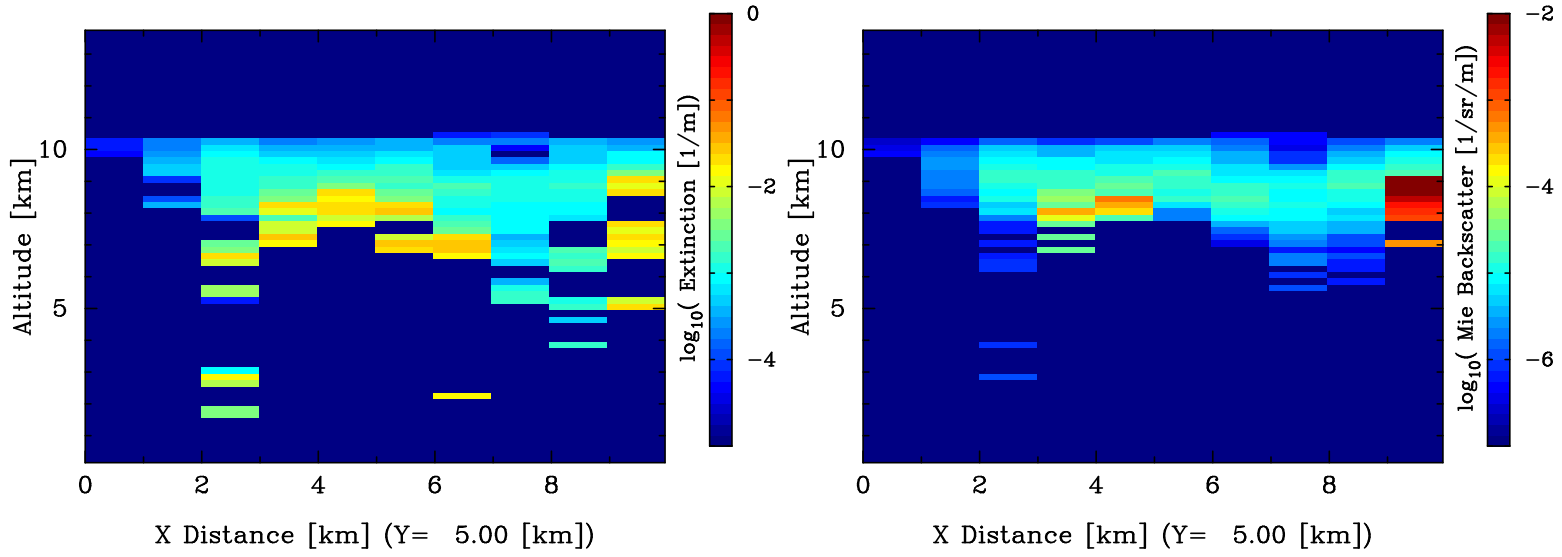


Figure 67: Retrieved lidar extinction and backscatters.

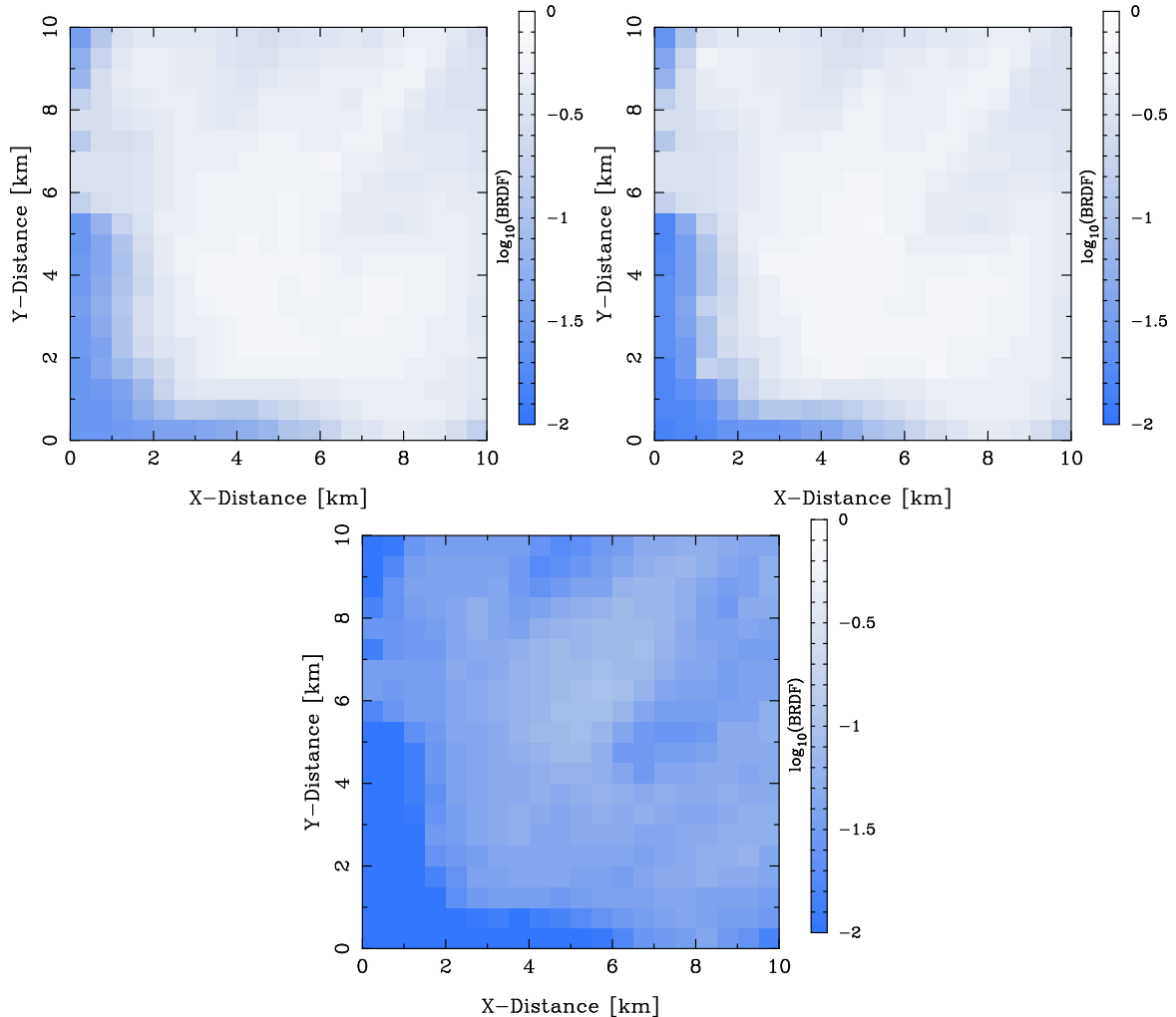


Figure 68: Short Wave MSI BRDFs. Top left Band 1 (660 nm), Top right, Band 2 (865 nm), Bottom left, Band 3 (1.61 microns) , Bottom right (2.2 microns).

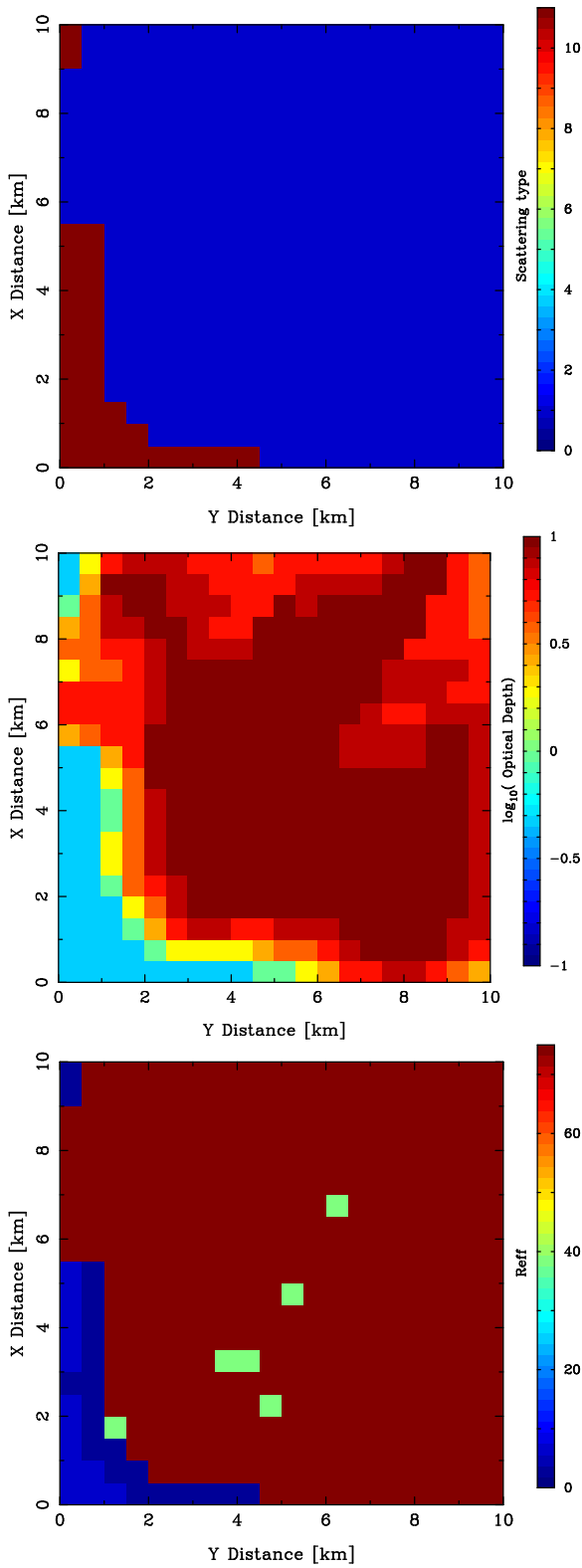


Figure 69: Results of Short Wave MSI retrievals

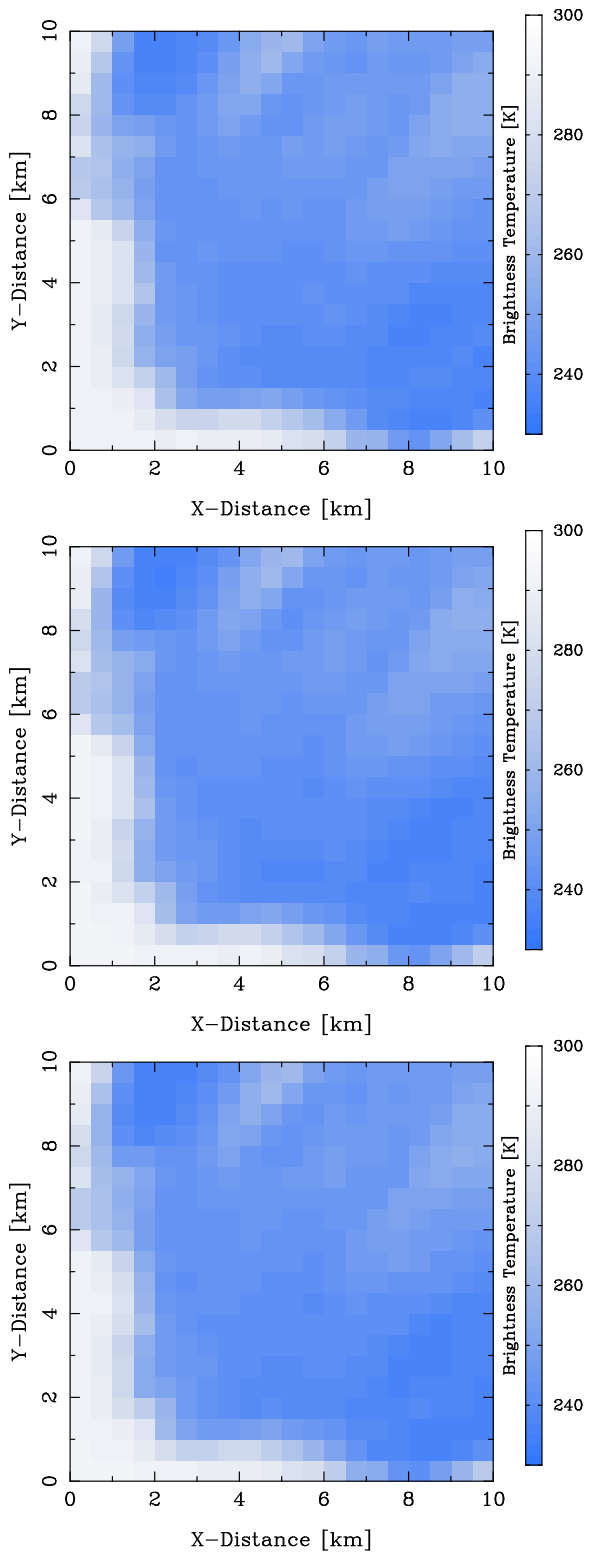


Figure 70: Long Wave MSI brightness temperatures. (Top) Channel 5 (8.85 microns), (Middle) Channel 6 (10.85 microns) and (Bottom) Channel 7 (11.85 microns).

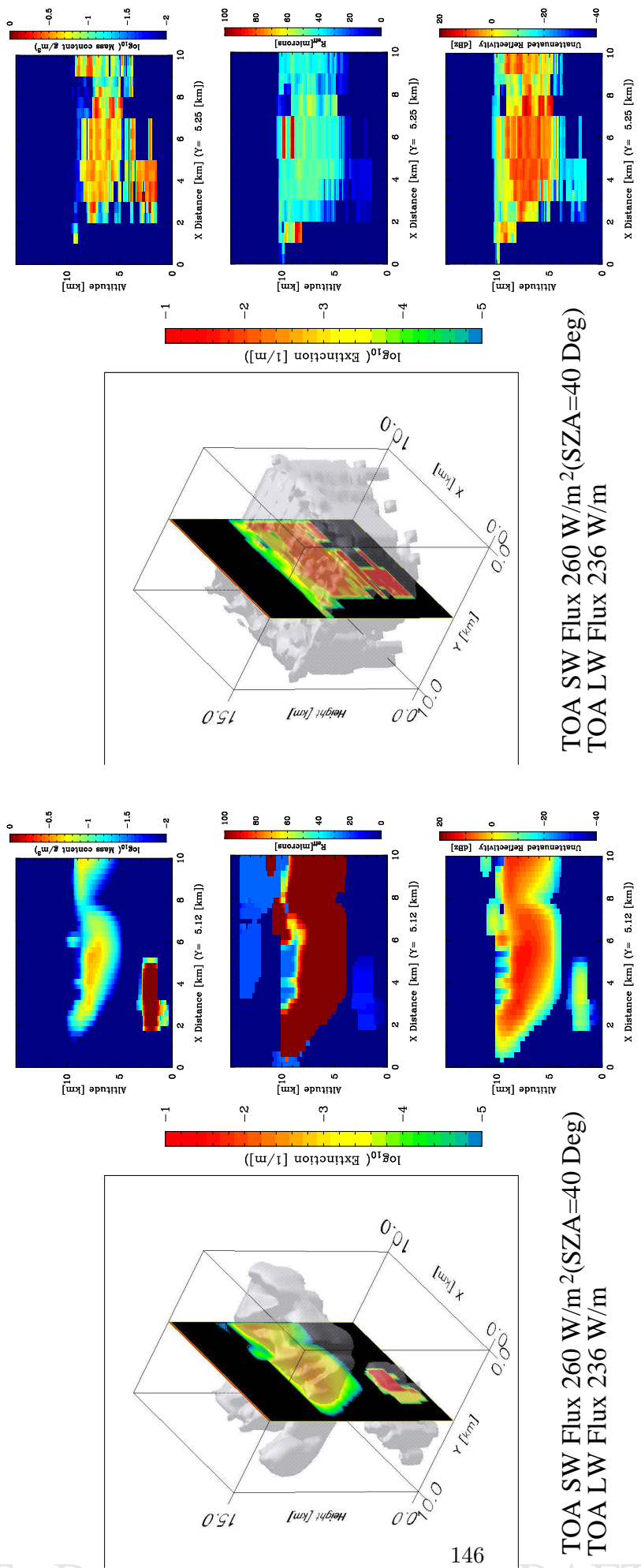


Figure 71: Three dimensional view of the original and reconstructed scenes. The panels show cross section of water content, effective radius, and reflectivity respectively.

4.5 Lidar HSR Aerosol Measurement Example

One of the major advantages of the HSR design is the potential for making independent measurements of the extinction and backscatter (as described in Section 2.2). This is particularly useful in the case of aerosols where the extinction-to-backscatter ratio may vary by a factor of 10 making it difficult for elastic backscatter lidars to even retrieve the extinction profile.

An example model retrieval of a boundary-layer aerosol extinction and backscatter profile is shown in Fig 4.5. Here the signals represent a 10 km averages and the model aerosol layer is comprised of sub-micron H_2SO_4 particles with an extinction coefficient of at $5 \times 10^{-5} \text{ m}^{-1}$ at 353 nm corresponding to an aerosol optical thickness of 0.1 at 500 nm. It can be seen that the error in the backscatter coefficient is less than 10% while the extinction coefficient error is about 30% however, retrieved within 10 scientific goals laid out for the instrument.

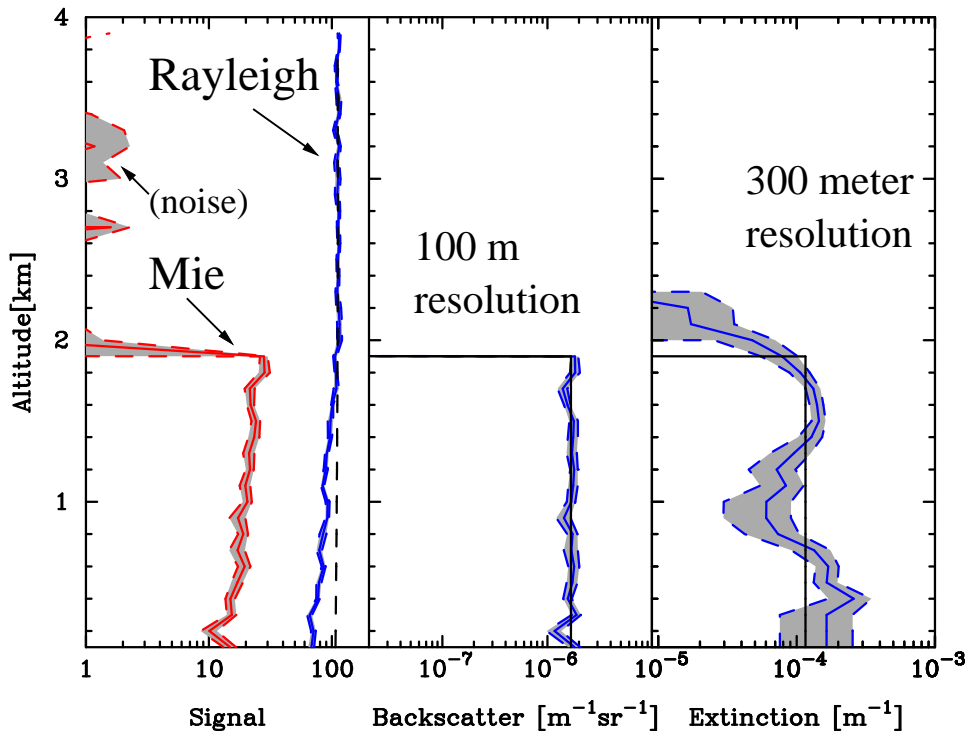


Figure 72: Rayleigh and Mie signals (Left) and retrieved backscatter (Middle) and extinction profile (Right). The dashed dark line in the left panel shows the Rayleigh signal that would be expected if aerosol attenuation was not present. The solid dark lines present in the middle and right panels show the ‘true’ values.

4.6 Multiple scattering Ecare-vs-Calypsio

Here

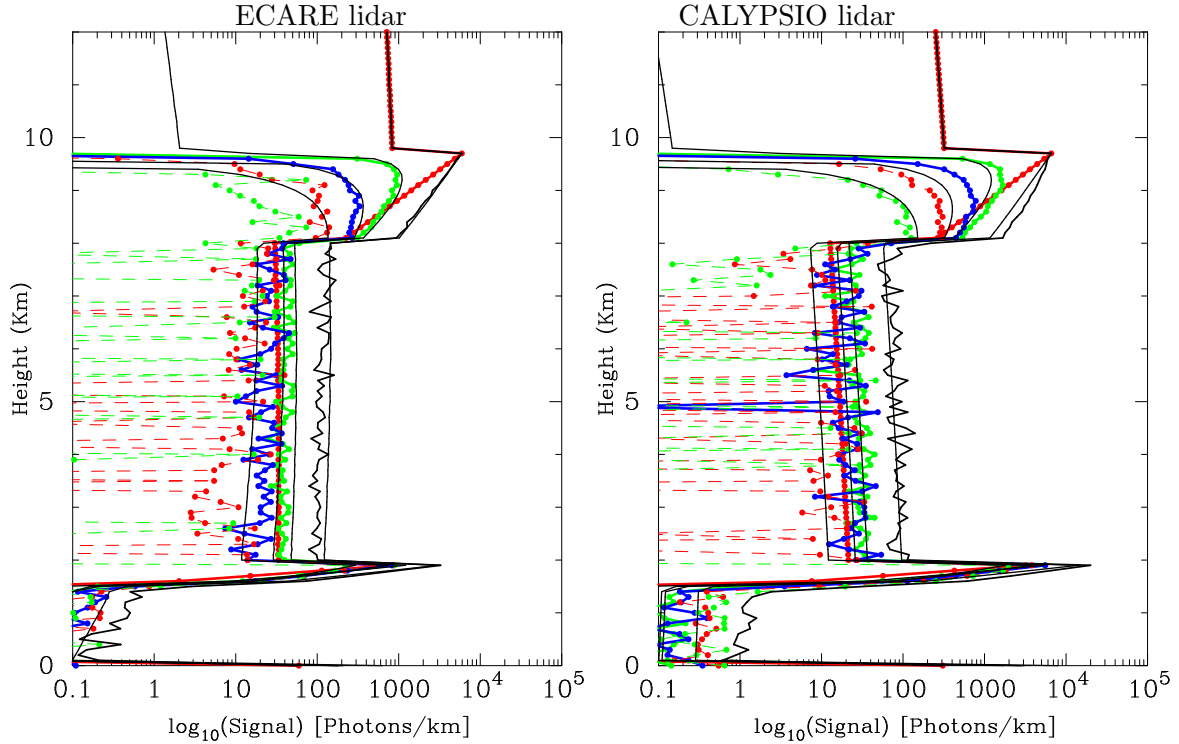


Figure 73: Comparison between the MC results of total power and the results predicted by the model of Eloranta for (Left) the EarthCARE configuration (altitude of 450 km and a full-angle fov of 0.0735 mrad) and (Right) a configuration similar to CALYPSIO ($\lambda = 532\text{nm}$, altitude=705 km, full-angle fov 0.13 mrad) the Cirrus cloud in both cases has an effective particle size of 25 micron and an extinction coefficient of 1/km.

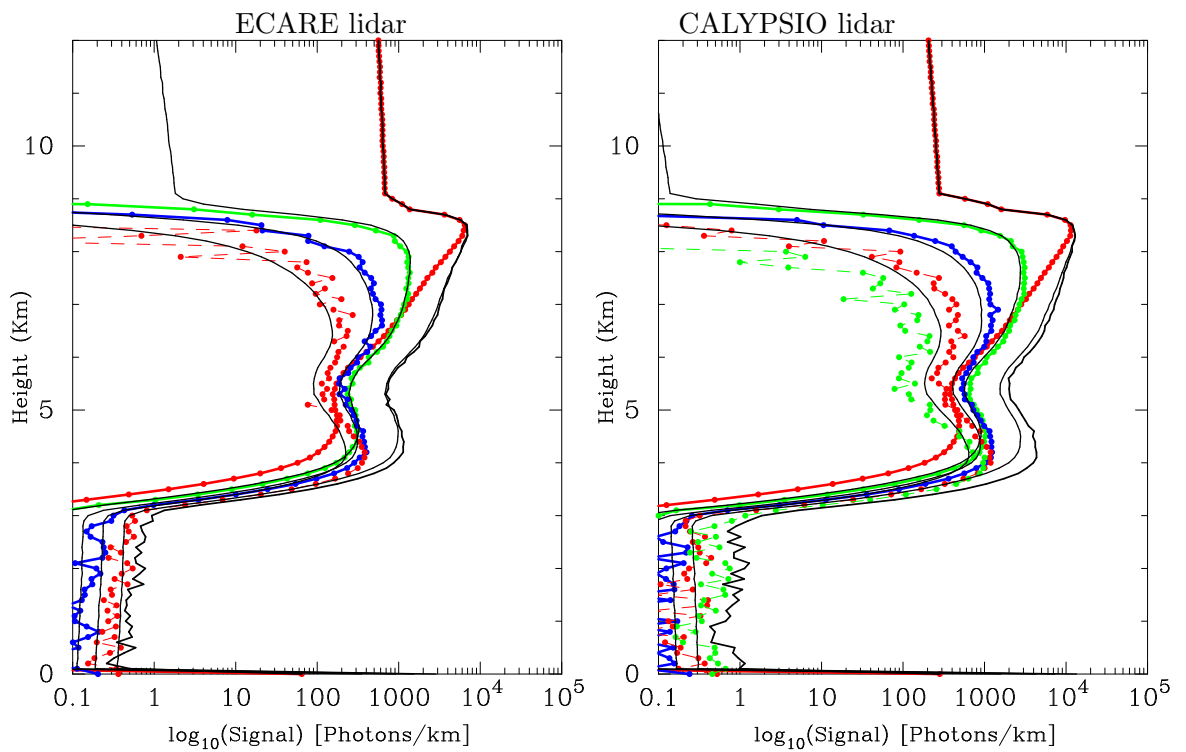


Figure 74: Comparison between the MC results of total power and the results predicted by the model of Eloranta for (Left) the EarthCARE configuration (altitude of 450 km and a full-angle fov of 0.0735 mrad) and (Right) a configuration similar to CALYPSIO ($\lambda = 532\text{nm}$, altitude=705 km, full-angle fov 0.13 mrad). Here the Cirrus cloud is based upon in-situ measurements made during EUCROS.

4.7 Stratocumulus: Ecare Radar vs. CLOUDSAT Results

Here results of running radar simulations on various Stratocumulus scenes generate by UQAM using the MC2 model (see Appendix F) corresponding to conditions encountered during the ASTEX1 and ASTEX2 field campaigns.

Runs were conducted using `rad_filter` and `radar` for both the EarthCARE configuration and a configuration corresponding to CLOUDSAT (lower resolution and 10 dBz lower sensitivity).

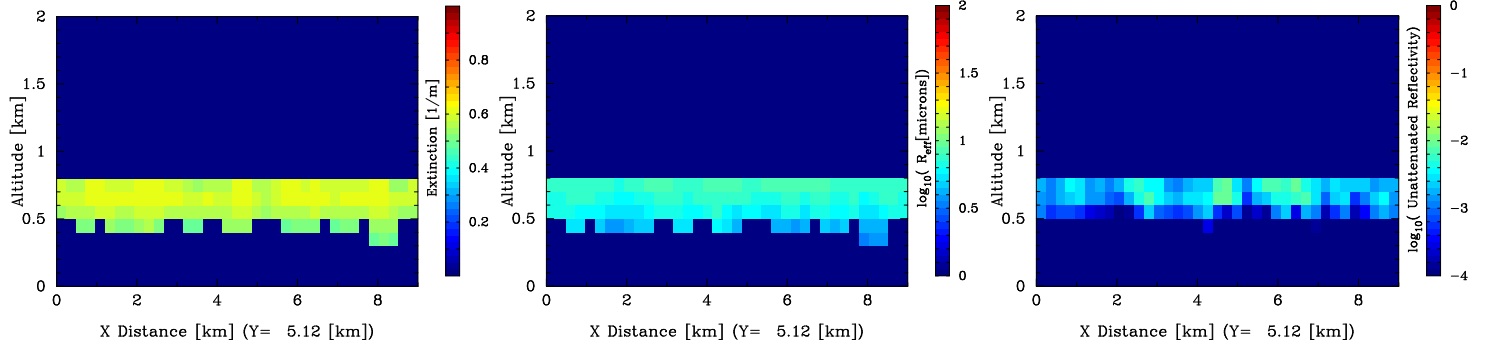
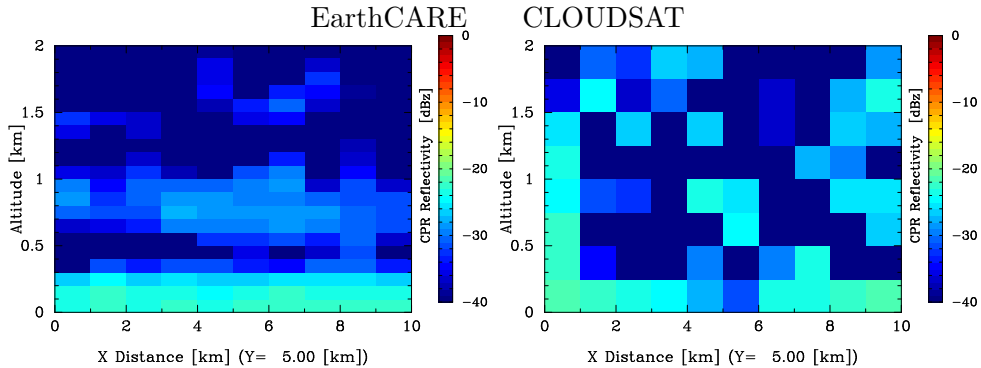


Figure 75: Extinction, effective radius and reflectivity for the UQAM ASTEX1_1 scene.



An example case is shown in Figs. 75 and 4.7. Other example are given in Appendix G. By reviewing the cases it can be seen that the oversampling capability and the higher sensitivity of the Earth care lidar will be a notable advantage over CLOUDSAT's capabilities for this case of clouds. These findings are consistent with the previous studies of Illingworth and Hogan described in Illingworth et al. (2000) where it was found that the detection threshold for Stratocumulus clouds was a very strong function of the radar sensitivity.

5 Conclusions

The EarthCARE simulator represents a novel attempt to construct a truly consistent mission simulator suitable for both instrument trade-off studies, novel algorithm development, and data-processing procedure prototyping. Though there is room (and likely always will be) for further developments and improvements, the project has largely succeeded in its intended objectives. Some of the important accomplishments of this project have been:

- The demonstration that the proposed EarthCARE instrument suite will be capable to making measurements well-suited for the purpose of reconstructing radiative property profiles in the Earth's atmosphere consistent with at TOA error on the order of 10 W/m² (see Sections 4.1–4.4)
- The demonstration that the EarthCARE lidar is well-suited for directly retrieving independent aerosol extinction and backscatter profiles (see Section 4.5). This is a major advantage over elastic backscatter lidars (i.e. CALYPSIO).
- The demonstration that the multiple scattering effects present in the Ecare lidar signal can be accurately accounted for using a simple analytical formulation (see Section 4.6). The smaller field-of-view and lower orbit of EarthCARE makes the treatment of Multiple scattering in the case of EarthCARE more tractable than in the case of CALYPSIO.
- The demonstration that the increased sensitivity and oversampling of the EarthCARE radar will be very useful in the radiatively important case of stratocumulus clouds.
- The development of what may be considered a prototype data processing chain that would serve as a useful guide to the development of an operational system if EarthCARE were to be launched.

In addition, the simulator code and sample scenes, are being released to the broad scientific community. It is hoped that member of the original project team and others will adapt and use components of the package as well as the package as a whole.

As mentioned, there are some areas of the simulator package that could/should be improved. Some obvious ones are:

- The UV-Vis-Ir ice scattering libraries are based on conventional ray-tracing results. The range of crystal habits considered should be improved and the ray-tracing results replaced by more accurate results from improved Ray-tracing and/or FTDF calculations.
- ,The aerosol scattering libraries should be expanded.
- The LW MC program should be expanded in order to calculate fluxes at levels other than the TOA.
- The radar instrument module should be expanded to process Doppler measurements,
- The treatment of surfaces in the long-wave MC code should be improved.
- The MSI retrieval program is rather crude and could be improved.

Hopefully, as time goes on, if there is a need, these and other issues will be addressed.

References

- Alcatel Espace, Pre-Phase A study of MM-WAVE Cloud Profiling Radar (MACSIM), ESTEC contract 11752/95/NL/CN, Final report, 1999.
- Barker, H.W., R. Kenji-Goldstein, D. E. Stevens, Monte Carlo Simulation of Solar Reflectances, Submitted to *J. Atmos. Sci.*, 2002.
- Cox C., and W., Munck W., Measurements of the roughness of the sea surface from the sun's glitter. *J. Opt. Soc. Am.*, **44**, 838-850 (1954)
- Doviak, R., and D. Zrnic, "Doppler Radar and Weather Observations, 2nd Ed.", Academic Press Inc., San Diego, 1993.
- Eloranta, E. W., A practical model for the calculation of multiply scattered lidar returns, *Appl. Opt.*, **37**, 2464-2472, 1998.
- Hess, M., and Matthias Wiegner, COP: a data library of optical properties of hexagonal ice crystals, *Appl. Opt.*, **33**, 7740-7746, 1994.
- Hess M., R. B. A. Koelemeijer, and P. Stamnes, Scattering matrices of imperfect hexagonal ice crystals ,*J. Quant. Spec. Rad. Transfer*, **60**, 301-308, 1998.
- Hu, Y. X., and K. Stamnes, An accurate parameterization of the radiative properties of water clouds suitable for use in climate models, *J. Clim.*, **6**, 728-742, 1993.
- Illingworth, A. J., R. J. Hogan, A. C. A. P. van Lammeren, D. P. Donovan, F. H. Berger, T. Halecker, C.-L. Liu, A. Feijt and H. I. Bloemink, *Quantification of the synergy aspects of the Earth Radiation Mission*. Final report, ESTEC Contract 13167/98/NL/GD, 2000.
- Kato, S., T.P., Ackerman, J.H., Mather, E.E. Clothiaux, The k-distribution method and correlated-k approximation for a shortwave radiative transfer model, *J. Quant. Spec. Rad. Trans.*, **62**, 109– 121, 1999.
- Key, J. and A.J. Schweiger, Tools for atmospheric radiative transfer: Streamer and FluxNet, *Computers and Geosciences*, **24**, 443-451, 1998.
- Lemke, H., and M. Quante, Backscatter characteristics of nonspherical ice crystals: Assessing the potential of polarimetric radar measurements,*J. Geophys. Res.*, **104** , 31,739-31,752, 1999.
- Liebe, H. J., An updated model for millimeter wave propagation in moist air, *Radio Sci.*, **20**, 1069-1089, 1985.
- Liou, K.N., "An Introduction to Atmospheric Radiation, 2nd Ed.", Internation Geophysics Series, Vol. 84, Academic press, San Diego, 2002.
- McClatchey, R. A., R. W. Fenn, J. E. A. Selby, F. E. Volz and J. S. Garing, Optical properties of the atmosphere (3rd. ed.), Air Force Cambridge Research Laboratories, Rep. No. AFCRL72-0497, L. G. Hanscom Field, 1972.
- Miles, R.B., W.R. Lempert and J.N. Forkey, Laser Rayleigh scattering, *Meas. Sci. Technol.*, **12**, R33–R51 (2001).

- Minnis P., D.P., Garber, F.Y. Young, R.F., Arduini, Y. Takano, Parameterization of Reflectance and Effective Emittance for Satellite Remote Sensing of Cloud Properties, *J. Atmos. Sci.*, **55**, 3313–3339, 1998.
- Pan X., Coherent Rayleigh-Brillouin Scattering, Ph.D. thesis, Princeton University, 2003.
- Papoulis, A., “Probability, Random Variables and Stochastics Processes”, McGraw-Hill, 1965
- Pinty, B., J.-L. Widlowski, N. Gobron, M. M. Verstraete and D. J. Diner, Uniqueness of Multiangular Measurements Part 1: An Indicator of Subpixel Surface Heterogeneity from MISR’, IEEE Trans. Geosci. Remote Sensing, MISR Special Issue, **40**, 1560-1573, 2002.
- Platt, C.M.R., Remote Sounding of High Cloud. III: Monte Carlo Calculations of Multiple-Scattered Lidar Returns, *J. Atmos. Sci.*, **38**, 156–167, 1981.
- Ulaby, F. T., R. K. Moore and A. K. Fung, “Microwave remote sensing, active and passive”. Artech House. Vol.1, 1981.
- Saleh B.E.A. and M.C. Teich, “Fundamentals of Photonics”, Wiley-Interscience, New York, 1991.

A Installation

The EarthCARE simulator has been developed and tested using a number of different environments. The main development platform has been a LINUX machine using the Portland Group F90 compiler (version 3.2-4) and the free Intel f90 compiler V8.0. The package has also been built under Win98 and WinXP and Win98 using the Compac F90 compiler version 6.6.

The programs comprising the package are designed to operate from a command console or be automatically called by a shell script in batch mode. Thus, for use with Windows machines, it is desirable that a UNIX like console environment be first installed. The CYGWIN/XFree86 (see www.cygwin.com⁶) distribution provides a UNIX like environment under windows and is the preferred means to run the simulation package under Windows.

The Simulator package itself is distributed as two zip archives which contain the source code as well as supporting data and example input files. The components are:

sim_main.zip Main archive

scatt_libs1.zip Scattering library information.

A.1 Unix/Linux

1. Create a new directory where you want to install the package (i.e. Simulator) this will be the root directory.
2. Copy the zip files to root directory
3. Unzip the file **sim_main.zip.zip**

Note: The package comes with pre-built executables built using the Portland Group f90 compiler (version 3.2-4) under Linux (kernel 2.4.x). If you wish to compile the programs then follow steps 4 to 7.

4. cd src
5. Inspect the **makefile** to and adjust the compiler flags as necessary. Also if you wish to use the **PGPLOT** based plotting programs you will need to insure that the appropriate library flags and paths are set correctly for your system. See <http://www.astro.caltech.edu/~tjp/pgplot/> for info on **PGPLOT**. For 3-D plotting code drawn (with some modifications) from the **PGPLOT** based package **PGXTAL** is included in the simulator distribution in the **pgxtal** directory. For information on **PGXTAL** see
<http://www.isis.rl.ac.uk/dataanalysis/dsplot/>.

⁶When installing it will be useful if the zip/unzip and tcsh options are selected.

6. After editing the makefile type:

```
make all
```

and

```
make allpgplot (if you want to use the PGLOT programs)
```

then:

```
cd mc  
make all
```

All the executables will be installed in the Simulator/bin directory

7. Install the default scattering libraries.

- (a) cd to the main directory
- (b) unzip scatt_libs1.zip
- (c) cd scatt_libs
- (d) Inspect the settings of the compiler flags in the script “**build_mie_tables.csh**” and change according to your system
- (e) **source build_mie_tables.csh**. NOTE: THE PROCESS OF BUILDING THE MIE SCATTERING LIBRARIES MAY TAKE SEVERAL HOURS DEPENDING ON YOUR SYSTEM.

8. You should now have a working basic installation.

9. See the documentation in the doc directory.

NOTE: Most programs are meant to be executed from the simulator main directory.

A.2 MS Windows

This package relies on certain Linux/Unix type tools being available. As a consequence the recommended way to use this package under windows is to first install the CYGWIN environment which provides a Unix/Linux like environment under windows (98, 2000 and XP) (see www.cygwin.com). When installing cygwin, make sure the c-shell or tch shells are chosen for installation.

Under Windows you must first make sure that the proper environment variables for the F90 compiler have been set so that the compiler can be used via the command prompt. For information on how to do this consult the documentation associated with the compiler environment you are using. For the Digital Visual Fortran compiler you can invoke the **Fortran command prompt** from the Dev Studio directory. Alternatively, if you are using CYGWIN, you can edit the file `c:/cygwin.bat` so that the file `dfvars.bat`⁷ is invoked at startup.

The following instructions are based on using the Digital Fortran compiler using **nmake**.

⁷The batch file `dfvars.bat1` is located in the `bin1` directory of the Digital Visual Fortran distribution.

1. Create a new directory where you want to install the package (i.e. Simulator) this will be the root directory.
2. Copy the zip files to root directory
3. Unzip the file **sim_main_zip.zip**
4. cd src
5. Inspect **makefile.win** to and adjust the compiler flags as necessary. Also if you wish to use the **PGPLOT** based plotting programs you will need to insure that the appropriate library flags and paths are set correctly for your system. See <http://www.astro.caltech.edu/~tjp/pgplot/> for info on **PGPLOT**. For 3-D plotting code drawn (with some modifications) from the **PGPLOT** based package **PGXTAL** is included in the simulator distribution in the **pgxtal** directory. For information on **PGXTAL** see
<http://www.isis.rl.ac.uk/dataanalysis/dsplot/>.
6. After editing **makefile.win** type:

```
nmake /f makefile.win all
```

and

```
nmake /f allpgplot (if you want to use the PGPLOT
programs)
```

then:

```
cd mc
nmake /f makefile.win all
```

All the executables will be installed in the Simulator/bin directory

7. Install the default scattering libraries.
 - (a) cd to the main directory
 - (b) unzip scatt_libs1.zip
 - (c) cd scatt_libs
 - (d) Inspect the settings of the compiler flags in the script “**build_mie_tables.csh**” and change according to your system
 - (e) **source build_mie_tables.csh**. NOTE: THE PROCESS OF BUILDING THE MIE SCATTERING LIBRARIES MAY TAKE SEVERAL HOURS DEPENDING ON YOUR SYSTEM.
8. You should now have a working basic installation.
9. See the documentation in the doc directory.

NOTE: Most programs are meant to be executed from the simulator main directory.

A.3 Compiler and Platform notes:

- When running in the CYGWIN environment under Windows XP using Digital Fortran use only unformatted versions of the UFF files. The mechanism that has been built into the program to automatically detect the UFF file format fails for ASCII format files under Windows XP.
- If extra backslashes appear in the labels of the PG PLOT based plotting programs then the occurrences of ' \\' within the PG PLOT function calls within the programs should be changed to '\\'

B Example scattering master list file

Here an example scattering master list file is shown. The #' symbols denote comment lines.

```

1   'MIE_WATER'
2   1           ,Files are stored in binary format
3   332          ,total number of files 310+11*2
4   2           ,num_temperatures
5   1           ,num_relative_humidities
6   166          ,num_wavelengths + 11
7   #
8   #-----#
9   # Radar file(s)
10  #-----#
11  #
12  '# MIE_RAD' ,name of file type (for reading purposes)
13  1           ,num_temperatures
14  1           ,number of radar wavelengths
15  #
16  #-----#
17  # Number of size bins
18  # to extrapolate (intepolate)
19  # to
20  #-----#
21  #
22  50
23  #
24  #-----#
25  #      wavelen[mic],t[K],rh[%],file
26  #-----#
27  #
28  00.200,240.0,-99.0,'./scatt_libs/cld_water/water_mie_t240_00p200.dat'
29  00.200,300.0,-99.0,'./scatt_libs/cld_water/water_mie_t300_00p200.dat'
30  00.250,240.0,-99.0,'./scatt_libs/cld_water/water_mie_t240_00p250.dat'
31  00.250,300.0,-99.0,'./scatt_libs/cld_water/water_mie_t300_00p250.dat'
32  00.300,240.0,-99.0,'./scatt_libs/cld_water/water_mie_t240_00p300.dat'
33  00.300,300.0,-99.0,'./scatt_libs/cld_water/water_mie_t300_00p300.dat'
34  00.350,240.0,-99.0,'./scatt_libs/cld_water/water_mie_t240_00p350.dat'
35  00.350,300.0,-99.0,'./scatt_libs/cld_water/water_mie_t300_00p350.dat'
36  00.355,240.0,-99.0,'./scatt_libs/cld_water/water_mie_t240_00p355.dat'
37  00.355,300.0,-99.0,'./scatt_libs/cld_water/water_mie_t300_00p355.dat'
38  00.400,240.0,-99.0,'./scatt_libs/cld_water/water_mie_t240_00p400.dat'
39  00.400,300.0,-99.0,'./scatt_libs/cld_water/water_mie_t300_00p400.dat'
40  00.450,240.0,-99.0,'./scatt_libs/cld_water/water_mie_t240_00p450.dat'
41  00.450,300.0,-99.0,'./scatt_libs/cld_water/water_mie_t300_00p450.dat'
42  00.500,240.0,-99.0,'./scatt_libs/cld_water/water_mie_t240_00p500.dat'
43  00.500,300.0,-99.0,'./scatt_libs/cld_water/water_mie_t300_00p500.dat'
44  00.532,240.0,-99.0,'./scatt_libs/cld_water/water_mie_t240_00p532.dat'
45  00.532,300.0,-99.0,'./scatt_libs/cld_water/water_mie_t300_00p532.dat'
46  00.550,240.0,-99.0,'./scatt_libs/cld_water/water_mie_t240_00p550.dat'
47  00.550,300.0,-99.0,'./scatt_libs/cld_water/water_mie_t300_00p550.dat'
48  00.600,240.0,-99.0,'./scatt_libs/cld_water/water_mie_t240_00p600.dat'
49  00.600,300.0,-99.0,'./scatt_libs/cld_water/water_mie_t300_00p600.dat'
50  00.650,240.0,-99.0,'./scatt_libs/cld_water/water_mie_t240_00p650.dat'
51  00.650,300.0,-99.0,'./scatt_libs/cld_water/water_mie_t300_00p650.dat'
52  00.660,240.0,-99.0,'./scatt_libs/cld_water/water_mie_t240_00p660.dat'
53  00.660,300.0,-99.0,'./scatt_libs/cld_water/water_mie_t300_00p660.dat'
54  00.700,240.0,-99.0,'./scatt_libs/cld_water/water_mie_t240_00p700.dat'
55  00.700,300.0,-99.0,'./scatt_libs/cld_water/water_mie_t300_00p700.dat'
56  00.750,240.0,-99.0,'./scatt_libs/cld_water/water_mie_t240_00p750.dat'
57  00.750,300.0,-99.0,'./scatt_libs/cld_water/water_mie_t300_00p750.dat'
58  00.800,240.0,-99.0,'./scatt_libs/cld_water/water_mie_t240_00p800.dat'
59  00.800,300.0,-99.0,'./scatt_libs/cld_water/water_mie_t300_00p800.dat'
60  00.850,240.0,-99.0,'./scatt_libs/cld_water/water_mie_t240_00p850.dat'
61  00.850,300.0,-99.0,'./scatt_libs/cld_water/water_mie_t300_00p850.dat'
62  00.870,240.0,-99.0,'./scatt_libs/cld_water/water_mie_t240_00p870.dat'
63  00.870,300.0,-99.0,'./scatt_libs/cld_water/water_mie_t300_00p870.dat'
64  00.900,240.0,-99.0,'./scatt_libs/cld_water/water_mie_t240_00p900.dat'
65  00.900,300.0,-99.0,'./scatt_libs/cld_water/water_mie_t300_00p900.dat'
66  00.950,240.0,-99.0,'./scatt_libs/cld_water/water_mie_t240_00p950.dat'
67  00.950,300.0,-99.0,'./scatt_libs/cld_water/water_mie_t300_00p950.dat'
68  01.000,240.0,-99.0,'./scatt_libs/cld_water/water_mie_t240_01p000.dat'
69  01.000,300.0,-99.0,'./scatt_libs/cld_water/water_mie_t300_01p000.dat'
70  01.050,240.0,-99.0,'./scatt_libs/cld_water/water_mie_t240_01p050.dat'
71  01.050,300.0,-99.0,'./scatt_libs/cld_water/water_mie_t300_01p050.dat'
72  01.064,240.0,-99.0,'./scatt_libs/cld_water/water_mie_t240_01p064.dat'
73  01.064,300.0,-99.0,'./scatt_libs/cld_water/water_mie_t300_01p064.dat'
74  01.100,240.0,-99.0,'./scatt_libs/cld_water/water_mie_t240_01p100.dat'
75  01.100,300.0,-99.0,'./scatt_libs/cld_water/water_mie_t300_01p100.dat'
76  01.150,240.0,-99.0,'./scatt_libs/cld_water/water_mie_t240_01p150.dat'
77  01.150,300.0,-99.0,'./scatt_libs/cld_water/water_mie_t300_01p150.dat'
78  01.200,240.0,-99.0,'./scatt_libs/cld_water/water_mie_t240_01p200.dat'
79  01.200,300.0,-99.0,'./scatt_libs/cld_water/water_mie_t300_01p200.dat'
80  01.250,240.0,-99.0,'./scatt_libs/cld_water/water_mie_t240_01p250.dat'
81  01.250,300.0,-99.0,'./scatt_libs/cld_water/water_mie_t300_01p250.dat'
82  01.300,240.0,-99.0,'./scatt_libs/cld_water/water_mie_t240_01p300.dat'
83  01.300,300.0,-99.0,'./scatt_libs/cld_water/water_mie_t300_01p300.dat'
84  01.350,240.0,-99.0,'./scatt_libs/cld_water/water_mie_t240_01p350.dat'
85  01.350,300.0,-99.0,'./scatt_libs/cld_water/water_mie_t300_01p350.dat'
86  01.400,240.0,-99.0,'./scatt_libs/cld_water/water_mie_t240_01p400.dat'
87  01.400,300.0,-99.0,'./scatt_libs/cld_water/water_mie_t300_01p400.dat'
88  01.450,240.0,-99.0,'./scatt_libs/cld_water/water_mie_t240_01p450.dat'
89  01.450,300.0,-99.0,'./scatt_libs/cld_water/water_mie_t300_01p450.dat'
90  01.500,240.0,-99.0,'./scatt_libs/cld_water/water_mie_t240_01p500.dat'
91  01.500,300.0,-99.0,'./scatt_libs/cld_water/water_mie_t300_01p500.dat'
92  01.550,240.0,-99.0,'./scatt_libs/cld_water/water_mie_t240_01p550.dat'
93  01.550,300.0,-99.0,'./scatt_libs/cld_water/water_mie_t300_01p550.dat'
94  01.600,240.0,-99.0,'./scatt_libs/cld_water/water_mie_t240_01p600.dat'
95  01.600,300.0,-99.0,'./scatt_libs/cld_water/water_mie_t300_01p600.dat'
96  01.650,240.0,-99.0,'./scatt_libs/cld_water/water_mie_t240_01p650.dat'
97  01.650,300.0,-99.0,'./scatt_libs/cld_water/water_mie_t300_01p650.dat'
98  01.700,240.0,-99.0,'./scatt_libs/cld_water/water_mie_t240_01p700.dat'
99  01.700,300.0,-99.0,'./scatt_libs/cld_water/water_mie_t300_01p700.dat'
100 01.750,240.0,-99.0,'./scatt_libs/cld_water/water_mie_t240_01p750.dat'
101 01.750,300.0,-99.0,'./scatt_libs/cld_water/water_mie_t300_01p750.dat'
102 01.800,240.0,-99.0,'./scatt_libs/cld_water/water_mie_t240_01p800.dat'
103 01.800,300.0,-99.0,'./scatt_libs/cld_water/water_mie_t300_01p800.dat'
104 01.850,240.0,-99.0,'./scatt_libs/cld_water/water_mie_t240_01p850.dat'
105 01.850,300.0,-99.0,'./scatt_libs/cld_water/water_mie_t300_01p850.dat'
106 01.900,240.0,-99.0,'./scatt_libs/cld_water/water_mie_t240_01p900.dat'
107 01.900,300.0,-99.0,'./scatt_libs/cld_water/water_mie_t300_01p900.dat'
108 01.950,240.0,-99.0,'./scatt_libs/cld_water/water_mie_t240_01p950.dat'
109 01.950,300.0,-99.0,'./scatt_libs/cld_water/water_mie_t300_01p950.dat'
110 02.000,240.0,-99.0,'./scatt_libs/cld_water/water_mie_t240_02p000.dat'
111 02.000,300.0,-99.0,'./scatt_libs/cld_water/water_mie_t300_02p000.dat'
112 02.050,240.0,-99.0,'./scatt_libs/cld_water/water_mie_t240_02p050.dat'
113 02.050,300.0,-99.0,'./scatt_libs/cld_water/water_mie_t300_02p050.dat'
114 02.100,240.0,-99.0,'./scatt_libs/cld_water/water_mie_t240_02p100.dat'
115 02.100,300.0,-99.0,'./scatt_libs/cld_water/water_mie_t300_02p100.dat'
116 02.150,240.0,-99.0,'./scatt_libs/cld_water/water_mie_t240_02p150.dat'
117 02.150,300.0,-99.0,'./scatt_libs/cld_water/water_mie_t300_02p150.dat'
118 02.200,240.0,-99.0,'./scatt_libs/cld_water/water_mie_t240_02p200.dat'
119 02.200,300.0,-99.0,'./scatt_libs/cld_water/water_mie_t300_02p200.dat'
120 02.250,240.0,-99.0,'./scatt_libs/cld_water/water_mie_t240_02p250.dat'
121 02.250,300.0,-99.0,'./scatt_libs/cld_water/water_mie_t300_02p250.dat'
122 02.300,240.0,-99.0,'./scatt_libs/cld_water/water_mie_t240_02p300.dat'
123 02.300,300.0,-99.0,'./scatt_libs/cld_water/water_mie_t300_02p300.dat'
124 02.350,240.0,-99.0,'./scatt_libs/cld_water/water_mie_t240_02p350.dat'

```



```
373 3.19,250.0,'./scatt_libs/cld_water/water_mie_t250_94GHz.dat'  
374 3.19,255.0,'./scatt_libs/cld_water/water_mie_t255_94GHz.dat'  
375 3.19,260.0,'./scatt_libs/cld_water/water_mie_t260_94GHz.dat'  
376 3.19,265.0,'./scatt_libs/cld_water/water_mie_t265_94GHz.dat'  
377 3.19,270.0,'./scatt_libs/cld_water/water_mie_t270_94GHz.dat'  
378 3.19,275.0,'./scatt_libs/cld_water/water_mie_t275_94GHz.dat'  
379 3.19,280.0,'./scatt_libs/cld_water/water_mie_t280_94GHz.dat'  
380 3.19,285.0,'./scatt_libs/cld_water/water_mie_t285_94GHz.dat'  
381 3.19,290.0,'./scatt_libs/cld_water/water_mie_t290_94GHz.dat'  
382 3.19,295.0,'./scatt_libs/cld_water/water_mie_t295_94GHz.dat'  
383 3.19,300.0,'./scatt_libs/cld_water/water_mie_t300_94GHz.dat'  
384 3.19,305.0,'./scatt_libs/cld_water/water_mie_t305_94GHz.dat'  
385 3.19,310.0,'./scatt_libs/cld_water/water_mie_t310_94GHz.dat'  
386 #  
387 #-----  
388 # size grid to interpolate things to  
389 # For both RT and DDA calculations  
390 # (data are bin-mid-points)  
391 #-----  
392 1.  
393 2.  
394 3.  
395 4.  
396 5.  
397 6.  
398 7.  
399 8.  
400 9.  
401 10.  
402 11.  
403 12.  
404 13.  
405 14.  
406 15.  
407 16.  
408 17.  
409 18.  
410 19.  
411 20.  
412 21.  
413 22.  
414 23.  
415 24.  
416 25.  
417 26.  
418 27.  
419 28.  
420 29.  
421 30.  
422 31.  
423 32.  
424 33.  
425 34.  
426 35.  
427 36.  
428 37.  
429 38.  
430 39.  
431 40.  
432 41.  
433 42.  
434 43.  
435 44.  
436 45.  
437 46.  
438 47.  
439 48.  
440 49.  
441 50.  
442 50.
```

C Example 1-D background atmospheric data input to scene_creator

```
1 -----  
2 subarctic winter  
3 -----  
4 z(km)      p(mb)       t(K)        wv(g/m3)      O3(  
5 -----  
6 0.0000E+00 0.1013E+04 0.2571E+03 0.1200E+01 0.4100E-04  
7 0.1000E+01 0.8878E+03 0.2591E+03 0.1200E+01 0.4100E-04  
8 0.2000E+01 0.7775E+03 0.2559E+03 0.1030E+01 0.4100E-04  
9 0.3000E+01 0.6798E+03 0.2527E+03 0.7470E+00 0.4300E-04  
10 0.4000E+01 0.5932E+03 0.2477E+03 0.4590E+00 0.4500E-04  
11 0.5000E+01 0.5158E+03 0.2409E+03 0.2340E+00 0.4700E-04  
12 0.6000E+01 0.4467E+03 0.2341E+03 0.9780E-01 0.4900E-04  
13 0.7000E+01 0.3853E+03 0.2273E+03 0.3290E-01 0.7100E-04  
14 0.8000E+01 0.3308E+03 0.2206E+03 0.1320E-01 0.9000E-04  
15 0.9000E+01 0.2829E+03 0.2172E+03 0.8370E-02 0.1600E-03  
16 0.1000E+02 0.2418E+03 0.2172E+03 0.5510E-02 0.2400E-03  
17 0.1100E+02 0.2067E+03 0.2172E+03 0.3790E-02 0.3200E-03  
18 0.1200E+02 0.1766E+03 0.2172E+03 0.2580E-02 0.4300E-03  
19 0.1300E+02 0.1510E+03 0.2172E+03 0.1670E-02 0.4700E-03  
20 0.1400E+02 0.1291E+03 0.2172E+03 0.1100E-02 0.4900E-03  
21 0.1500E+02 0.1103E+03 0.2172E+03 0.7330E-03 0.5600E-03  
22 0.2000E+02 0.5014E+02 0.2141E+03 0.3260E-03 0.5600E-03  
23 0.2500E+02 0.2256E+02 0.2112E+03 0.1490E-03 0.3200E-03  
24 0.3000E+02 0.1020E+02 0.2160E+03 0.6580E-04 0.1500E-03  
25 0.3500E+02 0.4701E+01 0.2222E+03 0.2950E-04 0.9200E-04  
26 0.4000E+02 0.2243E+01 0.2347E+03 0.1330E-04 0.4100E-04  
27 0.4500E+02 0.1113E+01 0.2470E+03 0.6280E-05 0.1300E-04  
28 0.5000E+02 0.5720E+00 0.2593E+03 0.3070E-05 0.4300E-05  
29 0.7000E+02 0.4000E-01 0.2457E+03 0.2280E-06 0.8600E-07  
30 0.1000E+03 0.1000E-02 0.2100E+03 0.2000E-08 0.4300E-10
```

D Example 3-D background atmospheric data input to scene_creator

In the following listing additional comments are printed in bold emphasized text.

```

1 | 3D                                     Flag string indicating that the file is '3D' format
2 | 3,3,25                                nx,ny,nz
3 |
4 | mid-latitude summer
5 | -----
6 | z(km)      p(mb)        t(K)       wv(g/m3)      O3
7 | -----
8 | start                                     Flag string indicating start of data
9 | ix=1,iy=1
10| 0.0 0.0 0.0000E+00 0.1013E+04 0.2940E+03 0.1400E+02 0.6000E-04
11| 0.0 0.0 0.1000E+01 0.9020E+03 0.2900E+03 0.9300E+01 0.6000E-04
12| 0.0 0.0 0.2000E+01 0.8020E+03 0.2850E+03 0.5850E+01 0.6000E-04
13| 0.0 0.0 0.3000E+01 0.7100E+03 0.2790E+03 0.3430E+01 0.6200E-04
14| 0.0 0.0 0.4000E+01 0.6280E+03 0.2730E+03 0.1890E+01 0.6400E-04
15| 0.0 0.0 0.5000E+01 0.5540E+03 0.2671E+03 0.1000E+01 0.6600E-04
16| 0.0 0.0 0.6000E+01 0.4870E+03 0.2610E+03 0.6090E+00 0.6900E-04
17| 0.0 0.0 0.7000E+01 0.4260E+03 0.2547E+03 0.3710E+00 0.7500E-04
18| 0.0 0.0 0.8000E+01 0.3720E+03 0.2482E+03 0.2100E+00 0.7900E-04
19| 0.0 0.0 0.9000E+01 0.3240E+03 0.2417E+03 0.1180E+00 0.8600E-04
20| 0.0 0.0 0.1000E+02 0.2810E+03 0.2352E+03 0.6430E-01 0.9000E-04
21| 0.0 0.0 0.1100E+02 0.2430E+03 0.2288E+03 0.2190E-01 0.1100E-03
22| 0.0 0.0 0.1200E+02 0.2090E+03 0.2223E+03 0.6460E-02 0.1200E-03
23| 0.0 0.0 0.1300E+02 0.1790E+03 0.2169E+03 0.1660E-02 0.1500E-03
24| 0.0 0.0 0.1400E+02 0.1530E+03 0.2158E+03 0.9950E-03 0.1800E-03
25| 0.0 0.0 0.1500E+02 0.1300E+03 0.2158E+03 0.8400E-03 0.1900E-03
26| 0.0 0.0 0.2000E+02 0.5950E+02 0.2182E+03 0.3800E-03 0.3400E-03
27| 0.0 0.0 0.2500E+02 0.2770E+02 0.2242E+03 0.1720E-03 0.3000E-03
28| 0.0 0.0 0.3000E+02 0.1320E+02 0.2342E+03 0.7850E-04 0.2000E-03
29| 0.0 0.0 0.3500E+02 0.6520E+01 0.2453E+03 0.3700E-04 0.9200E-04
30| 0.0 0.0 0.4000E+02 0.3330E+01 0.2575E+03 0.1800E-04 0.4100E-04
31| 0.0 0.0 0.4500E+02 0.1760E+01 0.2697E+03 0.9090E-05 0.1300E-04
32| 0.0 0.0 0.5000E+02 0.9510E+00 0.2762E+03 0.4800E-05 0.4300E-05
33| 0.0 0.0 0.7000E+02 0.6710E-01 0.2191E+03 0.4270E-06 0.8600E-07
34| 0.0 0.0 0.1000E+03 0.4906E-03 0.2107E+03 0.3240E-08 0.7600E-10
35| xi=1,iy=2
36| 0.0 5.0 0.0000E+00 0.1013E+04 0.2940E+03 0.1400E+02 0.6000E-04
37| 0.0 5.0 0.1000E+01 0.9020E+03 0.2900E+03 0.9300E+01 0.6000E-04
38| 0.0 5.0 0.2000E+01 0.8020E+03 0.2850E+03 0.5850E+01 0.6000E-04
39| 0.0 5.0 0.3000E+01 0.7100E+03 0.2790E+03 0.3430E+01 0.6200E-04
40| 0.0 5.0 0.4000E+01 0.6280E+03 0.2730E+03 0.1890E+01 0.6400E-04
41| 0.0 5.0 0.5000E+01 0.5540E+03 0.2671E+03 0.1000E+01 0.6600E-04
42| 0.0 5.0 0.6000E+01 0.4870E+03 0.2610E+03 0.6090E+00 0.6900E-04
43| 0.0 5.0 0.7000E+01 0.4260E+03 0.2547E+03 0.3710E+00 0.7500E-04
44| 0.0 5.0 0.8000E+01 0.3720E+03 0.2482E+03 0.2100E+00 0.7900E-04
45| 0.0 5.0 0.9000E+01 0.3240E+03 0.2417E+03 0.1180E+00 0.8600E-04
46|
47|
48|
49|
50| ix=2,iy=1
51| 5.0 0.0 0.0000E+00 0.1013E+04 0.2940E+03 0.1400E+02 0.6000E-04
52| 5.0 0.0 0.1000E+01 0.9020E+03 0.2900E+03 0.9300E+01 0.6000E-04
53| 5.0 0.0 0.2000E+01 0.8020E+03 0.2850E+03 0.5850E+01 0.6000E-04
54| 5.0 0.0 0.3000E+01 0.7100E+03 0.2790E+03 0.3430E+01 0.6200E-04
55| 5.0 0.0 0.4000E+01 0.6280E+03 0.2730E+03 0.1890E+01 0.6400E-04
56| 5.0 0.0 0.5000E+01 0.5540E+03 0.2671E+03 0.1000E+01 0.6600E-04
57| 5.0 0.0 0.6000E+01 0.4870E+03 0.2610E+03 0.6090E+00 0.6900E-04
58| 5.0 0.0 0.7000E+01 0.4260E+03 0.2547E+03 0.3710E+00 0.7500E-04
59| 5.0 0.0 0.8000E+01 0.3720E+03 0.2482E+03 0.2100E+00 0.7900E-04
60| 5.0 0.0 0.9000E+01 0.3240E+03 0.2417E+03 0.1180E+00 0.8600E-04
61| 5.0 0.0 0.1000E+02 0.2810E+03 0.2352E+03 0.6430E-01 0.9000E-04
62| 5.0 0.0 0.1100E+02 0.2430E+03 0.2288E+03 0.2190E-01 0.1100E-03
63|
64|
65| etc

```

The “3D”(line 1) and “start” (line 8) entries are necessary. The numeric entries specifying the dimensions of the file are also mandatory. The following text up to the “start” is ignored and can be any length.

E 3-D Cloud/Aerosol data input to scene_creator

Each single file will correspond to a single particular scattering type as defined in the `scene_creator` input file. In the following listing comments are printed in bold emphasized text.

```
1 1,4,4,5          num_modes, nx, ny, nz
2 -----
3 0.0,2.0,4.0,6.0  x(1),x(2)....x(nx)
4 -----
5 0.0,2.0,4.0,6.0  y(1),y(2)....y(ny)
6 -----
7 4.0,5.0,6.0,7.0,8.0 z(1),z(2)....z(nz)
8 -----
9 0.0,1000.0       Min Size, Max. Size
10 -----ix=1,iy=1---
11 0.0,0.0,0.0      Mass-density (g/m3) OR Extinction 1/m, g1, Reff for x(1),y(1),z(1)
12 0.0,0.0,0.0      etc..
13 0.0,0.0,0.0
14 0.0,0.0,0.0
15 0.0,0.0,0.0
16 -----ix=1,iy=2---
17 0.0,0.0,0.0
18 0.0,0.0,0.0
19 0.0,0.0,0.0
20 0.0,0.0,0.0
21 0.0,0.0,0.0
22 .
23 .
24 .
25 0.0,0.0,0.0
26 0.0,0.0,0.0
27 0.0,0.0,0.0
28 0.0,0.0,0.0
29 0.0,0.0,0.0
30 -----ix=2,iy=2---
31 0.0,0.0,0.0
32 0.0,0.0,0.0
33 0.001,3.0,100.0
34 0.001,3.0,100.0
35 0.0,0.0,0.0
36 .
37 .
38 .
39 .
40 -----ix=4,iy=4---
41 0.0,0.0,0.0
42 0.0,0.0,0.0
43 0.0,0.0,0.0
44 0.0,0.0,0.0
45 0.0,0.0,0.0
```

F Example ASCII UFF file

Here an example UFF (scene) file generated by `scene_creator` is presented. The example here was produced by a input file listed previously in Section D. Additional comments (those not present in the orginal file) have been inserted using bold italic text.

Example scene (UFF) file

```
1 -----  
2      3 ,Number of scatter types  
3 -----  
4 ./scatt_master_lists/water.list          Location of masterfile for scattering type 1  
5 ./scatt_master_lists/Col_hess_scatt_tilt_30.list Location of masterfile for scattering type 2  
6 ./scatt_master_lists/H2SO4_25.list       Location of masterfile for scattering type 3  
7 -----  
8      5 ,Number of atmospheric gasses  
9 -----  
10 O2  
11 N2  
12 CO2  
13 H2O  
14 O3  
15 -----  
16      nx,ny,nz (scene dimensions)  
17      20        20        105  
18 -----x1,y1,lat1,long1,z1-----  
19  0.0000  0.0000  0.0000  0.0000 -0.0500  
20 -----x2,y2,lat2,long2,z2-----  
21  10.0000 10.0000 0.0000  0.0000 110.0000  
22 -----  
23 Backgrnd scattering info (function of z only) Cloud+Aerosol properties specified in this section are treated as being horizontally homogeneous  
24 -----  
25 -5.0000001E-02           z(1)  
26  1    0                  No scatterers of Type 1 present  
27  2    0                  No scatterers of Type 2 present  
28  3    30                 Scattering of Type 3 (H2SO4 aerosol) are present (30 size bins)  
29 0.115734E+04 0.354767E+03 0.497820E+03 0.674572E+03 0.872755E+03 0.106188E+04 0.120090E+04 0.123399E+04 0.112370E+04 0.878024E+03  
30 0.564378E+03 0.283633E+03 0.104170E+03 0.257097E+02 0.383144E+01 0.301070E+00 0.104972E-01 0.130576E-03 0.439178E-06 0.280963E-09  
31 0.000000E+00  
32 5.0000001E-02           z(2)  
33  1    0  
34  2    0  
35  3    30  
36 0.115734E+04 0.354767E+03 0.497820E+03 0.674572E+03 0.872755E+03 0.106188E+04 0.120090E+04 0.123399E+04 0.112370E+04 0.878024E+03  
37 0.564378E+03 0.283633E+03 0.104170E+03 0.257097E+02 0.383144E+01 0.301070E+00 0.104972E-01 0.130576E-03 0.439178E-06 0.280963E-09  
38 0.000000E+00  
39 0.1500000           z(3)  
40  1    0  
41  2    0  
42  3    30  
43 0.115734E+04 0.354767E+03 0.497820E+03 0.674572E+03 0.872755E+03 0.106188E+04 0.120090E+04 0.123399E+04 0.112370E+04 0.878024E+03  
44 0.564378E+03 0.283633E+03 0.104170E+03 0.257097E+02 0.383144E+01 0.301070E+00 0.104972E-01 0.130576E-03 0.439178E-06 0.280963E-09
```

45 0.000000E+00
46 0.250000
47 .
48 .
49 .
50 .
51 1.950000
52 1 0
53 2 0
54 3 30
55 0.115734E+04 0.354767E+03 0.497820E+03 0.674572E+03 0.872755E+03 0.106188E+04 0.120090E+04 0.123399E+04 0.112370E+04 0.878024E+03
56 0.564378E+03 0.283633E+03 0.104170E+03 0.257097E+02 0.383144E+01 0.301070E+00 0.104972E-01 0.130576E-03 0.439178E-06 0.280963E-09
57 0.000000E+00
58 2.050000
59 1 0
60 2 0
61 3 0
62 2.150000
63 1 0
64 2 0
65 3 0
66 2.250000
67 .
68 .
69 .
70 120.0500 ***z(nz-1)***
71 1 0
72 2 0
73 3 0
74 130.0500 ***z(nz)***
75 1 0
76 2 0
77 3 0
78 -----
79 Info for column 1 1
80 -----
81 Surface type and sub 0 0
82 -----
83 0.250 0.250 0.0000 0.0000 -0.050 294.000 0.1013E+04 0.249561E+20 5
84 0.209460E+00 0.780840E+00 0.350000E-03 0.187564E-01 0.301714E-07
85 1.000 0.000 0.000 0.000
86 **x(1) y(1) lat long z(1) T(K) P(mb) ρ n/cm³ Number of gasses**
87 **Xv_gas1 Xv_gas2 Xv_gas3 Xv_gas4 Xv_gas5**
88 3 **3 scattering types**
89 1 0 **No scatterers of Type 1 present**
90 2 0 **No scatterers of Type 2 present**

```

91      3          0          No scatterers of Type 3 present
92      0.250     0.250     0.0000    0.0000    0.050   293.800  0.1007E+04  0.248285E+20
93      0.209460E+00 0.780840E+00 0.350000E-03 0.184709E-01 0.303263E-07
94      1.000     0.000     0.000     0.000
95      3
96      1          0
97      2          0
98      3          0
99      0.250     0.250     0.0000    0.0000    0.150   293.400  0.9955E+03  0.245755E+20
100     0.209460E+00 0.780840E+00 0.350000E-03 0.179131E-01 0.306383E-07
101     1.000     0.000     0.000     0.000
102 .
103 .
104 .
105 .
106 -----
107 Info for column           11       6
108 -----
109 Surface type and sub      0       0
110 -----
111     5.250     2.750     0.0000    0.0000   -0.050   294.000  0.1013E+04  0.249561E+20
112     0.209460E+00 0.780840E+00 0.350000E-03 0.187564E-01 0.301714E-07
113     1.000     0.000     0.000     0.000
114     3
115     1          0
116     2          0
117     3          0
118     5.250     2.750     0.0000    0.0000    0.050   293.800  0.1007E+04  0.248285E+20
119     0.209460E+00 0.780840E+00 0.350000E-03 0.184709E-01 0.303263E-07
120     1.000     0.000     0.000     0.000
121     3
122     1          0
123     2          0
124     3          0
125     5.250     2.750     0.0000    0.0000    0.150   293.400  0.9955E+03  0.245755E+20
126     0.209460E+00 0.780840E+00 0.350000E-03 0.179131E-01 0.306383E-07
127     1.000     0.000     0.000     0.000
128     3
129     1          0
130     2          0
131     3          0
132 .
133 .
134 .
135 .
136     5.250     2.750     0.0000    0.0000    1.550   287.250  0.8455E+03  0.213203E+20

```

137 0.209460E+00 0.780840E+00 0.350000E-03 0.113016E-01 0.353153E-07
138 1.000 0.000 0.000 0.000
139 3
140 1 50 **Cloud water (50 size bins) is present here.**
141 0.123018E+01 0.298457E+01 0.407303E+01 0.439185E+01 0.416218E+01 0.363526E+01 0.300111E+01 0.237749E+01 0.182506E+01 0.136661E+01 0.100296E+01 0.723956E+00 0.51
142 2 0
143 3 0
144 5.250 2.750 0.0000 0.0000 1.650 286.750 0.8357E+03 0.211079E+20 5
145 0.209460E+00 0.780840E+00 0.350000E-03 0.108982E-01 0.356707E-07
146 1.000 0.000 0.000 0.000
147 3
148 .
149 .
150 .
151 etc
152 .
153 .
154

G Example CLOUDSAT and EarthCARE radar Stratocumulus views.

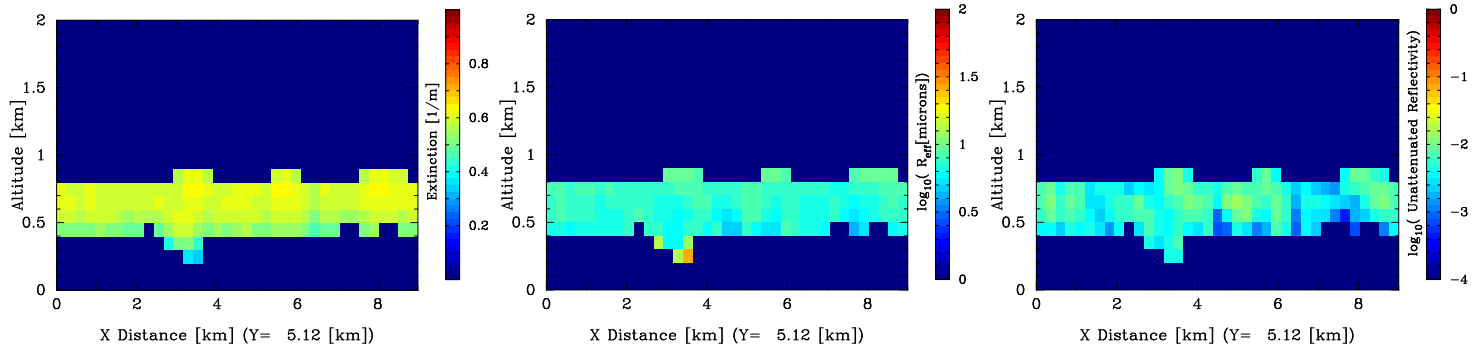


Figure 76: Extinction, effective radius and reflectivity for the UQAM ASTEX1_2 scene.

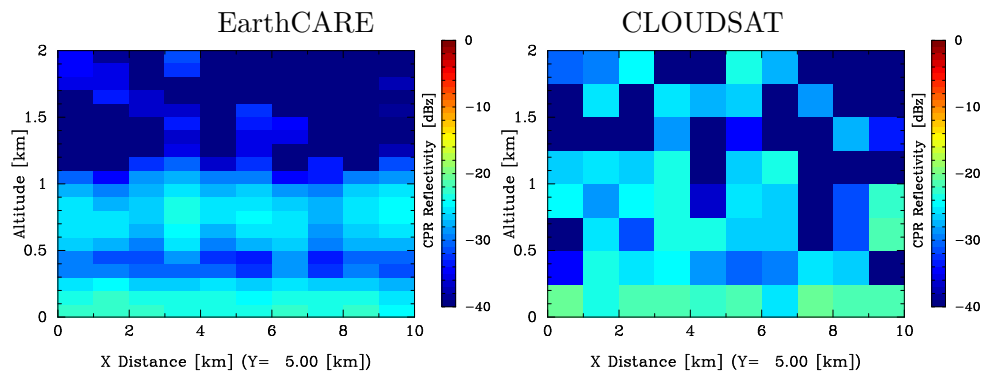


Figure 77: Measured reflectivities.

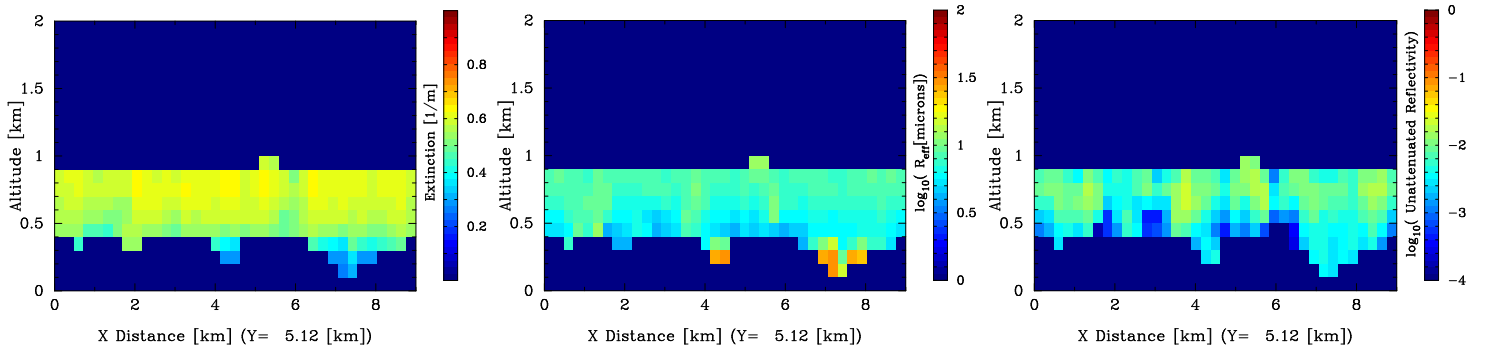


Figure 78: Extinction, effective radius and reflectivity for the UQAM ASTEX1_4 scene.

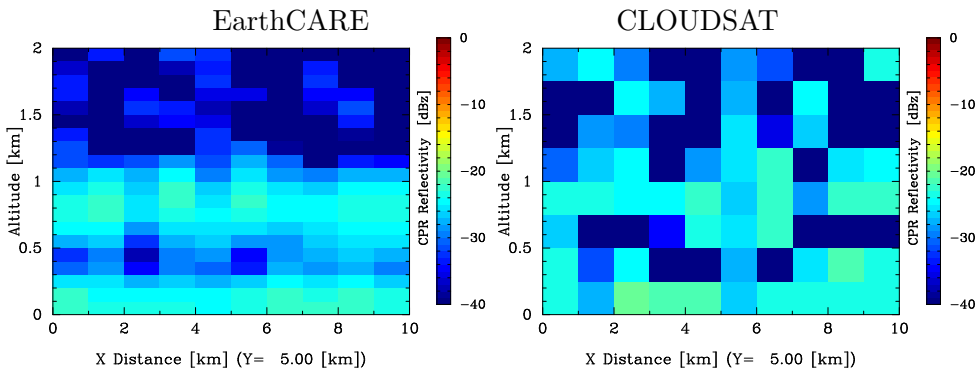


Figure 79: Measured reflectivities.

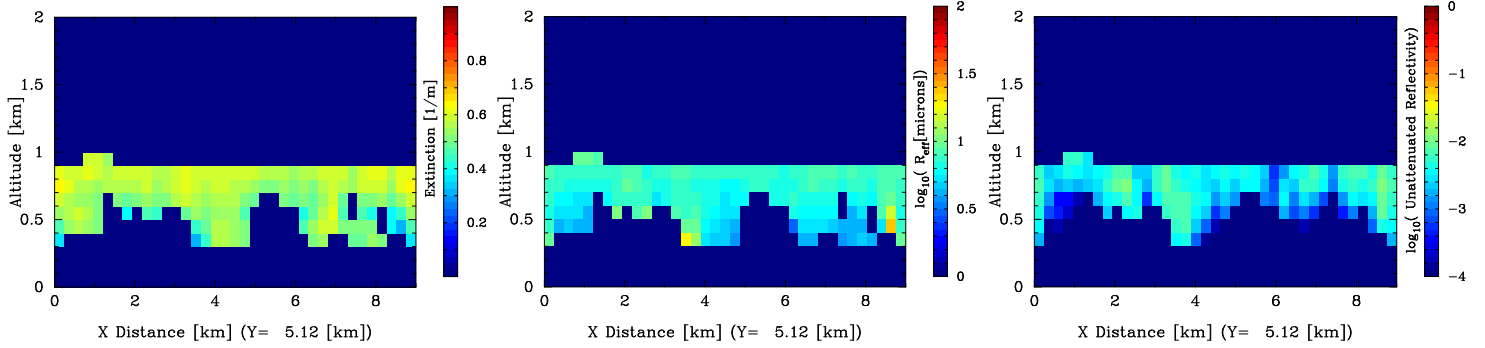


Figure 80: Extinction, effective radius and reflectivity for the UQAM ASTEX2_1 scene.

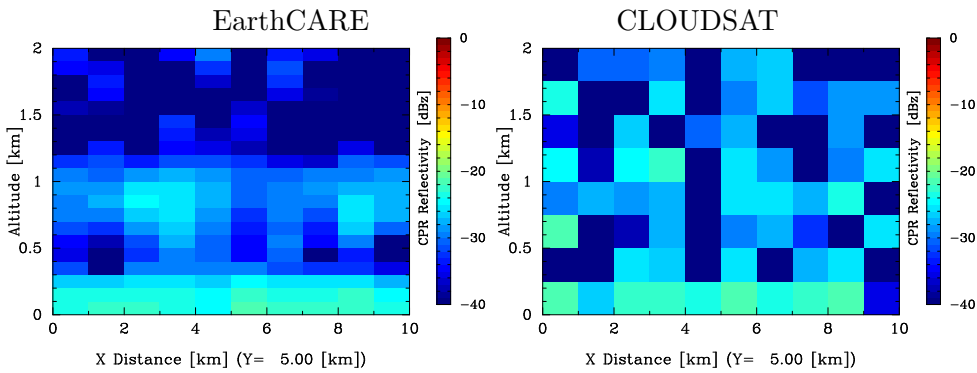


Figure 81: Measured reflectivities.

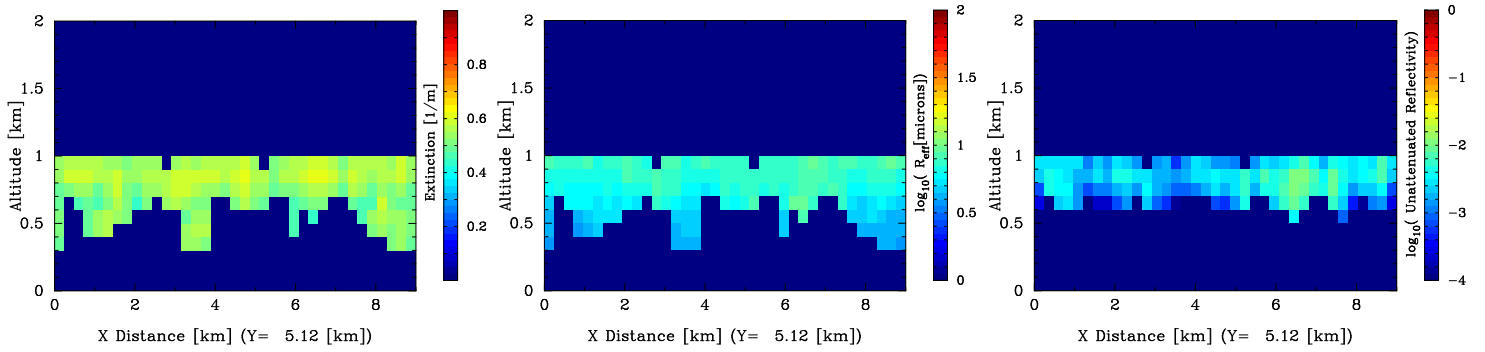


Figure 82: Extinction, effective radius and reflectivity for the UQAM ASTEX2_2 scene.

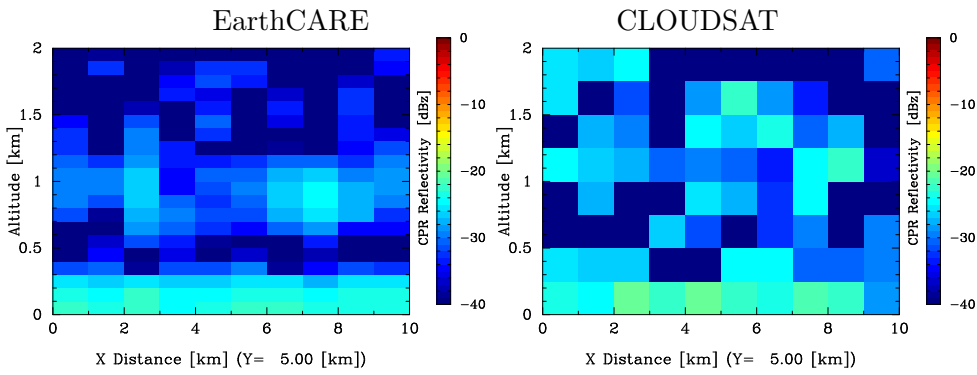


Figure 83: Measured reflectivities.

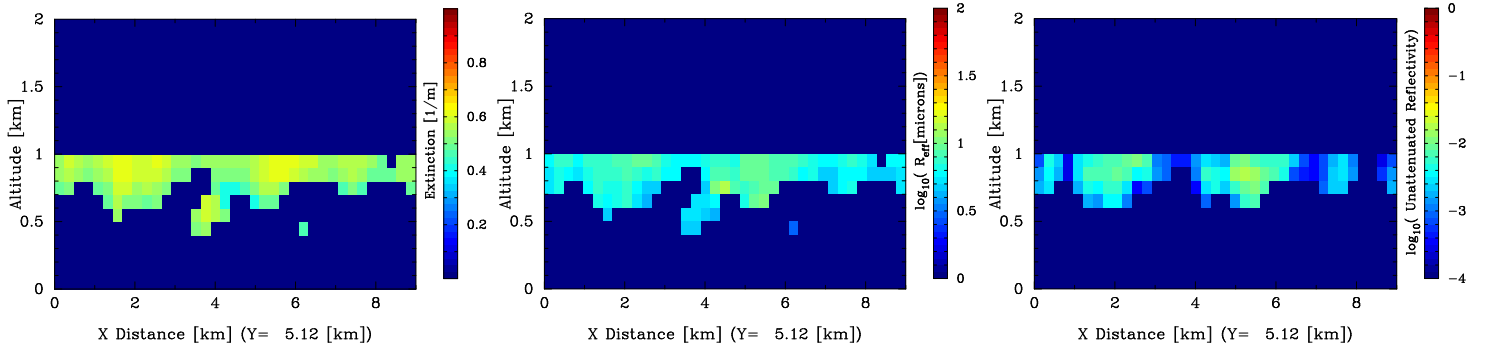


Figure 84: Extinction, effective radius and reflectivity for the UQAM ASTEX2_3 scene.

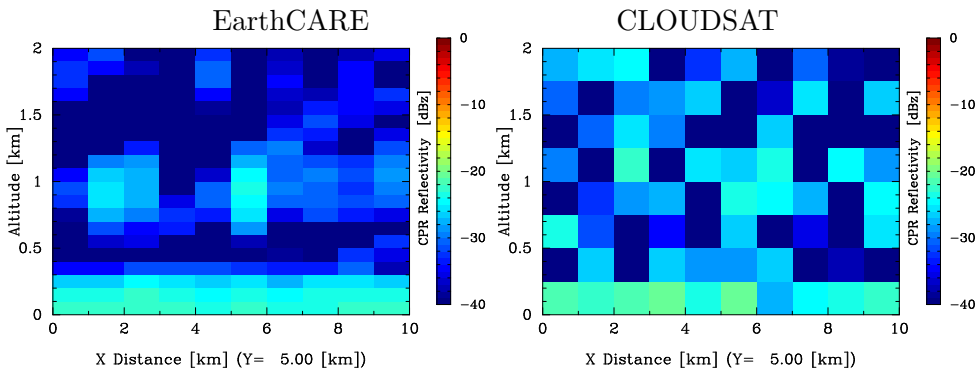


Figure 85: Measured reflectivities.

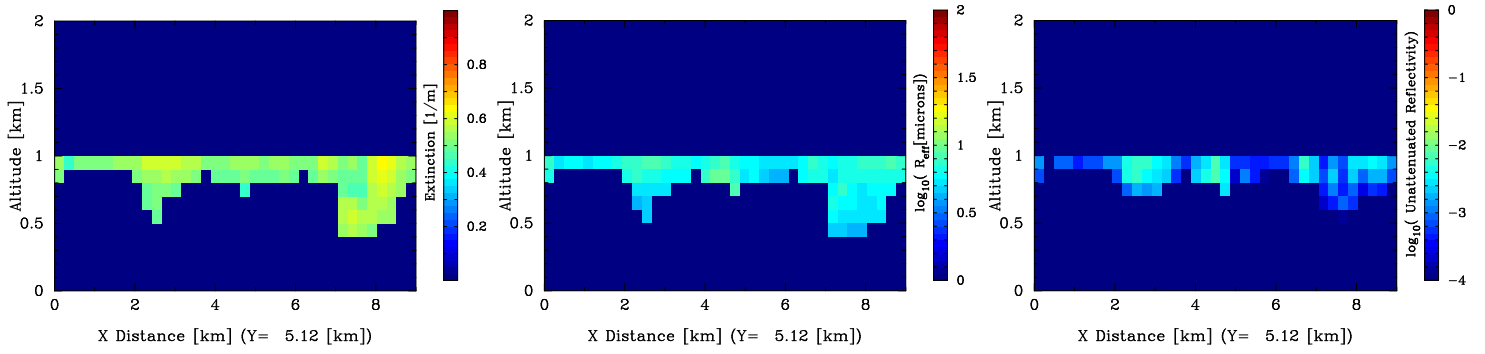


Figure 86: Extinction, effective radius and reflectivity for the UQAM ASTEX2_4 scene.

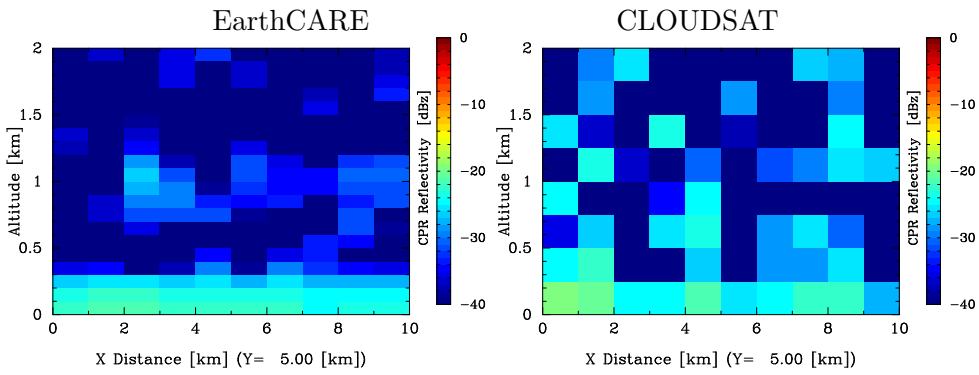


Figure 87: Measured reflectivities.

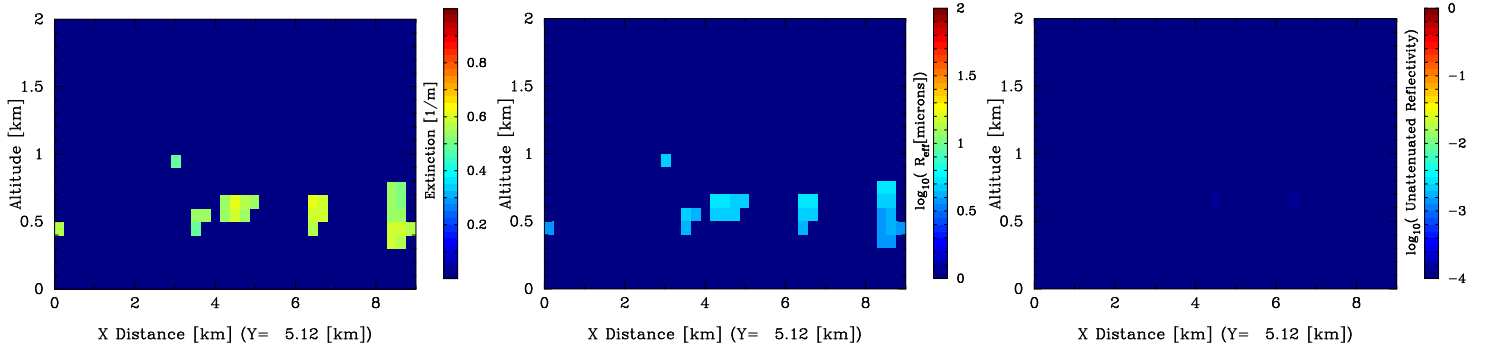


Figure 88: Extinction, effective radius and reflectivity for the UQAM ASTEX5_1 scene.

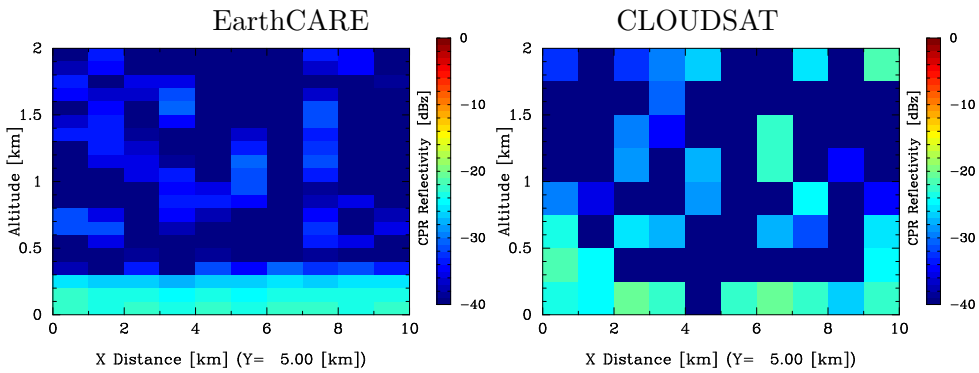


Figure 89: Measured reflectivities.

H RCM/NARCM/CRM model description

Because of the wide difference in processes involved and scales between clouds and aerosols, two versions of the Regional Climate Model (RCM) have been used in this study. One dedicated to the fine scales dominated by short characteristic times, mixing by small eddies and radiation. This is the Cloud Resolving Model (CRM). The second version is used to simulate large scale features like aerosols and cloud systems. The dynamic kernel, called MC2, is common to both versions.

The dynamical module that is a variant of the Canadian Mesoscale Community Compressible Model (MC2) (Tanguay et al. 1990; Bergeron et al. 1994; Laprise et al. 1997; Caya and Laprise 1999) is used in the RCM and adapted for use at very fine scale in the CRM. The model solves the fully elastic set of Euler equations using a semi-implicit marching algorithm designed to effectively slow down the high-frequency acoustic waves. It is combined with a three-time-level semi-Lagrangian advection scheme with tricubic (reduced to bicubic in two dimensions) spatial interpolation. For convenience in formulating a semi-implicit and semi-lagrangian time integration scheme, the thermodynamic variables (temperature and introduced dimensionless variable $q = \ln(p/p_o)$ where p_o is a constant reference pressure), are expressed in terms of a perturbation about the basic state. An isothermal atmosphere in hydrostatic equilibrium is used for the basic state. The spatial discretization uses the Arakawa-C type of staggering. A geometric altitude is used here as the vertical coordinate. The terms arising from the rotation and sphericity of the earth and orography are omitted in the CRM but included in the RCM.

H.1 Cloud Resolving Model Version (CRM)

The following further describes the cloud-resolving model (CRM) that is used to generate realistic model based scenarios. On top of the MC2 scheme described above, the 2D/3D cloud resolving model is composed of the following, fully coupled, parts:

1. The Smagorinsky-type subgrid turbulence scheme modified to include stability effects and calculations of turbulent mixing across cloud top (MacVean and Mason 1990). We are considering to use the turbulent kinetic energy closure scheme, with the energy as an additional prognostic variable as an alternative closure assumption.
2. The atmospheric radiation model for shortwave and longwave radiative transfer through clear, cloudy or partly cloudy air parcels the same as in the Canadian Regional Climate Model (CRCM) but adapted to fine-scale experiments and with cloud characteristics obtained from detailed microphysics scheme. For the thermodynamic equation, only plane parallel fluxes are considered to evaluate heating rates. For liquid clouds, the radiative parameters are calculated from droplets effective radius and liquid water content using the parameterization of Hu and Stamnes (1993), who performed an accurate non-linear fitting for different cloud droplet spectra with effective radii in the range from 2.5 to 60 microns.
3. A conventional one-moment bulk microphysical package with five hydrometeor categories: cloud droplets and ice crystals, raindrops, snowflakes and graupel particles is used.
4. A new bulk parameterization scheme for melting layer (Szyrmer & Zawadzki 1999) where wet snow is accounted for, besides its mixing ratio, is applied with an additional prognostic variable, namely, the diameter of the smallest snowflake not yet completely melted. This permits a more realistic transition between solid and liquid phases.

5. The detailed microphysics module predicting the evolution of the cloud droplet spectra (Brenguier and Grabowski 1993) in link with the CCN concentration. This scheme takes into account the major factors governing the evolution of the cloud droplet spectra in nonprecipitating clouds: nuclei activation, diffusional growth, and effects of mixing among parcels. In the formulation of this scheme, the conventional resolution in droplet size is replaced by so-called b^2 representation that is equivalent to the resolution in droplet surface. It is more practical since a surface distribution is only translated by adiabatic condensation/evaporation process and its shape remains unchanged if the solute and curvature effects are neglected. The elementary droplet population (EDP) is defined as an ensemble of droplets following the same trajectory after activation of their CCN. The spectrum of an EDP is simply derived from its spectrum after droplet activation by a translation on the r^2 scale. The translation b^2 represents the integral of supersaturation along the droplet trajectory in the cloud. Droplet spectra are expressed as a linear combination of spectra from EDPs. The probability of occurrence of each EDP, the probability density function, PDF, are the model prognostic variable, their advection and turbulent mixing are computed in physical space within the dynamical and turbulent modules. The effective radius of droplet population is calculated easily from the PDFs using the stored values of the second and third moments associated with each EDP. The parameters in the initial (nucleation) spectrum are related to the CCN activation spectrum.
6. The bulk scheme describing the drizzle category with prediction of two prognostic variables: concentration per unit mass (number mixing ratio) and mass mixing ratio. This relatively simple, computationally efficient scheme has been developed by Khairoutdinov and Kogan (2000) using a LES model with explicit microphysics as a data source and benchmark for comparison. Within this scheme, the shape of the drop size distribution is not prescribed explicitly. The rates of microphysical processes, the mass concentration and fall velocities are calculated from mass and concentration mixing ratio.

The separation radius between cloud water droplets and precipitable drizzle is fixed at $19\mu\text{m}$. The growth of droplets smaller than this radius is determined mainly by condensation process, while for the larger drops the accretion of smaller droplets is the dominant mechanism. The last process cannot be treated within the scheme of Brenguier-Grabowski (BG) used to describe the cloud droplet spectrum evolution growing by condensation. Moreover, the sedimentation that becomes non negligible for larger drops is also excluded from the BG scheme. The modal approach for droplets larger than 19 microns (drizzle mode) removes this constrain.

Three processes assure the transfer of liquid water droplets from cloud to drizzle category: *i.* Transfer of the largest droplets that grew via condensation only due to the long in-cloud residence time associated with the inhomogeneous entrainment process; *ii.* Conversion via collision-coalescence between cloud droplets (so-called autoconversion); and *iii.* Accretion of cloud droplets by the larger falling drizzle drops. The parameterization of the two last processes follows that in Khairoutdinov and Kogan (2000).

The introduction of the drizzle category needed some modifications and additions to the BG scheme, mainly:

In the presence of drizzle, the amount of condensation (evaporation) necessary to remove any supersaturated vapor (any saturation deficit) is partitioned between cloud and drizzle in proportion to the integral radius of each category; for evaporation, the partitioning takes into account the limits imposed by the amount of each category there are to evaporate.

The precalculated droplet integral radii for each EDP are used to the calculation of the integral radius of the whole cloud droplet spectrum from the PDFs.

An additional prognostic variable is added to the description of the cloud liquid water: the droplet concentration deficit in cloudy homogeneous undiluted part. This deficit is caused by the droplet transfer to the drizzle category. The tendency of the droplet concentration deficit is calculated for the three processes of the cloud droplet transfer to drizzle.

In the transfer to the drizzle category of the largest droplets grown by condensation, a zero value is put for the PDFs of the transferred EDPs. To maintain during this process the unchanged value of β (part of the air within the grid box being cloudy), the PDFs of the all EDPs not transferred to drizzle are adjusted. The PDFs are not modified in the conversion via the stochastic coagulation (autoconversion) and accretion processes.

Because we need the complete droplet distribution, we have to assume a particular form for the drizzle size distribution. We choose it to be an inverse normalized exponential function as in Wood (2002). The parameters defining the shape are found by continuity of the distribution function at the radius size separating the two droplet categories.

The model has been successfully tested with different spatial resolutions:

- A few microns: study of air flow and cloud droplet trajectories around the airborne temperature sensor (Szysrmer 1998)
- tens of meters: atmospheric melting layer (Szysrmer and Zawadski 1999) in summertime Arctic stratus.
- Hundred(s) meters: warm rain formation (Szysrmer 1998).
- Thousand(s) meters: supercooled clouds in the presence of snow with the kinematics version of the model (Zawadzki et al. 2000).

H.2 NARCM Version of RCM

To the standard RCM, we have added extensive treatment of aerosols microphysics (Gong et al, 2000). The RCM version that includes aerosols is the Northern Aerosol Regional Climate Model (NARCM).

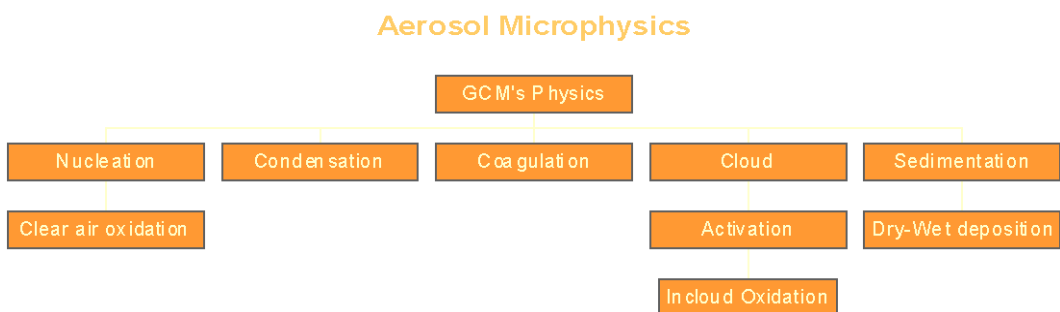


Figure 90: Diagram showing the structure of aerosol processes and routines within the physics package of the circulation model. (Gong et al, 2000)

The parameterization of the subgrid processes in RCM/NARCM is summarized in Fig. 90. They are borrowed from the physics package of the Canadian General Circulation Model (GCM) (McFarlane et al, 1992). It includes mixed layer ocean with thermodynamic ice, deep and shallow convective clouds, atmospheric and solar radiation, land processes like ponds and lakes, vegetation, CLASS hydrology, orography and rivers. In NARCM, a particular

attention is placed on cloud and aerosol microphysics: sources of wind driven soil, DMS and sea salt aerosols, for anthropogenic emission of sulfur, organics and black carbon. Aerosol microphysics includes nucleation of new particles, coagulation, condensation, deposition, basic oxidation chemistry, in cloud oxidation of SO_2 , wet and dry removal processes. The added aerosol modules are shown in a structured diagram in Fig. 90

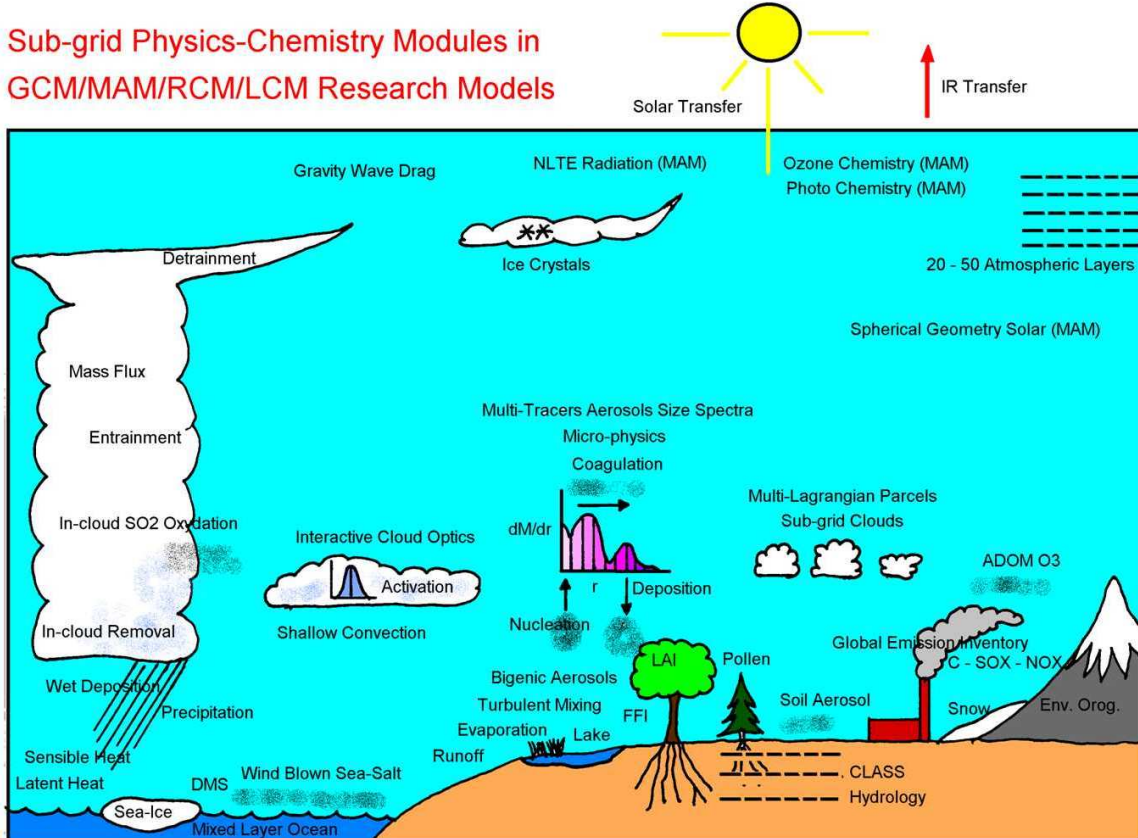


Figure 91: Schematic of the subgrid parameterized physical processes included in within each grid cells of full atmospheric circulation models (RCM). They are mixed layer ocean with thermodynamic ice, deep and shallow convective clouds, atmospheric and solar radiation, land processes like ponding, vegetation, CLASS hydrology, orography and rivers. A particular attention is placed on cloud and aerosol microphysics: sources of wind driven soil, DMS and sea salt aerosols, for anthropogenic emission of sulfur, organics and black carbon. Aerosol microphysics include nucleation of new particles, coagulation, condensation, deposition, basic oxidation chemistry, in cloud oxidation of SO_2 , wet and dry removal processes. The aerosol is represented by 12 bin size spectra and 5 species requiring 60 dynamic tracers to be exchanged by advection and convection with neighboring grid cells. A gridded frame treated by the model is composed of the order of one million cells of this type; each has a similar set of physical processes.

The aerosol model is generated by a detailed microphysics scheme within NARCM. The model is resolving species and size distribution in space and time domain. The scheme is based on the generic prognostic equation for active tracers with multiple sources and sinks. The physics involved in the model is summarized in Fig. 91. It is part of a larger package representing most of the atmospheric processes. In that respect, the cloud scenes generated by the model are consistent with the process orientation of EarthCARE.

In the current version, a total of 5 species with 12 size bins are used to represent broad types of aerosol materials: sulfate, soot, soil, sea salt and organics. Sulfate, soot and organics have both natural and anthropogenic sources while soil and sea salts are considered to be

natural in origin. The total aerosol distribution requires 60 prognostic equations similar to the above equation. One for each size ranges and each material type. The ensemble of 60 tracers describes the evolution of aerosol composition and shape of the particulate spectra at each point in space and at each time step. This is the most general representation of aerosol in today's models. The simulation can only be improved by increasing the resolution of size and species and refining the microphysical processes.

H.3 References

- Bergeron, G., R. Laprise, and D. Caya, 1994: *Formulation du modèle de mésoscale compressible communautaire (MC2)*. Centre coopératif pour la recherche en mésométéorologie (CCRM), 165 pp.
- Brenguier, J.-L., and W. W. Grabowski, 1993: A numerical model of droplet spectral evolution in small nonprecipitating cumulus. *J. Atmos. Sci.*, **50**: 120-136.
- Caya, D., and R. Laprise, 1999: A semi-implicit semi-lagrangian Regional Climate Model: the Canadian RCM. *Mon. Wea. Rev.*, **127**: 341-362.
- Gong S, Barrie L and Blanchet J-P, 1997: Modelling Sea-salt Aerosol in the Atmosphere: Model Development. *J. of Geoph. Res.* **102** 3805.
- Gong S, Barrie L, Prospero J M, Savoie D L, Ayers G P, Blanchet J-P, and Spacek L 1997: Modelling Sea-salt aerosols in the atmosphere: 2. Atmospheric Concentrations and Fluxes. *J. of Geoph. Res.* **102** 3819.
- S.L. Gong , L.A. Barrie , J.-P. Blanchet , K. von Salzen, U. Lohmann, G. Lesins, D. Lavoué, J. Jiang, H. Lin, E. Girard, R. Leatch, H. Leighton, P. Chylek and L. Spacek : CAM: Treatment of the size segregated atmospheric aerosols for climate and air quality models: 1. Module Development, *J. Geophys. Res.*
- Hu, Y. X., and K. Stamnes, 1993: An accurate parameterization of the radiative properties of water clouds suitable for use in climate models. *J. Climate*, **6**: 728-742.
- Khairoutdinov, M., and Y. Kogan, 2000: A new cloud physics parameterization in a large-eddy simulation model of marine stratocumulus. *Mon. Wea. Rev.*, **128**: 229-243.
- Laprise, R., D. Caya, G. Bergeron, and M. Giguère, 1997: The formulation of André Robert MC2 (Mesoscale Compressible Community) model. In The André J. Robert Memorial Volume (C. Lin, R. Laprise, and H. Ritchie, Eds.), companion volume to *Atmos.-Ocean*: 195-220.
- McFarlane, N.A., G.J. Boer, J.-P. Blanchet, and M. Lazare. 1992: The Canadian Climate Centre Second Generation General Circulation Model and its Equilibrium Climate. *J. Climate*.
- MacVean, M. K., and P. J. Mason, 1990: Cloud-top entrainment instability through small-scale mixing and its parameterization in numerical models. *J. Atmos. Sci.*, **47**: 1012-1030.
- de Roode, Stephan R., and Peter G. Duynkerke, 1997: Observed lagrangian transition of stratocumulus into cumulus during ASTEX: mean state and turbulence structure. *J. Atmos.*

Sci., **54**: 2157–2173.

Szurmer, W., 1998: *Étude des processus microphysiques dans l'atmosphère à l'aide d'un modèle numérique*. Ph.D. thesis, Université du Québec à Montréal, Montréal, Québec, Canada.

Szurmer, W., and I. Zawadzki, 1999: Modeling of the melting layer. Part I: Dynamics and Microphysics. *J. Atmos. Sci.*, **56**: 3573–3592.

Szurmer, W., J.-P. Blanchet, I. Zawadzki, and R. Laprise, 1999: Fine scale condensation processes at varying resolution: Sensitivity study within NARCM, *28th Congress CMOS*, Montréal, Canada.

Tanguay, M. A. Robert, and R. Laprise, 1990: A semi-implicit semi-lagrangian fully compressible regional forecast model. *Mon. Wea. Rev.*, **118**: 1970–1980.

K. von Salzen, H. G. Leighton, L. A. Barrie, S. L. Gong, J.-P. Blanchet, L. Spacek and U. Lohmann, 2000: The sensitivity of sulphate aerosol over North America to changing anthropogenic sulphur emissions. *J. Geophys. Res.*

Wood, R., 2002: Drizzle in stratocumulus clouds: observations and model results. 11th conference on cloud physics.

Zawadzki, I., W. Szurmer, and S. Laroche, 2000: Diagnostic of supercooled clouds from single-Doppler observations in regions of radar-detectable snow. *J. App. Meteor.*, **39**: 1041–1058.

I Generation of the cloud scenes

The cloud model that is used in the generation of the cloud scenes has been described briefly in H. The objective is to generate various high spatial resolution cloud fields containing order of a million of grid points with detailed microphysics that can be used for the instruments simulator.

To produce input dataset with a high level of physical basis can only be achieved by adjusting the model resolution of the fluid dynamics representation to the range that controls the cloud formation and its evolution. This resolution depends on the type of could that we need to simulate. Two cases have been identified as prime interest for the EarthCARE simulator study: the boundary layer stratocumulus family and the upper troposphere cirrus family. In these two cloud categories, processes are dominated by different scales. In the first part of the project, we have focused on warm clouds composed of liquid droplets. This is essentially the case in low level clouds.

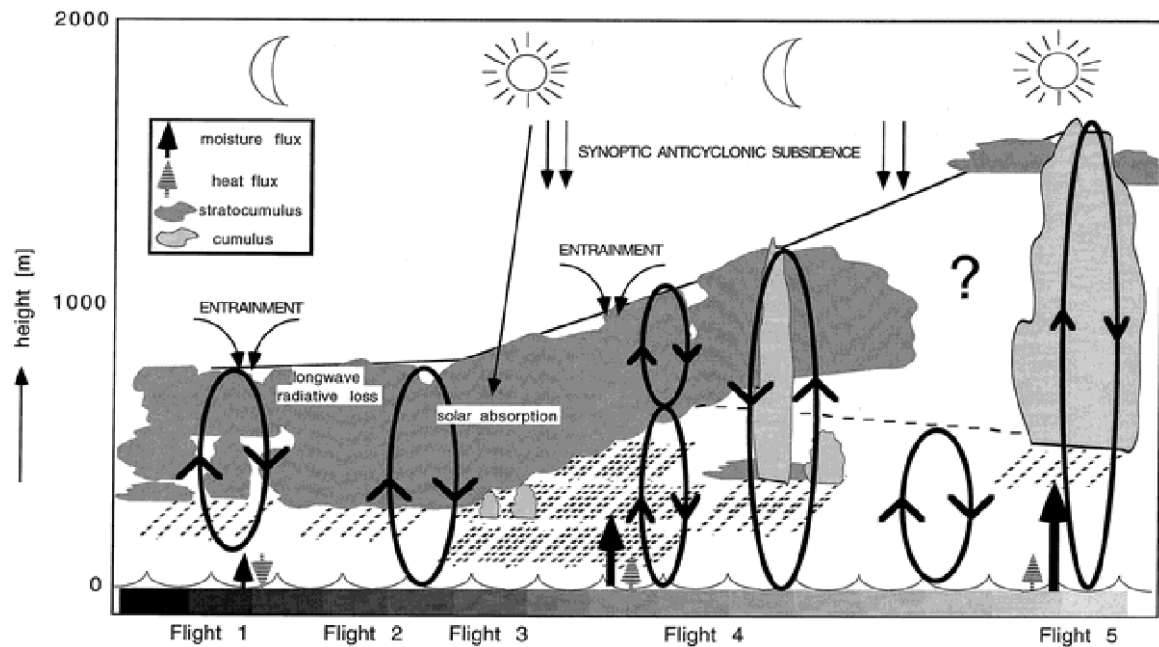


Figure 92: A schematic of the cloud evolution as observed during the First Lagrangian of ASTEX between 1719 UTC 12 June 1992 and 1302 UTC 14 June 1992. The flights are indicated below the horizontal border. The horizontal distance between Flights 1 and 5 is approximately 1300 km. The grayscale in the lowest horizontal bar represents changing sea surface temperature, with increasing values from left to right. Fluxes of moisture and heat and cloud type are indicated according to the legend. The magnitude of the arrow is proportional to the flux. Day-night changes are schematically represented by the sun or moon symbol. (From Fig. 2 of de Roode and Duynkerke, 1997)

I.1 Cloud types

The second issue is the generation of different cloud types. The three cloud types that are of interest are stratocumulus with drizzle, cumulus and cirrus.

The actual strategy for stratocumulus and cumulus follows Fig. 8.1 from de Roode and Duynkerke (1997). In this figure, we can observe the gradual change in cloud morphology and dynamic forcings from north to south (left to right). Starting with low stratocumulus, we observe a gradual evolution towards cumulus clouds. In the model, we propose to recreate in part this evolution by generating evolution of stratocumulus cases (Flights 1 to 4 on the

figure) and a separate cumulus cases. In the generating model, various parameters can be adjusted at any time during the integration to control the cloud properties. The parameters used to control the cloud evolution are:

- Lateral humidity advection
- Lateral temperature advection
- Background subsidence
- Incident solar radiation (solar intensity, zenith angle, day/night)
- Vertical wind shear
- Surface heat and humidity fluxes
- Upper boundary fluxes

At each desired time-interval, all prognostic variables can be allowing to restart any points along the time integration or to bifurcate towards an alternative cloud evolution. This procedure is very flexible. It permits to simulate various cloud evolution cases beginning from or a single adjusted field avoiding the spin-up time.

Stratocumuli are dominated by turbulent mixing at cloud edges with characteristic sizes of a few tens of meters. It is strongly influenced by the characteristics of the underlying surface. Surface temperature anomalies or irregular orography will influence the cloud structure. On the other hand, mixing at the cloud top produces evaporation and local cooling. Denser air starts to accumulate and sink while competing with updrafts. The active downdraft poke holes in the cloud field. This is shown in figure 7.2. Updrafts produce adiabatic cooling and condensation on existing droplets.

If no droplets exist in supersaturated air, the water will condense on aerosol to form fine droplets. These new droplets are predominantly located at the cloud base. They are hard to detect for the radar instrument but may be seen by the lidar in thin cloud layers. Fortunately, they are radiatively less important than the large droplet dominating in the body of the cloud.

The larger droplet appears near the cloud top where longer paths of condensation lead to water accumulation and possibly to coalescence for droplets exceeding $15\mu\text{m}$ and becoming dominant above $20\mu\text{m}$. The stochastic process in coalescence leads rapidly to precipitating size droplets in that range. Precipitation is a strong limitation on the total cloud water content in a layer.

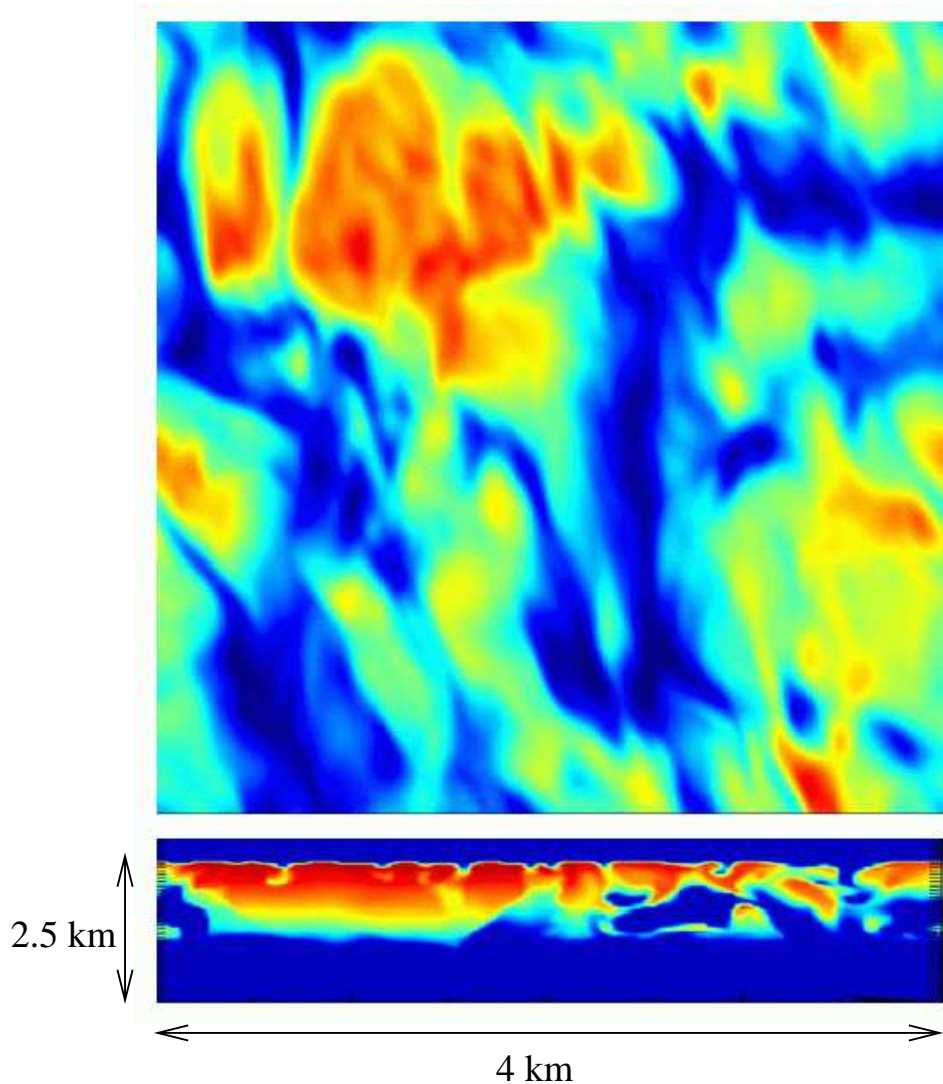


Figure 93: Single frame ($4 \times 4 \times 2.5 \text{ km}$ or $160 \times 160 \times 100$ points) showing the integrated liquid water path in stratocumulus field (upper part) and vertical cross section of effective radius for similar region (lower part). (Szyrmer 2002)

This is the reason for starting our drizzle model at $19\mu\text{m}$ (figure 7.3). These droplets dominate the radar reflectivity and lead to detection signals. It also attenuates the radar and the lidar signal to the expense of detecting lower portion of the clouds.

Above this region of maximum droplets size, the cloud top entrainment increasingly dominates and evaporates droplets and cools the air. In the upper region, eddies of various sizes produce filament of mixed clear and cloudy air. This represented by the prognostic equation of the Brenguier scheme using the b parameter which is the volume cloud fraction. Its value is generally 1 inside clouds but become a fraction in edges.

The transition region between clear and cloudy air can be very shallow in case where the boundary layer is capped by a strong thermal inversion. In unstable conditions, the cloud stretches vertically and the mixing region becomes much looser and spread out. Experiences have shown that in stratocumuli model resolution of 10 to 30 m are necessary while in small cumulus, a resolution of 30 to 60 m is adequate. This allows us to reduce the resolution in cumulus to the benefit on extending the vertical region where these cloud forms.

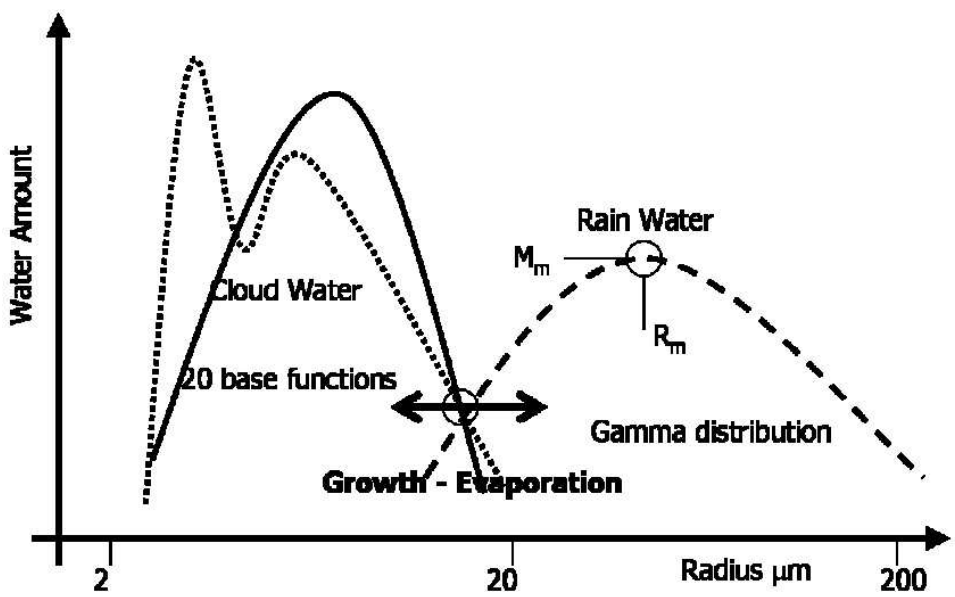


Figure 94: Schematic representation of the droplets model. In the small droplets region, an explicit representation is used (BG) with 20 EDP base functions. In the large droplet region, one mode is used with moments for number and mass concentration. Matching is done at $19\mu\text{m}$.

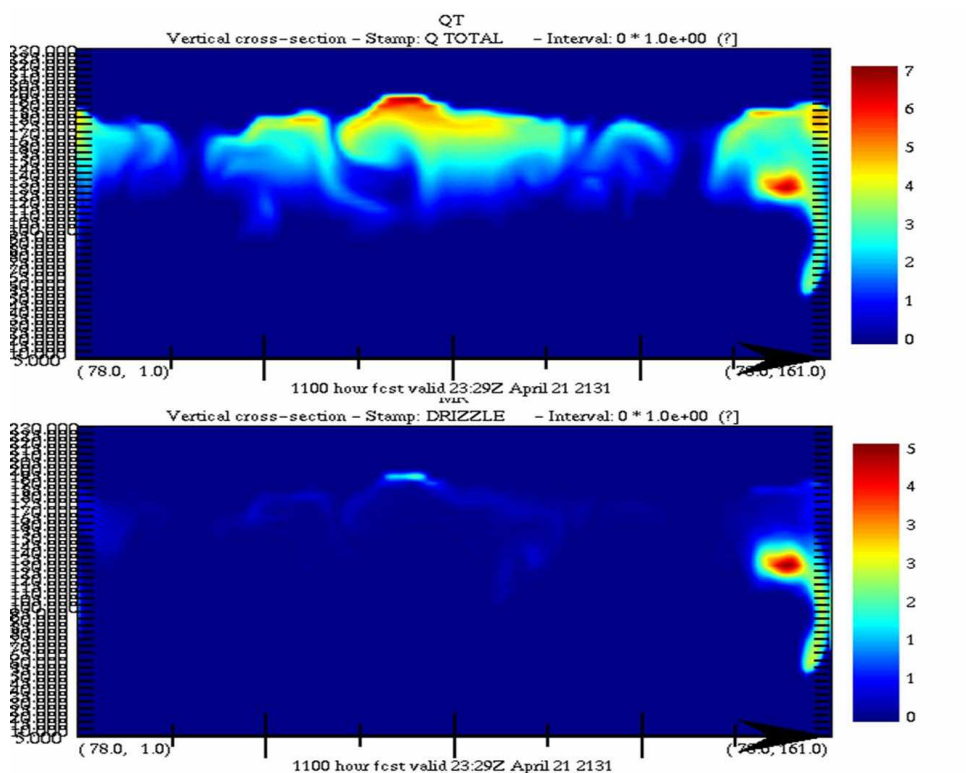


Figure 95: Single frame ($4 \times 4 \times 2.5 \text{ km}$ or $160 \times 160 \times 100$ points) showing the cross section of total liquid water path in stratocumulus field (upper part) and drizzle water content only (lower part). (Szyrmer 2002)

I.1.1 Stratocumulus with Drizzle

Precipitation is limited to the initiation stage for droplets between 20 and $50\mu\text{m}$. It corresponds only to the early stage of warm precipitation in clouds. Since the radar instrument on board the mission saturate quickly in precipitation and little signal is expected for larger droplets, this choice is adequate for the EarthCARE simulator.

The simulation of the initial stage of precipitation in stratocumulus is illustrated in Fig. 95. We refer to it as drizzle due to the characteristic size of droplets in that range. As discussed in the non precipitating cloud case, large droplets form in the upper region of the cloud and are more likely to reach the precipitation size. The water in the drizzle mode is a distinct prognostic variable. Simulation shows clearly the dynamical process of precipitation formation. It is mostly generated by condensation and coalescence in updraft regions. In the first stage, precipitation water accumulates in upper region of the clouds. It is suspended into the updraft reaching semi equilibrium between production growth and sedimentation. As the mass of precipitating water increases, the gravitational weight on the cloud imposes a drag on the opposite updraft. At some point the vertical lift can collapse and open the way to precipitation shafts. Alternatively, the mass of precipitation can find its way in the cloud and “leak” on the sides where downdraft dominates.

As precipitation progresses downward it has to compete against updrafts. It can evaporate or be pushed upward but other times it finds its way to the surface. Evaporation is another important factor in determining the depth of precipitation. Dry air may evaporate the precipitation while moist updraft can increase the condensation rate. This process is a complex balance between dynamical and thermodynamic processes. It is important to have them reproduced in physically based manner so that we can assess the extent to which the EarthCARE instruments can capture the cloud structure and evolution together with precipitation. Resolution and sensitivity of the instruments will be a key factor in performance of these measurements.

For drizzle, water mass and drops concentration are the two parameters available to define variables carried prognostically during the time integration. Starting with a specified drop size distribution shape, we can calculate the mean size and corresponding concentration. However the distribution shape and the merging point with small cloud droplets are prescribed. We follow the suggestion of Wood (2002). From various flights observations of drizzle, he concluded that the size distribution could be well represented by an inverse normalized exponential.

I.1.2 Cumulus Clouds

We must simulate independently stratocumulus and cumulus cases since they are controlled by different dynamic conditions. Cumulus clouds require an adequate resolution of updrafts inside cells and downdrafts in the cloud environment. Hence, an adequate grid resolution for cumulus clouds is 50m in the horizontal resulting in an 8km x 8km horizontal frame for an horizontal grid of 160 x 160 cells. Vertical resolution would remain unchanged at 25m.

I.1.3 Cirrus Clouds

Cirrus must be treated using a different scheme than low level warm clouds for two reasons: they require ice cloud microphysics and their altitude need a particular grid definition focusing on the cloud region with adequate resolution. Experiments indicate that a resolution around 100m is adequate for most cirrus. The main reason is that in general eddies affecting the cloud evolution are typically larger than in the boundary layer and the cloud life cycle leads to longer characteristic time scales.

The cloud resolution in the mid and upper troposphere is achieved by steps. First, we start with Objective analysis for NMC reanalysis to provide initial conditions and boundary condition during integration. Next, we run a low resolution simulation, typically near 50km grid cells, to reproduce the large scale features corresponding to the date and time of observations. At this stage we produced a coarse time series of a real case sequence of the meteorology. Then we begin identifying the region of interest where particular cloud type are to be further detailed. Only simple bulk microphysics is needed at this stage. From the coordinate and dimension of the region of interest we determine the resolution necessary to resolve the cloud processes. This permits us to initiate an increasing resolution cascade reaching the resolved cloud range. For short runs corresponding to the characteristic time scale of the cloud, we can accept a variable vertical grid having a higher density of level in the cloud region. The other regions of low interest can be treated at lower resolution. As a general rule, at each stage of the zooming cascade we increase the resolution by a factor 5. Once the desired scale is reached, we include the detailed cloud microphysics and use the next lower resolution scale to drive the current one. The final simulation is typically of the order of a few hours. This strategy is in development and will soon be tested. In this way, we are attempting to build a database of cloud frames to be used individually or in a composite atmosphere.

The cloud microphysics is based on a bulk scheme. The particle size is represented by two modes with double moments approach. The small mode represent ice crystals that do not precipitate significantly (smaller than $50\mu\text{m}$) while the second mode represents the ice crystals with significant terminal velocity. Each mode has two prognostic variables corresponding to number concentration and mass concentration. The distribution width is prescribed with a matching condition between the two modes.

I.1.4 Bulk microphysics for cirrus

Microphysical prognostic variables; description of hydrometeor categories The mixing ratios of mass (q_x) and number concentration (N_x/ρ_a with N_x : concentration, ρ_a : air density) are predicted for three following categories of condensed water:

- cloud droplets (c) with negligible fall speed
- pristine ice crystals (i) with diameter $D_i < D_{smin}$
- snow crystals (s), individual larger crystals or aggregates with diameter $D_s \geq D_{smin}$.

Moreover, the number concentrations:

- of aerosol particles (N_a), larger than about $0.1 \mu\text{m}$, and
- of population of potential ice-forming nuclei, IFN, (N_n)

are introduced as tracers in the model. N_n is a subpopulation of N_a . The droplet activation/evaporation and ice nucleation/sublimation processes are the rates of changes of N_a and N_n . Thus, the rates of these processes are limited by the number advected particles of appropriate category.

The concept of two modes for solid particles, corresponding separately to small ice particles with large number concentration, and larger crystals with lower number concentration, is used in many recent models. It is based on the fact that observed crystal size distribution in the cirrus clouds are very frequently characterized by a high incidence of such bimodality (among others: Mitchell et al. 1996, Ryan 2000). The chosen value for D_{smin} that separates the two categories is $100 \mu\text{m}$. It is in accord with the fact that the dimensional relationships for mass and area, and consequently fallspeed, change, in general around $D=100 \mu\text{m}$ for a given crystal habit (Mitchell 1996; Khvorostyanov & Curry 2002)

In the presented parameterization, the growth by vapor diffusion and aggregation are considered as the growth mechanisms for the category of the pristine ice. The riming process

does not occur on small ice particles (smaller than 50-150 μm depending on the crystal habit) and thus, it does not need to be introduced. Comparatively to the vapor diffusional growth, the aggregation process is much less important for this category of crystals.

The sedimentation process is associated with the two ice categories even than the pristine ice crystals have relatively small fall speed, their Re (Reynolds number) is around 1. The reason is that the sedimentation process is likely to have a strong impact on the buildup or decay of cloud ice mass and cloud lifetime, and consequently on the cloud radiative forcing. The comparison of different model results within WG2 project (GCSS Working Group 2 on cirrus cloud systems) identified the ice water mass flux as potentially a key factor influencing the discrepancy between models, the ice fallspeed being a critical variable within the bulk model.

a. Size distributions

The specified continuous particle size distribution, assumed for each of the three hydrometeor category, is represented by a generalized gamma distribution described by Walko et al. (1995):

$$n(\xi) = N \frac{1}{\Gamma(\mu)} \frac{1}{\xi_n} \left(\frac{\xi}{\xi_n} \right)^{\mu-1} \exp \left[-\frac{\xi}{\xi_n} \right] \quad (73)$$

N : Total concentration of particles per unit volume of air (cm^{-3}) for non truncated distribution.

μ : Shape of the distribution, independently specified for each category; it controls the relative amount of smaller vs. larger hydrometeors in the distribution and is related to the distribution relative variance

ξ_n : Scaling dimension, i.e. distribution characteristic size used to nondimensionalize ξ ; it is related to the mean value by

$$\bar{\xi} = \frac{\int_0^\infty \xi n(\xi) d\xi}{\int_0^\infty n(\xi) d\xi} = \mu \xi_n \quad (74)$$

The symbol $\xi_{\bar{m}}$ is used to describe the size of the particle having mean mass, i.e. its mass is equal to the water content of given category divided by number concentration.

For liquid hydrometeors, ξ describes the droplet volume ($\xi = V \equiv \frac{\pi}{6} D^3$ and $\xi_n = V_n$, as in Ziegler, 1985), while for solid hydrometeors, the distribution is in terms of particle diameter, D ($\xi = D$ and $\xi_n = D_n$, as in Walko *et al.*, 1995). The shape parameters are chosen equal to 1 for cloud components: liquid water (as in Williams and Wojtowicz, 1982; Carrio and Nicolini, 1999 and others) and cloud ice (as in Harrington *et al.*, 1995; Field, 2000). The value of 3 is imposed for snow distribution expressed in terms of diameter following Harrington *et al.* (1995). However, these values may be changed, especially for solid categories. For example, these shape parameters may differ for tropical and mid-latitude cirrus.

b. Ice particle characteristics; treatment of the different ice habits

The power-law relationships between the individual x -category particle size and their mass (m_x), projected area (p_x), and terminal velocity (u_x) are assumed. They have the following general forms:

$$m_x(D) = \alpha_{m,x} D^{\beta_{m,x}} \quad (75)$$

$$p_x(D) = \alpha_{p,x} D^{\beta_{p,x}} \quad (76)$$

$$u_x(D) = \alpha_{u,x} D^{\beta_{u,x}} \quad (77)$$

where $x = i$ or s . The coefficients and exponents in the above relations depend on crystal habit. For most habits, two or three values of coefficients are necessary to cover the full range of observed crystal sizes. Moreover, the different crystal shapes have different forms for the

capacitance in the equation for the rate of vapor deposition, besides the different ventilation effect. The collection efficiency depends also on the crystal habit. And, of course, crystalline habit is very important to the radiative properties of clouds.

The model does not keep track of the history of crystal population, and thus of their habits. The relative abundance of different ice crystal shapes is diagnosed in each gridpoint in function of ambient temperature and mean size of crystals (it is planned to introduce also dependence on the cirrus cloud type: the percentage of different shapes seems to be different within mid-latitude vs tropical and convective vs non-convective cirrus clouds). The diagnosed crystal habits are used to calculate all the habit-dependent parameters. These parameters are calculated as the value weighted by the percentage of various crystal shapes (Mitchell 1988, 1994; Mitchell & Arnott 1994) and are put in the two-dimensional look-up table.

c. Crystal terminal velocity

The new formulation of ice fall speed of Khvorostyanov & Curry (2002) is used. The parameters $\alpha_{u,x}$ and $\beta_{u,x}$ are there calculated in function of the coefficients in (1.3a,b), and size of particle corresponding to the particle of mean flux-weighted size, for given ambient conditions.

In the used bulk approach with two moments, the average mass-weighted ($U_{M,x}$) and number-weighted ($U_{N,x}$) fall velocities for each hydrometeor category are needed. For the assumed size distribution:

$$U_{Mx} \equiv \frac{\int_{X_{\min}}^{X_{\max}} u_x(D) m_x(D) n_x(D) dD}{\int_{X_{\min}}^{X_{\max}} m_x(D) n_x(D) dD} \approx \frac{\Gamma(\mu_x + \beta_{u,x} + \beta_{m,x})}{\Gamma(\mu_x + \beta_{m,x})} \alpha_{u,x} D_{nx}^{\beta_{u,x}} f_z = g_{u,x} u_x(D_{\bar{m},x}) f_z \quad (78)$$

with

$$g_{u,x} \equiv \frac{\Gamma(\mu_x + \beta_{u,x} + \beta_{m,x})}{\Gamma(\mu_x + \beta_{m,x})} \left[\frac{\Gamma(\mu_x)}{\Gamma(\mu_x + \beta_{m,x})} \right]^{\beta_{u,x}/\beta_{m,x}}$$

and

$$U_{Nx} \equiv \frac{\int_{X_{\min}}^{X_{\max}} u_x(D) n_x(D) dD}{\int_{X_{\min}}^{X_{\max}} n_x(D) dD} \approx \frac{\Gamma(\mu_x + \beta_{u,x})}{\Gamma(\mu_x)} \alpha_{u,x} D_{nx}^{\beta_{u,x}} f_z \quad (79)$$

or

$$U_{Nx} = g_{ur,x} U_{Mx} \quad (80)$$

$$\text{with } g_{ur,x} \equiv \frac{\Gamma(\mu_x + \beta_{m,x})}{\Gamma(\mu_x)} \frac{\Gamma(\mu_x + \beta_{u,x})}{\Gamma(\mu_x + \beta_{u,x} + \beta_{m,x})}.$$

Thus, the average fall velocities are expressed in terms of the terminal velocity of the mean mass particle of a given category. The coefficients $\alpha_{u,x}$ and $\beta_{u,x}$ are calculated for particle of size $D_{\bar{m},x}$. However, for pristine ice category with value of Re around 1, the approximate relation are used giving $\alpha_{u,x}$ and $\beta_{u,x}$ independent on size, as demonstrated in Khvorostyanov & Curry (2002).

f_z is a correction factor applied to the fall-speeds that expresses the dependence on air density and also air viscosity. It is calculated as Khvorostyanov & Curry (2002); in this form the increase of velocity with altitude is not the same for smaller and larger particles.

2. Nucleation processes

Since the importance of the nucleation processes is not in the mass transfer (the nucleation process itself does not provide a major source of condensate water), but in injection of new particles (it acts as a seed), the rate of these processes, discussed below, represents the rate of change of number concentration. The initial mass of nucleated particles is a tunable parameter. In general, the model results are not sensitive on the exact value of this initial average particle mass.

a. Local or Lagrangian approach

One of the question concerning the calculation of the rate of nucleation process in the models is: the formulas used to describe the number concentration of nucleated particles (droplets or ice crystals) have to be treated: i) locally , or ii) in the Lagrangian approach?

In the first approach, the number predicted by the formula is given as a total number which nucleate under given environmental conditions. If the activated particles already exist locally on a given time step, the nucleation produces fewer particles so that the total number will equal to the number predicted by the formula. When the existing number of particles exceeds this amount, they are allowed to remain, and no nucleation process. Thus, for $x = c$ or i , the nucleation rate is found from

$$NUC_x \equiv \frac{dN_x}{dt} \Big|_{NUC} = \frac{1}{\Delta t} \max [N_{nx} - N_x, 0] \quad (81)$$

where N_{nx} is predicted number concentration of active nuclei in given conditions, and N_x is the number concentration of particles already activated att. This treatment of the nucleation process has been used for ice nucleation by Meyers (1995), Girard & Blanchet (2001), among others.

In the Lagrangian approach, as in the laboratory experiments, a number of activated nuclei within the given volume, is equal to dN_x . Thus, in the model, if the time characteristic of activation is less than the displacement time between two gridpoints, the Lagrangian approach seems to describe better the physics of process and to be in better accord with the manner in which the applied formulas have been obtained. With this approach, the nucleation rate, given by the change in the concentration of activated nuclei through parcel lifting, is obtained from

$$NUC_x \equiv \frac{dN_x}{dt} \Big|_{NUC} = - \frac{dN_{nx}}{d\gamma} \frac{d\gamma}{dt} \quad (82)$$

where γ may describe the temperature or supersaturation. This approach is found in the model of Khvorostyanov & Sassen (1998), Cotton et al. (1982) and others.

c. Droplet nucleation

For droplet activation, the number concentration of CCN concentration, i.e. N_{nc} in (2.1-2.2), limited by the advected concentration of aerosol, N_a , is determined in function of water supersaturation, s_w (in %):

$$N_{nc} (N_{CCN}) = C_a s_w^{k_a} \quad (83)$$

DeMott et al. (1994, 1998) used the values of 200 and 1.5 for spectral concentration and power coefficients. The same values are used in this scheme. However, it is planned to introduce the size spectra of deliquescent haze based on simple analytical model with account for hygroscopic growth developed by Khvorostyanov & Curry (1999), that gave good results in Girard & Blanchet (2001).

The present calculations of the number of activated droplet using (83) are done as in Khairoutdinov & Kogan (2000). The supersaturation $s_{w\max}$ is introduced as the supersaturation needed to activate the total particle counts: $N_a + N_c$. Thus, the rate of droplet nucleation is given by

$$NUC_c = \frac{1}{\Delta t} \left[(N_a + N_c) (s_w / s_{w\max})^{k_a} - N_c \right] \quad (84)$$

On the other hand, as shown by Soong (1974), at each time step, the maximum mass of liquid water added by CCN activation is evaluated as

$$(NUC_c \cdot \Delta t)_{\max} = \frac{1}{m_{CNN}} \frac{q_v - q_{sw}}{1 + \frac{\varepsilon L_v^2 e_s}{R_v c_p T^2}} \quad (85)$$

New droplets enter as 1 μm radius particles and it is assumed that they nucleate at the end of the time step; their further rapid growth by condensation is calculated during the next time step.

d. Heterogeneous nucleation of ice from water vapor

Ice formation in cirrus clouds may result from both homogeneous freezing of solution droplets formed on soluble CCN and heterogeneous nucleation of ice by insoluble or partially insoluble particles. The homogeneous nucleation dominates below -40 °C. The importance of heterogeneous nucleation has been open to question due to a shortage of information on concentration and properties of ice-forming nuclei. The physical mechanisms considered for heterogeneous nucleation of ice are: a) deposition and condensation freezing (transfer of water vapor to crystal), b) immersion-freezing, and c) contact nucleation.

The parameterization of the measured IFN concentration active via nucleation by deposition (D) and by condensation-freezing (F) from water vapor is combined to form one expression due to their sensitivity to vapor mass concentration. The more common approach to parameterize the number concentration of these N_{IFN} , i.e. N_{ni} in (81) and (82), limited by advected number concentration of N_n , is the use of the empirically-based parameterization of Meyers et al. (1992). This formula is based on analysis of the data from a continuous-flow diffusion chamber. It shows an exponential variation of IFN concentration with ice supersaturation, $s_i = (S_i - 1)$:

$$N_{ni}(N_{IFN(D,F)}) = \exp[a_i \cdot s_i - b_i] \text{ (in } l^{-1}) \quad (2.6)$$

The coefficients a_i and b_i are dependent on the environmental conditions. The assumed values are: 12.96 and 0.639, respectively. The measurements agree to within an order of magnitude for -7°C to -20°C temperature range and for ice supersaturations up to 25%. Here, and in the other numerical models this relation is used for a wider range of conditions than it was originally proposed. The parameterized IFN concentration by this formula may exceeds the range of concentration measured. For example, in Rogers et al. (1998) the range was 0.0001 to 0.1 cm^{-3} with processed aerosols at conditions from about -15°C to -40°C and from ice saturation to about 15% water supersaturation. N_{ni} from formula equal to 1 cm^{-3} when $S_i=1.38$. Thus, the above formula is expected to represent a maximum of the ice particle formation due to heterogeneous nucleation. To prevent the unrealistically high numbers of pristine ice crystals, at temperatures below -27°C, the IFN concentration is set to the ice concentration at -27°C.

In general, using the Lagrangian approach, the problem of overestimation of the IFN concentration is avoided. Then, the rate of nuclei activated when a parcel of air passes through a gridbox can be approximated by

$$NUC_{i(D,F)} = \frac{dN_i}{dt} \Big|_{NUC_{(D,F)}} = \frac{dN_{IFN(D,F)}}{ds_i} \frac{ds_i}{dt} = a_i N_{IFN(D,F)} \frac{ds_i}{dt} \text{ if } ds_i/dt > 0 \quad (2.7)$$

$N_{IFN(D,F)}$ is still assumed to be the maximum possible value of ice crystal concentration for a given supersaturation. The $s_i(t)$, i.e. s_i at the previous time step, is calculated from $T(t)$ and $q_v(t)$, derived in the manner described in Section 3.d.

The relation (2.6) may be replaced by the modified Fletcher relation, or by a fit to in situ ice crystal measurements by Cooper (1986).

Some modellers consider that the concentration of active nuclei via the immersion-freezing mechanism is included in (2.6) (Meyers et al. 1997; Kong & Yau (1997; Cotton et al. 1982)). They consider that the activity of the IFN population via immersion-freezing is already accounted within the deposition/condensation freezing parameterization. The other modellers consider that the immersion-freezing is not included in (2.6), and the separated calculation is done that injects additional number of ice particles activated via immersion-freezing process (Levkov et al. 1992; Ovtchinnikov & Kogan 2000; Yin et al. 2000). The chosen treatment here is the same as in Girard & Blanchet (2001): IFN acting as immersion-freezing nuclei are

included in the Meyers relation, but their number is calculated using the formula obtained for this process exclusively taking into account the number concentration of unfrozen droplets. The Meyers formula is used as the maximum value.

e. Heterogeneous nucleation by contact

The parameterization for the number of IFN available for contact freezing (C) nucleation is taken from Meyers et al. (1992):

$$N_{IFN(C)} = \exp[-2.8 - 0.2629T_c] \text{ (in } l^{-1}) \quad (2.8)$$

based on an accumulation of various laboratory data for natural aerosols. They analyzed nearly all available data. T_c is in Celsius degrees. The fraction of the activity realized in any time step is determined by the collection rates of ice nuclei by cloud droplets due to combined effects of Brownian collection, thermophoresis, diffusiophoresis, and aerodynamic capture.

The rate of nucleation by contact freezing via Brownian diffusion may be written as (Levkov et al. 1992; Cotton et al. 1986; Lohmann and Roeckner 1996)

$$NUC_{i(C)} = \frac{1}{\Delta t} F_{ct} D_{ae} \quad (86)$$

where D_{ae} is the aerosol diffusivity, and $F_{ct} = 4\pi r_{c,\bar{m}} N_{IFN(C)} N_c$. $r_{c,\bar{m}}$ is the mean volume cloud droplet radius. The Brownian aerosol diffusivity is calculated from

$$D_{ae} = \frac{kTC_c}{6\pi\eta r_{am}} \quad (87)$$

where k is the Boltzmann constant, η temperature-dependent viscosity of air, r_{am} the aerosol mode radius, and $C_c = 1 + 1.26 \frac{\lambda}{r_{am}} \frac{p_0}{p} \frac{T}{T_0}$ is the Cunningham correction factor with λ describing the molecular free pathlength of air (Lohmann 2002).

In this parameterization the Brownian-diffusion contact nucleation results from random collision of aerosol particles with supercooled droplets. The more detailed parameterization for this process is planned. The proposed scheme is that described by Ovtchinnikov & Kogan (2000).

It can be noted that the counts of active IFN according to (2.6) and (2.8) are of the same order in the cirrus cloud conditions. The collision efficiencies of the scavenging are rather small. Thus, the concentration of ice particles generated by the contact freezing may be by a factor of about 1000 smaller than that generated via deposition/condensation-freezing. For warmer conditions, it is not true. However, the deposition/condensation-freezing process forms only very small crystals, while in the contact freezing large frozen drops can be produced.

f. Immersion-freezing nucleation

The immersion-freezing process is treated as in Girard & Curry with two important modifications:

- 1) the droplet distribution at the start point is considered as truncated at the volume $V_c^0(t)$
- 2) the mean mass of droplets transferred to ice is taken for droplet with the volume $V_c^0(t + 0.5\Delta t)$, i.e. at the mid-time.

The used formula, first suggested by Heverly (1940), is the experimentally derived relation that predicts the supercooling (T_{sup}) that expresses the median freezing temperature below 0 °C of a population of drops of volume V_c^0 . The stochastic hypothesis leads then to the following relation (transformed eq. 9.54 in PK1997)

$$V_c^0 = \frac{a_{htn} \ln 2}{B_{htn}} \left(-\frac{dT}{dt} \right) \exp [-a_{htn} T_{sup}] \quad (88)$$

where $-dT/dt$ is a cooling rate. For the parameter a_{htn} is chosen its mean value, $0.65(\text{ }^\circ)^{-1}$, independent of the type of water. The values of B_{htn} vary from $2.9E - 8$ (found by Bigg for water of high purity) to $2.0E - 4$ (PK1997 for rain water) $\text{cm}^{-3} \text{ s}^{-1}$.

The calculations in the model are done as follows. Assuming constant cooling rate during the time step, the value of the volume at which the droplet distribution is truncated at the beginning of the time step, $V_c^0(t)$, is calculated from $T_{sup}(t)$ using (88). The new value of $V_c^0(t + \Delta t)$ corresponds to the supercooling at $t + \Delta t$: $T_{sup}(t + \Delta t)$. Thus, from (88):

$$\frac{V_c^0(t + \Delta t)}{V_c^0(t)} = \exp[a_{htn}\Delta T] \equiv R_{vol} \quad (89)$$

where $\Delta T = T(t + \Delta t) - T(t)$. Since during freezing, the parameters describing droplet size distribution do not change (besides, of course, the truncation limit), the number concentration of droplet population truncated at $V_c^0(t + \Delta t)$ is related to the $N_c(t)$ by

$$N_c(t + \Delta t) = N_c(t) \frac{1 - \exp[-R_{vol}X_v]}{1 - \exp[-X_v]} \quad (90)$$

for the assumed droplet size distribution; $X_v \equiv V_c^0(t)/V_{nc}$. Thus, the number concentration of droplets that freeze via immersion-freezing during the time step is

$$-\Delta N_c = N_c(t) \left\{ 1 - \frac{1 - \exp[-R_{vol}X_v]}{1 - \exp[-X_v]} \right\} \quad (91)$$

The estimation of the value of X_v is required in the above relation.

The value of X_v may be found from the following relation, obtained for the assuming droplet distribution, truncated at V_c^0

$$\frac{V_c^0}{V_{c,\bar{m}}} = \frac{1}{\frac{1}{X_v} - \frac{\exp[-X_v]}{1 - \exp[-X_v]}} \quad (92)$$

where $V_{c,\bar{m}} = (1/\rho_{liq}) q_c \rho_a / N_c$ is the volume of the mean mass droplet, known at t . To avoid the iteration procedure, (92) is treated separately for three different regimes for the ratio $V_c^0/V_{c,\bar{m}} \equiv Y_v$:

1. for $Y_v \geq 5.3$, the approximation $X_v \approx Y_v$ constitutes a good approximation
2. for $2.4 \leq Y_v < 5.3$, the precalculated by iteration the look-up table contains the values of X_v having the range between 1 and 5.3
3. for $Y_v < 2.4$, X_v is < 1 and it is extremely sensitive to Y_v . However, in this case, it can be demonstrated, by using the Taylor series, that the term in the parentheses in Eq. (91) is almost independent on X_v and may be approximated by $1 - R_{vol}$.

The nucleation rate $NUC_{i(I)} = \Delta N_c / \Delta t$, that represents the number of droplets that freeze during the time step and are transferred to the pristine ice category, may be found from (91). To determine the mass of liquid water that is transferred to pristine crystal category, it is assumed that the mean size of droplets that became frozen during this time step, is equal to $V_c^0(t + 0.5\Delta t)$.

g. Homogeneous nucleation

The parameterization of the homogeneous freezing process assumes nucleation upon two separate population: activated cloud droplets where the solute and curvature effects are negligible, and unactivated haze solution droplets.

The homogeneous freezing of cloud droplets is formulated following deMott et al. (1994):

$$NUC_{i(\text{hom } c)} = - \left. \frac{dN_c}{dt} \right|_{NUC_{i(\text{hom } c)}} = \frac{1}{\Delta t} \int [1 - \exp(-J_{hc} V_c \Delta t)] n_c(V_c) dV_c \quad (93)$$

$J_{hc} = J_{h0}$ is the nucleation rate for pure water. It is taken from Heymsfield and Sabin (1989) who used the temperature dependent formulation given by Eadie (1971):

$$J_{h0} = 10^{y_{hc}}$$

$$\text{with } y_{hc} = -606.3952 - 52.6611T_c - 1.7439T_c^2 - 0.0265T_c^3 - 1.536 \cdot 10^{-4}T_c^4$$

For the homogeneous freezing of haze particles, the parameterization of Kärcher & Lohmann (2002) has been chosen. The rate of number of newly frozen ice crystals via homogeneous nucleation at temperatures below -35 °C is calculated from

$$NUC_{i(\text{hom } h)} = \frac{dN_i}{dt} \Big|_{NUC_{(\text{hom } h)}} = \max \left[\frac{m_w}{\rho_i} \left(\frac{b_2}{2\pi b_1} \right)^{1.5} \frac{a_1 S_{cr}}{a_2 + a_3 S_{cr}} \frac{w}{\sqrt{\tau}}; N_a \right] \Big/ \Delta t \quad (94)$$

with m_w and ρ_i : molecular weight of water and ice density, respectively. The variables: a_1 , a_2 , a_3 , b_1 , b_2 are temperature-dependent variables described in Kärcher & Lohmann (2002). S_{cr} is the critical supersaturation where freezing starts, and τ describes the characteristic timescale for the nucleation event, and it is related to the cooling rate of the air parcel.

3. Vapor diffusional growth

The variability of the temperature and pressure may be important in the conditions where the cirrus clouds are generated. Thus, the temperature and pressure dependent functions: coefficients of diffusion and thermal conductivity, dynamic viscosity and latent heat of vaporization and sublimation, are not longer maintained constant, but they are calculated in function of temperature and pressure.

Addition of the radiative effects on the diffusional growth is planned, but not done yet.

The calculated rates are the rates of mass transfer (i.e. of mixing ratio change) during the diffusion process.

a. Cloud droplets

The rate of growth by diffusion of cloud droplets is calculated using the diffusional growth of the mean-mass droplet:

$$VDF_c = \frac{1}{\rho_{air}} N_c \frac{dm_c}{dt} \Big|_{V_c=V_{\bar{m},c}} \quad (95)$$

The growth equation takes into account gas kinetic effects, very important for small droplets, using the approximation proposed by Clark (1974):

$$\frac{dm_c}{dt} = 4\pi \left(\frac{3}{4\pi\rho_{liq}} \right)^{1/3} \frac{\delta_w}{q_{sw}(A' + B')} \frac{m_c^{2/3}}{m_c^{1/3} + l_o^*} \quad (96)$$

where $A' + B'$ is a function of temperature and pressure (RY1989), q_{sw} is the saturation mixing ratio in respect to liquid water, $\delta_w = q_v - q_{ws}$, and l_o^* corresponds to a length scale: $l_o^* = \left(\frac{4\pi}{3} \rho_{liq} \right)^{1/3} l_o$ with $l_o = 5 \mu\text{m}$.

b. Pristine ice crystals

The deposition term, VDF_i , is calculated using the empirical formula proposed by Koenig (1972) applied to the crystal with the mean-mass of the distribution, $\bar{m} = q_i \rho_a / N_i$:

$$VDF_i = \frac{1}{\rho_{air}} N_i (a_{k1} \bar{m}^{a_{k2}}) G_i \quad (97)$$

with a_{k1} and a_{k2} temperature-dependent parameters which include the influence of particle habit. These parameters were inferred by Koenig from growth rate calculations for temperature between 0 and -31°C and a pressure of 1000 mb, and they refer to water saturation. Gierens (1996) has performed the calculations of these parameters at temperatures between -40 and -60°C at a pressure of 250 mb. Here, the Gierens's values have been recalculated for 1000 mb to be consistent with the values in Koenig. Between -31 and -40°C, the values have been interpolated at integer temperatures. For temperatures below -60°C, the values have been set to the values at -60°C. The actual supersaturation at the gridpoint is accounted for by

multiplying the growth rate by the factor $\delta_i/(q_{sw} - q_{si})$, where $\delta_i = q_v - q_{si}$. The pressure conditions are introduced by multiplying by the ratio: p/1000mb. The term G_i represents these two factors. The correction factor, introduced by Girard & Blanchet (2001), to compensate the effect of dispersion of the particle size distribution on the expression for the total diffusional rate, is here approximated by 1.

c. Snow crystals

The growth by diffusion of the larger crystals (snow) is done as in Meyers et al. (1997) or Harrington et al. (1995) taking into account the ventilation effect and the shape factor. The capacitance is calculated as the value weighted by the percentage of various crystal shapes present at the given gridpoint.

d. Treatment of the simultaneous diffusional growth of drops and ice crystals

For correct description of the evolution of the mixed phase clouds, a rigorous treatment of supersaturation is required.

The expressions for the rate of change of the mixing ratio of the x th category via the vapor diffusion processes (as described in 3.a to c) may be written as

$$VDF_x = \frac{dq_x}{dt} \Big|_{VDF} = \delta_{w,i} F_x \quad (98)$$

where $\delta_{w,i} = q_v - q_{sw,i}$ (δ_w , q_{sw} and δ_i , q_{si} for liquid and solid hydrometeors, respectively). Thus, the change of the mixing ratio during one time step is equal to

$$\Delta q_x = \int_t^{t+\Delta t} \delta_{w,i} F_x dt \quad (99)$$

It is assumed that the change of F_x is negligible during one time step and thus:

$$\Delta q_x = F_x \int_t^{t+\Delta t} \delta_{w,i} dt = F_x I_{\delta_{w,i}} \quad (100)$$

The integral $I_{\delta_{w,i}}$ is calculated as in Reisin et al. (1996) using their relations (32) and (33) for liquid and solid particles respectively that have been developed for the bin-microphysics model. They have been obtained from a set of two partially coupled differential equations, (B8) and (B9) in Reisin et al. giving the rate of change in time of δ_w and δ_i . However, this equations are treated locally, and do not include the progressive saturation increase within the parcel due to the updraft. Thus, I added the terms that represent the updraft w in (B8) and (B9), and the final form of the (32) and (33) is modified, and becomes

$$I_{\delta_w} \equiv \int_t^{t+\Delta t} \delta_w(t') dt' = \\ \delta_w(t) \Delta t - \frac{\Delta t}{R_w + R_i} \left[R_w \delta_w(t) + P_i \delta_i(t) - \frac{\Gamma_{dry} w}{R_w + R_i} \left(\frac{dq_{sw}}{dT} R_w + \frac{dq_{si}}{dT} P_i \right) \right] \times \\ \left\{ 1 - \frac{1 - \exp[-(R_w + R_i) \Delta t]}{(R_w + R_i) \Delta t} \right\} \quad (101)$$

$$I_{\delta_i} \equiv \int_t^{t+\Delta t} \delta_i(t') dt' = \\ \delta_i(t) \Delta t - \frac{\Delta t}{R_w + R_i} \left[P_w \delta_w(t) + R_i \delta_i(t) - \frac{\Gamma_{dry} w}{R_w + R_i} \left(\frac{dq_{sw}}{dT} P_w + \frac{dq_{si}}{dT} R_i \right) \right] \times \\ \left\{ 1 - \frac{1 - \exp[-(R_w + R_i) \Delta t]}{(R_w + R_i) \Delta t} \right\} \quad (102)$$

The functions R_w , R_i , P_w , P_i are defined in the same manner that in Reisner; their are functions of F_x and thermodynamical fields.

The values of $\delta_w(t)$ and $\delta_i(t)$ at the start point of the parcel can be calculated directly from the temperature and humidity fields at the initial point in the advection calculations. Since, in the MRC model this operation may be more complicated and requires the additional

information from the dynamical module, this fields are calculated here within the microphysical scheme as follows: the humidity field is stored at the beginning of the subroutine (humidity field doesn't change during advection only); the temperature field in the subroutine input represents the intermediate state after integrating all the other than microphysical processes. If the horizontal and radiation effect are neglected, the temperature at the start point is evaluated from:

$$T(t) = T * (t + \Delta t) + \frac{g}{c_p} w \Delta t \quad (103)$$

where the symbol $*$ describes the value at this intermediate state.

As in Reisin et al., if δ_w or δ_t change sign within one time step, the time, Δt^1 , required to change the sign, is calculated, and the calculation is split within the time step on Δt^1 and $\Delta t - \Delta t^1$.

The initial mass of the nucleated particles is chosen sufficiently small to not lead to important changes of humidity and temperature fields. Their further rapid diffusional growth is included into the rate of diffusional growth of droplets or pristine ice crystals. For these reasons, the nucleation terms is not included in the calculated $I_{\delta_{w,i}}$.

During the course of a time step, the temperature and the hydrometeor characteristics, change. If the time step is not too large, these values may be treated as constant for practical purposes. However, for the longer time steps when the changes may be important, the calculations may be done by dividing the time step into the smaller substeps for diffusional growth.

4. Collection processes riming growth of snow particles, collection of ice crystals by snow and aggregation among snow particles

The general form of the collection term for x particle collecting y particle is

$$\left. \frac{dm_x}{dt} \right|_{XCY} = \int_0^\infty \frac{\pi}{4} (D_x + D_y)^2 |u_x(D_x) - u_y(D_y)| E(D_x, D_y) m_y(D_y) n_y(D_y) dD_y \quad (104)$$

This expression is simplified as follows:

- $E(D_x, D_y)$ is replaced by an average value:

$$E_{xy} = \frac{\iint E(D_y, D_x) m_y(D_y) n_y(D_y) n_x(D_x) dD_y dD_x}{\iint m_y(D_y) n_y(D_y) n_x(D_x) dD_y dD_x} \quad (105)$$

- $(D_x + D_y)^2 \approx (D_{\bar{m},x} + D_{\bar{m},y})^2$
- $|u_x(D_x) - u_y(D_y)| \approx |u_x(D_{\bar{m},x}) - u_y(D_{\bar{m},y})|$

The integration of (104) with the simplifications above over the entire distribution of particles of x category gives the following general relationship:

$$XCY = \frac{1}{\rho_a} \int \left. \frac{dm_x}{dt} \right|_{XCY} dN_y = \frac{\pi}{4} (D_{\bar{m},x} + D_{\bar{m},y})^2 |u_x(D_{\bar{m},x}) - u_y(D_{\bar{m},y})| E_{xy} q_x \rho_a N_y \quad (106)$$

In spite of the fact that the sedimentation of the cloud droplets is neglected, it is taken into account in the calculation of the collection rate. The used formula is the one for droplets with diameter smaller than 60 μm in RY1989: $u_c(D_c) = k_c D_c^2$ with $k_c = 0.3E + 6 \text{ cm}^{-1} \text{ s}^{-1}$.

The average values of the collection efficiency are:

- for cloud droplets collected by snow particles: $E_{cs} = 0.572 \log_{10} [464D_{\bar{m},c} - 0.25] + 1.69$ as in Reisner et al. (1998)

- for ice pristine crystals collected by snow particles: $E_{is} = \min \left\{ \frac{e}{e_{is}} E_{o,\chi} \exp [0.05T_c], 1 \right\}$ where $E_{o,\chi}$ is calculated in function of the crystal habits, and T_c is the temperature in deg C.

The factor e/e_{is} introduces the dependence of collection efficiencies on vapor pressure over ice according to the experimental data presented by Hosler et al. (1957).

The rate of decrease of the number concentration of collected particles is given by:

$$-\frac{dN_y}{dt}\Big|_{XCY} = \frac{N_y}{M_y} XCY \quad (107)$$

The aggregation between pristine ice crystals with the conversion rate to snow is parameterized as in Murakami (1990).

The self-collection process for snow, called aggregation, is treated as proposed by Passarelli (1978) using the Gauss' hypergeometric function. The decrease in number concentration of snow due to aggregation among snow crystals is given by

$$-\frac{dN_s}{dt}|_{SCS} = g_{ss} E_{ss} U_{Ms} q_s \rho_a N_s \quad (4.5) \quad (4.5)$$

$$\text{with } g_{ss} = \frac{\pi}{4} \frac{I_{Pass}(\mu_s - 1, \beta_{u,s})}{\Gamma(\mu_s)\Gamma(\mu_s + \beta_{u,s} + 2)} \frac{1}{\alpha_{m,s}}$$

where

$$I_{Pass}(\mu_s - 1, \beta_{u,s}) = \int \int (x_1 x_2)^{\mu_s - 1} (x_1 + x_2)^2 \left| x_1^{\beta_{v,s}} - x_2^{B_{v,s}} \right| \exp[-(x_1 + x_2)] dx_1 dx_2 \quad (108)$$

defined in Abramowitz and Stegun (1964). The parameter μ_s is fixed, and $\beta_{u,s}$ is evaluated from the present crystal shapes and mean-mass crystal from Khvorostyanov & Curry (2002). As for other shape dependent values, I_{Pass} is taken from precalculated look-up tables. The collection efficiency is assumed temperature dependent and in the same form as E_{is} . U_{Ms} represents the mass-weighted terminal velocity for snow.

5. Conversion of small pristine ice to snow

The concentration and mass mixing ratio transferred between the pristine ice and snow spectra (ITS) are calculated by the method developed by Harrington et al. (1995) during conditions of ice supersaturation and subsaturation. In an ice supersaturated conditions, the calculations of the transfer from the pristine to the snow have been modified to be consistent with the pristine vapor deposition calculations. From Harrington et al. (1995):

$$ITS = -\frac{dq_i}{dt}\Big|_{ITS} = \frac{dq_s}{dt}\Big|_{ITS} = \frac{1}{\rho_a} m(D_{s \min}) \frac{dD}{dt}\Big|_{VDF \text{ for } D=D_{s \min}} \cdot n_i(D_{s \min}) + \frac{1}{\rho_a} \int_{D_{s \min}}^{\infty} \frac{dm}{dt} n_i(D) dD \quad (5.1)$$

The two terms on the RHS are expressed in terms of VDF_i , the deposition rate for the pristine ice, as follows:

$$\begin{aligned} \frac{1}{\rho_a} m(D_{s \min}) \frac{dD}{dt}\Big|_{VDF \text{ for } D=D_{s \min}} \cdot n_i(D_{s \min}) &= \frac{1}{\rho_a} m(D_{s \min}) \left[\frac{1}{\beta_{m,i}} \frac{D_{s \min}}{m(D_{s \min})} \frac{dm}{dt}\Big|_{VDF \text{ for } D=D_{s \min}} \right] \cdot n_i(D_{s \min}) \\ &= VDF_i \left(\frac{D_{s \min}}{D_{m,i}} \right)^{\beta_{m,i} a_{k2}} \frac{1}{\Gamma(\mu_i)} \frac{1}{\beta_{m,i}} X_{bi}^{\mu_i} \exp[-X_{bi}] \end{aligned} \quad (109)$$

and

$$\frac{1}{\rho_a} \int_{D_{s \min}}^{\infty} \frac{dm}{dt} n_i(D) dD = VDF_i \cdot \left[\int_{D_{s \min}}^{\infty} \frac{dm}{dt} n_i(D) dD \Big/ \int_0^{\infty} \frac{dm}{dt} n_i(D) dD \right] = VDF_i \cdot \frac{\Gamma(\mu_i + 1, X_{bi})}{\Gamma(\mu_i)} \quad (5.1b)$$

The number of particles transferred is:

$$-\frac{dN_i}{dt}\Big|_{ITS} = \frac{dN_s}{dt}\Big|_{ITS} = n_i(D_{s \min}) \frac{dD}{dt}\Big|_{VDF \text{ for } D_i=D_{s \min}} \quad (110)$$

calculated using (109).

X_{bi} is given by $X_{bi} = \frac{D_{s\min}}{D_{ni}} = \frac{D_{s\min}}{g_{ni} D_{\bar{m},i}}$ with $g_{ni} = \left[\frac{\Gamma(\mu_i)}{\Gamma(\mu_i + \beta_{m,i})} \right]^{1/\beta_{m,i}}$.
The truncated gamma function is calculated from:

$$\Gamma(n+1, X) \equiv \int_X^\infty Y^n \exp(-Y) dY = n! \exp(-X) \sum_{i=0}^n \frac{1}{i!} X^i \quad (111)$$

In the conditions subsaturated with respect to ice, the transfer of snow particles to pristine ice (*STI*) is described by

$$\begin{aligned} STI &= -\left. \frac{dq_s}{dt} \right|_{STI} = \left. \frac{dq_i}{dt} \right|_{STI} \approx -\frac{1}{\rho_a} m(D_{s\min}) \left. \frac{dD}{dt} \right|_{VDF \text{ for } D=D_{s\min}} \cdot n_s(D_{s\min}) \\ &= \frac{1}{\rho_a} \frac{4\pi}{q_{si}(A''+B'')} I_{\delta_i} \frac{1}{\Gamma(\mu_s)} N_s \chi_s D_{s\min} \frac{1}{\beta_{m,i}} X_{bs}^{\mu_s} \exp(-X_{bs}) \\ -\left. \frac{dN_s}{dt} \right|_{STI} &= \left. \frac{dN_i}{dt} \right|_{STI} = -n_s(D_{s\min}) \left. \frac{dD}{dt} \right|_{VDF \text{ for } D_i=D_{s\min}} \\ &= \frac{4\pi}{q_{si}(A''+B'')} I_{\delta_i} \frac{1}{\Gamma(\mu_s)} N_s \chi_s D_{s\min} \frac{1}{\beta_{m,s}} X_{bs}^{\mu_s} \exp(-X_{bs}) \cdot \left[\alpha_{m,s} D_{s\min}^{\beta_{m,s}} \right]^{-1} \end{aligned}$$

where $X_{bs} = \frac{D_{s\min}}{D_{ns}} = \frac{D_{s\min}}{g_{ns} D_{\bar{m},s}}$ with $g_{ns} = \left[\frac{\Gamma(\mu_s)}{\Gamma(\mu_s + \beta_{m,s})} \right]^{1/\beta_{m,s}}$

The term describing the loss of snow mass mixing ratio in the region $[0, D_{s\min}]$ due to sublimation is dropped here, as in Harrington et al.

I.2 References

Bonardet, Pierre, 2002: Etude du transport d'aérosols avec le modèle NARCM et calcul des paramètres optiques. Rapport de stage d'étude du LMD, Paris, 101pp.

de Roode, Stephan R., and Peter G. Duynkerke, 1997: Observed lagrangian transition of stratocumulus into cumulus during ASTEX: mean state and turbulence structure. *J. Atmos. Sci.*, **54**: 2157–2173.

ERM Final Report, 2000 : *Study on synergetic observations of Earth Radiation Mission instruments*. Final Report, European Space Agency, ESA MPBT 512SR006, Version 2.0 (October 3, 2000).

Grabowski, W. W., X. Wu and M.W. Moncrieff, 1998: Cloud-resolving Modeling of Cloud Systems during Phase III of GATE. Part II: Effects of Resolution and the Third Spatial Dimension. *J. Atmos. Sci.*, **55**, 3264-3282.

Liu, C., M.W. Moncrieff and W.W. Grabowski, 2000: Explicit and parameterized realizations of convective cloud systems in TOGA COARE. *Mon. Wea. Rev.*, **129**

Wood, R., 2002: Drizzle in stratocumulus clouds: observations and model results. *11th conf. on cloud physics*. (Available online from <http://www.ametsoc.org/ams/>)

Yano, J.-I., M.W. Moncrieff, and W.W. Grabowski, 2001: Walker-type mean Circulations and Convectively Coupled Tropical Waves as an Interacting System. *J. Atmos. Sci.*, **59**, 1566-1577.